

5-2015

High-precision time-series photometry for the discovery and characterization of transiting exoplanets.

Karen Alicia Collins 1962-
University of Louisville

Follow this and additional works at: <https://ir.library.louisville.edu/etd>

 Part of the [Astrophysics and Astronomy Commons](#), and the [Physics Commons](#)

Recommended Citation

Collins, Karen Alicia 1962-, "High-precision time-series photometry for the discovery and characterization of transiting exoplanets." (2015). *Electronic Theses and Dissertations*. Paper 2104.
<https://doi.org/10.18297/etd/2104>

This Doctoral Dissertation is brought to you for free and open access by ThinkIR: The University of Louisville's Institutional Repository. It has been accepted for inclusion in Electronic Theses and Dissertations by an authorized administrator of ThinkIR: The University of Louisville's Institutional Repository. This title appears here courtesy of the author, who has retained all other copyrights. For more information, please contact thinkir@louisville.edu.

HIGH-PRECISION TIME-SERIES PHOTOMETRY FOR THE
DISCOVERY AND CHARACTERIZATION OF TRANSITING
EXOPLANETS

By

Karen A. Collins

B.S., Georgia Institute of Technology, 1984

M.S., Georgia Institute of Technology, 1990

M.S., University of Louisville, 2008

A Dissertation

Submitted to the Faculty of the

College of Arts and Sciences of the University of Louisville

in Partial Fulfillment of the Requirements

for the Degree of

Doctor of Philosophy

in Physics

Department of Physics and Astronomy

University of Louisville

Louisville, Kentucky

May 2015

HIGH-PRECISION TIME-SERIES PHOTOMETRY FOR THE
DISCOVERY AND CHARACTERIZATION OF TRANSITING
EXOPLANETS

By

Karen A. Collins
B.S., Georgia Institute of Technology, 1984
M.S., Georgia Institute of Technology, 1990
M.S., University of Louisville, 2008

A Dissertation Approved On

April 17, 2015

by the following Dissertation Committee:

Dissertation Director
Dr. John F. Kielkopf

Dr. James Lauroesch

Dr. Gamini Sumanesekera

Dr. John F. Naber

Dr. Gerard M. Williger

ACKNOWLEDGEMENTS

I would like to sincerely thank my research advisor and dissertation director, Dr. John F. Kielkopf, for his guidance, for somehow working uncountable all night sessions to support my research while maintaining his daytime teaching responsibilities, for his tireless efforts to build Moore Observatory into a competitive research facility and to keep it in top operating condition, and for just being a kind and thoughtful mentor and friend. I would also like to thank my high school mathematics teacher, Gerald Hite, who took me under his wing and set me on a path toward the mathematically rich fields of science and engineering. I would like to thank my parents, Betty Ann Causey and Wilton Eugene Collins, for providing me the opportunity to obtain my BSEE degree from the Georgia Institute of Technology, which equipped me with a solid educational foundation and enabled my pursuit of advanced degrees. I would like to thank Dr. Gerard M. Williger for opening a connection with the KELT team. I would like to thank the KELT team leaders, Dr. B. Scott Gaudi, Dr. Keivan G. Stassun, and Dr. Joshua Pepper who have graciously extended incredible research and learning opportunities to me, and I would like to thank KELT science team members, Dr. Thomas G. Beatty, Dr. Jason D. Eastman, and Robert J. Siverd, for sharing experience and knowledge that have greatly enriched my research experience. I would like to thank my dissertation committee members, Dr. James Lauroesch, Dr. Gamini Sumansekera, Dr. John F. Naber, and Dr. Gerard M. Williger, for supporting my research and graciously agreeing to participate as committee members.

I would like to thank my best friends Beanie, Emily, Jenny, Georgia, Nicky,

Snoopy, Abbie, and Zoey for (mostly) quiet friendship and companionship during many long nights of observing, AstroImageJ coding, and writing.

And finally, thanks to my partner, Angela Dee White, who encouraged me to follow a path that is important and rewarding to me, even at the expense of living on opposite day/night schedules for years.

This research was supported by graduate fellowships from the Kentucky Space Grant Consortium (KSGC). This research has made use of the Exoplanet Orbit Database and the Exoplanet Data Explorer at exoplanets.org, the Extrasolar Planets Encyclopaedia at exoplanets.eu, the SIMBAD database, operated at CDS, Strasbourg, France, and the Systemic Console software package for RV and TTV analysis. I would like to thank Antonio Claret for computing the quadratic limb darkening coefficients for the CBB and Open filter bands which were critical to properly fitting many of the light curves presented herein.

ABSTRACT

HIGH-PRECISION TIME-SERIES PHOTOMETRY FOR THE DISCOVERY AND CHARACTERIZATION OF TRANSITING EXOPLANETS

Karen A. Collins

April 17, 2015

The discovery of more than a thousand planets orbiting stars other than the Sun (i.e. exoplanets) over the past 20 years has shown that planetary systems are commonplace in the Milky Way galaxy. However, these discoveries are only a starting point in the quest to answer one of the most compelling questions posed by mankind for centuries – "are we alone in the universe?". This research aims to help build the foundation needed to search for that answer by optimizing data reduction techniques, determining and refining fundamental properties of known exoplanets, and searching for new exoplanets. Many exoplanets have been discovered using the radial velocity (RV) technique to measure small variations in a star's motion that are gravitational induced by an orbiting planet. The RV signal reveals the planetary mass, orbital period, and orbital eccentricity. If an exoplanet crosses the face of its host star (i.e. transits) from the perspective of the observer, it causes an apparent periodic dimming of the star. The depth and shape of those brightness variations reveal the planet's radius, its transit time, and some orbital characteristics. Combining the mass and radius measurements, a planet's mean density can be calculated, thus constraining its composition. During transit, part of the star's light

passes through the planetary atmosphere on its way to Earth, facilitating atmospheric measurements. Monitoring a planet's transit timing variations (TTVs) on many epochs may reveal the presence of another planet in the system due to gravitational interactions. I report the development of a new tool, AstroImageJ (AIJ), that provides an interactive environment for the optimal extraction and analysis of high-precision photometry from time-series observations. Based on AIJ photometry, I report high-precision measurements of system parameters and tight upper limits on TTVs derived from global analyses of 23 WASP-12b and 18 Qatar-1b complete transits. I also report the detection of sodium in the atmosphere of the exoplanet HD 189733b, the detection of z' band emission from the recently discovered hot brown dwarf, KELT-1b, and the discovery and characterization of the transiting hot-Saturn exoplanet, KELT-6b. Data for this research have been collected using the research-grade 0.6 m Moore Observatory RC (MORC) telescope, which is located near Louisville, Kentucky, and operated by the University of Louisville.

TABLE OF CONTENTS

	Page
ACKNOWLEDGEMENTS	iii
ABSTRACT	v
LIST OF TABLES	xiii
LIST OF FIGURES	xiv
CHAPTER	
1 INTRODUCTION	1
1.1 Star and Planet Formation	2
1.2 The Discovery of Exoplanets	3
1.3 Hot Jupiter Formation	4
1.4 Exoplanet Discovery Methods	5
1.4.1 Direct Imaging	5
1.4.2 Radial Velocity Method	6
1.4.3 Transit Method	7
1.4.4 Transit Timing Variations	10
1.4.5 Other Methods	12
1.5 Characterization Methods	12
1.5.1 Primary Transit Light Curve Modeling	13
1.5.2 Rossiter-McLaughlin Effect	16
1.5.3 Characterization of Exoplanet Atmospheres	18
1.6 Wide-field Transit Surveys	26
1.6.1 Ground-based	27
1.6.2 Space-based	32

2	HIGH-PRECISION PHOTOMETRY	37
2.1	CCD Overview	37
2.2	CCD Image Calibration	38
2.2.1	Bias Subtraction	38
2.2.2	CCD Nonlinearity Correction	38
2.2.3	Dark Subtraction	40
2.2.4	Flat-field Correction	42
2.2.5	Median Combining	44
2.2.6	Science Image Calibration	45
2.3	Telescope Guiding	45
2.4	Defocusing	47
2.5	Aperture Photometry	47
2.6	Variable Radius Aperture Photometry	49
2.7	Differential Photometry	50
2.8	Comparison Star Selection	51
2.9	Detrending Time Series Photometry	54
2.10	Real-time Monitoring of Observations	55
2.11	Error Calculations	56
3	INSTRUMENTATION	60
3.1	MORC Telescope	60
3.2	CCD camera	62
3.3	Filters	63
3.4	Dome Enclosure	65
3.5	Observatory Control Software	67
3.5.1	XmTel Telescope Mount Control	67
3.5.2	XmCCD Camera Control	68
3.5.3	PyDome and PyFocus	68
3.5.4	Guiding Scripts	71

3.5.5	Time of Day	73
3.5.6	Remote Operation	74
4	ANALYSIS TOOLS	76
4.1	AstroImageJ	76
4.1.1	AIJ Toolbar	77
4.1.2	Astronomical Image Display	78
4.1.3	Data Processor	81
4.1.4	Multi-Aperture	84
4.1.5	Multi-Plot	87
4.1.6	Light Curve Fitting and Detrending	92
4.1.7	Comparison Ensemble Management	97
4.1.8	Coordinate Converter	97
4.1.9	FITS Header Editor	101
4.1.10	Astrometry/Plate Solving	103
4.1.11	Image Alignment	106
4.1.12	AstroImageJ Updater	106
4.2	EXOFAST	108
4.3	Multi-EXOFAST	109
5	WASP-12b CHARACTERIZATION AND TTV ANALYSIS	111
5.1	Introduction	111
5.2	Observations	112
5.3	Data Reduction	112
5.4	Global Fit	114
5.5	System Parameter Results	119
5.6	TTV Results	123
5.7	Conclusions	127

6	QATAR-1b CHARACTERIZATION AND TTV ANALYSIS	131
6.1	Introduction	131
6.2	Observations	132
6.3	Data Reduction	132
6.4	Global Fit	134
6.5	System Parameter Results	137
6.6	TTV Results	142
6.7	Conclusions	142
7	HD 189733Ab ATMOSPHERIC CHARACTERIZATION	147
7.1	Introduction	147
7.2	HD 189733Ab Overview	148
7.3	Observing Strategy	149
7.3.1	Target and Atmospheric Species Selection	149
7.3.2	Na D Measurement Methods and Trade-offs	150
7.3.3	Filter Choices and Design	152
7.4	Observations	155
7.5	Data Reduction	156
7.6	Global Fit	157
7.7	Results	163
7.8	Discussion	166
7.8.1	Results of this Work Compared to the Literature	166
7.8.2	Detection of Na D in Transit Duration	166
7.9	Summary and Conclusions	171
8	KELT-6b DISCOVERY AND CHARACTERIZATION	173
8.1	KELT-6b Abstract	173
8.2	Identification of Contributions	174
8.3	Introduction	175

8.4	Discovery and Follow-up Observations	177
8.4.1	KELT-North Observations and Photometry	177
8.4.2	Radial-Velocity Observations	178
8.4.3	Follow-up Time-Series Photometry	180
8.4.4	Adaptive Optics Observations	187
8.5	Host Star Properties	189
8.5.1	Properties from the Literature	189
8.5.2	Spectroscopic Analysis	192
8.5.3	UVW Space Motion	194
8.5.4	SED Analysis	194
8.6	Characterization of the System	195
8.6.1	Light Curve Detrending	197
8.6.2	Global Fits	198
8.6.3	Transit Timing Variations	203
8.7	Evidence for a Tertiary Companion	207
8.8	False Positive Analysis	208
8.9	Evolutionary Analysis	213
8.9.1	Stellar Models and Age	213
8.9.2	Insolation Evolution	215
8.10	Discussion	217
8.11	KELT-6b Acknowledgements	219
9	KELT-1b SECONDARY ECLIPSE CHARACTERIZATION	225
9.1	Introduction	225
9.2	Ground-based Observations	227
9.3	Light curve Fitting	228
9.3.1	Secondary Eclipse Model	228
9.3.2	Model Fit to MORC z' Data	230
9.4	Secondary Eclipse Detection Results	232

9.5	Discussion	232
9.6	Summary and Conclusions	233
10	CONCLUSIONS AND NEXT POSSIBILITIES	235
10.1	Summary of Results	235
10.2	Near-IR Photometry From Small Telescopes	237
10.3	The Transiting Exoplanet Survey Satellite	239
10.4	James Webb Space Telescope	241
10.5	Other Upcoming Space Telescopes	241
10.6	Final Thoughts	242
	REFERENCES	243
	APPENDICES	257
A	COPYRIGHT AGREEMENTS	257
B	KELT-6b AUTHORS AND AFFILIATIONS	260
	CURRICULUM VITAE	261

LIST OF TABLES

TABLE		Page
1	WASP-12b Summary of Photometric Observations	113
2	WASP-12b System Parameter Values	121
3	WASP-12b Parameter Comparison	122
4	WASP-12b Transit Times	124
5	Qatar-1b Summary of Photometric Observations	133
6	Qatar-1b System Parameter Values	140
7	Qatar-1b Parameter Comparison	141
8	Qatar-1b Transit Times	143
9	HD 189733b Summary of Photometric Observations	156
10	HD 189733b Na D Filter System Parameters	168
11	KELT-6 Radial Velocity and Bisector Measurements	181
12	KELT-6 Summary of Photometric Observations	188
13	KELT-6 Stellar Properties	193
14	KELT-6b Selected System Parameters from Six Global Fits	202
15	KELT-6b Fiducial System Parameters	204
16	KELT-6b Transit Times	205
17	Summary of MORC Light Curves of Known Planets	238

LIST OF FIGURES

FIGURE		Page
1	Transiting Planet Orbital Phase Diagram	8
2	Primary Transit Model	14
3	Transit Light Curve Limb Darkening	17
4	Illustration of R-M Effect	19
5	Dependence of RM on λ	20
6	Transiting Planet Atmosphere Diagram	22
7	HD 189733b Thermal Phase Curve	25
8	RV and Transit Discoveries by Year	28
9	KELT Telescopes	31
10	<i>Kepler</i> Candidate Radius vs. Period	36
11	MORC U16M CCD Linearity	41
12	MORC Telescope	61
13	U16M QE and Broadband Filters	64
14	Telescope Enclosure Outside View	66
15	Telescope Enclosure Inside View	67
16	XmTel User Interface	69
17	XmCCD User Interface	70
18	AIJ Toolbar	78
19	AIJ Image Display	80
20	AIJ Data Processor	83
21	AIJ Multi-Aperture	85
22	AIJ Multi-plot Main Panel	88

23	AIJ Multi-plot Y-data Panel	90
24	AIJ Multi-Plot Example Plot	93
25	AIJ Multi-Plot Fitting Panel	94
26	AIJ Reference Star Settings Panel	98
27	AIJ Coordinate Converter	100
28	AIJ Add Data to Table Panel	102
29	AIJ FITS Header Editor	104
30	AIJ Astrometry/Plate Solve Panel	105
31	AIJ Stack Aligner Panel	107
32	AstroImageJ Updater Panel	108
33	WASP-12b Transit Light Curves	115
34	WASP-12b Binned Light Curve	116
35	WASP-12b Phased RVs	118
36	WASP-12b In-transit RVs	118
37	WASP-12b TTVs	125
38	WASP-12b TTV Periodogram	126
39	WASP-12b TTVs Phased at 4.0 d	127
40	WASP-12b TTVs with Literature TTVs	128
41	Qatar-1b Transit Light Curves	135
42	Qatar-1b Binned Light Curve	136
43	Qatar-1b Phased RVs	138
44	Qatar-1b In-transit RVs	138
45	Qatar-1b TTVs	144
46	Qatar-1b TTV Periodograms	145
47	Na D Filter Transmittance Curve	153
48	Red Continuum Filter Transmittance Curve	154
49	Typical Na D Field-of-View of HD 189733	158
50	Typical RC Field-of-View of HD 189733	159

51	The Field within $\sim 1'$ of HD 189733 in Na D	160
52	The Field within $\sim 1'$ of HD 189733 in RC	161
53	HD 189733b Transit Light Curves in the Na D Filter	164
54	HD 189733b Transit Light Curves in the RC Filter	165
55	HD 189733b Binned Na D Light Curve	167
56	HD 189733b Binned RC Light Curve	167
57	HD 189733b Na D and RC Light Curves	170
58	KELT-6b Discovery Light Curve	178
59	KELT-6 Phased Radial Velocity Measurements	182
60	KELT-6b Transit Follow-up Photometry	184
61	KELT-6b Combined and Binned Transit Follow-up Photometry	185
62	KELT-6 Keck Adaptive Optics Image	190
63	KELT-6 Keck Adaptive Optics Contrast Sensitivity	191
64	KELT-6 Measured and Best-Fit SED	196
65	KELT-6b Transit Time Variations	206
66	KELT-6 Unphased Radial Velocities	209
67	KELT-6 Tertiary Mass Limits Versus Separation in AU	210
68	KELT-6b Phased Secondary Transit Follow-up Observations	212
69	KELT-6 Theoretical HR Diagrams Based on Yonsei-Yale Stellar Models	216
70	KELT-6 Incident Flux Versus Age	218
71	KELT-6b Planet Mass and Period Comparison	220
72	KELT-6b Planet Incident Flux and $\log g_p$ Comparison	221
73	KELT-6b Metallicity and $\log g_p$ Comparison	222
74	KELT-6 Comparison of Transit Depth and V Mag	223
75	KELT-1b Secondary Eclipse Light Curves	229
76	KELT-1b Secondary Eclipse Depth Constraints	231
77	KELT-1b Planet-to-Star Flux Ratios	234

CHAPTER 1

INTRODUCTION

The answer to one of the most compelling questions – "are we alone in the universe?" has been debated by mankind for centuries from both philosophical and scientific perspectives. The technological revolution of the 20th century has enabled astronomers to collect direct evidence to help shape the scientific perspective. The discovery of over a thousand planets orbiting stars other than the Sun (i.e. extra-solar planets or exoplanets) over the past 20 years has confirmed that the Sun is not unique among stars in hosting planets. However, these discoveries are only a starting point in the quest to determine if life exists beyond our solar system.

Perhaps a more practical question for scientists to answer in the near term is – "do conditions exist on planets outside the solar system that could support life as we understand it here on Earth?" The National Research Council Decadal Survey of Astronomy and Astrophysics (NRC, 2010) specifies seeking nearby habitable planets as one of three priority science objectives for the decade 2012-2021. More specifically, the report states "The ultimate goal is to image rocky planets that lie in the habitable zone – at a distance from their central star where water can exist in liquid form – and to characterize their atmospheres. In its astrobiology roadmap (Des Marais et al., 2008), NASA defines the principal habitability criteria as "extended regions of liquid water, conditions favorable for the assembly of complex organic molecules, and energy sources to sustain metabolism." This research focuses on the discovery of new exoplanets and measuring fundamental characteristics of known and new exoplanets such as mass, radius, density, temperature, orbital parameters, atmospheric composition, etc., which have a direct impact on the habitability of an exoplanet. This research has been conducted using the

0.6 m, research-grade, Moore Observatory RC (MORC) telescope located near Louisville, Kentucky. Moore observatory is operated by the University of Louisville. The results of this program could couple into larger-scale ground-based, as well as NASA space-based programs.

1.1 Star and Planet Formation

Although the study of young stellar environments, with the goal of furthering our understanding of how stars and planetary systems form, continues to be a topic of intense astrophysical research, much progress has already been made. I provide a brief summary of our current understanding of star and planet formation here, but see Collins (2008) for a more detailed overview. The standard model of the birth of a star (Shu, Adams, & Lizano, 1987) from a molecular cloud (mostly H₂ gas) begins with the formation of a slowly rotating dense core in the molecular cloud. As the cloud condenses, its core crosses a threshold of instability and collapses from inside-out. Material with low angular momentum collapses under its own gravity to form the protostar and material with higher angular momentum starts to collapse into a rotating disk structure (i.e. a protoplanetary disk). Some of the disk material accretes onto the star, but accretion eventually slows. Collapse of the remaining material onto the disk continues, which increases the opening angle of the stellar outflow, and eventually fully reveals the star and protoplanetary disk.

As the disk cools, it is thought that small dust grains form, which may eventually coagulate into kilometer-sized planetesimals. Depending on disk characteristics, runaway disk accretion onto the planetesimals may create larger protoplanets. Collisions and mergers of protoplanets are thought to eventually produce terrestrial planets. The protoplanets of gas giants are thought to form in the same way as terrestrial protoplanets, but they form beyond the snow line (the distance from the central star where volatiles condense into solid ice grains). Since the disk material is solid ice, gas giant protoplanets can be several times more massive than terrestrial protoplanets. After a protoplanet reaches a critical mass of $5 - 10 M_{Earth}$, gas from the disk starts to accrete onto the

protoplanetary core. The accretion continues until the gas in the disk near the planet is exhausted. Ice giants like Uranus and Neptune are thought to be cores that formed after most of the disk had disappeared. A detailed review of planet formation theory is provided in Lissauer (1993).

Changes to a planet's orbital period and/or eccentricity, called planet migration, can occur through planet interactions with nearby disk material, through gravitational scattering by other planets, or through tides between the host star and planet. Planet migration is complex and our current understanding of all the mechanisms is incomplete. Ford (2014) provides a review of the current understanding of the late-stages of the evolution of planetary systems, including migration theory. Also see Benítez-Llambay, Masset, Koenigsberger, & Szulágyi (2015) for the recent report of a proposed "heating torque" mechanism that can, under certain circumstances, prevent newly forming gas giant cores from migrating in towards their parent stars. This mechanism could explain why $\sim 15\%$ of planetary systems, including our own solar system, have a gas giant planet surviving at orbits beyond 1 AU. Their computer simulations show that the accretion of small bodies onto the planetary embryo heats the gas nearby, causing it to expand. The region behind expands more than the region ahead, resulting in an increase in the embryo's angular momentum that can overcome the loss in angular momentum due to gravitational interactions with the disk.

1.2 The Discovery of Exoplanets

Until just over 20 years ago, the understanding of planetary system formation and evolution was constrained only by the properties of the planets in our solar system. Then, the first legitimate discovery of (two) planets outside our solar system was announced by Wolszczan & Frail (1992). The planetary system orbits a neutron star (the supernova remnant of a star with mass $\gtrsim 8 M_{\odot}$), which is a millisecond radio pulsar known as PSR1257+12. The planets were discovered through high-precision timing of the radiation beaming from the host star. This radiation is deadly to life as we know it, so these planets

were designated "dead worlds". The planets are believed to be the rocky cores of former gas giants or planets formed from the supernova remnants in a second round of planet formation.

Three years later, Mayor & Queloz (1995) announced the discovery of the first exoplanet found to orbit another sun-like star. The $0.5 M_J$ planet in a 4.2 day orbit around the star 51 Peg was discovered while conducting a survey of 142 G and K dwarf stars with a radial velocity (see §1.4.2) precision of 13 m s^{-1} , which is high enough to detect Jupiter-mass or higher sub-stellar companions. Gas giants were not generally expected to exist in orbits so close to the host star, since planet formation theory implied that gas giants must form beyond the snow line. This discovery of the first hot Jupiter, and the many other exoplanet discoveries that followed, mandated a reexamination of our understanding of planetary system formation and evolution. More than 99.9% of all planets known today orbit stars other than the Sun, so exoplanet data now play a key role in planet formation and evolution theory.

1.3 Hot Jupiter Formation

Current theory suggests that hot-Jupiters get their start from the formation of a rocky core at a larger separation from the host star. Then they accrete a gaseous envelope, and migrate to their "hot" location (Ford, 2014). The mechanism for migration is less clear, but the measurement of the Rossiter-McLaughlin (RM) effect (see §1.5.2) for many transiting (see §1.4.3) hot Jupiters has helped show that at least two mechanisms may be involved. The RM measurements have shown that although the orbital angular momentum of many planets is well-aligned with the host stars rotational angular momentum, a significant fraction are severely misaligned. There are differing theories explaining how misalignment can happen, but Ford (2014) suggests that the well aligned hot Jupiters migrate as a result of the chaotic interactions of a multi-planet system (Rasio & Ford, 1996), and the misaligned systems are the result of secular interactions with a highly inclined binary companion (Holman, Touma, & Tremaine, 1997) or a stellar flyby

(Laughlin & Adams, 1998). In both cases, the migration occurs when the interactions result in a highly eccentric planetary orbit that passes near the host star. Tidal interactions with the host star then circularize the planet's orbit, resulting in the hot Jupiters we observe today. While the orbit of the planet is circularizing, many believe that the gas giant cleans out the inner solar system by scattering any rocky planets into the star or to the outer regions of the planetary system (Mandell, Raymond, & Sigurdsson, 2007; Ford, 2014).

1.4 Exoplanet Discovery Methods

Exoplanet discovery is difficult primarily because the planet is extremely faint compared to the host star, and the separation between the star and planet on-the-sky is extremely small. However, several methods have been successfully used for both the discovery and characterization of exoplanets. Each method has its own advantages, disadvantages, and selection effects in mass, radius, and semi-major axis parameter space.

1.4.1 Direct Imaging

Direct imaging is the most straightforward method to understand, but is one of the most difficult to achieve with current technology. The idea is to take an image of the planetary system that clearly separates the blinding light of the star from the faint light of the planet. The contrast ratio between a sun-like star and an earth-like planet is $\sim 10^{-7} - 10^{-10}$, depending on the wavelength of the observation. Because of the physics of diffracted light and the difficulty of managing scattered light in telescopes, the required contrasts are technologically difficult to achieve. However, a handful of large, massive, young planets located far from the host star have already been directly imaged (Marois et al., 2008; Kalas et al., 2008; Kuzuhara et al., 2013). Four to five orders of magnitude improvement in planet-to-star contrast capability is needed to directly image solar-like systems.

When direct imaging becomes more generally practical, direct spectroscopy will also become practical, as long as enough photons are available from the planet. Exoplanet

spectroscopy will provide a direct measurement of the components of the planet's atmosphere and will provide a path to search for potential indicators of life on the planet.

1.4.2 Radial Velocity Method

Gravitational interactions between a star and one or more orbiting planets cause the star to orbit the center of mass of the star – planet system. The radial velocity (RV) discovery method takes advantage of the shift in the wavelength of light, due to the Doppler effect, to measure the velocity of a star along the line-of-sight, as a function of time. The radial velocity curve of a star (e.g. Figure 59) can be measured accurately by observing a time-series of high-resolution spectra and comparing the measured wavelengths of spectral lines to their known stationary wavelengths. For the simplified case of a single planet system, the period, P , and eccentricity, e , of the planet's orbit can be determined directly from the shape of the periodic RV curve. Then the mass of the planet, m_p , can be calculated using the radial velocity equation (Lehmann-Filhés, 1894; Paddock, 1913),

$$K = \left(\frac{2\pi G}{P} \right)^{\frac{1}{3}} \frac{m_p \sin i}{m_*^{2/3} \sqrt{1-e^2}} \quad (1)$$

from the mass of the host star, m_* , and the radial velocity semi-amplitude, K , to within a factor of the $\sin i$, where i is the inclination of the orbit relative to the line of sight, and G is the gravitational constant.

The RV method is responsible for the discovery of the first planet found to orbit a solar-type star (see §1.2). The RV method was the most successful technique used to find exoplanets prior to the Kepler mission (see §1.6), producing ~ 450 RV planet discoveries so far¹. The RV method is most sensitive to more massive planets orbiting near the star. However, with current technology, 1 m s^{-1} RV precision has been achieved, which is sensitive to the RV variations produced by a Neptune mass planet at the distance of Earth from a solar-type star. The disadvantage of the RV technique is that only the minimum

¹The Exoplanet Encyclopedia at <http://exoplanet.eu> (Schneider et al., 2011)

mass of the planet can be determined, since the inclination of the orbit cannot be determined from the RV data alone.

1.4.3 Transit Method

The transit method is sensitive to planets with orbits that take them directly across of the face of the star from the observer’s perspective. As the dark disk of the planet passes in front of the disk of the bright star (i.e. transits the star), part of the stellar flux is blocked by the planet, which causes an apparent dimming of the star (see Figure 1). The relative brightness of a star can be measured to a precision of better than one part in a thousand from ground-based telescopes and the Kepler spacecraft has achieved better than 40 parts per million per 6.5 hours of integrated exposure time. Ground-based observations can easily detect the periodic $\sim 1\%$ apparent dimming of a solar-type star due to a Jupiter-size object passing in front it, and have so far been responsible for the discovery of $\sim 200^1$ transiting planets. Kepler can detect planets as small as earth transiting a solar-type star, and has produced $\sim 1000^1$ confirmed planet discoveries so far. However, the stars in the Kepler field are generally too faint for detailed characterization studies.

One disadvantage of the transit discovery method is that planets can only be detected if a chance alignment of the orbit causes the planet to cross the face of its host star from the perspective of the observer. For a random orientation of circular orbit inclinations, the probability, p , that a planet (with radius much smaller than that of the host star) transits is

$$p = \frac{R_*}{a}, \quad (2)$$

where a is the semimajor axis of the planet’s orbit, and R_* is the radius of the star. Hot Jupiter planets orbiting solar-like stars have $p \approx 10\%$, but planets orbiting at the distance of the Earth from the Sun have $p \sim 0.5\%$. Wide field surveys are responsible for the discovery of most known transiting exoplanets (see §1.6). Since the exposure cadence of wide-field surveys is generally relatively long and the photometric data can be sparse (for ground-based surveys in particular), the orbital periods of most known transiting planets

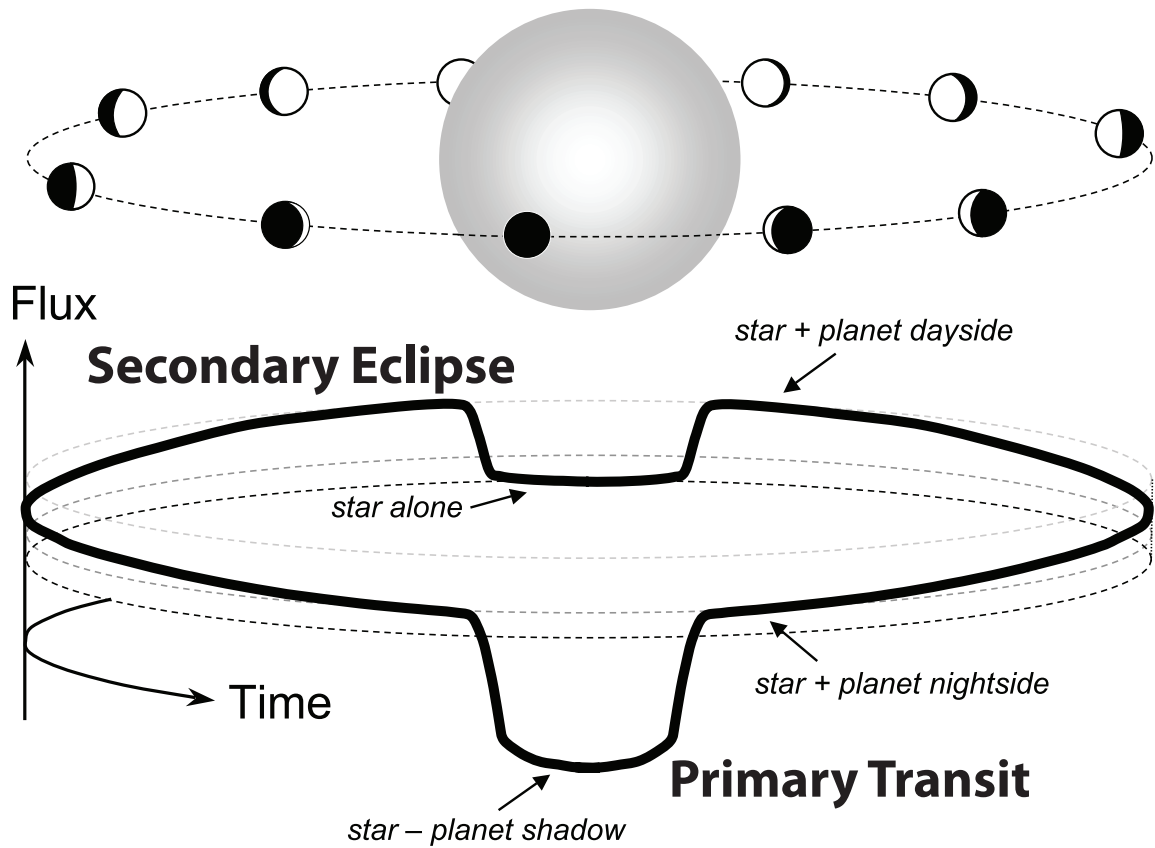


Figure 1. Transiting planet orbital phase diagram illustrating primary transit and secondary eclipse. The combined flux of the star and planet is observed. During a transit, the flux drops because the planet blocks a fraction of the starlight. Then the flux rises as the planet's dayside comes into view. The flux drops again when the planet is occulted by the star during secondary eclipse. Adapted from Winn (2010).

are $\lesssim 10$ days. The result is that transiting planet discovery is biased toward short period planets, and for ground-based searches, also biased toward planets with radii larger than Saturn.

Another disadvantage is that there are several astrophysical configurations of blended eclipsing stellar binary or triple systems that can mimic some of the observable signatures of transiting planetary companions to single stars (i.e. false positives). There are however several methods available to help confirm the planetary nature of a companion, including measurement of mass from radial velocities, investigation of correlations between bisector span and RV data, exclusion of color-dependent primary transit observations, exclusion of a detectable secondary eclipse in the optical bands, exclusion of detectable companions in adaptive-optics imagery, etc. See §8.8 for a detailed description of false positive analysis and the results for KELT-6b.

The advantage of a transiting planet discovery is that much information about the system can be determined by fitting a physical model of the system to the light curve data (see §1.5.1). The planet's orbital inclination and planetary radius (when combined with an estimate of the host star radius) are key values that can be estimated from the light curve data. The inclination, i , enables the true planetary mass to be calculated from the RV derived minimum mass. The planetary radius can then be combined with the planetary mass to determine the bulk density of the planet.

When a planet passes in front of its host star, the event is called a primary transit (or simply transit). When a planet passes behind its host star, the event is called a secondary eclipse (see Figure 1). The orbital phase and duration of the secondary eclipse relative to the primary transit places constraints on the shape of the orbit (Sterne, 1940; de Kort, 1954). The drop in combined brightness measured during secondary eclipse is proportional to the brightness of the planet relative to the brightness of the star, and thus provides a measurement of the planet's combined thermal radiation and reflected stellar radiation. In optical filter bands, the secondary eclipse should not be detectable with the precision achievable from ground-based observations. An obvious secondary eclipse in

optical bands suggests that the apparent primary transit is a false positive, and that a multi-star blend is masquerading as an apparent transiting planet.

Transiting planets also enable the discovery of additional planets in the system (§1.4.4), the measurement of the planet's orbital alignment relative to the host star's spin axis (§1.5.2), and the measurement of components in the atmospheres of exoplanets (§1.5). Interestingly, the stellar mean density can also be calculated strictly from the parameters of the transit light curve (§1.5.1). Combining the semi-amplitude, eccentricity, and orbital period from the RV curve, the planet's surface gravity can be derived without knowledge of the host star's properties.

1.4.4 Transit Timing Variations

In a transiting single planet system, the transit of the star happens precisely at a constant interval equal to the orbital period. If a star hosts multiple planets, the planetary orbits will no longer be Keplerian due to gravitational interactions between the planets and the host star, resulting in deviations in the constant transit interval referred to as transit timing variations (TTVs). The TTV amplitude increases with the orbital period of the transiting planet and with the mass of the perturbing planet, and is greatly amplified if the perturbing planet is locked in a low-order orbital resonance with the transiting planet (Agol et al., 2005). TTVs can be measured to high enough precision, even with ground-based observations, to detect an Earth-mass planet (that is not necessarily transiting) in a low-order resonant orbit with the transiting planet (Holman & Murray, 2005; Agol et al., 2005). For example, Agol et al. (2005) show that an Earth-mass planet in 2:1 resonance with a 3-day period transiting hot Jupiter would cause timing variations of ~ 3 minutes, which would be accumulated over a year. Ground based timing precision can reach 20–30 s (see Chapters 5 and 6).

To properly characterize a TTV signal, good phase coverage and a long baseline of measurements are needed. Ideally, nearly all transits during the baseline period should be observed. This is of course nearly impossible from the ground due to weather. Plus, for a

single observatory, many transits during the baseline period will likely occur during daylight. Veras, Ford, & Payne (2011) show that in most cases at least 50 consecutive transit observations are necessary to have a reasonable chance of characterizing the perturbing planet and its orbit.

Even if a TTV curve is well sampled, it is notoriously difficult to uniquely infer the perturbing planet's mass and orbital parameters strictly from the TTV data (Ford & Holman, 2007; Nesvorný & Morbidelli, 2008; Payne, Ford, & Veras, 2010; Boué, Oshagh, Montalto, & Santos, 2012; Lithwick, Xie, & Wu, 2012). Degeneracies exist in orbital period, eccentricity, and inclination. RV data, transit duration variations, or systems with multiple transiting planets can help to break the degeneracies.

So far, no large amplitude TTVs have been reported for planets discovered by ground-based wide-field transit surveys. However, several authors have claimed evidence of low-amplitude periodic TTVs, followed by other authors with differing conclusions. For example, analysis of WASP-3b TTVs by multiple authors has produced differing conclusions. Maciejewski et al. (2010) analyzed 13 WASP-3b transits and reported a sinusoidal TTV with period ~ 127 d and peak value ~ 2 min. Then Eibe et al. (2012) found a lower significance in the TTV detection, but a possible detection of transit duration variations. Montalto et al. (2012) studied 38 WASP-3b light curves and found no evidence of periodicity in the TTVs. Small amplitude TTV claims are inconsistent across ground-based timing measurement analyses and, so far, no perturber planet has been confirmed from them.

But, García-Melendo & López-Morales (2011) show that the method typical used to search for transits in wide-field transit survey data (box-least-squares or BLS, Collier Cameron et al. 2006), is not sensitive to transits with significant TTVs, which could explain why no large TTVs have been found in planets discovered by ground-based surveys.

On the other hand, the almost continuous Kepler light curves have demonstrated a number of clear TTV detections (e.g Holman et al. 2010; Lissauer et al. 2011; Ballard et

al. 2011; Steffen et al. 2013; Yang et al. 2013). The Kepler TTV data are responsible for the discovery of non-transiting planets and provide confirmation of the planetary nature of the transiting planet(s) and estimates of their masses, without the necessity of RV data.

Steffen et al. (2012) searched six quarters of Kepler data for planetary companions orbiting near hot Jupiter planet candidates ($1 \leq P \leq 5$ d) by looking for multiple transiting planets and evidence of TTVs. Special emphasis was given to companions between the 2:1 interior and exterior mean-motion resonances. They found no evidence for nearby companion planets to 63 hot Jupiter candidates. However, five out of 31 warm Jupiter systems ($6.3 \leq P \leq 15.8$ d) do show multiple transiting planets and/or evidence of TTVs.

1.4.5 Other Methods

The first known exoplanets were discovered using pulsar timing (see §1.2). Many other exoplanet discovery methods are in use or have been proposed including gravitational microlensing, astrometry, additional timing methods, etc., but are beyond the scope of this work.

1.5 Characterization Methods

Transiting planets offer a wealth of opportunities for characterization of the planetary system. RV characterization of the companion mass is typically pursued for all planet candidate discoveries from ground-based wide-field transit surveys, because a mass determination is a powerful and straight forward false positive indicator, and the host stars are typically bright enough for cost effective spectroscopic observations using ~ 1.5 m telescopes. One exception is for systems with rapidly rotating host stars. Standard RV measurements require well defined stellar spectral lines. However, rapid rotation smears (or broadens) the lines causing the spectral shift to be difficult or impossible to measure. KELT-7 rotates fairly rapidly at $v \sin i_* \sim 73 \text{ km s}^{-1}$, but Bieryla et al. (2015) use a combination of low-precision RVs (due to the rapid rotation) and the RM effect (see §1.5.2) to confirm the planet and measure its mass. Based on work with the KELT survey

(see §1.6), host stars rotating at $\gtrsim 100 \text{ km s}^{-1}$ are out of reach of current RV techniques.

1.5.1 Primary Transit Light Curve Modeling

Several system parameter values can be extracted from high-precision follow-up light curves by fitting a physical model of the system to the time-series data. The model used by the two light curve fitting tools used in this work, AstroImageJ (see §4.1) and multi-EXOFAST (see §4.3), is described by Mandel & Agol (2002). The transit is modeled as an eclipse of a spherical star by an opaque planetary sphere. The model is parameterized by six physical values, plus a baseline flux level, F_0 . The six physical parameters are the planetary radius in units of the stellar radius, R_p/R_* , the semi-major axis of the planetary orbit in units of the stellar radius, a/R_* , the transit center time, T_C , the impact parameter of the transit, b , and the quadratic limb darkening parameters, u_1 and u_2 . The orbital inclination can be calculated from the impact parameter as

$$i = \cos^{-1} \left(b \frac{R_*}{a} \right). \quad (3)$$

A simplified illustration of the transit light curve model is shown in Figure 2. Four contact times are defined. The time of first contact, t_1 , is defined as the instant that the edge of the planet’s disk first touches the edge of the stellar disk. The time of second contact, t_2 , is defined as the instant that the planet’s disk has first moved completely inside the stellar disk. At the time of third contact, t_3 , the planet’s disk starts to exit the stellar disk, and at the time of fourth contact, t_4 , the planet has just moved completely outside the stellar disk. In a grazing eclipse, second and third contacts do not occur. The time duration $t_2 - t_1$ is the ingress duration and $t_4 - t_3$ is the egress duration. For an elliptical orbit, the ingress and egress durations can be different due to the changing speed of the planet as it transits the host star. However, the time difference is generally small, so the single parameter τ is normally used to represent both durations.

Ignoring limb darkening (which is discussed below), the fractional decrease in flux (i.e. transit depth) during full eclipse (i.e. between t_2 and t_3) is the ratio of the size of the

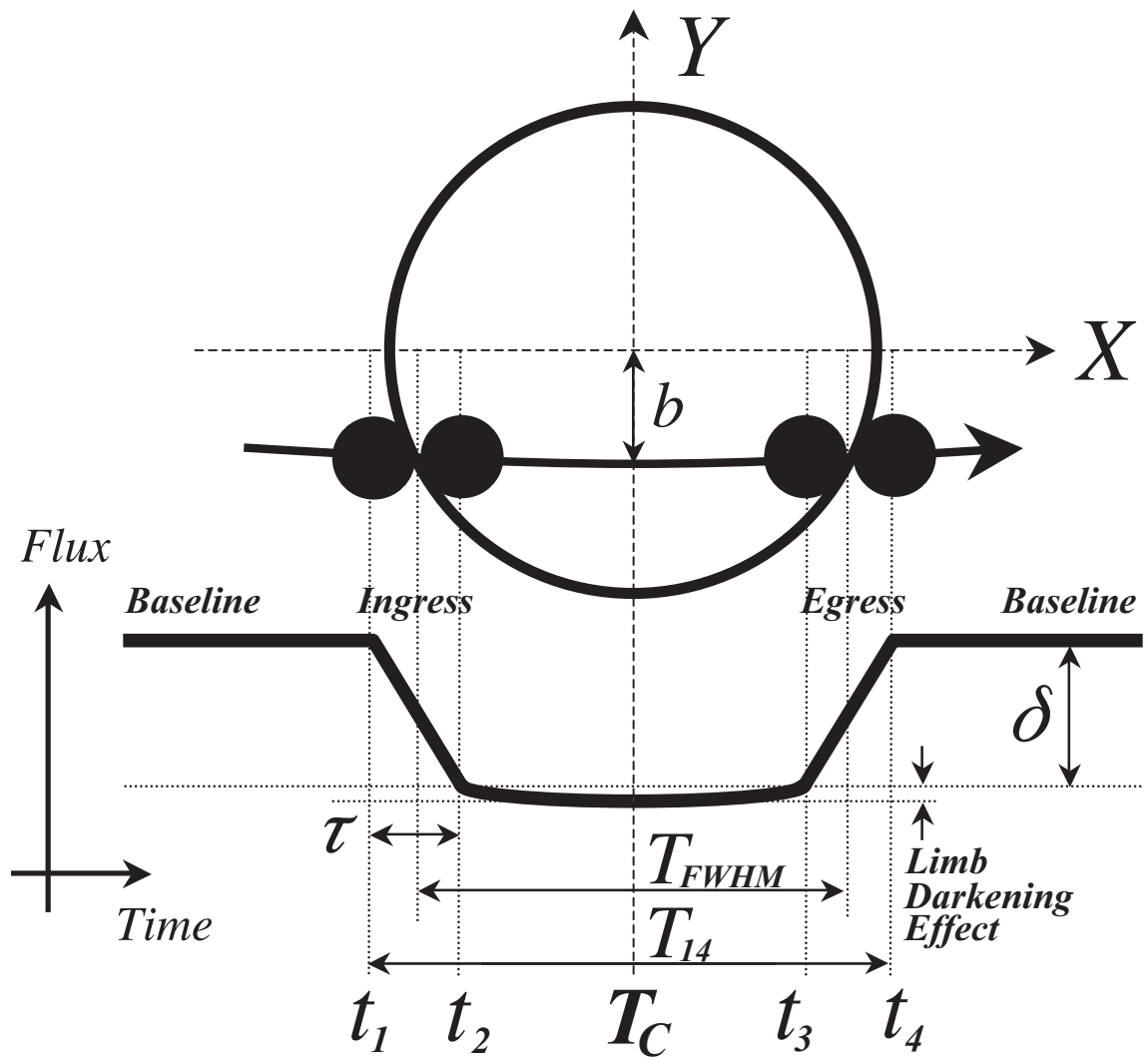


Figure 2. Primary transit model illustrating the relation of model parameters to light curve features. Adapted from Seager & Deming (2010).

planet's disk to the size of the star's disk, or

$$\delta = \left(\frac{R_P}{R_*} \right)^2. \quad (4)$$

The detailed equations describing the fractional flux decrease for all times of the eclipse are given in Mandel & Agol (2002) and are coded into the fitting routines of AstroImageJ and multi-EXOFAST. I will show simpler relations here that are more useful for developing an intuition about how the physical system parameters affect the light curve shape (see Winn 2010). The very small effects of exoplanetary atmospheric refraction on the light curve (see Misra & Meadows 2014) have been ignored in this section. The total transit duration for a circular orbit is

$$T_{14} = t_4 - t_1 = \frac{P}{\pi} \sin^{-1} \left[\frac{R_*}{a} \frac{\sqrt{(1 + \frac{R_P}{R_*})^2 - b^2}}{\sin i} \right], \quad (5)$$

where P is the orbital period of the planet. In the limits $R_P \ll R_* \ll a$ and $\tau \ll T$ for non-grazing planets in circular orbits, the impact parameter and the ratio of the orbital semi-amplitude to the stellar radius are

$$b^2 = 1 - \sqrt{\delta} \frac{T_{FWHM}}{\tau}, \quad (6)$$

$$\frac{a}{R_*} = \frac{\delta^{1/4}}{\pi} \frac{P}{\sqrt{\tau T_{FWHM}}}, \quad (7)$$

where $T_{FWHM} = [(t_4 - t_1) + (t_3 - t_2)]/2$ as shown in Figure 2.

As mentioned in §1.4.3, the stellar density, ρ_* , can be derived exclusively from the light curve parameters, with only one assumption. Using Kepler's third law, Seager & Mallén-Ornelas (2003) show that

$$\rho_* + \delta^{3/2} \rho_P = \frac{3\pi}{GP^2} \left(\frac{a}{R_*} \right)^3, \quad (8)$$

where ρ_P is the planetary density. With the typically valid assumption that $\delta^{3/2} \rho_P$ is negligible compared to ρ_* , the stellar density is then:

$$\rho_* \approx \frac{3\pi}{GP^2} \left(\frac{a}{R_*} \right)^3. \quad (9)$$

The comparison of stellar density derived from the light curve with stellar density derived from spectroscopy is an important part of false positive analysis (see §8.8).

Limb darkening (Milne, 1921) is an optical effect seen in stars, which causes the central part of the stellar disk to appear brighter than the edge (or limb). This causes the bottom part of the transit light curve to be rounded and smears the second and third contact points (see Figure 3). The limb darkening effect is more pronounced at shorter (blue) wavelengths than at longer (red) wavelengths. The quadratic limb darkening parameters, u_1 and u_2 , are not well constrained by typical ground based data, so in this work, I typically fix the parameters to values from the quadratic limb darkening models of Claret & Bloemen (2011).

To calculate the physical planetary radius, R_p , from the model values that are in units of R_* (and the physical planetary mass, M_p , from the RV data), the Yonsei-Yale Stellar Models (Demarque et al., 2004) or the empirical Torres relations (Torres et al., 2010) can be used to estimate M_* and R_* from the spectroscopic properties effective temperature, T_{eff} , stellar surface gravity, $\log g_*$, and metallicity, $[\text{Fe}/\text{H}]$.

The transit model parameter errors are non-Gaussian and are often correlated, so an alternative to typical error propagation is required to estimate model parameter uncertainties. Multi-EXOFAST uses Markov Chain Monte Carlo (MCMC) simulations to estimate parameter uncertainties (see §4.3).

1.5.2 Rossiter-McLaughlin Effect

The Doppler effect causes light to shift in wavelength depending on the velocity of the emitting source relative to the observer. For each point on the face of a rotating star, the velocity vector includes contributions from both the stellar motion and the rotational speed at that point. Since standard spectroscopic observations do not resolve the stellar disk, the star's spectral lines are both shifted and broadened due to the motion of the star and the differing rotational velocity components across the face of the star. When an exoplanet passes in front of its rotating host star, the stellar disk velocities obscured by the

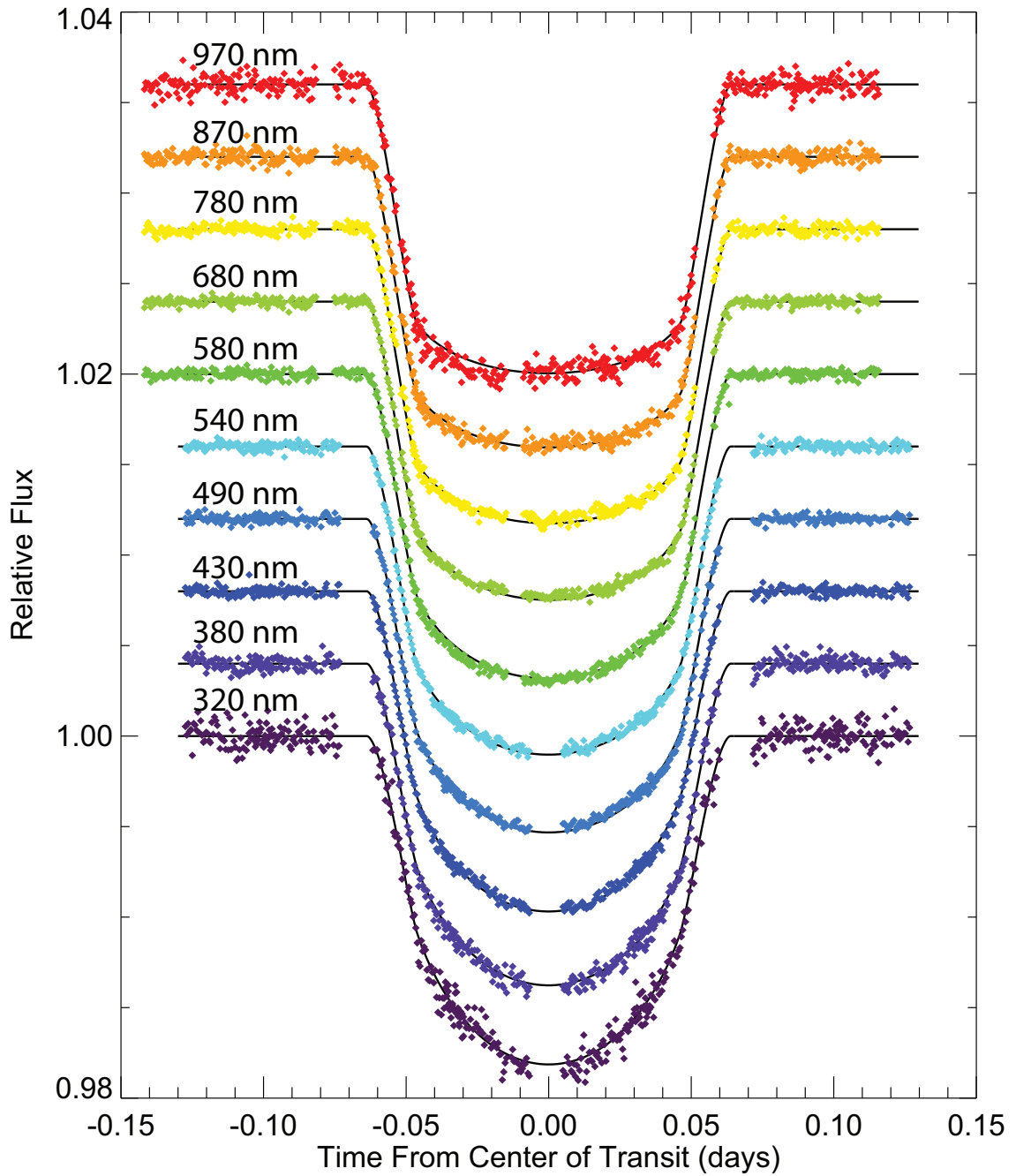


Figure 3. An illustration of how limb darkening affects transit light curves. The ten HD 209458b transit light curves are from HST/STIS spectroscopy. The center wavelength for each band of integrated wavelengths is shown for each light curve. Notice that limb darkening affects the bottom curvature and the smearing of contact points two and three more strongly for shorter wavelengths. Adapted from Knutson et al. (2007). Wavelength identifications are from Winn (2010).

planet no longer contribute to the disk integrated spectrum. The result is a bump that moves through the broadened stellar line profile as the transit progresses (see Figure 4). The anomaly in the spectral line profile, the Rossiter-McLaughlin (RM) effect, causes a shift in the radial velocity derived from the profile. A time-series of spectroscopic observations covering a full transit will produce a RM waveform.

The shape of the RM waveform reveals $v \sin i_*$, the sky projected rotation speed of the stellar surface, and λ , the angle between the sky projections of the stellar spin axis and the orbit normal. λ provides information about the alignment of the planet's orbital angular momentum with the host star's spin angular momentum (i.e. the planet's spin-orbit alignment). Figure 5 shows three example waveforms for different values of λ . The top left panel shows a planetary orbit that is aligned with the stellar rotation ($\lambda = 0^\circ$) and the bottom left panel shows the corresponding RM waveform. The planet blocks part of the stellar disk that is rotating toward the observer during the first half of the transit and then away from the observer during the last half of the transit. The resulting RM waveform is anti-symmetric with respect to the nominal RV curve. The middle panels show an example with $\lambda = 30^\circ$. Note that the RM waveform is no longer anti-symmetric since the planet occults parts of stellar disk that are rotating away from the observer for more than half of the transit. The right-hand panels show an example with $\lambda = 60^\circ$. In this configuration, the planet always covers parts of the stellar disk that are rotating away from the observer for the entire transit. For this case, the RM waveform is completely below the nominal RV curve. Multi-EXOFAST optionally fits the analytic formulae of Ohta, Taruya, & Suto (2005) to the RM data to determine the best fit value of λ .

1.5.3 Characterization of Exoplanet Atmospheres

Given the faintness of exoplanets at the distance of Earth, and the large contrast ratio of the host star-to-planet brightness, the prospect of studying the atmospheres of exoplanets is a daunting task. Even so, by taking advantage of special geometric configurations of transiting systems, favorable system parameters, very large or

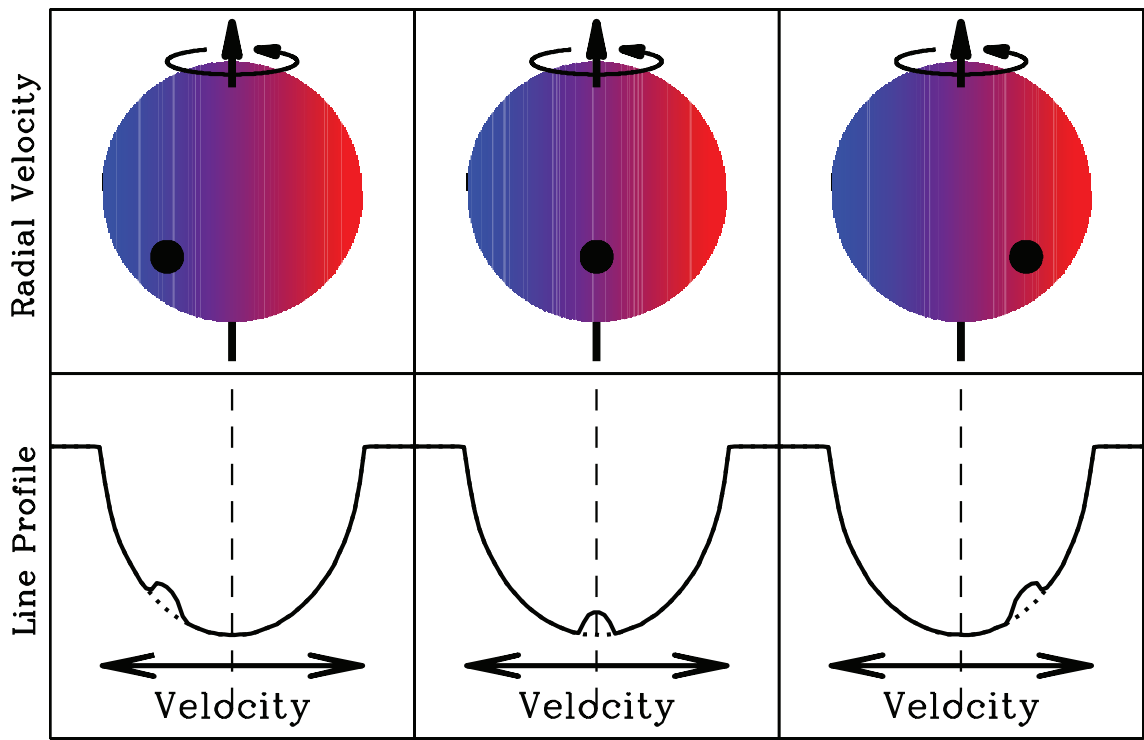


Figure 4. An illustration of the physics of the Rossiter-McLaughlin effect. *Top row.* Three successive phases of an exoplanetary transit. The projected stellar rotation speed at each point has been color coded with blue representing rotation toward and red representing rotation away from the observer, respectively. *Bottom row.* Illustration of an observed stellar absorption line, for the case of purely rotational broadening. The missing velocity component is manifested as a time-variable bump in the line profile. Adapted from Gaudi & Winn (2007).

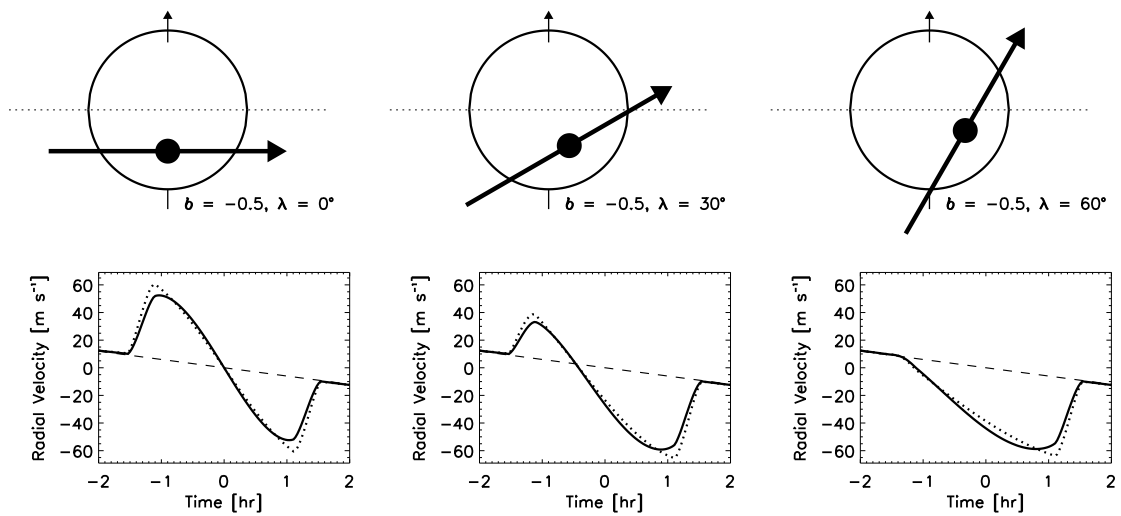


Figure 5. The dependence of the RM waveform on λ . Three different possible trajectories of a transiting planet are shown, along with the corresponding RM waveforms (as computed from the formulae of Ohta, Taruya, & Suto 2005). The trajectories all have the same impact parameter and produce the same photometric light curve, but they differ in λ and produce different RM curves. The dashed lines show the nominal RV curve. The dotted lines show the RM waveform for the case of no limb darkening, and the solid lines show the case for an arbitrary value of limb darkening. Adapted from Gaudi & Winn (2007).

space-based telescope, and novel ideas, several atomic and molecular components have been detected in the atmospheres of a few exoplanets (e.g. Charbonneau et al. 2002; Vidal-Madjar et al. 2003, 2004; Redfield et al. 2008; Snellen et al. 2008; Lecavelier Des Etangs et al. 2010).

Transmission Spectroscopy

As a transiting planet crosses the face of its host star, a small part of the stellar flux passes through the planet's atmosphere as it travels along its path to the observer (see primary transit phase in Figure 6). The small fraction of stellar flux with the planet's transmission spectrum imprinted on it is mixed with the remaining pure stellar flux. Certain wavelengths of stellar flux will be absorbed by the planet's atmosphere depending on the atomic and molecular components of the atmosphere. At the wavelengths of strong atomic or molecular absorption, the atmosphere is more opaque, and the planet's effective shadow is larger. Therefore, with high enough spectroscopic resolution and signal-to-noise ratio, a wavelength dependent transit depth should be detectable.

The difference in depth at a strong absorption line depends on the height of the atmosphere compared to the nominal radius of the planet in broadband optical filters (or compared to the radius in the continuum of a spectrum). For a strong absorption line, the planet radius will appear larger by a few atmospheric scale heights H (e.g. Seager & Sasselov 2000; Brown 2001), where

$$H = \frac{kT}{\mu_m g}, \quad (10)$$

and k is Boltzmann's constant, T is the atmosphere's mean temperature, μ_m is the mean molecular mass of the atmosphere, and g is the gravitational acceleration at the surface of the planet. With R_p defined as the nominal planetary radius in broadband optical filters, the additional depth due to the absorption in one scale height of atmosphere is

$$\Delta\delta = \frac{(R_p + H)^2}{R_*^2} - \frac{R_p^2}{R_*^2} = \frac{2HR_p + H^2}{R_*^2} \approx 2\delta \left(\frac{H}{R_p} \right), \quad (11)$$

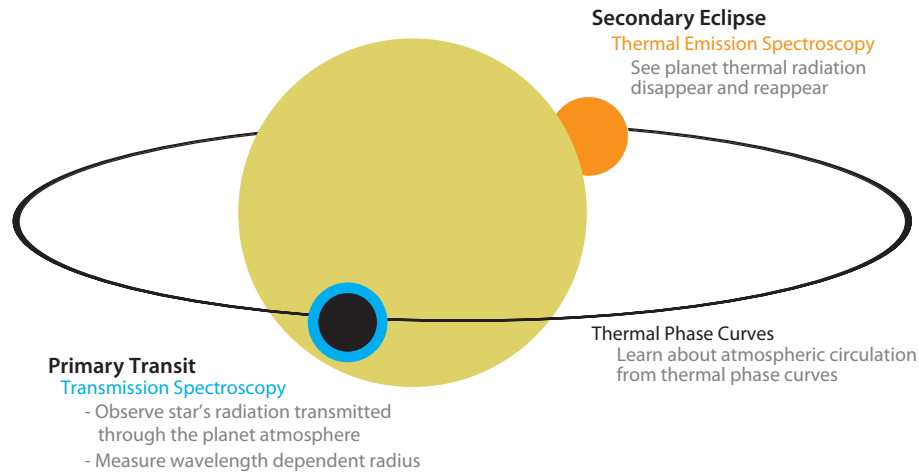


Figure 6. Transiting planet atmosphere diagram illustrating the geometry of transmission spectroscopy at the primary eclipse, thermal emission spectroscopy at secondary eclipse, and thermal emission phase curves. Adapted from Seager & Deming (2010).

with the approximation that $H \ll R_*$. Using the hot Jupiter exoplanet HD 189733b as an example, $R_p \approx 75,000$ km, $\delta = 0.025$, $T = 1200$ K, $g = 25$ m s⁻² (see Table 10), and estimating $\mu_m = 2$ amu, the atmospheric scale height is $H \approx 200$ km and the depth difference due to a single scale height of atmosphere is $\Delta\delta \approx 10^{-4}$. Therefore, the total atmospheric signal should be a few times 10^{-4} .

This wavelength dependent depth should be detectable from high resolution spectra or from depth measurements in multiple narrow-band filters. Bright host stars are required to reach a signal-to-noise ratio high enough to detect the 10^{-4} signal. If the spectral integration or narrow-band filter includes significant continuum coverage, the $\Delta\delta$ signal will be diluted and more difficult to detect. Therefore, the bandwidth of the spectral integration or filter should be limited such that it includes only the wavelengths of the broadened line profile of interest.

Emission Spectroscopy

The thermal emission spectra of a transiting exoplanet can be measured by comparing the combined stellar plus planet emission spectrum just before secondary eclipse with the pure stellar spectrum from when the planet is completely hidden by the star during secondary eclipse (see secondary eclipse phase in Figure 6). The differential spectrum then represents the disk averaged, day-side, thermal radiation from the planet. The spectrum is best measured in the near- or mid- infrared where the planet is bright and the star is dim relative to optical wavelengths. Also, in the optical bands, the differential spectra could contain some contributions from stellar reflected or scattered light, if the planetary albedo is relatively high.

Under the assumption that a planet radiates uniformly as a blackbody across its entire surface, the secondary eclipse depth, in the Rayleigh-Jeans limit, due to thermal emission, $\delta_{s,therm}$ is

$$\delta_{s,therm} = \delta \left(\frac{T_P}{T_*} \right), \quad (12)$$

where δ is the usual primary transit depth, and T_P and T_* are the planet and star temperatures, respectively (e.g. Madhusudhan et al. 2014). The planet temperature can be estimated from the stellar temperature and radius, and the distance between the star and planet as

$$T_P \simeq T_* \sqrt{\frac{R_*}{2a}}, \quad (13)$$

where a is the semi-major axis of the planetary orbit (Madhusudhan et al., 2014).

Combining equations 12 and 13, the secondary depth, δ_s , can then be estimated as

$$\delta_s = \delta \sqrt{\frac{R_*}{2a}}, \quad (14)$$

in the Rayleigh-Jeans limit, neglecting any scattered or reflected light contributions, and assuming the planet's Bond albedo (the fraction of incident light reflected across all wavelengths) is zero, which is a reasonable approximation for most hot Jupiters (see Madhusudhan et al. 2014 and references therein). If the planet absorbs and re-radiates all

of the incident flux on its dayside alone, the predicted temperature will increase by a factor of $2^{1/4}$. Using HD 189733b as an example again, the estimated secondary depth $\delta_s = 0.57\%$. Charbonneau et al. (2008) measured the secondary depth of HD 189733b to be $0.598\% \pm 0.038\%$ at $24 \mu\text{m}$ from *Spitzer Space Telescope* times series photometry.

Orbital Phase Variations

Short period ($1 \lesssim P \lesssim 5$ d) exoplanets are expected to be tidally locked, with permanent day and night sides (Guillot et al., 1996). These planets rotate once per orbital period, which is slower than the 10-17 hour rotation periods of giant planets in the solar system. Given the difference in incident flux and rotation period from the solar system giants, it is interesting to investigate what portion of the incident flux energy is transported to the night side of the planet. Understanding the energy transport will provide constraints on atmospheric circulation of hot Jupiters. See Showman, Menou, & Cho (2008) for a review of hot Jupiter atmospheric circulation.

Photometric observations of a complete orbit will provide a measurement of the combined brightness of the star and planet as the planet goes through all phases from day side to night side and back. If the observations are in the near- or mid-IR, the mean temperature of the planetary surfaces facing Earth at each phase of the orbit can be estimated. Figure 7 shows the phase curve of HD 189733b measured in the *Spitzer* 4.5 μm IRAC band. The brightness measured during secondary eclipse sets the baseline stellar flux level. The difference between the peak flux and the stellar baseline yields the brightest (and hottest) phase of the orbit. The difference between the lowest flux of the phase curve (other than when in transit or secondary eclipse) and the baseline stellar flux indicates the coldest phase of the orbit. Notice that the night side flux of the planet only dips to about 50% of the dayside flux suggesting heat transfer from the day side to the night side. In the absence of winds, the hottest and coldest regions of the planet's atmosphere are expected to be at the substellar and anti-stellar points, respectively, corresponding to a flux maximum centered on the secondary eclipse and a flux minimum

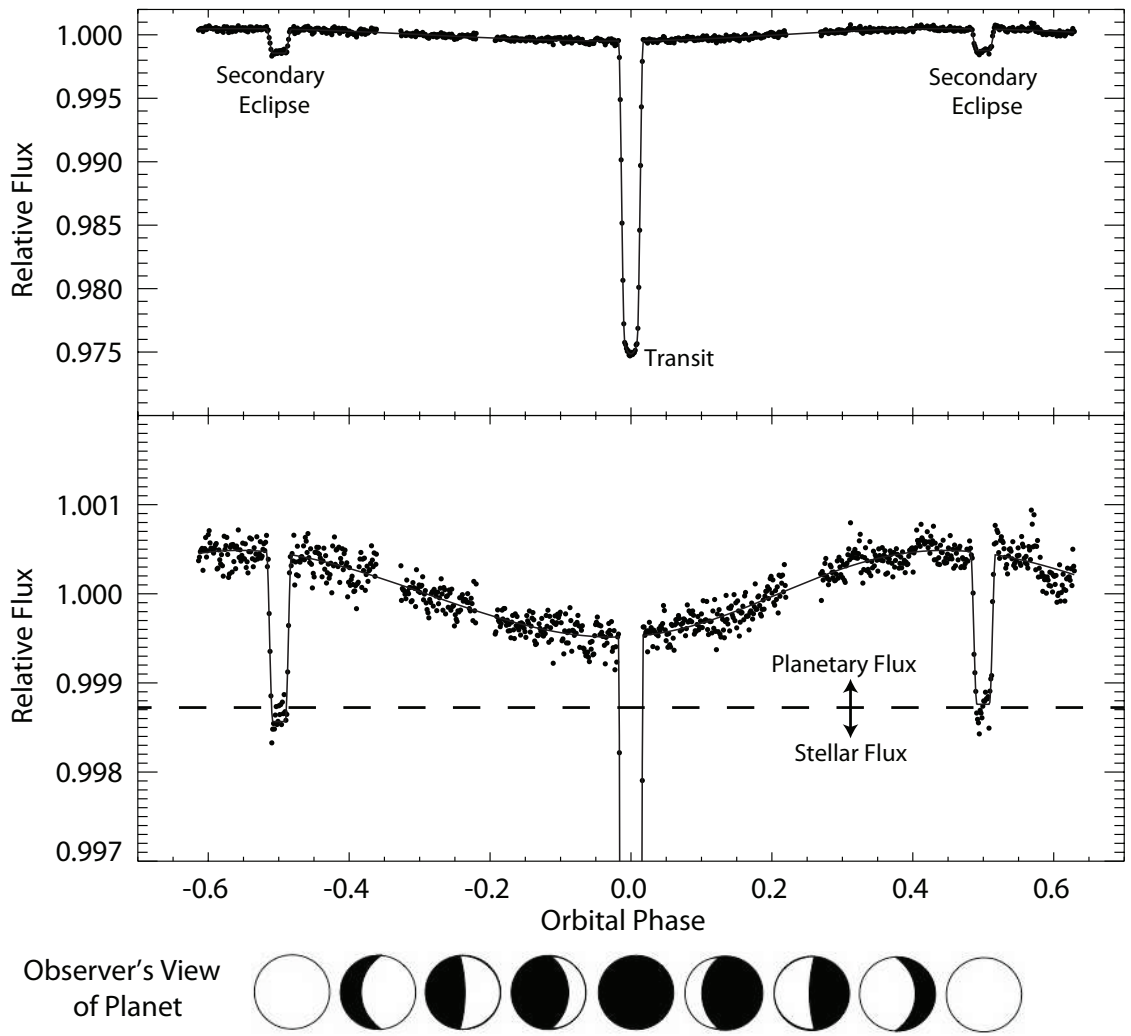


Figure 7. Phase curve of hot Jupiter HD 189733b measured in the *Spitzer* 4.5 μm IRAC band. The transit and secondary eclipses are labeled on the upper panel. The lower panel shows the same data as the upper panel, but with a reduced y axis range in order to better illustrate the change in flux as a function of orbital phase. The horizontal dashed line shows the flux level measured during secondary eclipse, and indicates the baseline stellar flux. The flux from the planet at any given phase can be calculated as the difference between the total measured flux and the dashed line. Beneath the plot panels is a diagram indicating the part of the planet that is visible at different orbital phases, with the planet's day side shown in white and the night side shown in black. Adapted from Madhusudhan et al. (2014).

centered on the transit. Note that for HD 189733b, there is a slight shift in the peak brightness and the full day side phase suggesting that winds are offsetting the hottest part of the planet from the expected center of the day side.

Reflected Light Detection

Reflected light spectroscopy and photometry is beyond the scope of this work, but I mention it briefly for completeness. Measurements of the light reflected from hot Jupiter planets is more challenging than thermal emission because the star-planet contrast ratio is much larger in the optical bands than in near- to mid-IR bands. Polarimetry is a potential method to detect reflected light from extrasolar planets. The basic principle is that reflected light is partially polarized, whereas the direct light emitted by the stellar photosphere has negligible linear polarization. It has also been suggested that the detection of specular reflection (or glint) from an exoplanet could reveal the presence of oceans on the surface (Robinson, Meadows, & Crisp, 2010). Madhusudhan et al. (2014) list references for several reflected light detections, non-detections, and upper limits. As this work was in the final stages of review, Martins et al. (2015) reported the first tentative detection of reflected optical-band light from an exoplanet (51 PEG b).

1.6 Wide-field Transit Surveys

Although a few transiting exoplanets were first discovered by RV searches and then found to transit later (e.g. HD 209458b, HD 189733b, 55 Cnc e), most transiting exoplanets have been discovered by wide-field transit surveys. Because RV surveys started earlier, and because of the chance orbital alignment required for transit discoveries, many more RV-only planets were discovered initially. Even so, ground-based transit surveys became productive as the time baseline of observations increased and survey instrumentation and data processing techniques became more sophisticated. As of 2015, ~ 200 transiting planets have been discovered by ground based surveys. In 2014, the number of confirmed space-based transiting planet discoveries surged due to the Kepler

mission (see §1.6.2) and now the total number of known transiting planets is ~ 1000 , compared to a total of ~ 450 RV-only planets. Figure 8 shows the distribution of RV and transiting planet discoveries by year. The distributions of RV planet discoveries, ground-based transit discoveries, and space-based transit discoveries are shown by the thin solid red line, thick solid green line, and dashed black line, respectively. In the following subsections, I review the key ground- and space-based transit surveys responsible for the discovery of the first ~ 1000 known transiting planets. Note the differences in photometric precision, sky coverage, and host star brightness targeted by the different surveys.

1.6.1 Ground-based

The **Optical Gravitational Lensing Experiment (OGLE)** was originally started in 1992 with the goal of discovering dark matter using the microlensing technique. The third phase of the project ran from 2001 to 2009 and was primarily devoted to surveying 14–17th magnitude stars for the purposes of detecting gravitational microlensing events and transiting planets with a 1.3 m dedicated telescope at Las Campanas Observatory, Chile. The project conducted six campaigns of three or four $35' \times 35'$ fields each (Udalski, 2003, 2007). In 2003, the narrow-field, deep OGLE search produced the first transit method exoplanet discovery, OGLE-TR-56, and eventually discovered a total of 8 transiting planets. However, due to the faintness of the OGLE host stars, false-positive investigation and detailed characterization of OGLE planets is difficult.

The **Trans-atlantic Exoplanet Survey (TrES)** was the first wide-field transit survey. TrES used three small telescopes located at Lowell Observatory, Palomar Observatory, and the Canary Islands (Alonso et al., 2004). The telescopes had a 100 mm diameter aperture, a field of view of $6^\circ \times 6^\circ$, and a pixel scale of $11''$. TrES produced the second transiting exoplanet discovery, and the first from a small, wide-field telescope targeted at relatively bright stars ($8 \leq R \leq 12.5$). The host star has $V = 11.79$, which allowed RV follow-up with a modest 1.5 m telescope. The planet, TrES-1b, is a hot Jupiter with mass $0.75 M_J$, radius $1.1 R_J$, and orbital period of 3.03 days. The planet is

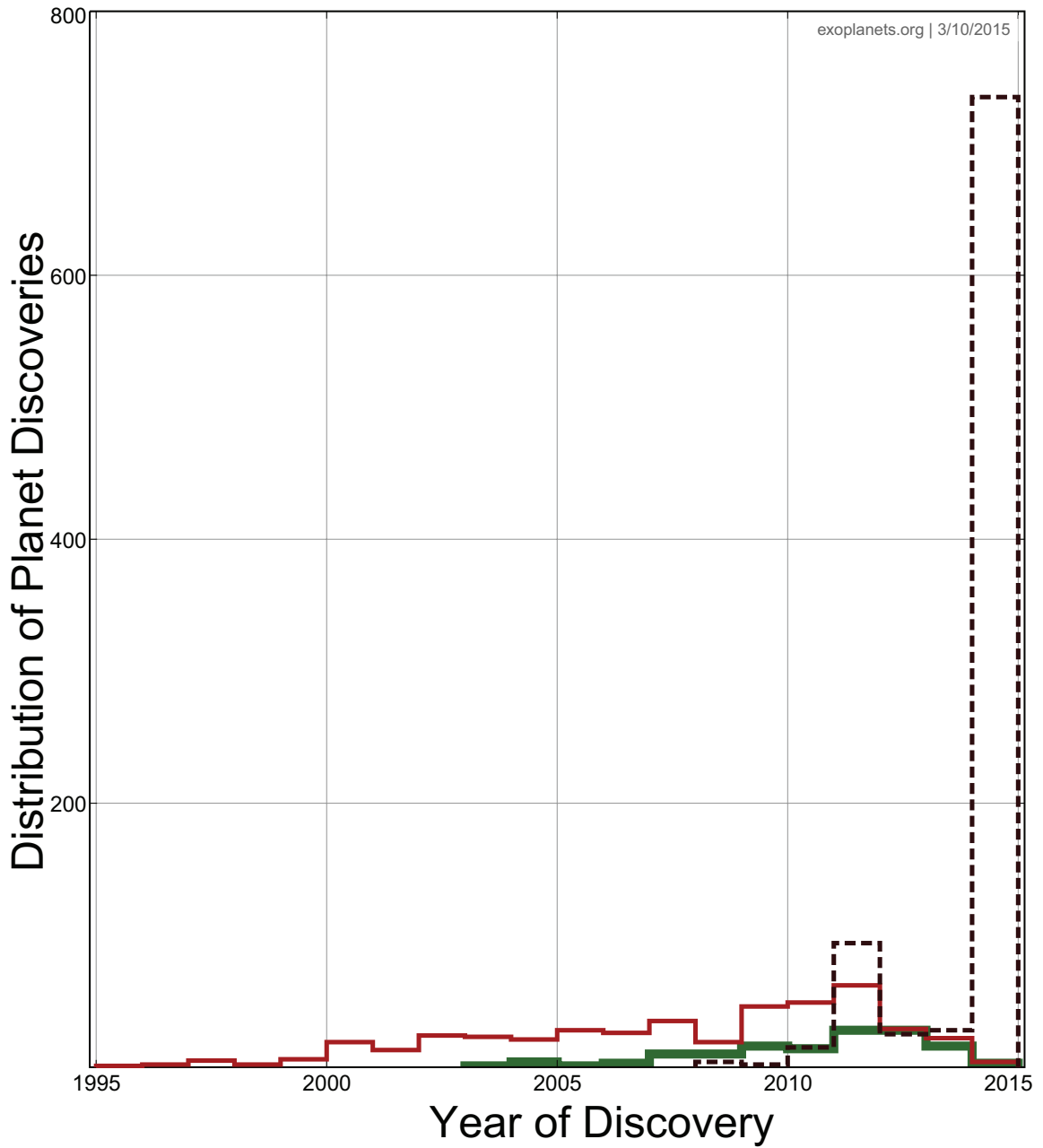


Figure 8. RV and transiting planet discoveries by year. The distribution of RV planet discoveries is shown by the thin solid red lines. The distribution of ground-based transiting planet discoveries is shown by the thick solid green line. The distribution of space-based (CoRoT and Kepler) transiting planet discoveries is shown by the dashed black line. The data were extracted from exoplanets.org on March 10th, 2015.

typical of the following ~ 200 transiting exoplanets discovered by ground-based transit surveys. TrES produced a total of 5 hot Jupiter planets, all having host star brightness of $V \sim 12$. The last TrES planet discovery was announced in 2011, and the survey is no longer operational.

The **XO Project** (McCullough et al., 2005) was a wide-field transit survey similar to TrES. The XO survey's objective was to find hot Jupiters transiting bright stars ($9 \lesssim V \lesssim 12$), which enabled high-precision follow-up observations. The survey started observations in 2003 using two ~ 100 mm aperture telescopes on a common mount located on the Haleakala summit on Maui, Hawaii. The pointing of the two telescopes tracked the same location on the sky to increase photon detection, and to provide failure mode redundancy. The cameras simultaneously observed 7° wide strips of the sky in drift-scan mode. The CCD detector pixel scale was $25'' \text{ pixel}^{-1}$, more than twice that of the TrES detectors. The survey's first planet discovery, XO-1b, orbits a $V = 11$ sun-like star (McCullough et al., 2006). In total, the survey produced five transiting hot Jupiter discoveries (although XO-3b may be a low-mass brown dwarf). The last planet discovery was announced in 2008.

The **Wide Angle Search for Planets (WASP)** consortium was established in 2000 and has produced more planets than any other ground-based transit survey. After some prototype camera testing, the group obtained funding for SuperWASP-N located at the Observatorio del Roque de los Muchachos on La Palma in the Canary Islands and SuperWASP-S at the Sutherland Station of the South African Astronomical Observatory (Pollacco et al., 2006). SuperWASP-N and SuperWASP-S started observations in 2003 and 2005, respectively. Each SuperWASP instrument consists of an equatorial mount on which up to eight wide-field cameras can be deployed. Each camera has an aperture diameter of 111 mm, a $7.8^\circ \times 7.8^\circ$ field of view, and a pixel scale of $13.''7 \text{ pixels}^{-1}$. With eight cameras mounted, the field of view of each multi-detector instrument is $\sim 482 \text{ deg}^2$. The survey targets stars with $9 \lesssim V \lesssim 13$. The first two confirmed SuperWASP planets, WASP-1b and WASP-2b, were announced in 2007. So far, the Extrasolar Planets

Encyclopedia lists ~ 100 transiting hot Jupiter discoveries by WASP.

The **Hungarian-made Automated Telescope Network (HATNet)** survey (Bakos et al., 2004, 2007) is a network of seven small telescopes optimized for detecting transiting hot Jupiter exoplanets. Five of the telescopes are located at the Fred Lawrence Whipple Observatory (FLWO) at Mount Hopkins in Arizona, and two are located at the Mauna Kea Observatory in Hawaii. Each telescope has an aperture diameter of 110 mm, an $8.2^\circ \times 8.2^\circ$ field of view, and a pixel scale of $14'' \text{ pixels}^{-1}$. The first telescopes started observations in 2003, and the first planet discovery, HAT-P-1b, was announced in 2007 (Bakos et al., 2007). HAT-South is a newer set of six telescope systems in the southern hemisphere that started observations in 2010 (Bakos et al., 2013). Two multi-camera telescope systems are located at each of Las Campanas Observatory (LCO) in Chile, the High Energy Stereoscopic System (HESS) site in Namibia, and at the Siding Spring Observatory (SSO) in Australia. Each telescope system has a 2×2 array of cameras with a total field of view of $8.2^\circ \times 8.2^\circ$. Each individual camera has an aperture diameter of 180 mm and a pixel scale of $3.''7 \text{ pixels}^{-1}$. The HAT-South detectors saturate at $r' \sim 10.5$. HATNet has been the second most productive survey and, so far, has announced 66 transiting exoplanets with host star brightnesses in the range $9 < V < 13$.

The **Kilodegree Extremely Little Telescope (KELT)** transit survey (Pepper et al., 2003, 2007) aims to fill the brightness gap between RV surveys ($V \lesssim 8$) and the other wide-field surveys described above ($V \gtrsim 9-10$). Planet's with $8 < V < 10$ are of particular interest because they allow for detailed false positive analysis, detailed planetary system characterization, and atmospheric characterization. The KELT survey uses single camera telescopes with very wide fields of view. The KELT-North telescope, shown in the left panel of Figure 9, is located at Winer Observatory near Sonoita, Arizona and started science operations in 2005. The telescope has a Mamiya 645 80 mm focal length f/1.9 lens, resulting in a 42 mm aperture diameter, a $26^\circ \times 26^\circ$ field of view, and a pixel scale of $23'' \text{ pixels}^{-1}$. Over the course of a year, the telescope images 13 survey fields in a strip around the sky centered at a declination of +30 degrees. The KELT-South



Figure 9. KELT North and South Telescopes. *Left Panel:* The KELT-North telescope at Winer Observatory near Sonoita, Arizona. *Right Panel:* The KELT-South telescope at the South African Astronomical Observatory observing station near Sutherland, South Africa.

telescope, shown in the right panel of Figure 9, is a twin of the KELT-North telescope and is located at the South African Astronomical Observatory (SAAO) observing station near Sutherland, South Africa and has been operating since 2012. Due to the large pixel scale of the KELT cameras, KELT photometry suffers from significant blending with nearby stars in many cases. To help sort out which of the blended stars are exhibiting transit-like events in the KELT data, and to conduct high-precision follow-up observations, the KELT team has assembled a world-wide consortium of more than ~ 30 professional, student, and high-capability amateur astronomers. The first KELT discovery, KELT-1b, was announced in 2012 and orbits a $V = 10.7$ host star. In Chapter 8 of this work, I present KELT-6b, which is the fourth planet discovery announced by the KELT survey. So far, KELT has announced five planet discoveries, and at least six more are in the analysis and publication pipeline. Of these discoveries, the distribution of host brightness includes one $V = 7$, three $V = 8$, two $V = 9$, and four $V = 10$. Although the KELT survey is not competing with the large volume of planet discoveries by SuperWASP and HATNet, it is producing a good number of very bright, high value exoplanets, as per the original design intent.

The **Qatar Exoplanet Survey (QES)** (Alsubai et al., 2013) aims to fill the

brightness gap between the capabilities of OGLE and most of the other wide-field surveys described above (i.e. $12 < V < 15$). The first telescope array is located in New Mexico and has been operating since 2009. The array consist of 4 cameras targeted at the $12 < V < 15$ brightness range and a fifth camera targeted at the $8 < V < 10$ brightness range. The first QES discovery, Qatar-1b, was announced in 2011. So far, QES has produced two transiting hot Jupiters, both orbiting $V \sim 13$ stars.

1.6.2 Space-based

Although the large number of hot Jupiters discovered so far continue to teach us about planetary system formation and the diversity of planetary systems, the ultimate goal is the discovery and characterization of earth-like planets in the habitable zone of sun-like stars, with the hopes of eventually having enough sensitivity to search for signs of life on the planets. Transits of earth-like planets across sun-like stars produce a small change in a star's brightness of 84 parts per million (ppm), or equivalently ~ 0.09 mmag, lasting for 1 to 16 hours depending on the orbital inclination and period. Ground-based observations suffer from the detrimental effects of the Earth's atmosphere on systematics and noise, and from the limited duration of continuous observations. One obvious (albeit expensive) solution to overcome both issues is to conduct exoplanet searches from space-based observatories.

The first space-based transit survey was conducted by Gilliland et al. (2000) using the *Hubble Space Telescope* (*HST*; Adorf 1987). The goal was to determine the frequency of hot Jupiters. Based on simulations, they expected to find 17 planets in the ensemble of 34,000 main-sequence stars in the globular cluster 47 Tucanae, but no planets were found in the 8.3 days of time-series observations from the Wide Field Planetary Camera 2 (WFPC2; Trauger & Brown 1992). The reason now favored to explain the null detection is the cluster's low metallicity (Weldrake, Sackett, Bridges, & Freeman, 2005).

The **CONvection ROTation and planetary Transits (CoRoT)** spacecraft (Baglin, 2003) was the first spacecraft dedicated to the study of astro-seismology and the detection

of transiting extrasolar planets. The mission targeted stars with $11 < V < 16$ for the planet search, and was sensitive enough to detect planets $2\times$ the size of earth for $V < 14$ and gas giants over the entire range. It had a 27 cm diameter aperture, a $2.7^\circ \times 3.05^\circ$ field of view, a pixel scale of $2''/37 \text{ pixels}^{-1}$, and started collecting science data in 2007. Near the start of the mission, the two-hour photometric precision ranged from 0.1 mmag at $R = 11.5$ to 1.0 mmag at $R = 16$ (Aigrain et al., 2009). CoRoT typically observed 3 to 4 different fields per year for an average of 78 continuous days each. There were two exoplanet detectors on the spacecraft, but one failed in 2009. A total of 5640 stars per detector could be observed resulting in a total of more than 150,000 stellar light curves (Moutou et al., 2013). In total, CoRoT has announced 1 transiting brown dwarf and 21 transiting planet discoveries, including two super earths. The smallest, CoRoT-7b (Léger et al., 2009; Queloz et al., 2009), has radius $1.68 R_\oplus$, mass $4.8 M_\oplus$, transit depth 350 ppm, orbital period 0.85 days, and a G9V host star with brightness $V = 11.7$. The CoRoT planet radii range from 0.144 to $1.49 R_J$, and the orbital periods range from 0.85 to 95.3 days. The mission ended when a spacecraft computer failed in 2012.

The **Kepler Mission** (Borucki et al., 2010) launched in 2009 and conducted a space-based transit survey that was designed to determine the frequency of earth-sized planets in and near the habitable zone of sun-like stars. Since the probability that an earth-like planet transits its sun-like host star is only $\sim 0.5\%$, the mission was designed to search more than 100,000 stars, in case earth-like planets are rare. Since habitable zone planets were desired around sun-like stars, the mission needed to be sensitive to planets with orbital periods of up to a year. To reliably confirm the periodicity of a transit signal, four consecutive transits need to be observed. To achieve this goal, the spacecraft was designed to stare at the same place in the sky for 3.5 years. The fixed location was selected to be centered in Cygnus at RA = 19h 22m 40s, Dec = $45^\circ 30'$.

To enable a reliable 4σ detection of the ~ 80 ppm Earth-Sun transit signal, the photometric precision needed to be ≤ 20 ppm (including 10 ppm allocated for stellar variability). Viewed from a distance, Earth would take 13 hours to cross the center of the

Sun. However, to allow for the detection of earth-like planets that have an orbital inclination of $< 90^\circ$, the goal was set to reach a precision of 20 ppm in 6.5 hours of integration. This requirement combined with the need to monitor stars with Kepler Mag ≤ 12 set the diameter of the telescope aperture to 0.95 m. To continuously and simultaneously monitor 100,000 stars, the detector field of view was set at 105 square degrees, and 42 CCDs with a pixel scale of $3''.98 \text{ pixels}^{-1}$ were designed to cover the field of view. The detectors were read out every 6 seconds and integrated off-detector to limit saturation of bright stars, resulting in a dynamic range of coverage of $9 < V < 16$. The telescope was intentionally defocused to give a $10''$ point-spread-function (PSF).

In operation, *Kepler* reached a combined differential photometric precision (CDPP), which included photometric and stellar noise, of about 30 ppm for stars with Kepler Mag = 12 (Caldwell et al., 2010; Lissauer, Dawson, & Tremaine, 2014), rather than the expected 20 ppm. Nevertheless, a number of studies were conducted to pinpoint the extra noise sources, and advanced data processing and decorrelation techniques helped to mitigate the effects to allow reliable detection of 80 ppm signals. In May 2013, the second of four reaction wheels on the Kepler spacecraft failed, leaving the telescope unable to point precisely at its original target field, and ending its primary mission. In the four years it operated, *Kepler* produced planet discoveries ranging from the size of Earth's Moon at short periods, and larger planets with orbital periods as long as 1-2 years. Figure 10 (from Lissauer, Dawson, & Tremaine 2014) shows the planetary radius and orbital period of *Kepler* planet candidates from the first three years of *Kepler* data. Planet multiplicity in the system is represented by different symbols. The legend above the figure defines the multiplicity represented by each symbol and gives the total number of systems discovered for each multiplicity.

Only about a third of the *Kepler* planet candidates have been confirmed as planets. The difficulty is that RV measurements of stars becomes too time intensive, or even impossible, for stars as faint as typical *Kepler* planet hosts. However, from the significant number of multiple planet systems that have been discovered, many planet masses and

orbits have been determined solely from TTV data. Kepler determined the distribution of planets for sun-like stars with reasonable accuracy for $R_p \gtrsim 1 R_E$ in the range $P \lesssim 50$ days, and for $R_p \gtrsim 2R_E$ in the range $P \lesssim 150$ days. However, care must be taken to estimate the mean number of habitable zone earth-like planets, η_E , from *Kepler* data, because there are not enough samples to make a statistically reliable prediction. So, one must extrapolate downward in size and upward in orbital period from the region where *Kepler* has a statistically reliable planet sample, which introduces uncertainty. Three independent studies of *Kepler* light curves yield $\eta_E = 0.09$, $\eta_E = 0.12$, and $\eta_E = 0.02$ (see the *Kepler* review by Lissauer, Dawson, & Tremaine 2014 for details). Clearly the η_E question has not been completely resolved by the current *Kepler* data results. However, more candidates will likely be confirmed as planets, and more candidate systems will be extracted from the *Kepler* data over time.

Kepler, with its two remaining reaction wheels, was re-purposed to a new mission, **K2** (Howell et al., 2014), and started collecting data again in June 2014. The K2 mission points near the ecliptic, observing fields for ~ 75 days each as it orbits the Sun. K2 is a community proposal driven project, and although targets can be proposed for a variety of scientific goals, exoplanet discovery and characterization is a key goal of the mission. Spacecraft pointing was compromised by the loss of the second reaction wheel and as a result, photometric precision will be compromised. Early testing has demonstrated that K2 can reach a photometric precision of 82 ppm for a 12th magnitude star over six hours of integration. Vanderburg & Johnson (2014) have demonstrated that when accounting for the non-uniform pixel response function of K2's detectors, by correlating flux measurements with spacecraft pointing, improvements by factors of 2-5 over raw K2 photometry can be achieved, resulting in photometric precision similar to *Kepler* at the same magnitudes. In the first few months of operation, K2 has already produced discoveries of two super-earth, multi-planet systems (Armstrong et al., 2015; Crossfield et al., 2015).

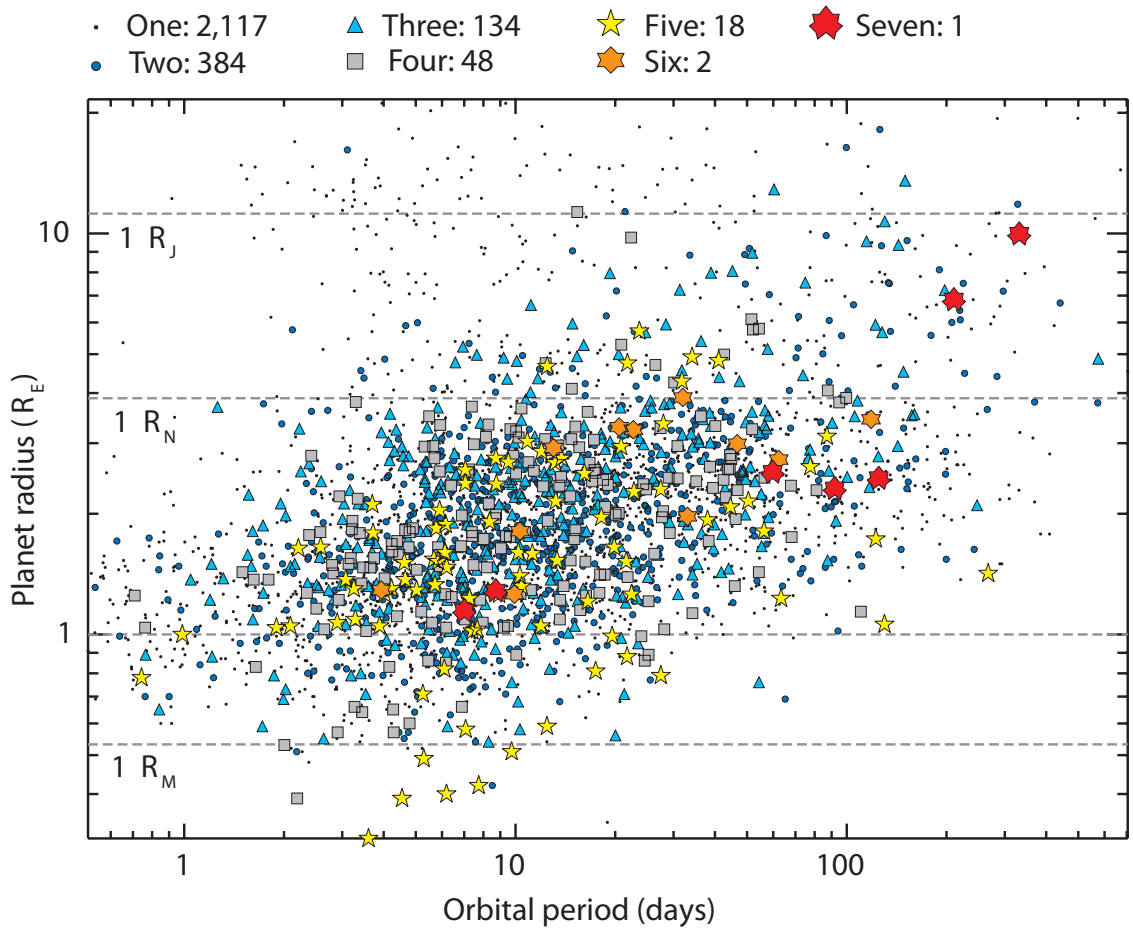


Figure 10. *Kepler* planet candidate radius vs. orbital period. Colored symbols represent the number of planetary candidates in the system found by analyzing the first three years of *Kepler* data. The numbers shown above the figure represent the total number of systems of a given multiplicity. Planets with shorter orbital periods are over-represented because geometric factors and frequent transits make them easier for *Kepler* to detect. R_E , radius of Earth; R_J , radius of Jupiter; R_M , radius of Mars; R_N , radius of Neptune. (from Lissauer, Dawson, & Tremaine 2014).

CHAPTER 2

HIGH-PRECISION PHOTOMETRY

Although space-based observatories avoid the detrimental effects of the Earth's atmosphere, Earth-based observatories can produce high-precision photometry through careful planning and execution of the observations, and by taking advantage of many specialized data reduction techniques that help to minimize the atmospheric effects and maximize the photometric precision of the final data product. In this chapter, I discuss how to measure and approach the theoretical limits of high-precision ground-based photometry.

2.1 CCD Overview

All of the results presented in this work are based on precise measurements of the brightness of a star of interest (the target star) in a time-series of science images observed using a charge-coupled device (CCD) detector. See Mackay (1986) for a review of the use of CCDs in astronomy applications. A CCD has an array of charge collection wells, or pixels, that convert photons into electrical charge. After being exposed to light, the charge in the wells is shifted to the edge of the device, where the number of electrons in each well is converted to a digital value called an analog-to-digital unit (ADU) and is stored in an image array to be further processed and analyzed. The conversion factor when going from electrons to ADU is referred to as the gain, G , which is in units of electrons/ADU. The gain of the two cameras used to collect data for this research is $G = 1.5$ electrons/ADU. This process of moving the data out of the CCD is generally referred to as reading the device, or simply read-out.

2.2 CCD Image Calibration

CCDs introduce various artifacts, nonlinearities, and noise into the digital representation of the light detected by each pixel. The Data Processor (DP) module of AstroImageJ (AIJ; see §4.1) provides the tools needed to optimize the science image data using various calibration images that can be obtained separate from the science observations.

2.2.1 Bias Subtraction

CCD detectors exhibit a bias level that creates a shift in the zero point of the digital value representing the number of photons detected by each pixel. The zero point of each pixel can be determined by taking a zero second exposure and reading the resulting ADU values to create a bias image. In this work, I median combine (see §2.2.5) a large number (21-45) bias images to create a master bias image. This master bias image is then subtracted from each science, dark, and flat image to set the zero point of the ADU values back to zero (i.e. zero ADU represents zero photons detected). AIJ's DP module automatically generates the master bias image and uses it to calibrate all other calibration and science images.

2.2.2 CCD Nonlinearity Correction

CCDs are not perfectly linear devices, so the bias-subtracted ADU values are not exactly proportional to the number of incident photons. When the wells start to fill, the nonlinear behavior changes to saturation at which point continued exposure to light will not add charge to the well. The unsaturated nonlinear behavior can be characterized by taking exposures of varying length of a highly stabilized light source.

To characterize the nonlinearity of the two detectors I used to collect data for this work, I affixed a piece of plain white paper over the baffle in the center of the telescope primary mirror and illuminated the paper with the stabilized light source. I set the light

source brightness such that a 100 sec exposure produced an average of $\sim 50,000$ ADU across the 16-bit detector. After collecting bias frames, I took test exposures of the illuminated paper ranging in duration from 2 sec to 110-120 sec (which pushed the detector near saturation at $\sim 60,000$ ADU). I also took a 2 sec exposure between all test exposures to provide a measure of the light source stability. I used the very small variations in the bias-subtracted 2 sec exposures to adjust the mean ADU values measured from the bias-subtracted test images.

A plot of scaled exposure time (which represents a scaled version of the actual number of photons incident on the detector) versus the adjusted mean ADU is shown in Figure 11. Note that the axes are plotted reversed from typical linearity plots so that the best second-degree polynomial fit to the data provides the coefficients needed to correct linearity using AstroImageJ. For simplicity in the values used to correct the nonlinearity, I desired a zero point corresponding to zero ADUs, so I forced the fit to go through the origin, and I iteratively scaled the exposure times until the linear coefficient of the fit was equal to one. The resulting quadratic coefficient of the fitted polynomial was $\sim 8 \times 10^{-7}$ for both CCDs measured. It is often stated in the literature that data were obtained from the linear region of a CCD detector. However, note in the Figure 11 that the full range of ADUs exhibits some level of nonlinearity, so there is no completely linear region for the U16M CCD (and likely most CCDs). The result is that linearity correction is useful to correct all ADU values, regardless of exposure level.

AIJ's DP module provides the option to correct the nonlinearity in the bias subtracted science data by replacing the bias-subtracted ADU with the corrected value. The correction I used in this work is:

$$ADU_{corrected} = ADU_{measured} + (8 \times 10^{-7})ADU_{measured}^2, \quad (15)$$

resulting in a correction of 2000 ADU for a measured value of 50,000 ADU (or about 4%). The CCD specification states that nonlinearity is $\leq 2\%$. However, if the fit to my test data is not forced through the origin, the deviation from linearity would be split between both the high and low ends of the ADU range, resulting in an overall $\lesssim 2\%$ nonlinearity

and possibly explaining the manufacturers specification value. AIJ also applies the nonlinearity correction to the bias-subtracted dark and flat images (see the next two subsections) before using them to calibrate the science images.

2.2.3 Dark Subtraction

When a CCD is operated with no light incident on its pixels (e.g. by keeping the camera shutter closed), a charge termed dark current builds up in the wells due to thermal processes. Dark current can be minimized by cooling the detector, but is always present to some degree and must be accounted for and removed from the data for high-precision measurements. Dark current varies from pixel-to-pixel, with the charge in some "hot" pixels being dominated by dark current. Dark current can be measured for a specific science exposure time by exposing the CCD for the same exposure time, but with the camera's shutter closed. Since dark current is affected by shot noise (see §2.11) and is thus time varying, I median combine (see §2.2.5) a large number (21-45) of raw dark images so that the dark current can be determined to high precision for each pixel in the master dark image.

The raw dark images are first bias subtracted and then scaled for nonlinearity. The bias subtracted dark images are then median combined to form the master dark image. AIJ's DP module will build the master dark image as described here and apply it to the flat and science images automatically.

Since the master dark has the bias signal removed, if one makes the assumption that dark current increases linearly over time, then a master dark can be scaled to be acceptable as a master dark for science images that have exposure times differing from the dark images. In practice, dark scaling seems to work acceptably well for science images with exposure times ranging from $\sim 50\%$ to $\sim 150\%$ of the dark exposure time. Some hot pixels do not seem to scale linearly in time, so exposure time scaling works less favorably to correct them.

If nonlinearity correction and exposure time scaling are not needed, bias

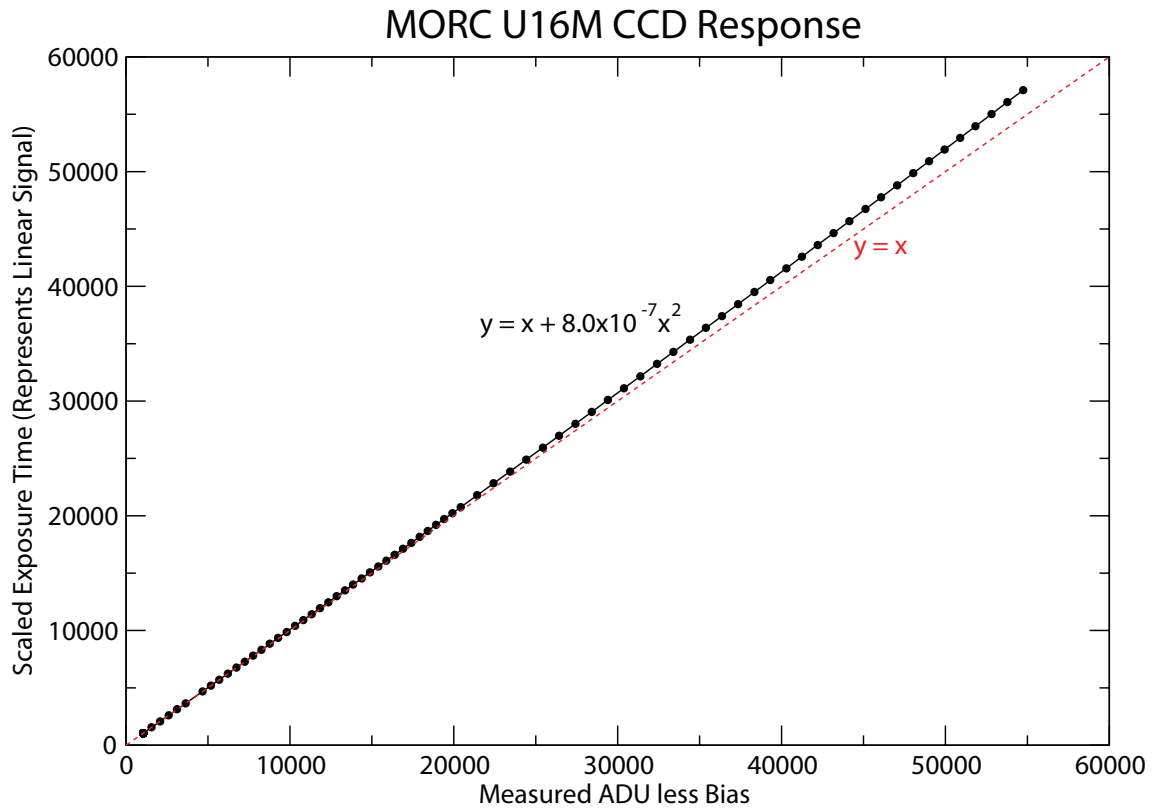


Figure 11. MORC U16M CCD linearity measurements. The black dots show scaled exposure time (which represents a scaled version of the actual number of photons incident on the detector) vs. measured bias subtracted ADU. The red dashed line shows the linear response. Note that the axes are plotted reversed from typical linearity plots so that the best second-degree polynomial fit to the data provides the coefficients needed to correct linearity using AstroImageJ. Also note that there is essentially no completely linear region in the CCD's response curve.

subtraction is not required since the bias signal is combined with the dark current in the master dark. Since all of my data are corrected for nonlinearity, I have used bias subtraction separate from dark subtraction for all of my image calibrations.

2.2.4 Flat-field Correction

Pixel sensitivity to a photon flux that is constant across a CCD array varies from pixel-to-pixel. These inter-pixel sensitivity variations can greatly increase time series photometric noise if a source falls on different sets of pixels from exposure to exposure. The sensitivity variations can be measured on a pixel-by-pixel basis by uniformly illuminating the CCD with a flat-field of light. Optical vignetting and dust specs on optical surfaces (especially on filters and the glass cover of the CCD, since they are near the focal plane) will also cause a varying response at each pixel to a flat-field of light, when observed through a telescope. If a flat-field of light is projected onto the CCD through a telescope's optical path, the system-wide response to a flat-field can be determined. Once this response has been measured, the science images can be divided by the normalized flat-field response to remove much of the pixel-to-pixel variations.

Two different approaches are widely used to create flat-field images. Dome flats are obtained by observing a uniformly illuminated surface attached to the telescope enclosure. Alternately, twilight flats are obtained by observing the clear sky at morning or evening twilight at elevations near $\sim 45^\circ$ directly opposite the Sun, which provides a flat-field with a minimal gradient. The amount of residual gradient depends on the angular size of the field-of-view of the detector.

While dome flats are more convenient to obtain because the observations do not depend on time critical and time limited ranges of sky brightnesses, it is difficult to uniformly illuminate the dome flat surface. Because of this, I used twilight flats to calibrate all science images used in this research. Because the optical response may be different at different wavelengths of light, and because each filter will have its unique set of dust specs, the flat-field response must be measured for each filter used.

To create a master flat-field image in a particular filter during evening twilight, I start taking 2 s exposures of the twilight sky every minute or so at an elevation near $\sim 45^\circ$ in the east (directly opposite the Sun). Once the sky brightness drops enough that the 2 s images are no longer saturated, I expose more frequently until the sky brightness reaches a level that gives an average ADU of $\sim 40,000$ counts per pixel in a 5 s exposure. The exposures before that point are discarded because a significant shutter open/close pattern is imprinted on images with exposure times less than ~ 5 s. At this point, I slew the telescope $\sim 1'$ west, take another the 5 s exposure as soon as practical, and repeat as fast as practical, until the average ADU in the image is down to $\sim 20,000$ counts. The twilight flat-field images will be contaminated with stars, so the telescope slew between exposures is included to allow the stars to be removed by the data reduction "median" operation described below. Next, I double the exposure time to 10 sec (which should give an average of $\sim 40,000$ ADU again), slew $\sim 1'$ west, expose, and repeat until the average ADU is again $\sim 20,000$ counts. As exposure times become longer, I attempt to extend the exposure time to keep the average ADU at $\sim 30,000$ counts. When the exposure time reaches ~ 4 minutes for an average ADU of $\sim 20,000$ counts, I stop collecting flat-field data and prepare for science observations. For morning twilight flats, the process is similar except the counts are increasing from exposure to exposure, and the telescope is pointed at $\sim 45^\circ$ elevation in the west.

The individual twilight flat images must be combined to produce a master flat-field image that is used to calibrate the science images. Calibrating with a flat will increase the noise of the science image due to the shot noise in the light from the twilight sky. To minimize the added noise, I attempt to obtain enough raw flats such that the master flat has ~ 1 mmag per pixel of shot noise. For a CCD gain of $G = 1.5$, the total counts per pixel needed is then $\sim 650,000$ (see §2.11). Since most of the measurements I make combine the ADUs of hundreds of pixels, the noise contributed by the flat-field operation is then a negligible component of the total measurement noise (again, see §2.11).

To create the master flat image, each raw twilight flat is bias-subtracted using the

master bias image. The bias-subtracted images are then corrected for CCD non-linearity according to equation 15 and are then dark-subtracted using the master dark. Next, a plane is fit to, and then subtracted from, the dark-subtracted twilight flat to remove any residual gradient in the twilight sky. The resulting images are normalized such that the pixels in each image have a mean value of 1.0. Finally, the master flat image is formed by median combining (see §2.2.5) the normalized twilight flat images. The median operation essentially ignores all outlier pixel values in the normalized raw images. The ignored outliers include the pixels from each raw image that have counts above the median sky background due to bright stars. The DP module of AIJ automates the process of building a master flat-field image.

2.2.5 Median Combining

Master calibration images are often created by median combining several individual images to reduce the effects of outlier pixel values. The value of each pixel (x,y) in the median combined image is taken as the center value resulting from a numerical sort of the values of pixel (x,y) from all of the individual images. If there are an even number of individual images, the median combined pixel value is taken as the average of the two values nearest the center after sorting. Median combining effectively ignores the contributions of outlier pixel values in the individual images caused by temporal hot pixels, cosmic ray hits, stars in the case of individual flat-field images that are shifted on the sky from exposure-to-exposure, etc. Average combining is sometimes preferred over median combining when creating master bias and master dark images, however, care must be taken to ensure that all persistent charge has dissipated from the detector before starting the raw bias and raw dark exposures. Median combining is more forgiving of charge that persists from the last exposure taken prior to starting bias or dark exposures.

2.2.6 Science Image Calibration

After the linearity correction coefficients have been determined, and the master bias, master dark, and master flat images have been created, AIJ's DP module will automatically apply the corrections to a time-series of science images. The science images are calibrated by subtracting the master bias image, correcting for CCD non-linearity according to equation 15, subtracting the master dark image, and dividing by the normalized flat-field image.

Even with a high-quality master flat, my fully calibrated science images retain a flat-fielding error of up to 5% for areas on the detector that are obscured by dust specs on the glass window of the CCD. I believe the dust spec residuals are significant because the sides of the telescope are open between the primary and secondary mirrors, which allows significant off-axis scattered light to reach the CCD during twilight. Since significant light is arriving at the dust spec on the CCD window from all angles, rather than perpendicular to the focal plane, the loss of light at the detector due to a dust spec measured during twilight is less than the loss of light from a night-sky point source for which the proportion of scattered light is much less.

2.3 Telescope Guiding

In the best case, flat-field calibration leaves residuals of $\gtrsim 0.5\%$ RMS in an individual corrected image (Mackay, 1986). In this work, I am attempting measurement precisions of $\sim 0.1\%$, or even less in some cases, but my calibrated images have flat-field errors of up to 5% for the pixels under dust specs. Because the measurements in this work are differential (see §2.7), the flat-fielding residuals can be mitigated if each star involved in a differential measurement can be kept fixed at the same position on the detector for all images of the time-series. However, telescopes never track a position on the sky perfectly, so position errors must be fed back to control the telescope pointing. This technique is called guiding.

For telescope mounts with poor tracking or periodic tracking errors, pointing errors must be fed back to the telescope control system more often than the rate at which science image exposures are taken. This can be achieved by using a second off-axis detector to measure the telescope pointing at a high rate. Depending on the rate at which corrections are required, the star used to measure the telescope's pointing may need to be significantly brighter than the target star. These off axis detectors are normally small to keep cost down, so the placement of a bright star on a small guide camera detector significantly limits the placement of the target and surrounding field on the science detector. This also often requires that the science detector be rotated to cumbersome odd angles, rather than, for example, a convenient north-up, east-left orientation. Another issue is that imperfect polar alignment of the telescope will result in the field on the science detector slowly rotating about the center of the star on the guide detector. This field rotation limits the power of guiding to mitigate the effects of flat-field residual errors.

The MORC telescope (see §3.1) used to observe all data presented in this work has excellent free-running tracking and no perceptible periodic pointing error. It can maintain the position of a field on the detector to within a few arc-seconds ($\sim 1'' - 3''$ depending the altitude of the target) for up to 5 minutes. The exposure times used in this work are all less than 5 minutes, so we guide from the science images by measuring the difference in the position of the centroid of the target star from an initial reference position, and feedback pointing corrections to the telescope mount between each exposure. This method of guiding minimizes field rotation due to polar misalignment, and maintains the same orientation of the field in all images from the telescope.

Another advantage of the MORC guiding system is that if clouds or equipment failure cause a break in the observing sequence, the target star can be placed exactly back on the same pixels on the detector. While placing a target back on a precise position on the science detector may be possible when a separate guide camera is used, it is difficult to do in many cases. The implementation of the MORC guiding system is discussed in §3.5.4.

2.4 Defocusing

The exploitation of the telescope defocusing technique has helped me achieve exceptional photometric precision. The effects of residual inter-pixel sensitivity variations after imperfect flat-fielding can be minimized by spreading the light to be measured over many pixels and combining the ADU from all of the pixels. The atmosphere naturally causes light from a point source to be broadened, but often it is advantageous to defocus the telescope slightly to spread the light over more pixels. When a large number of ADUs are summed, the precision of the total ADU value will benefit from the averaging of the sensitivities of all pixels involved. This technique is a third line of defense against imperfect flat-fielding and imperfect telescope guiding.

Another positive side effect of defocusing is that the dynamic range of source flux that can be incident on the detector without causing saturation is greatly increased. This is very beneficial for the differential measurements used in this research (see §2.7), since it likely provides more non-saturated sources on the detector that can be used to find the differential brightness of the target source. However, defocusing in crowded fields can cause problems and may need to be minimized if a source of interest begins to overlap (or blend) with a nearby source as the sizes of the sources on the detector increase with increasing amounts of defocus.

2.5 Aperture Photometry

Photometry is a technique used to measure the amount of flux detected within a fixed set of pixels on a CCD. The fixed set of pixels is defined as the aperture. The sum of the calibrated science image ADUs from all pixels that fall within the aperture gives the total flux in the aperture, which is sometimes referred to as the integrated counts. If the aperture encloses all of the flux from a source (such as a star), we can measure the total integrated counts from the source. A radius of $3 \times \text{FWHM}$ (full-width half-maximum) includes $\sim 98\%$ of the flux from a Gaussian point spread function (PSF). In addition to the

source's contribution, the integrated counts will contain counts contributed by the brightness of the night sky called sky background. The ADUs/pixel contributed by the local sky background at the source need to be estimated so that the ADUs contributed exclusively by the source can be determined.

All apertures used in this research are circular, so the sky background can be estimated from the pixels in an annulus that is centered at the center of the aperture. The inner edge of the annulus should be far enough away from the wings of the source's PSF so that the pixel ADUs are correct representations of the sky background only. The outer edge of the annulus should be close enough to the source so that the background is still representative of the local background in the aperture. Furthermore, the sky background has shot noise, so the region needs to be large enough to minimize the overall contribution to the total error of the measurement (see §2.11). Ideally, the sky background annulus should enclose as many, or even more, pixels than are enclosed by the aperture to minimize the noise contribution.

Crowded fields complicate the estimation of the local sky background since stars near the target of interest often fall within the background annulus. The photometer in AIJ removes the contributions of flux from stars in the background annulus by iteratively removing pixels from the background set that have ADU values differing from the mean by more than 2σ . The iteration continues until the mean ADU of the pixels remaining in the background set converges or the maximum number of allowed iterations has been reached without convergence.

The resulting mean ADU from the background region is adopted as the local sky background and is subtracted from each pixel in the aperture. AIJ also offers the option to fit a plane to the final set of pixels remaining in the background region. Then the value of the plane at each pixel in the aperture is subtracted from the pixel's ADU. The sum of the background subtracted ADU values within the aperture is then the net integrated counts from the source. If the source's net integrated counts from a time-series of calibrated images is plotted against time, a light curve representing the source's relative brightness

over time is created. There is still at least one major source of contamination in the light curve of the star. The molecules in the Earth's atmosphere absorb and scatter some of the photons from an astronomical source, resulting in time-varying changes in the PSF size and apparent brightness of the source, even though the source brightness is constant.

2.6 Variable Radius Aperture Photometry

Variable radius aperture photometry is an extension of the fixed radius aperture photometry discussed in section 2.5. Rather than keeping a fixed size aperture for all exposures in the time series, the radius of all apertures in a particular exposure is set to a user specified constant factor times the average FWHM of the stellar PSFs in the image. AIJ determines the average FWHM in each image from all the sources measured with an aperture. As the FWHM changes throughout the time-series, the aperture size for each image is proportionally adjusted.

The advantage of the variable radius aperture is that the same fraction of the total stellar flux can be captured as the PSF size varies throughout the night, improving signal-to-noise and reducing systematics in many cases. Variable apertures should not be used for cases where one or more target and/or comparison stars have a nearby neighbor that will start to blend into the aperture of the star of interest in exposures with poor seeing. The variable aperture will produce more scatter in the light curve in this case because not only will the neighbor's flux be spread toward the variable aperture of interest, the variable aperture will grow at the same time and will include a larger fraction of the neighbor's flux than a fixed aperture.

Howell (1989) showed that the theoretical aperture radius which produces the highest photometric precision is $\sim 1 \times \text{FWHM}$, but that the optimal radius varies depending on star brightness, sky background, and the other parameters included in the calculation of photometric error (see equation 21). Through trial and error, I have found that a good nominal setting for the FWHM scaling factor in AIJ is ~ 1.2 for MORC images. The FWHM scaling factors I have used range from ~ 0.9 to ~ 1.3 , and the

optimal setting depends on the level of telescope defocus, the brightness of the target and comparison stars, the amount of sky-background, and the proximity of neighboring stars near an aperture.

2.7 Differential Photometry

If only the fractional change in the brightness of a source is needed throughout a time-series of observations (i.e. the absolute brightness of a source is not required), then the net integrated counts from the target of interest can be compared with the net integrated counts from other sources that are expected to have constant brightness and that fall on the detector in all exposures of the time-series. The measurement of the brightness of a target that is based on the brightness of one or more other objects (or the comparison ensemble) is called differential photometry. In this work, my sources are always stars, so I will use that designation in the remainder of this work. Differential photometry is performed in AIJ using the Multi-Aperture (MA) module described in §4.1.4.

The differential photometric measurement is made by performing aperture photometry on the target star plus any number of comparison stars, and then dividing the target star's net integrated counts, F_T , by the sum of the net integrated counts of all the stars in the comparison ensemble (i.e. the sum of F_{C_i} , where i ranges from 1 to the number of comparison stars n). Then the differential flux is calculated as:

$$f_T = \frac{F_T}{\sum_{i=1}^n F_{C_i}}. \quad (16)$$

We are left with a signal that is unitless and is often referred to as relative flux. In AIJ, the result of equation 16 is labeled as `rel_flux_T1`. Although the terms relative photometry and differential photometry are sometimes differentiated by other authors, they are used in this work and in AIJ interchangeably.

One point mentioned above is that the comparison stars are assumed to be constant in equation 16. This is often not the case, so one must investigate each comparison star to ensure that it behaves as a constant source. To verify that a comparison star is indeed

non-varying, it can be compared to a different set of comparison stars, or to the other comparison stars in the ensemble. The latter method can be investigated most easily in AIJ and ensures that all good comparison stars in an image can be used as part of the comparison ensemble. AIJ calculates a differential flux for each star in the comparison ensemble by comparing it to all other stars in the ensemble. The calculation is:

$$\text{rel_flux_C}_j = \frac{F_{C_j}}{\sum_{i=1}^n F_{C_i}, i \neq j}, \quad (17)$$

where j identifies the comparison star being measured.

Since all of the target and comparison star fluxes in an image suffer (nearly) the same degradations when passing through the Earth's atmosphere, the division operation in the differential photometry calculation removes much of the atmospheric contamination from the target star differential flux, resulting in greatly improved photometric precision. However, there are some common residuals that remain in the differential data that limit measurement precision (see §2.8).

The goal of transit photometry is to measure the change in brightness of the target star over time due to the planet passing in front of it. Using transit modeling (see §1.5.1), several physical parameters can be determined from the fractional change in the flux of the target star over time. Fortunately, those fractional flux changes can be measured directly with differential photometry, so transit photometry and light curve modeling can benefit from the precision improvements afforded by differential photometry.

2.8 Comparison Star Selection

Although differential photometry provides large gains in the photometric precision of ground-based observations, there are still residual systematics in the differential data. The systematics can sometimes be minimized through comparison star choices, as long as comparison stars with the desired characteristics are available in the image.

In my experience, the most critical comparison star characteristic to consider is brightness. Because of CCD non-linearity (even after near-perfect correction), comparing

a target star to a significantly brighter or dimmer star will leave systematics in the data as sky transparency changes throughout the observations. Consider the extreme example of a target star with flux that falls within a single pixel and produces a nominal ADU of 5,000 counts, and a one pixel comparison star that produces a nominal ADU of 50,000 counts. The resulting target star differential flux is $f_T = 0.1$. Using the nonlinearity characteristics of the U16M CCD shown in equation 15 as an example, a perfectly linear detector would have an ADU of 5,020 for the target star and 52,000 ADU for the comparison star. Now consider a 20% drop in sky throughput. The linear detector would show 4,016 ADU for the target and 41,600 ADU for the comparison. Using the inverse of equation 15, the nonlinear device would now show 4,003 ADU for the target and 40,300 ADU for the comparison star, resulting in a target star differential flux of 0.09933. While the target star brightness remained the same, the change in sky throughput caused a change in the measured differential flux of 0.67% or about 7 mmag. High precision modeling of hot Jupiter transits requires ~ 1 mmag photometric precision. Hot Jupiter transits of sun-like stars cause a ~ 10 mmag deep transit. Clearly, the 7 mmag systematic (albeit with no linearity correction) due to a change in sky throughput is not acceptable. In practice, I have found that comparison stars with brightness in the range of 50–150% of the target star brightness give good results.

Hot Jupiter transits require 2–6 hours of continuous observations to record the full transit. During that time, the target will move through significant changes in altitude as measured from the horizon. Light from a star passes through the minimum possible amount of atmosphere on its way to the surface of the Earth when it is at an altitude of 90° (i.e. is at the zenith, or is directly overhead). This amount of atmosphere is called one airmass. As the position of the star moves toward the horizon in any direction, the angled path of its light through the atmosphere causes the light to encounter more atmosphere than if it were overhead. At an altitude of 30° , the path of the light through the atmosphere has doubled in length. The light now encounters two airmasses of light on the way to the Earth's surface. At two airmasses, the atmospheric attenuation (or extinction) of the stellar

flux will be double the amount at one airmass. This can contribute to the detector non-linearity systematic discussed above. It also introduces another systematic based on the wavelength of light. In very narrow optical bands, atmospheric extinction can be very high (e.g. see Chapter 7). In wide optical bands, atmospheric extinction per airmass is relatively low (~ 0.3 mag), but the precise amount is dependent on the wavelength content of the target star's flux. Blue wavelengths preferably scatter off of molecules and dust in the atmosphere, and thus suffer a greater extinction than red wavelengths. The phenomenon is referred to as differential extinction. The result is that hotter/bluer stars will be more attenuated by the atmosphere than cooler/redder stars.

Because of the dramatic changes in airmass during a transit, differential extinction can cause a large systematic, sometimes called color trend or airmass trend, in a light curve that is proportional to the airmass at each exposure. To minimize this systematic, comparison stars should be chosen that have the same color as the target star. This is usually a requirement that is hard to meet. However, since the trend is so strongly correlated with airmass, if good baseline data are available, the systematic can be compensated for at the expense of one more fitted parameter in the transit model fit (see §2.9).

Atmospheric characteristics vary at differing spacial locations on the sky. Although the typical angular coverage of a telescope is small, differential atmospheric effects can become noticeable across the field of view of a typical telescope, especially under non-ideal observing conditions. To minimize the effects of these atmospheric gradients, comparison stars should be selected as a near as possible to the target star. Also, stars far from the target will possibly experience a significantly different airmass than the target, especially in very wide fields of view and/or at very low altitudes. If the field is rich with good comparison star candidates, selecting a comparison ensemble that encircles the target can help average out these residual systematics.

Fields rarely have comparison stars available that are the same brightness, same color, and are near the target star, but there are methods available that I discuss in the next

section, which can help reduce the effects introduced by using non-ideal comparison stars. Also, AIJ allows the user to interactively redefine which comparison stars belong to the comparison ensemble without having to perform differential photometry on the time-series of images again. This allows the user to quickly determine which comparison stars are adversely affecting the quality of the target star light curve, and makes it easy to exclude them from the ensemble.

2.9 Detrending Time Series Photometry

If data are available that may be correlated with systematics in differential photometry, additional parameters can be included in the light curve model to remove or minimize the impact of systematics on the light curve. Both AIJ and EXOFAST (see §4.2) provide the capability to simultaneously detrend (using one or more trend datasets) and fit a transit model to the light curve, at the expense of adding an extra fitted parameter for each trend dataset. If good pre-ingress and post-egress baseline data are available, a few detrend parameters can be included in a light curve fit without causing problems with the correctness of the model fit. Ideally, the same amount of time should be spent observing baseline data as spent observing the transit. If baseline data are of short duration or only exist on one end of the transit, detrending can adversely impact the correctness of the transit model fit. If multiple transits of the same system are available to fit simultaneously (i.e. globally) using multi-EXOFAST (see §4.3), the number of detrending parameters can be increased because the total number of transit model parameters are decreased, as compared to fitting each transit individually, because a common set of physical transit parameters are fit to all light curves. I take advantage of these global fitting and detrending benefits for all of the results reported herein.

Although some telescope and camera control software adds various system data to the header of each image, our control system adds only basic info, of which the most useful for detrending is time. However, AIJ has an astronomical calculator module called Coordinate Converter (CC; see §4.1.8) that can use the time from the image header, along

with user entered target and observatory coordinates to calculate various values such as airmass, altitude, hour-angle, etc., that are often useful for detrending. The Multi-Aperture module of AIJ calculates even more datasets that are useful for detrending.

Detrending is accomplished by including a χ^2 penalty for the detrend parameters in the overall light curve fit. The detrend χ^2 value at each step in the fitting process represents the goodness of the linear fit of the detrend parameters to the light curve after subtracting the light curve model corresponding to the current fit step. The χ^2 contribution for all n detrend parameters is calculated at each step of the fitting process as

$$\chi_D^2 = \sum_{k=1}^m \frac{\left(O_k - \left(\sum_{j=1}^n c_j D_{jk}\right) - E_k\right)^2}{\sigma_k^2}, \quad (18)$$

where j indexes the detrend parameters, k indexes the samples of the light curve, m is the total number of samples in the light curve, O_k is the observed normalized differential target flux, c_j is the fitted linear coefficient for the detrend parameter values D_{jk} , E_k is the expected value of the flux (which is the normalized transit model value corresponding to the time of the k^{th} data sample), and σ_k is the error in the normalized differential target flux for each sample.

The detrend parameters I have determined to be most useful for reducing systematics in the MORC data are airmass, time, sky background, FWHM of the average PSF in each image, total comparison star counts, and target x-centroid and y-centroid positions on the detector. Time is recorded in the image header by the camera control software (XmCCD; see §3.5.2), airmass is calculated by AIJ's DP module, and the rest are calculated by AIJ's MA module. I used these seven detrend parameters for the data presented in Chapters 5, 6, and 7.

2.10 Real-time Monitoring of Observations

In the early phases of conducting observations for this research, I wasted a number of nights because I set up the observations incorrectly, or at least not optimally, and I was not aware of the problem until data reduction was completed, usually the next day. For

example, an incorrect exposure time setting might result in a saturated target and/or critical comparison star. I searched for a pseudo-real-time data reduction package that could be used to follow the progress of observations as the exposures come in from the telescope, but didn't find anything readily available. Over time, I developed the AIJ package to provide the real-time data reduction capability (part of the DP module), and to provide multi-platform image viewing, differential photometry, plotting, light curve modeling, etc. (see §4.1).

AIJ solved the incorrect setup problems, because I could see within a few seconds of a new image being written from the camera if there was a problem in the automatically updated light curve plot. However, another advantage gained from real-time data reduction is probably just as important. Since the light curve plot updates as new images come in from the telescope, I can tweak exposure time, telescope focus, aperture size, filter selection, and the comparison star ensemble to ensure high-precision photometric results are being achieved. Obviously, this optimization requires starting prior to the event of interest to give time to tweak the parameters, but after some experience, an observer gains insight into the trade-offs of the different observing parameter settings, and the time needed to tune the observations drops dramatically.

2.11 Error Calculations

In this work, the error in a measurement is defined to be the standard deviation of the measurement's probability distribution. Proper estimation of the error in each photometric measurement is important for reporting the significance of the measurement and plotting error bars on the light curve plot, but it is also important for the proper calculation of the best fit model to the data, since the standard deviation of each measurement, σ , is part of the χ^2 calculation used in the fitting process (e.g. see equation 18). In short, the χ^2 contribution from each data point is weighted by a factor of $1/\sigma^2$, which places more weight on data with small errors, and less weight on data with large errors.

Discrete energy packets called photons are emitted from a source randomly and independently from all other photons, resulting in a Poisson distributed random number of photons arriving at a detector per unit time. This time varying arrival of photons causes variations in the number of photons detected per unit time called shot noise. Since the variation is Poisson distributed, a signal with mean flux F will have a standard deviation, or shot noise of \sqrt{F} (e.g. Fried 1965). Shot noise is the fundamental limitation to measuring the flux from a star at high precision. As an example, if our instrumentation detects the arrival of 10^6 photons, the noise in the measurement is then $\sqrt{10^6} = 1000$ photons. This leads to a noise-to-signal ratio of 0.1% or equivalently a measurement precision of ~ 1 mmag. Clearly, we need to ensure the detection of $\geq 10^6$ photons in each measurement of a constant brightness star to limit the RMS of the scatter in a light curve to ≤ 1 mmag.

Mortara & Fowler (1981) and Howell (1989) discuss the noise contributions to the measurement of a point source using CCD aperture photometry and develop the "CCD equation" to estimate the signal-to-noise ratio of a measurement. Merline & Howell (1995) construct a computer model of the same measurement and develop the more rigorous "revised CCD equation". The equation gives the total noise for a CCD aperture photometry measurement as:

$$N = \frac{\sqrt{GF_* + n_{pix}(1 + \frac{n_{pix}}{n_b})(GF_S + F_D + F_R^2 + G^2\sigma_f^2)}}{G}, \quad (19)$$

where G is the gain of the CCD in electrons/ADU, F_* is the net (background subtracted) integrated counts in the aperture in ADU, n_{pix} is the number of pixels in the aperture, n_b is the number of pixels in the region used to estimate sky background, F_S is the number of sky background counts per pixel in ADU, F_D is the total dark counts per pixel in electrons, F_R is read noise in electrons/pixel/read, and σ_f is the standard deviation of the fractional count lost to digitization in a single pixel ($\sigma_f \simeq 0.289$ ADU for f uniformly distributed between -0.5 and 0.5).

If the net integrated counts from the source, F_* , dominates the other terms, and the

gain $G = 1$, the total noise approaches the Poisson noise limit of $\sqrt{F_*}$. The noise increases as the number of pixels in the aperture increases (due to all of the secondary terms in the equation), but recall that for a non-ideal CCD, noise introduced by inter-pixel variations decreases with increasing aperture size (except in the case of perfectly guided telescope), so the aperture size needs to be selected after considering both factors. The number of background region pixels should be chosen to be as large as possible, but not so large that the pixels far from the aperture are no longer representative of the local background at the aperture. If a source is faint relative to the local sky background, the Poisson noise of the sky background may dominate the overall measurement noise.

The photometer in AIJ performs the noise calculation described by equation 19 for each aperture automatically, as long as the user has entered the dark current and read noise for the CCD device used to collect the data. For differential photometry, AIJ propagates the noise from all apertures to derive the error in differential flux measurements. First, the noise from the apertures of each comparison star are combined in quadrature to give the total comparison ensemble noise:

$$N_E = \sqrt{\sum_{i=1}^n N_{C_i}^2}, \quad (20)$$

where i indexes the comparison stars of the ensemble, and N_{C_i} is the noise for each comparison star as calculated by equation 19, and n is the number of comparison stars. Error is then propagated through the relative flux quotient to find the relative flux error for the target star as:

$$\sigma_{\text{rel_flux}} = \frac{F_T}{F_E} \sqrt{\frac{N_T^2}{F_T^2} + \frac{N_E^2}{F_E^2}}, \quad (21)$$

where F_T is the net integrated counts in the target aperture, F_E is the sum of the net integrated counts in the ensemble of comparison star apertures, N_T is the noise in the target star aperture from equation 19, and N_E is the ensemble noise from equation 20. AIJ labels the relative flux error columns as `rel_flux_err_Txx`, and `rel_flux_err_Cxx` for target and comparison stars, respectively, where `xx` is the aperture number corresponding to a particular aperture.

Atmospheric scintillation adds another noise source to the photometric noise described by equation 19 that can dominate for short exposures and/or telescopes with small apertures. Reiger (1963) described the theoretical approach to estimating the amount of scintillation noise, Young (1967) conducted observations to confirm the theory and formalized the equation, and Gilliland et al. (1993) clarified a factor in the equation. The resulting scintillation noise equation is

$$\sigma_{scintillation} = 0.09D^{-\frac{2}{3}}\chi^{1.75}(2t_{int})^{-\frac{1}{2}}e^{-\frac{h}{8000}}, \quad (22)$$

where D is the telescope diameter in centimeters, χ is the airmass, t_{int} is the exposure time in seconds, and h is the altitude of the observatory in meters.

The MORC telescope has an aperture diameter of $D = 60$ cm and is located at an altitude of $h = 229$ m. For an airmass of $\chi = 1.15$ and an exposure time $t_{int} = 100$ s, the estimated atmospheric scintillation contribution that would be added in quadrature to the single aperture noise of equation 19 is $\sigma_{scintillation} = 0.0005$, or about 0.55 mmag. It is unclear how much of that noise is canceled when performing differential photometry. With favorable weather conditions, I have observed bright stars in 100 s exposures with the MORC telescope and achieved 0.6 mmag of RMS scatter in the light curve. Apparently, differential photometry is capable of canceling a significant portion of the scintillation noise.

Additional sources of photometric noise include the variable leakage of flux from neighboring stars into the aperture as seeing changes slightly from exposure to exposure, Poisson noise in the master dark and master flat images, slight variations in CCD bias in the time-series, cosmic ray impacts on the detector, varying contributions of square pixels to a circular aperture, camera shutter open/close variations, inaccurate determination of sky-background from exposure-to-exposure, etc.

AIJ estimates the error in each measurement based only on the factors included in equation 19. Scintillation and the other noise sources are not included. However, multi-EXOFAST scales light curve data errors such that the best fitting model has $\chi_{red}^2 = 1.0$ to ensure the resulting system parameter uncertainties are roughly accurate.

CHAPTER 3

INSTRUMENTATION

3.1 Moore Observatory Ritchie-Chretien 0.6 m Telescope

All data presented in this work have been observed using the 0.6 m Moore Observatory Ritchie-Chretien (MORC) telescope shown in Figure 12. The MORC telescope was manufactured by RC Optical Systems and was installed in August 2006. The instrument features a very robust fork mounting with an absolute Renishaw precision encoder on the polar axis that provides highly accurate free-running tracking of the sky. Unguided exposures of up to ~ 5 minutes result in a tracking error of less than $1'' - 3''$, depending on the altitude of the object.

The telescope's Zerodur optics were made by Star Instruments. The $f/8$ system has a diffraction limit of $0''.2$ at 500 nm, peak-to-valley wavefront variation of 0.242 wave, and 0.039 RMS, with a Strehl Ratio of 0.941. The mirrors have Spectrum Coatings enhanced aluminum coating with a reflectivity peaking at 96.9% at 528 nm, decreasing slightly to 95.7% at 450 and 650 nm. The efficient well-corrected optics are useful from the atmospheric UV cutoff below 380 nm through the near infrared above $2 \mu\text{m}$.

The instrument is focused by a precision adjustment of the secondary mirror to bring the focal plane into coincidence with a fixed focal position 255 mm from the back of the primary mirror cell. Spacers are used to put the camera or other instruments at the proper position, and an encoded focus motor moves the focal plane $5 \mu\text{m}$ per encoder count. The image scale in the focal plane is $42''.3$ per mm, so that $1''$ corresponds to approximately $24 \mu\text{m}$. At $f/8$, the telescope can focus precisely to within its diffraction limit since the least count on the focus encoder translates to a image size for a point source

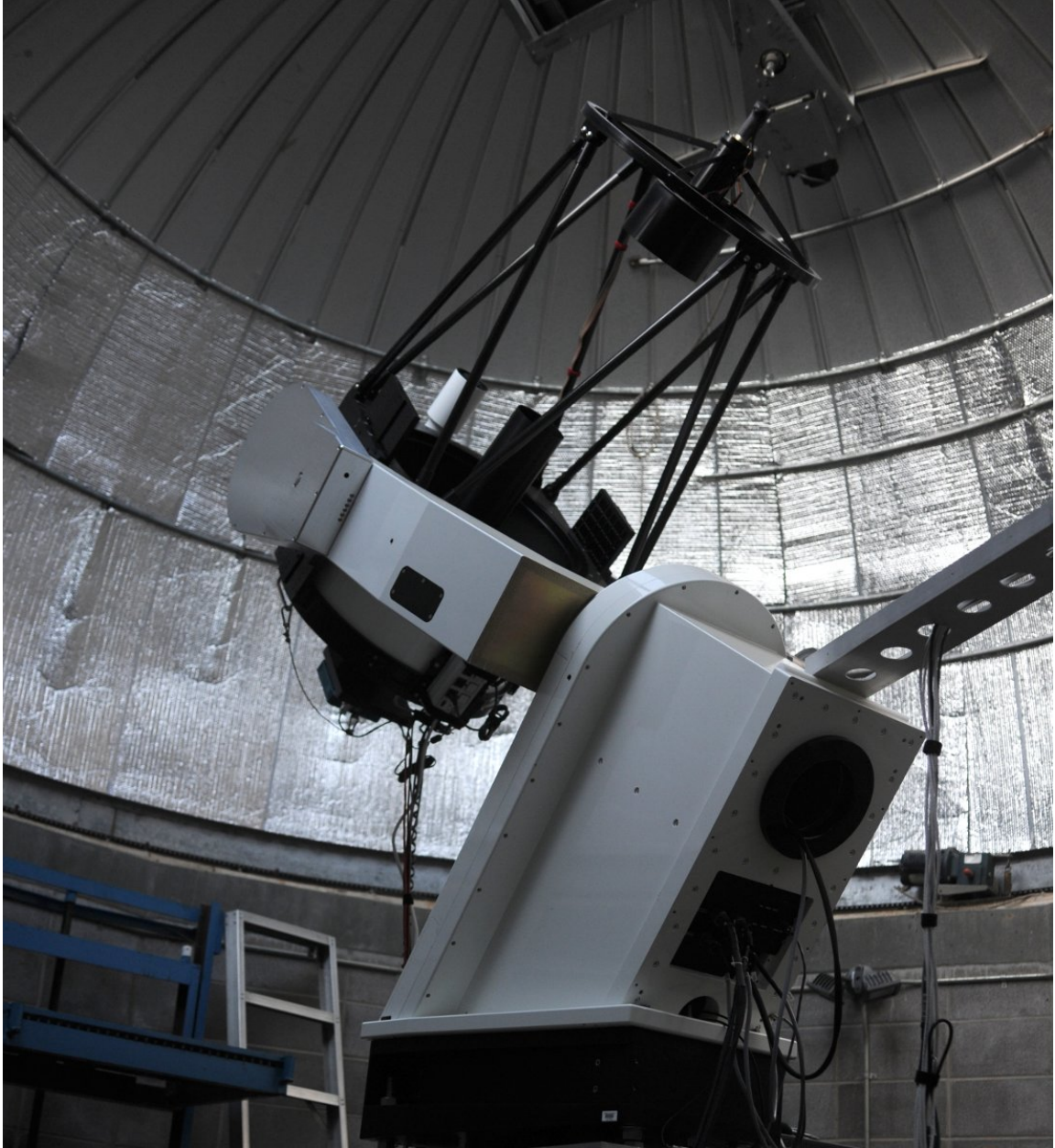


Figure 12. Moore Observatory Ritchie-Chretien (MORC) 0.6 m telescope. All observations presented in this work were collected with the MORC telescope.

of $0''.026$. In long exposure imaging with averaging seeing of $1''$, focusing precision of 40 encoder counts is typical. A focal plane corrector and instrument rotator are available but are not used for photometry.

3.2 CCD camera

An Apogee U16M CCD camera is used with the MORC telescope for exoplanet transit photometry. The camera has a Kodak KAF-16803 CCD detector with a 4096×4096 array of $9 \times 9 \mu\text{m}$ microlensed pixels which oversample the seeing and permit very accurate photometry and imaging over a wide dynamic range. The pixel scale is $0''.39$ per pixel, which provides a field of view of $26'.2 \times 26'.2$. The wide field of view helps to improve differential photometry by offering a wider selection of comparison stars (see §2.8). The oversampled seeing improves photometry by sampling the light from a point source with more pixels (similar to telescope defocusing), improving the dynamic range of possible brightness measurements within an image, and reducing noise resulting from inter-pixel variations combined with imperfect guiding.

The camera has a read noise of 9 electrons, a dark current of 3 electrons/pixel/sec at 25°C , and a dark current doubling temperature of 6.3° . Most of the data collected for this research was observed after cooling the detector to -20°C , resulting in a dark current of ~ 0.02 electrons/pixel/sec. Figure 13 shows the detector's quantum efficiency versus wavelength (thin brown line). Peak quantum efficiency is 60% at 550 nm. A gain setting of 1.5 has been used for this research. Saturation occurs at 100 K electrons, corresponding to an ADU just above the 0-65535 range of the 16-bit analog to digital converter. Linearity deviation is specified as 2%, but see §2.2.2 for measurements performed at Moore Observatory to characterize the linearity of the device.

3.3 Filters

The telescope is equipped with an Optec IFW3 filter wheel which supports interchangeable wheels. Each wheel is configured to hold up to six 50×50 mm square filters. Two filter wheels are routinely used with the MORC telescope. One wheel contains a set of broadband filters, and the other contains a set of narrowband filters.

The broadband filter wheel contains the Astrodon Sloan filters g' , r' , i' , z' , and a clear with blue block (CBB) filter. The bandpass of each filter is shown in Figure 13. When performing follow-up photometry for transit surveys to qualify and characterize candidate transiting planets, the comparison of transit depth in multiple broadband filters is important to ensure the achromaticity of a transit in optical bands. Exoplanets are dark relative to the brightness of the host star in the optical, so transit depths should be the same in all optical bands. Apparent transits that show different depths in different broadband filters are likely false positives caused by a blend of two or more unresolved stellar objects in the aperture (see §1.4.3). The g' and i' filters are often used to measure achromaticity since the bandpasses are separated somewhat in wavelength and the total system throughput is similar in those filters for sun-like stars. The quantum efficiency of the detector is low in the z' band, so the z' filter is good for observing bright stars that would saturate quickly in the other filters ($V \lesssim 9$ for MORC). The downside is that the detector suffers from inter-exposure image persistence in the infrared, so light curve systematics tend to be worse in the z' filter. The r' filter is usually the best choice for intermediate brightness stars ($9 \lesssim V \lesssim 12$ for MORC) when high photometric precision is the key observational goal, because that band tends to result in the least systematics in the light curve and on average tends to have the most signal of all of the Sloan filters for sun-like stars. The CBB filter is optimal for faint star photometry ($V \gtrsim 12$ for MORC) since it has the widest bandpass, but at the expense of no chromaticity information. The blue end of the spectrum is blocked to minimize airmass trend in the light curve.

The narrowband filter wheel contains a custom Na D interference filter with a FWHM of 1 nm (in addition to other narrowband filters not used in this research) and an

Astrodon Sloan and CBB Filter Bandpasses

U16M / KAF-16803 Quantum Efficiency

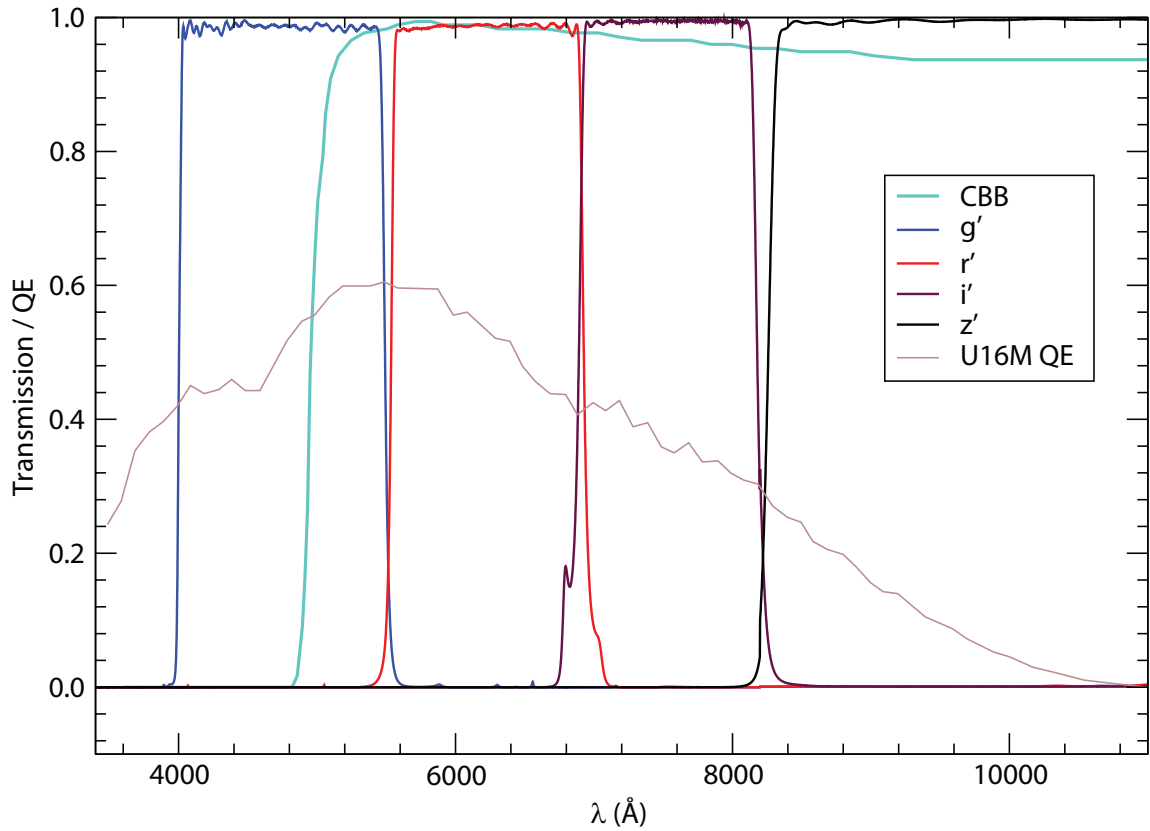


Figure 13. U16M/KAF-16803 quantum efficiency and Astrodon broadband filter throughput versus wavelength. U16M/KAF-16803 quantum efficiency with no cover glass versus wavelength is shown by the thin brown line. The peak quantum efficiency is about 60% at 550 nm. Throughput versus wavelength is shown for each of the Astrodon Sloan filters, g' (blue line), r' (red line), i' (purple line), and z' (black line), and the Astrodon clear with blue block (CBB; teal line) filter.

Astrodon red continuum (RC) filter with a 5 nm FWHM. The Na D and RC filters are used to search for sodium in the atmospheres of exoplanets and are described in detail in §7.3.3.

The filter wheel position can be controlled by the camera user interface (see §3.5) or by an observer written script. As part of this work, I wrote several Linux bash scripts to control the camera, telescope guiding, and filter wheel operation (see §3.5). The scripts provide the capability to automatically alternate between two filters from exposure to exposure, so that a time series of observations of an event can be obtained pseudo-simultaneously in two filters. The filter change happens during CCD readout to maximize total exposure time on the sky. This observing mode is important to test for the achromaticity of candidate transiting exoplanets, and for the narrowband observations presented in Chapter 7.

3.4 Dome Enclosure

The MORC telescope and instrumentation are housed in an Ash-Dome brand dome which sits atop a tetradecagon-shaped (14-sided) concrete block building with a rectangular control room on one side. Figure 14 shows an outside view of the dome with the upper and lower shutters raised and the MORC telescope inside. Figure 15 shows an inside view with only the upper shutter raised, which gives access to target altitudes ranging from 38° to 90° above the horizon. Raising both shutters gives access to altitudes ranging from the treeline up to 54° . The lower portions of the dome have been insulated to reduce daytime heating by radiation from the warm metal dome. A large cooling fan in the doorway mixes cool air during the daytime and promotes rapid equilibration at night. The outside of the concrete block is painted with a highly reflective insulating white paint to minimize heat gain during the day.

Although steps have been taken to minimize heat buildup in the dome, the combination of the metal roof and block walls results in excess heat retention inside the dome, which causes reduced seeing through the dome shutter. Although this deteriorates image quality slightly, there is little effect on photometry (except for targets in crowded



Figure 14. Outside view of MORC telescope enclosure. The enclosure is a dodecagon-shaped concrete block building with a rectangular control room on one side. An Ash-Dome brand dome sits on top of the block walls. The upper and lower shutters are raised and the MORC telescope is visible inside.

fields where the flux from a nearby star may blend into the aperture) because the telescope is almost always defocused beyond the seeing-limited PSF size (see §2.4). An important gain from the heat retention in the building is that dewing on surfaces in the optical path has never been a problem in the five years I have been conducting research. This is critically important for transit observing, since the events often require continuous observations for an entire night.

The upper shutter and dome rotation are computer controlled locally or remotely through a bank of power relays (see §3.5). Low light cameras are installed inside the dome to enable monitoring of the telescope and dome operation during observations, and to facilitate remote operation via the Internet.



Figure 15. Inside view of MORC telescope enclosure. The inside view shows the upper shutter raised giving access to target altitudes ranging from 38° to 90° above the horizon.

3.5 Observatory Control Software

The MORC control system runs on a Linux based computer that is located inside the dome to minimize electrical interference in the telescope encoder lines. The computer controls power inside the dome, dome rotation, dome shutter position, telescope mount pointing, telescope focus, CCD camera operation, filter wheel operation, and provides access for authorized users to control the telescope and instrumentation from any network connected location.

3.5.1 XmTel Telescope Mount Control

XmTel provides a Linux-based graphical user interface for control of various brands of telescope mounts and is developed and supported by John Kielkopf at the University of Louisville. Figure 16 shows the intuitive user interface that allows manual control over telescope pointing, automatic pointing to coordinates loaded from a target

queue file or entered by hand, and several tracking and guiding modes. It also links to the Xephem Sky View program (Downey, 2011) which shows a simulated sky view and the position of the telescope, and it provides point-and-click control for telescope pointing. XmTel is also designed to allow direct control of the telescope mount from scripts for automated observations and telescope guiding.

3.5.2 XmCCD Camera Control

XmCCD provides a Linux-based graphical user interface for control of astronomical CCD cameras and filter wheels and is developed and supported by John Kielkopf at the University of Louisville. The user interface is shown in Figure 17. XmCCD allows the set up of single or multiple exposures, including file naming pattern, exposure time, maximum number of exposures, subarea selection, filter selection, and various values for Flexible Image Transport System (FITS; Wells, Greisen, & Harten 1981; Pence et al. 2010) header storage. XmCCD stores files in FITS image format and links with DS9 (Smithsonian Astrophysical Observatory, 2000) for interactive display of images written from the telescope. Settings are available to capture bias, dark, and flat-field images. The program also provides for scripted control of the camera and filter wheel and links with a script for telescope guiding.

3.5.3 PyDome and PyFocus Dome and Focus Control

PyDome provides for local or remote operation of a telescope dome and is developed and supported by John Kielkopf at the University of Louisville. PyDome includes code to calculate the requisite dome azimuth given the celestial coordinates of the telescope for automatic control of dome rotation. RFID tags are distributed at $\sim 4^\circ$ spacing around the inside of the dome to provide absolute encoding of the dome azimuth as developed by Kielkopf et al. (2014). An RFID tag reader informs PyDome of the current dome azimuth. PyDome also allows manual or scripted control over the dome rotation and the upper shutter position, and although connections to the lower shutter are

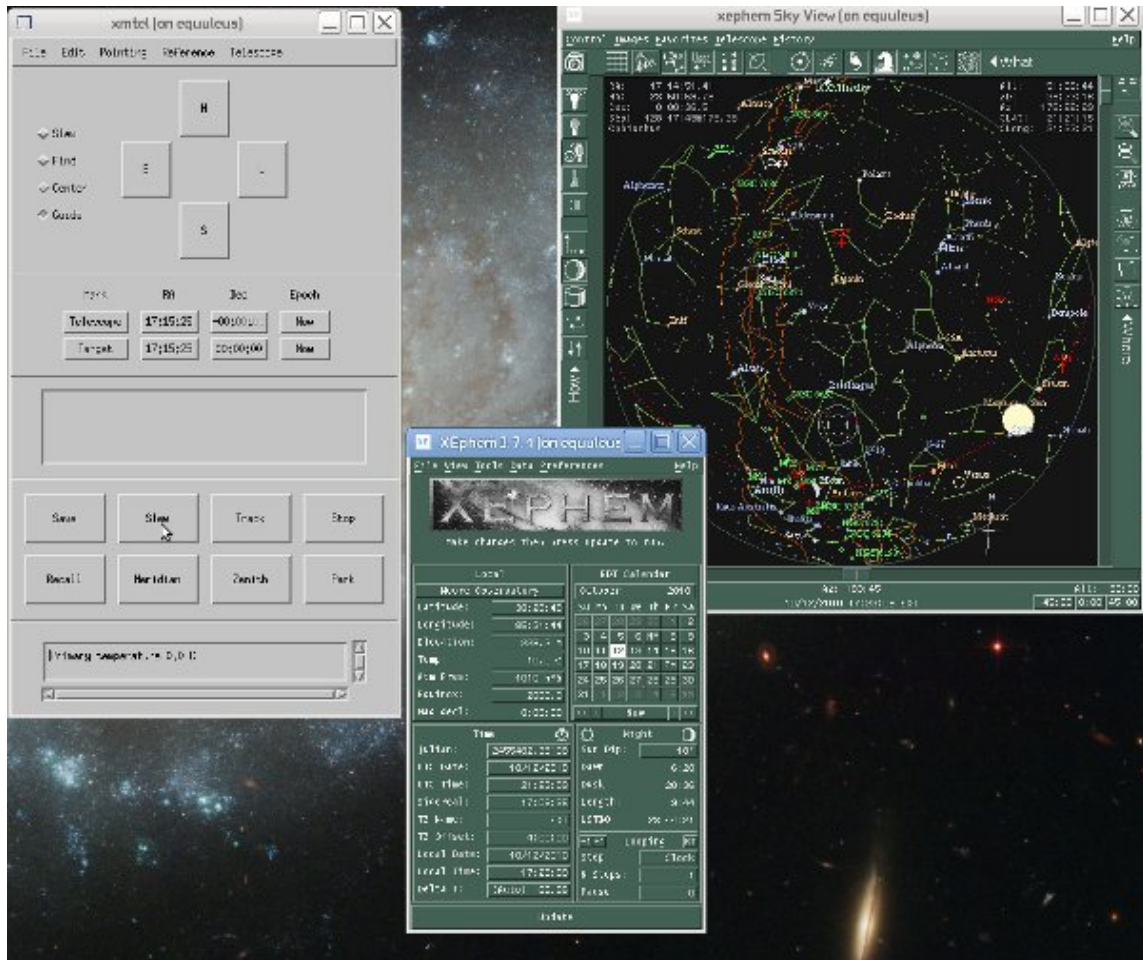


Figure 16. The XmTel telescope mount control user interface. The top-left panel shows the XmTel control interface. The top-right and bottom-middle panels show the Xephem Sky View program interfaces. See text for details.

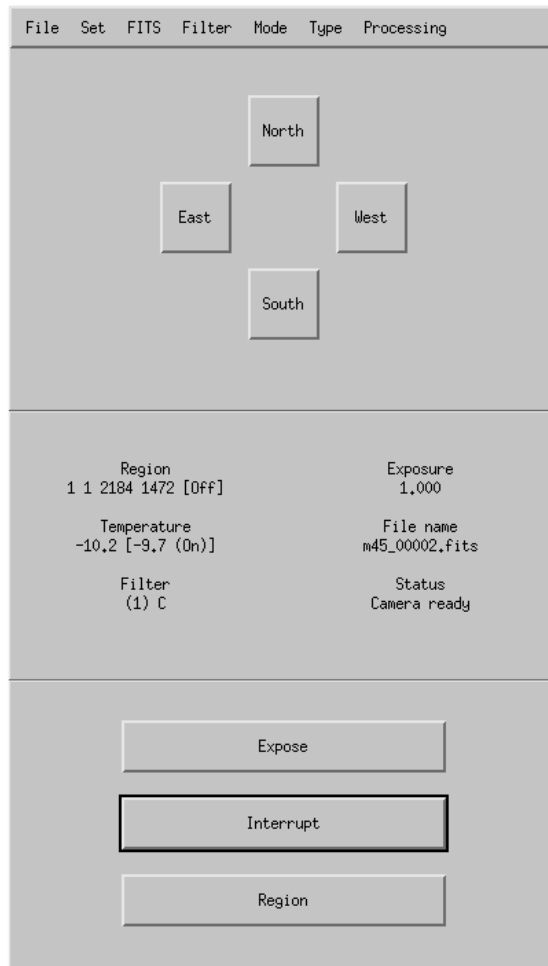


Figure 17. The XmCCD camera control user interface. XmCCD provides control over the camera and filter wheel and various FITS image header settings. See text for more details.

under construction, the software already has the capability to control it too.

PyFocus provides for local or remote operation of the MORC telescope focuser and interfaces with temperature sensors.

3.5.4 Guiding Scripts

Guiding While Observing in One Filter

As discussed in §3.1, the MORC telescope mount has excellent free running tracking, so we make guiding corrections between exposures based on the science images. MORC guiding is controlled by a Linux bash script which communicates with DS9 to determine if the target has shifted on the detector in each new image and XmTel to feedback pointing corrections to the telescope.

To initialize guiding, a test exposure is taken of the field of interest, and using the graphical user interface of DS9, the telescope operator places a green circular region around the star to be used as the guide star. In most cases, I use the target star as the guide star since that minimizes any field rotation that occurs due to imperfect polar alignment of the mount. The guide script is then started. The script first issues a command to DS9 (through its XPA interface) to perform a centroid operation on the circular region. This ensures that the region is centered on the star. Then the script extracts the x, y coordinates of the center of the centroided circular region as the guiding reference point, and issues a new command to DS9 to draw a small red circular region centered at the reference point. The script uses the red color of the region to uniquely identify it as the reference region. At this point, the green and red circles are centered at the same point.

The script then looks for a new image from the camera by polling for the file name of the image displayed in DS9. Recall that XmCCD displays a new image from the camera in DS9 (replacing the previously displayed image). When a new file name is detected, the script issues a command to DS9 to re-centroid the green region on the guide star in the new image, retrieves the centroided region's center coordinates and compares with center coordinates of the stationary red reference region. If a difference between the

two center points is found, the telescope pointing has drifted and must be corrected.

The telescope mount normally tracks the sky at 15'' per second to the west to compensate for the Earth's rotation. XmTel has a "guide" slew speed (see Figure 16), which is slightly faster than the normal tracking speed if the telescope is commanded to slew to the west, slightly slower if commanded to move east, and is a slow fixed rate if commanded to move north or south (for which the tracking speed is nominally zero). If the guide star's center coordinates are different from the reference coordinates in the new image, the script commands the telescope to slew at the slightly different guide rate for an amount of time proportional to the determined x and y pixel offset. The result is that the guide star will be placed back to the center of the reference region at the beginning of the next exposure.

Once the guiding commands have been completed, the guide script closes a loop and returns to polling DS9 for the arrival of a new image from the camera. The guide script loop provides continuous automatic guiding for the duration of a time-series of exposures. If observations have been interrupted by weather or technical problems, guiding can resume by taking another test image and placing the green region around the guide star. If the old reference region is still available, guiding will resume using it rather than the centroid of the guide star. This feature is very important for long transit observations, since a shift of the field on the detector can introduce a step function in the photometry due to inter-pixel sensitivity variations and imperfect flat-fielding.

Guiding While Observing in Two Filters

Time-series observations in two filters pseudo-simultaneously (alternating the filter from one exposure to the next) are handled by an enhanced guiding script. Guiding works the same as above, except the two-filter script also controls the exposure duration, the exposure start time, the image file names, and the filter change during CCD readout. Images in one filter need to be easily identifiable and sortable by filename from the images in the other filter to facilitate separate data reductions. The two-filter guiding script

handles the file name changes between each exposure. Also, stars may have different brightness in each filter, so the script allows for and sets the exposure time for each new image based on the filter setting.

A filter change takes ~ 10 seconds. To maximize the amount of time available for observations, it is desirable to change the filter during the ~ 20 second CCD read out period. To provide that capability, the script controls the exposure start time. Since the exposure duration is also known by the script, it keeps an internal timer to ensure that the filter change starts after the camera shutter has closed and finishes before the end of CCD read out.

3.5.5 Time of Day

For transit timing studies, it is critical to accurately time stamp each image with its exposure start time. Knowing the exposure start time and the exposure duration, the mid-exposure time can be calculated by data reduction software. The Linux computer that controls the MORC telescope and instrumentation synchronizes with several time servers using Network Time Protocol (NTP). The control computer communicates directly with two local tertiary stratum 2 NTP servers and takes into account the transmission delay between the server and the computer. The tertiary servers communicate with secondary stratum 1 NTP servers around the regional network. The timing network maintains the control computer's timing accuracy to within a few microseconds of UTC1 set by the National Institute of Standards and Technology. Also, a GPS-based timing system is installed locally at the observatory and provides a stratum 1 NTP server. This server allows observations to continue if Internet connectivity is not available.

Timing errors of a few microseconds are negligible for the > 20 second transit timing variations that we are able to detect from ground-based observations. However, due to the finite speed of light, the position of the Earth in its orbit around the Sun can cause a 15 minute peak-to-peak variation in UTC1 time from the absolute time of an extraterrestrial event. The absolute time standard adopted by the exoplanet community is

based on a reference frame centered at the barycenter of the solar system, and is referred to as Barycentric Julian Date in the Barycentric Dynamical Time (BJD_{TDB}) time standard. BJD_{TDB} is used as the time base of all data presented in this work. Eastman et al. (2010) describe the various timing standards (including JD, UTC1, TAI, TT, etc.), the variations in terrestrial-based clocks from absolute time due to choice of reference frame, and the overall rationale for the BJD_{TDB} time base for exoplanet research.

XmCCD writes the UTC1 date and time of exposure start (based on the NTP synchronized Linux operating system time) and the exposure duration into the FITS header of all images. AIJ reads the UTC1 date, time, and exposure duration from the FITS header and calculates BJD_{TDB} for each image based on the coordinates of the target. The resulting mid-exposure time in BJD_{TDB} format is used as the time-base for all plots and all global system fits presented herein.

3.5.6 Remote Operation

For the first couple of years of this research, the MORC telescope and dome could only be operated by an observer on-site at the observatory. The main limiting factor was that dome rotation and dome shutter operation could not be computer controlled. The dome position relative to telescope pointing had to be assessed by eye from within the dome and the dome position had to be tweaked about every 15 minutes. Eventually, the A/C power system for the dome and all instrumentation was upgraded to provide computer control. Then the relay control system for the dome was upgraded to provide computer control, and the dome was equipped with RFID tags to provide absolute dome azimuth encoding. Finally, PyDome enabled automated computer control of the dome. At this point, partial remote operation was possible if the 1.5 Mbps network service to the observatory could handle the traffic, and if someone was on-site to open and close the dome shutter by hand.

After testing various remote connectivity solutions and authorization schemes, it was determined that observations could be conducted remotely by transporting the full set

of graphical user interfaces to a remote computer using compression. The last 2-3 years of observations were mostly conducted remotely. Upper shutter control was added in 2014, enabling full remote operation for targets with altitudes higher than 38° above the horizon. Lower shutter remote control is currently being added, which will allow remote observations of any targets that would be accessible to an on-site observer.

CHAPTER 4

ANALYSIS TOOLS

4.1 AstroImageJ

AstroImageJ (AIJ) is an astronomical image analysis software package that is based on ImageJ (IJ; Rasband 1997-2014), but it includes customizations to the base IJ code and a packaged set of software plugins that provide an astronomy specific image display environment and tools for astronomy specific data reduction, analysis, modeling, and plotting. AIJ and IJ are public domain, open source, Java programs inspired by NIH Image for the Macintosh computer. The AIJ photometer capabilities are derived from the basic *Astronomy* plugins package written by Frederic V. Hessman et al. of the Inst. f. Astrophysik, Georg-August-Universität Göttingen¹. Because AIJ is Java code, the package is compatible with computers running Apple OS X, Microsoft Windows, and the Linux operating system (OS).

The creation of the AIJ package was started as part of this research to enable efficient data collection and analysis and was used to produce the times series photometric data presented herein. Working with the KELT-N wide-field transit survey (see §1.6.1) follow-up team, it was clear that a tool was needed to efficiently reduce and present data to the KELT-N science team. The requirements of such a tool were essentially the same as what I had developed for this research, so many of the other KELT follow-up observers have adopted AIJ as a data reduction tool as well. To facilitate access to many users, a webpage² was developed to host the installation packages and documentation. Over time, many other professional and amateur astronomers around the world started using AIJ, so a









¹<http://www.astro.physik.uni-goettingen.de/hessman/ImageJ/Astronomy/>

²<http://www.astro.louisville.edu/software/astroimagej/index.html>

user forum³ was set up to facilitate more efficient support for the software. I do not track the number of times AIJ has been downloaded from the website, but I estimate ~ 200 active users based on the number of views of some topics on the support forum.

The intent of this chapter is to give an overview of the astronomy specific capabilities of AIJ and to present the AIJ specific user interfaces. A detailed user guide is available for download from the AIJ website⁴. Most of the AIJ user interface panels include "tool-tip" help that optionally pops up when the mouse pointer is positioned over an item in the display for more than a second. AIJ inherits all of the basic image manipulation and analysis functionality from IJ. The IJ website⁵ provides detailed user guides and descriptions of its functionality.

4.1.1 AIJ Toolbar

When AIJ is started, the AIJ Toolbar opens and presents the eight AIJ-specific toolbar icons labeled as 1-8 in Figure 18. Each of those icons provides direct access to an AIJ analysis tool. The icon shown depressed and labeled as 1 () indicates that AIJ is in astronomy mode. In this mode, all images open into the astronomical image display mode discussed in §4.1.2. Icon 2 () starts single aperture photometry mode. Icon 3 () starts the Multi-Aperture photometer module discussed in §4.1.4. Icon 4 () clears all labels and apertures from the image display. Icon 5 () starts the Multi-Plot module discussed in §4.1.5. Icon 6 () opens previously saved photometry measurements tables. Icon 7 () opens the Data Processor module discussed in §4.1.3. Icon 8 () opens the Coordinate Converter module discussed in §4.1.8.

The 12 icons to the left of the AIJ icons and all of the menu options are standard IJ tools. These tools can also be used in AIJ, but normally only the File menu options are used for typical time series data reductions. A single image is opened from the AIJ Toolbar using File->Open. A time-series of images is opened into an image "stack" from

³<http://astroimagej.1065399.n5.nabble.com/>

⁴http://www.astro.louisville.edu/software/astroimagej/guide/AstroImageJ_User_Guide.pdf

⁵<http://imagej.nih.gov/ij/>

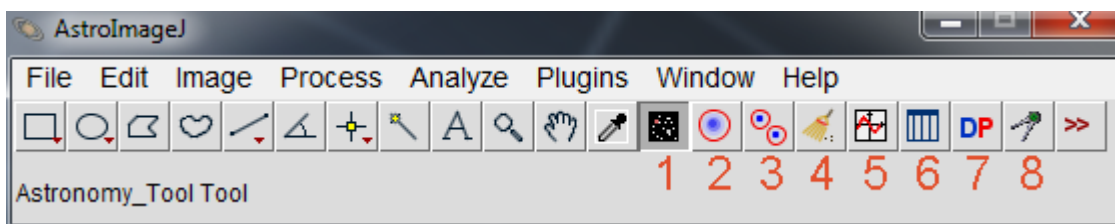


Figure 18. The AIJ Toolbar. The icon shown depressed and labeled as 1 indicates that AIJ is in astronomy mode. In this mode, all images open into the Astronomical Image Display mode discussed in §4.1.2. Icon 2 starts single aperture photometry mode. Icon 3 starts the Multi-Aperture photometer module discussed in §4.1.4. Icon 4 clears all labels and apertures from the image display. Icon 5 starts the Multi-Plot module discussed in §4.1.5. Icon 6 opens previously saved photometry measurements tables. Icon 7 opens the Data Processor module discussed in §4.1.3. Icon 8 opens the Coordinate Converter module discussed in §4.1.8.

the AIJ Toolbar using File->Import->Image Sequence. Alternatively, an image or an image sequence can be opened by dropping the file or directory, respectively, onto the bottom area of the AIJ Toolbar, or OS options can be enabled to automatically open images into AIJ in response to a double click on the file in an OS window. If all images in a sequence will not fit into the computer memory allocated to AIJ, the sequence can be opened as a "virtual stack". In this mode, the stack of images can be processed as if all images exist in memory, but AIJ loads only the single active/displayed image into memory. Virtual stacks perform more slowly than standard stacks, but memory requirements are minimal. All AIJ settings are persistent across sessions. Settings for specific configurations can be saved and reloaded later as needed.

4.1.2 Astronomical Image Display

Many popular image file formats are supported by AIJ, including the Flexible Image Transport System (FITS; Wells, Greisen, & Harten 1981; Pence et al. 2010) file format, which is the standard used by most astronomers. The astronomical image display shown in Figure 19 is unique to AIJ and offers numerous display options useful to

astronomers. An image can also be displayed in plain IJ display mode, which has no contrast controls, analysis controls, or mouse pointer data decorating the image, by deselecting the astronomy mode icon (1) on the AIJ toolbar.

In astronomy mode, a menu system is available at the top of the image display window to provide access to all astronomy specific AIJ features. A row of quick access icons for control of some frequently used image display options and image analysis tools is located directly above the image. Pixel and World Coordinate System (WCS; Greisen & Calabretta 2002; Calabretta & Greisen 2002; Greisen, Calabretta, Valdes, & Allen 2006) information from the image location under the current mouse cursor is displayed in the three rows above the quick access icons. Image and WCS format information is displayed under the image menus. Image contrast and brightness is controlled by the interactive histogram and direct entry fields under the image. The image overlay optionally displays active apertures (green=target, red=comparison), object annotations, plate scale, and image orientation on the sky.

The blue aperture shown near the center of the image moves with the mouse pointer and the peak and integrated counts in the aperture are shown in real time as the mouse is moved around in the image. The interactive mouse photometer helps to quickly assess which stars are suitable comparison stars during differential photometry set up. When AIJ is used in real-time data reduction mode (see §4.1.3), the mouse photometer helps to quickly determine an appropriate exposure time and defocus setting.

The zoom setting of the image display is most easily set by rolling the mouse wheel to zoom in and out. If a mouse wheel is not available, image zoom can be controlled by the four magnifying glass icons on the right side of the quick access row. Image pan is controlled by a left-click and drag in the image. The five quick access icons shown as depressed in Figure 19 control whether the aperture identifiers are displayed, which components of the aperture are displayed, and if the aperture is to be centroided on the star when it is placed.

If a time series of images is opened as an image stack, a scroll bar is displayed

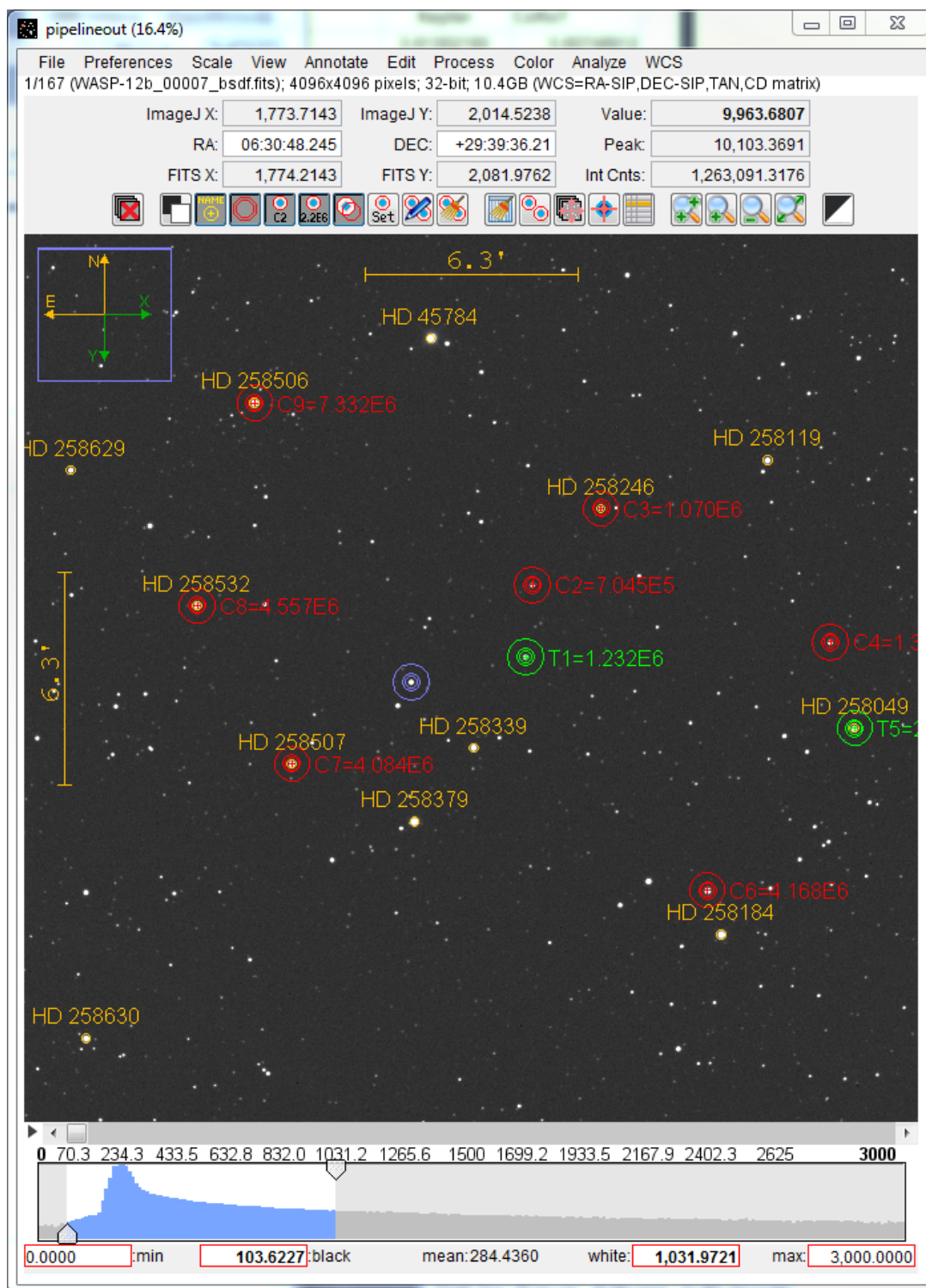



Figure 19. The AIJ image display. A wide range of astronomy specific image display options and image analysis tools are available from the menus, quick access icons, and interactive histogram. See text for details.

directly under the image as shown in Figure 19. The scroll bar can be moved left and right to display different images in the sequence. The right-pointing arrow to the left of the scroll bar will animate the image sequence at a predefined speed.

If WCS header information is available, AIJ will automatically calculate the x -axis and y -axis plate scales and the orientation of the image on the sky, and optionally display this information in the image overlay. A right-click and drag in an image will report arc-length in place of integrated counts in the lower-right-hand box above an image. New object annotations can be added manually or target names can be extracted from SIMBAD and displayed by right-clicking on an object in an image.

4.1.3 Data Processor

The Data Processor (DP) module provides tools to automate the build of master calibration images, automate calibration of a time series of science images, and optionally perform differential photometry and light curve plotting. The DP module is started by clicking the "DP" icon () on the AIJ Toolbar (labeled 7 in Figure 18). The user interface is shown in Figure 20. DP operates much like a script in that it processes selected calibration and science images in a user defined manner. Fields are provided to define the directory/folder locations and filename patterns of data to be processed. Checkboxes are provided to enable various tasks that can be included in the data processing session. Disabling certain checkboxes will automatically disable other related input fields as appropriate to help the user understand which input fields are interconnected.

The path and image filename pattern matching the raw science images to be processed are set in the Science Image Processing sub-panel. Files can be dragged and dropped from the OS into a field of the DP panel to minimize typing. The number of files matching the pattern at the specified path shows in the right-hand column labeled Totals. The science images can be further filtered based on the image sequence numbers in the filename by entering minimum and/or maximum numbers in the second row of the sub-panel.

Master bias, dark, and flat images are created as discussed in §2.2. The paths and filename patterns matching the raw calibration images are set in the "build" line of the Bias Subtraction, Dark Subtraction, and Flat Division sub-panels. As with the science images, the number of files matching the pattern for each calibration set shows in the right-hand column labeled Totals. If the master calibration files have been previously constructed, the Build checkbox in each sub-panel can be disabled to skip any or all of the master builds processes.

Bias subtraction, dark subtraction, and flat-field division are implemented as discussed in §2.2 and can be individually enabled. The master calibration image paths and filenames are specified on the Enable line of each sub-panel.

The Image Correction sub-panel provides the option to implement CCD nonlinearity correction as specified and measured in §2.2.2. The FITS Header Updates sub-panel provides options to automatically plate solve each science image and/or add new calculated astronomical data such as airmass, time in BJD_{TDB} , target altitude, etc. to the science image header information. The Save Calibrated Images sub-panel offers several file format and file naming conventions available for saving the calibrated images.

The Post Processing sub-panel provides options to run Multi-Aperture (see §4.1.4) and Multi-Plot (see §4.1.5) after each image is calibrated to build and display a light curve as the data are calculated. This feature is particularly useful for real-time reduction of data at the telescope. Other options allow the current light curve plot and image display to be written to a file after each science image is calibrated. These images can be used to update websites to show the progress of observations.

The Control Panel sub-panel provides control over the data reduction process. If the Polling Interval is set to zero, all of science images will be processed and then DP will return to the stop state. This mode is ideal for post-observation calibration of data. To calibrate data in real-time, the Polling Interval is set to a positive number n (in seconds).

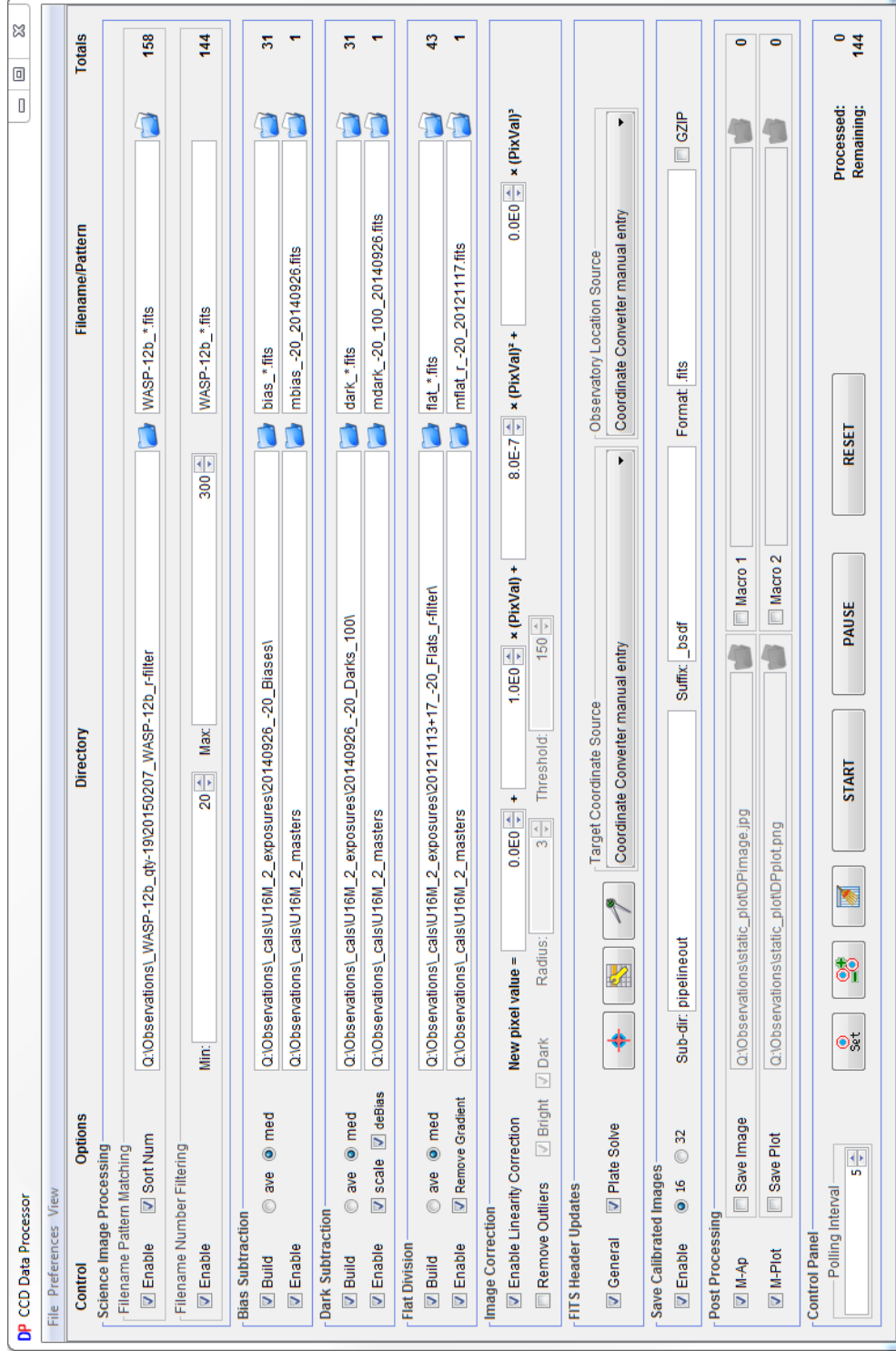



Figure 20. The AIJ Data Processor user interface. Data Processor automates the building of master calibration files, calibration of a time series of images, and optionally performs differential photometry and light curve plotting. See text for more details.

After all science images matching the filename and number filters have been processed, DP will search for new files matching the pattern every n seconds. If DP is operating in this mode while observations are underway, calibration of a new image written from the camera will be started within n seconds, and optionally processed by Multi-Aperture to update the light curve plot.

4.1.4 Multi-Aperture

Multi-Aperture (MA) automates the task of performing differential photometry on a time-series of images. Various settings are presented in a set-up panel, and then the apertures are placed and adjusted interactively by clicking near stars directly in the image display. The algorithms used to calculate the photometry, differential photometry, and uncertainties in those values are discussed in Chapter 2.

The MA module is launched by clicking the MA icon () above an image or in the AIJ Toolbar. The MA set-up panel shown in Figure 21 opens. The top two scroll bars allow the user to set the range of images to be processed. The three scroll bars immediately below set the aperture radius in pixels, the inner radius of the sky background region, and the outer radius of the sky background region.

The "Use previous apertures..." checkbox allows the previously defined set of apertures to be re-used. Aperture definitions can also be stored and reopened from disk in the File menu of the image display. If WCS headers are available and the "Use RA/Dec..." checkbox is selected, the saved apertures will be placed according to RA and Dec rather than by x and y pixel coordinates. If the "Reposition aperture to object centroid" checkbox is selected, a centroid algorithm will attempt to center the aperture on the nearest star. The "Remove stars from background" checkbox enables the iterative 2σ cleaning of the sky-background region described in §2.5.

If "Vary photometer aperture radius based on FWHM" is enabled, the user defined multiplicative factor and the average of the FWHM values measured in all apertures is used to set the aperture radius in each image of the time-series. This mode may improve

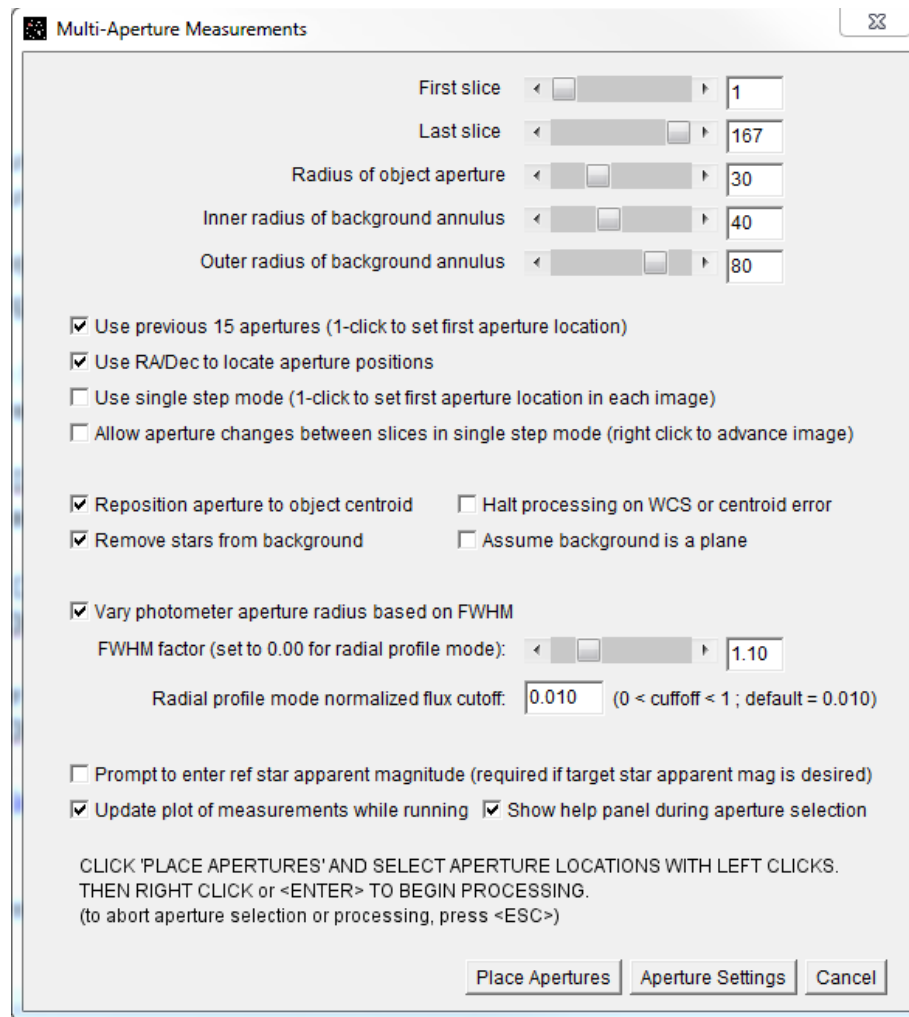


Figure 21. The AIJ Multi-Aperture set-up user interface. Multi-Aperture automates the task of performing differential photometry on a time-series of images. Various settings are available in the set-up panel, and then the apertures are placed and adjusted interactively by clicking near stars directly in the image display. See text for more details.

photometry when seeing is varying significantly throughout a time-series. As discussed in §2.6, this mode should not be used in crowded fields. The other option settings on this page are described in the AIJ user manual.

The Aperture Settings button at the bottom provides access to two panels containing detailed settings for the photometric measurements. When all options have been set, the "Place Apertures" button causes the set-up panel to close and the program waits for the apertures to be defined by user clicks near stars in the first image of the time-series. If the "Use previous apertures..." option is enabled, the user clicks near the first star in the set (usually the target star), and all other apertures are placed relative to the first aperture. If the "Use RA/Dec..." option is also enabled, no clicks are required to apply the stored apertures since they are placed automatically at the calculated pixel locations corresponding to the stored WCS coordinates.


By default, a help panel opens that describes actions available at each step during aperture definitions. Left-clicking inside an aperture deletes the aperture. An aperture can be moved by left-clicking inside it and dragging it to a new position. An aperture can be changed from a target to comparison aperture and vice-versa by shift-left-clicking inside the aperture. Other options are available as listed in the help panel.

When all apertures have been defined as desired, a right-click or press of the <Enter> key will start the automated differential photometry process on all images defined in the set-up panel. If the "Use RA/Dec..." option is enabled, apertures will first be located on each image in the series according to the WCS information in the image header. If not, the aperture placements start on each subsequent image in the series at the same place in x, y space as in the previous image. In both cases, if centroid is enabled for a particular aperture, the centroid function will attempt to center the aperture on the nearest star. For telescopes with poor tracking/guiding or requiring a "meridian flip" during the time-series, the images should be plate solved so that the "Use RA/Dec..." option can be enabled to properly find the initial aperture placements in each image.

The photometry data is written to a "measurements table" and optionally plotted by

the Multi-Plot program as MA progresses through the time-series.

4.1.5 Multi-Plot

Multi-Plot (MP) provides a multi-curve plotting facility that is tightly integrated with differential photometry and light curve fitting. MA can automatically start MP, or MP can be manually started by clicking the MP icon () on the AIJ Toolbar. If a measurement table has been created by MA or opened from the OS, MP will automatically create a plot based on the last plot settings. Alternatively, plot templates can be saved and restored to easily format commonly created plots. Plotting controls are accessed in two main user interface panels.

The Multi-plot Main panel is shown in figure 22. Controls include the selection of the default x -axis dataset from a pull-down list of all data columns in the measurements table, the maximum number of dataset controls and detrend variables displayed in the Multi-plot Y-data panel shown in Figure 23, plot title and subtitle, legend placement and options, x - and y -axis label and scaling options, and the overall plot size in pixels. The V.Marker 1 and 2 controls provide the option to plot up to two vertical red dashed lines with labels. These are commonly used to mark the predicted ingress and egress times on exoplanet transit plots.

The bottom row provides access to other x -axis controls that are used for the plotting and fitting of all y -datasets. The Meridian Flip settings allow the time of the telescope's meridian flip to be specified (if applicable) and to optionally mark that time with a light blue dashed vertical line. If `meridian_flip` is selected as a detrending parameter for a dataset in the Multi-plot Y-data panel, the fitting routine attempts to remove any baseline offsets from one side of the meridian flip to the other. The Fit and Normalize Region Selection options allow the user to specify additional x -axis points used in fitting. For example, the Left and Right settings are used to mark the regions used to normalize the data (which normally exclude the in-transit portion of the light curve). Also, the x -axis mid-point between the Left and Right settings is used as the model fit starting

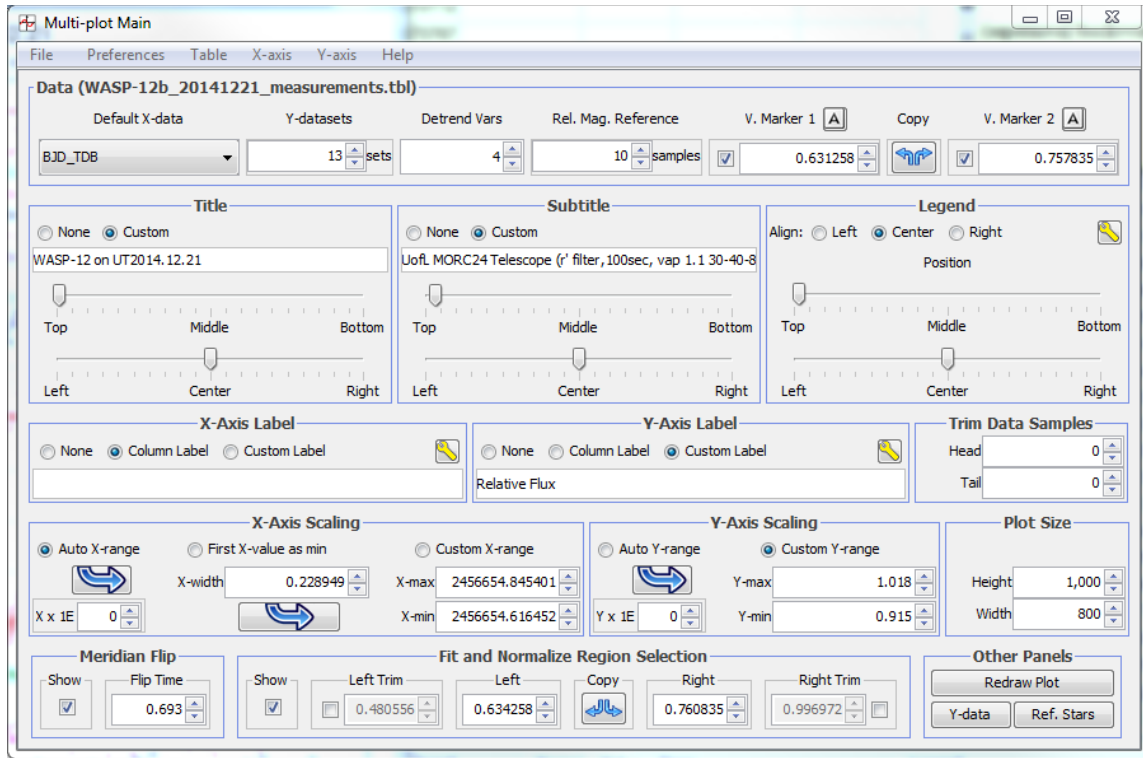




Figure 22. The AIJ Multi-plot Main panel user interface. The Multi-plot Main panel provides access to plotting controls that affect the overall plot. Important controls include the default x -axis dataset (usually a time dataset such as BJD_{TDB}), the title, legend, and axis labels, and plot size and scaling settings. The bottom row provides several settings used for detrending, normalization, and light curve modeling. See text for more details.


point for the transit model parameter T_C . The Left Trim and Right Trim settings can be used to exclude leading and/or trailing data from the normalization and fitting processes. A gray dashed line can optionally be displayed for any of these x -axis settings.

Figure 24 shows an example plot that demonstrates many of the Multi-plot Main settings mentioned above. Additional options are available in the menus at the top of the Multi-plot Main panel.

The Multi-plot Y-data panel is shown in Figure 23. Each horizontal row in the user interface corresponds to an individual plotted dataset. The sample shown allows up to 13 datasets to be plotted on a single plot. The settings shown in Figures 22 (Multi-plot Main)

and 23 (Multi-plot Y-data) produce the plot shown in Figure 24. The top row of controls labeled "1" under the Dataset heading produce the raw normalized light curve shown as solid blue dots near the top of the plot. Note in particular the Y-data column selected (rel_flux_T1) and the Norm/Mag Ref mode selected (). The green areas in the Norm/Mag Ref mode icon indicate the regions of the light curve (relative to the Left and Right markers on the Multi-plot Main panel) that are used to normalize the data. In this case, the in-transit data are not included in the calculation of the normalization parameter.

The second row of plot controls (Dataset 2) again plot the rel_flux_T1 data, but this time after simultaneously detrending and fitting the data as set up in the fit panel shown in Figure 25, which will be discussed in §4.1.6. Note the reduced systematics and scatter in the data. This row of controls uses the Fit Mode selection () to enable the fit panel. Note that the "then Shift" column is set to -0.01 which shifts the transit baseline down to $y = 0.990$ on the plot for clarity. The light curve model residuals are shown as open red circles. The residuals plot controls are available in the fit panel corresponding to the light curve.

Plot datasets 3-9 display the first seven comparison star differential light curves. The Fit Mode selection (), being completely green, selects all data for detrending, and the flat red line indicates that no transit model is fit (since no transit event is expected in the comparison stars). Note that the normalize mode used is all green also, since all comparison star data can be used for normalization. Each comparison star light curve is shifted from the other light curves for clarity using the "then Shift" setting. Note that datasets 5, 8, and 9 have been binned by 2 using the Bin Size setting to reduce the scatter for plotting purposes.

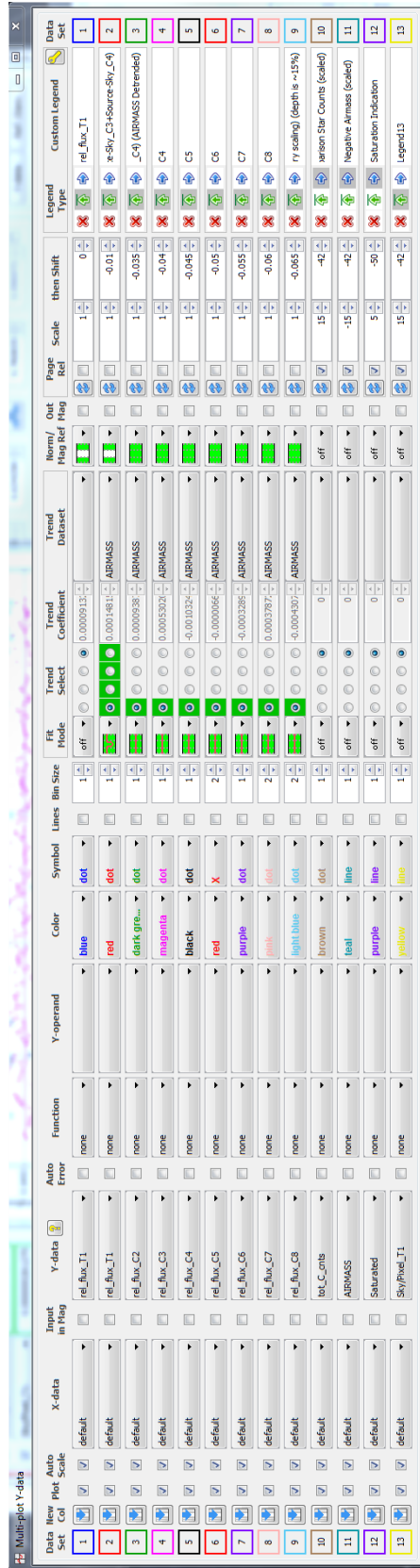



Figure 23. The AIJ Multi-plot Y-data user interface. The Multi-plot Y-data panel provides access to plotting controls that affect individual plotted datasets. Each horizontal row provides controls for plotting the dataset selected under the Y-data heading. See text for more details.

Each comparison star light curve has been detrended against airmass. In this example, MP is set to allow up to four trend datasets to be selected for detrending. Note that the first Trend Select button is enabled and AIRMASS is showing in the Trend Dataset column for all comparison stars. If the resulting comparison star light curves are relatively flat, then they should perform well as part of the comparison ensemble.

Plot datasets 10-13 display four diagnostic curves. These curves are plotted relative to the size of the plot page by selecting the Page Rel option on each row. In this mode, the Scale setting forces the plot of the data to fit within a fixed percentage of the plot range. The "then Shift" value in this mode is also a percent of the plot range with 0 being in the middle of the plot. This mode makes scaling of data to fit on a plot easy when the shape of a curve is important, but the actual values of the data are not important.

Many other plotting options are available, including plotting of error bars (Auto Error), legend options, input and output in magnitudes, data binning, and the option to select independent x -axis datasets for each y -axis dataset (i.e. the X-data pull-down menus in the Multi-plot Y-data panel).


Datasets displayed in a plot have typically been modified in one or more ways (e.g. normalized, detrended, converted to/from magnitude, scaled, shifted, binned, etc.). The displayed values can be added to the measurements table as new data columns for further manipulation or permanent storage using the New Col button () on the left-hand side of the row corresponding to the plotted data. Model residuals and sampled versions of the model can also be saved to the measurements table using this button.

The automatically created (optional) legend entries are shown at the top of the plot in Figure 24, with the light curves plotted below. Most of the legend entries are automatically generated based on the dataset names known to be produced by MA. By default, the RMS values are automatically calculated and displayed in the legend for detrended and/or fitted light curves. The light curve model parameter values are optionally shown for fitted light curves. The predicted time of ingress and egress are shown as red dashed vertical lines. The meridian flip time is indicated by the light blue vertical dashed

line (no meridian flipped actually occurred for the example observations), and the Left and Right gray dashed vertical lines show the boundaries of the normalization, detrending, and fitting regions.

The plot can be zoomed by placing the mouse pointer inside the plot image and rolling the mouse scroll wheel. Also, a left-click in the plot image zooms in by one step, and a right-click zooms back out to the full plot. The plot can be panned with a left-click and drag with the mouse. Data points can be removed from the plot and measurements table by holding the shift key and moving the mouse over the data point until it is highlighted. Then, while continuing to hold shift, a left click will remove the data point. In case a mistake is made, a shift-right-click will retrieve the deleted point. As shortcuts, the Left vertical marker can be positioned at the mouse pointer with a control-left-click and the Right vertical marker can be positioned with a control-right-click.

4.1.6 Light Curve Fitting and Detrending

Light curve fitting is enabled for a particular dataset in the Multi-plot Y-data panel by selecting the Fit Mode icon showing the red transit model on a full green background (). When this mode is selected, a Fit Settings panel will be displayed for the dataset as shown in Figure 25. The settings in the figure produce the light curve model fit shown in the example plot of Figure 24. The transit model fitted to the data is described in §1.5.1. AIJ is currently limited to finding the best fit model parameter values and does not provide estimates of the parameter uncertainties. Tools for estimating the parameter uncertainties are described in §4.2 and §4.3.

Before making adjustments in the Fit Settings panel, refer to paragraph three of §4.1.5 and properly configure the Fit and Normalize Region Selection settings and optionally the Meridian Flip settings in the Multi-plot Main panel. Also make sure the Norm/Mag Ref mode and other settings are configured properly in the Multi-plot Y-data panel, as described in the last three paragraphs of §4.1.5.

The parameter settings in the User Specified Parameters sub-panel are not fitted.

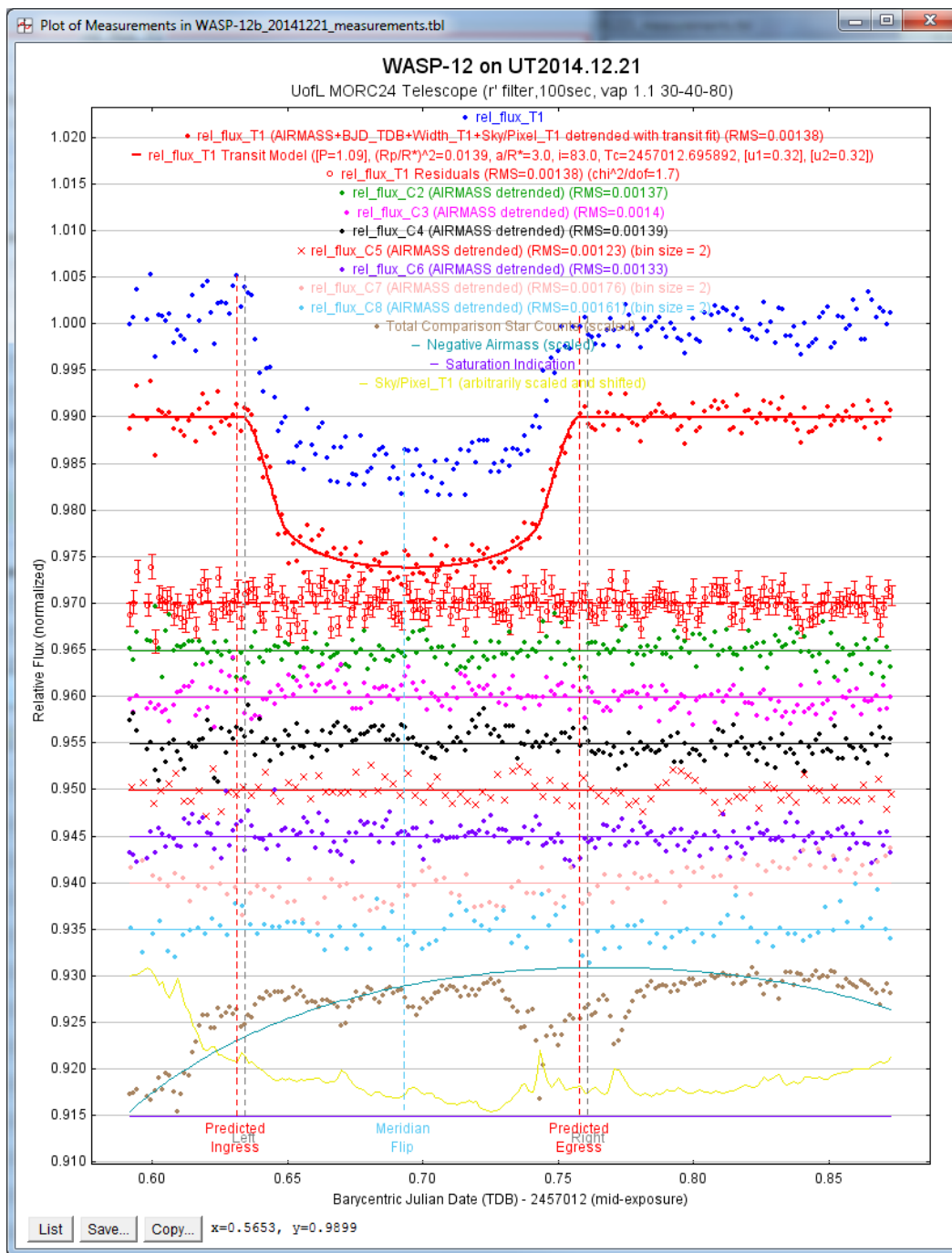


Figure 24. An AIJ Multi-Plot example plot. The plot of a WASP-12b transit under poor observing conditions is shown. The top dataset plotted with solid blue dots is the raw normalized differential photometry. The solid red dots show the light curve after simultaneously detrending and fitting to an exoplanet transit model, which is shown by the red line through the data. Note the reduced systematics and scatter in the detrended data. The open red dots show the model residuals. See the text for descriptions of the other plotted data.

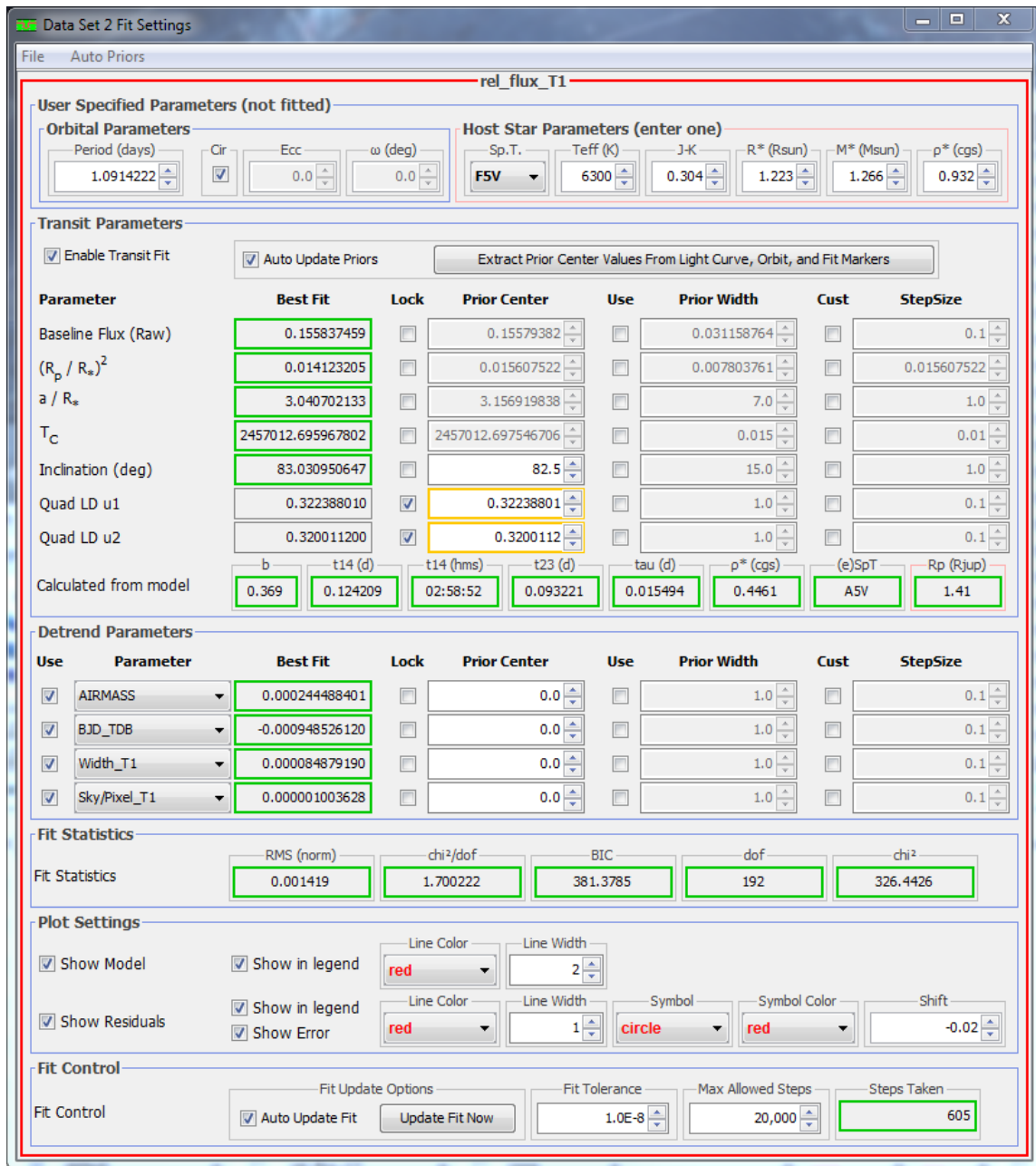


Figure 25. The AIJ light curve model fitting and detrending panel. The settings produce the light curve model fit shown in the example plot of Figure 24. Light curve prior center and width values can optionally be set by the user to constrain the model fit. Direct access to all detrending parameters is also provided along with more flexible settings. Several values calculated from the model parameters are displayed, along with several statistical values usual for assessing data quality and model validity. See text for more details.

The period of the exoplanet's orbit is not well constrained by the transit model, but its value will impact the best fit values of some of the fitted parameters, so the Period value must be entered. Normally, the orbital period is known from RV or wide-field survey photometric data. The Host Star Parameters in the same sub-panel are only used to estimate the true planet radius from the fitted parameter R_P/R_* . The host star parameter values are interrelated by tables in Cox et al. (2001) for main sequence stars. The only value used in the calculation of R_P (displayed near middle of the right-hand side of the panel) is R_* , so that value should be entered directly if known. Otherwise, entering any one of the other host star parameters will produce an estimate of R_* .

The Transit Parameter sub-panel has seven rows for the seven transit model parameters described in §1.5.1. Prior Center values will need to be set for the seven parameters to ensure the correct χ^2 minimum is found. The top four parameters shown in the sub-panel are extracted from the light curve data by default. In the odd case that those estimated values are not correct, the values can be entered directly by the user. In the example shown, the Inclination prior center value has been set by the user, but no constraints have been placed on the range of valid final fitted values (although the upper end is limited to 90° by the definition of inclination). The Quad LD u1 and u2 coefficient values have been set by the user, and the fitted values have been locked to those values by enabling the Lock checkbox beside each one. The fixed values of u1 and u2 were extracted from the Claret & Bloemen (2011) theoretical models using a website tool⁶. The best fit transit model parameter values are displayed in the Best Fit column. A green box around the fitted parameter values indicates that the minimization converged to a value less than the Fit Tolerance within the Max Allowed Steps. Both minimization parameters can be set at the bottom of the fit panel in the FIT Control sub-panel, but the default values normally work well.

The bottom row in the Transit Parameter sub-panel shows several values that are calculated from the best fit model as described in §1.5.1. The host star's density, ρ_* , is

⁶<http://astroutils.astronomy.ohio-state.edu/exofast/limbdark.shtml>

particularly interesting, since a good estimate can be derived from the transit light curve data alone.

The Prior Width column allows the user to optionally limit the range of a parameter's fitted value. Prior Width values are not normally needed, but may be helpful in fitting an ingress- or egress-only partial transit. The StepSize column allows the user to set a custom initial minimization step size. However, the default values for each parameter normally work well, so setting custom values is not usually necessary.

The Detrend Parameters sub-panel duplicates the detrend settings on the Multi-plot Y-data panel. However, the fit panel provides direct access to all detrend parameters and settings. Prior center values, widths, and fitting step sizes can optionally be set for detrend parameters as well.

The Fit Statistics sub-panel lists five statistical values that allow the user to assess the quality of the data and validity of fitted model. The values displayed from left to right are RMS of the model residuals, χ^2 per degrees of freedom (or reduced χ^2), Bayesian Information Criterion (BIC), the number of degrees of freedom, and the total χ^2 . BIC is defined as

$$\text{BIC} = \chi^2 + p \ln n, \quad (23)$$

where p is the number of fitted parameters, and n is the number of fitted data points. The BIC can be used to determine whether the addition of a new parameter value to a model (in particular an optional one such as a detrend parameter) provides a significant improvement in the fit. If the BIC value decreases by more than 2.0 when a model parameter is added, then the new model is preferred over the model with fewer parameters. A larger decrease in the BIC value suggests a stronger preference for the new model.

The Plot Settings sub-panel provides options for plotting the light curve model and the residuals. The Fit Control sub-panel settings are not normally needed, since by default the model fit recalculates any time a value in the panel is changed, and since the Fit Tolerance and Max Allowed Steps settings work for most light curve datasets.


4.1.7 Comparison Ensemble Management

The MP environment allows the user to include or exclude comparison stars from the comparison ensemble without re-running MA, as long as apertures were defined for all potentially good comparison stars in the original MA run. The Multi-plot Reference Star Settings panel shown in Figure 26 provides a checkbox corresponding to each target and comparison star included in the original MA differential photometry run. Deselected stars are considered target stars and selected stars are comparison stars belonging to the comparison ensemble. When a star is added to or removed from the ensemble, the relative flux values for each star are recalculated and the measurements table and plot are updated.

The Cycle Enabled Stars Less One button allows the user to quickly cycle through the comparison ensemble removing one star at a time so that poor comparison stars can be quickly identified and removed from the ensemble. Or, the Cycle Individual Stars button can be used to quickly assess the quality of each comparison star individually by quickly cycling through each one as a single comparison star.

4.1.8 Coordinate Converter

Coordinate Converter (CC) converts astronomical coordinates and times to other formats based on observatory location and target coordinates. CC can be operated as a module under full control of the user, and it can be operated under the control of DP and MP to provide automated calculations within those modules. When operated by the user, all fields are available to be set as desired by the user. When controlled by DP and MP, only a subset of fields are enabled for user entry of data, while the other fields are under the control of the program and disabled (grayed-out) to prevent user input. A version of CC called AstroCC runs completely independent of AIJ and is available for download from the AIJ website.

The user controlled instance of CC is started by clicking the CC icon () on the AIJ Toolbar. Figure 27 shows the panel after entering WASP-12 in the SIMBAD Object ID field, selecting the Observatory ID, and entering the date and time as UTC 2014-04-06

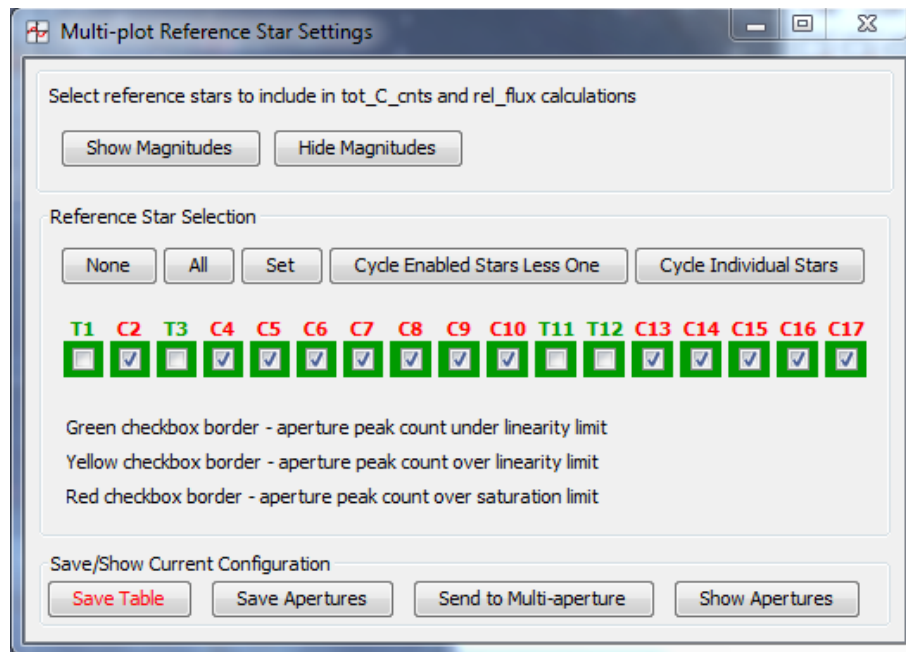


Figure 26. The Multi-plot Reference Star Settings panel. Stars can be switched from the comparison ensemble to target stars and vice-versa. All relative photometry values are recalculated and the the table is updated each time a star type is changed. Target star IDs start with the green T prefix and have a deselected checkbox. Comparison star IDs start with the red C prefix and have a selected checkbox. The "Cycle Enabled Stars Less One" and the "Cycle Individual Stars" buttons speed the task of finding and excluding poor comparison stars. See text for more details.

01:40:49. All other coordinate formats, time formats, solar system object proximities and altitudes, and moon phase are automatically calculated. Note that the red background of the Moon proximity box indicates that the moon is less than 15° from the target (12.68° in this case).

The active coordinate source used to calculate the other coordinate formats has a green border (J2000 Equatorial in this case). Any coordinate or time format can become the active source by directly entering a value into the field and pressing <Enter>. The two fields in the UTC-based Time sub-panel shown in Figure 27 with a green background show the time of PM nautical twilight (upper) and AM nautical twilight (lower) for the date and observatory location specified. If the time showing in the other time fields is during dark time, the two twilight field backgrounds are green, otherwise they are gray.

The BJD_{TDB} format that is preferred for exoplanet research requires dynamical time as the time-base. Dynamical time accounts for the changing rotational speed of the Earth by implementing leap-seconds. Leap-second updates are not periodic, but are announced six months before taking effect. The US Naval Observatory website posts a list of all leap seconds along with the effective date of each one. To ensure that conversion to BJD_{TDB} time format is accurate, CC's leap second table should be updated by clicking the Update button in the Dynamic Time sub-panel every 6 months or so.

DP creates an instance of CC (DPCC), and depending on user settings, data can be extracted from FITS header information or entered manually to control the settings used by DPCC to calculate new astronomical values to add to the calibrated image's FITS header information. If the FITS header contains the time of observations, the target's SIMBAD ID or coordinates, and the observatory's ID or coordinates, DPCC calculations can be executed with no user input. If target and/or observatory information is not available in the header, that missing information can be entered by the user as previously shown in Figure 27.

MP creates an instance of CC (MPCC), which allows the user to calculate new astronomical data and add it to the measurements table. The menu item at Multi-plot

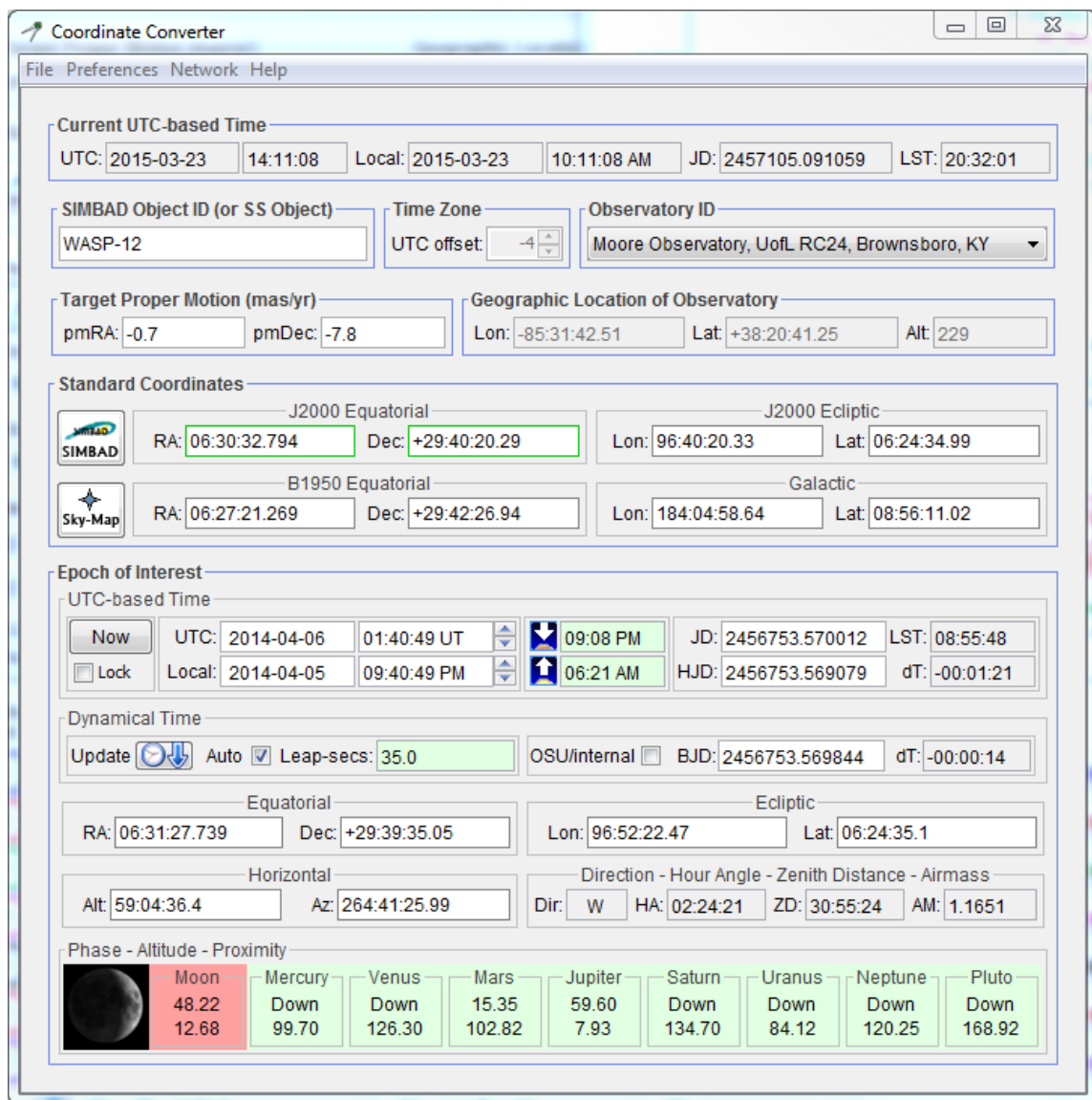



Figure 27. The AIJ Coordinate Converter panel. The displayed state of the panel is shown after entering WASP-12 in the SIMBAD Object ID field, selecting the Observatory ID, and entering the date and time as UTC 2014-04-06 01:40:49. All other coordinate formats, time formats, solar system object proximities and altitudes, and moon phase are automatically calculated. Note that the red background of the Moon proximity box indicates that the moon is less than 15° from the target (12.68° in this case). The active coordinate source used to calculate the other coordinate formats has a green border (J2000 Equatorial in this case). Any coordinate or time format can become the active source by directly typing a value into the field and pressing <Enter>. See text for more details.

Main->Table->"Add new astronomical data columns to table" opens the panel shown in Figure 28. In that panel, the user sets the time format and data column name to be used for extraction of time from each row in the measurements table. An instance of CC referred to as MPCC is also opened along with the Add Data panel. In the RA/Dec Source "Manual" mode shown in Figure 28, the target coordinates and observatory location should be manually entered into the MPCC panel. Then, when the Update Table button is clicked, the settings shown in Figure 28 will cause new data columns AIRMASS, HJD_UTC, and BJD_TDB to be calculated and added to the measurements table. The new data columns can now be used for plotting, detrending, etc., and the updated measurements table can be saved to disk.

4.1.9 FITS Header Editor

Information contained in the header of any FITS image open in AIJ can be displayed and optionally edited. The information is displayed by clicking the FITS Header Editor icon () above any image display. The user interface of the header editor is shown in Figure 29. A FITS header is made up of keywords and associated value and comment fields. FITS header keywords and values should not be edited unless the user understands the impact the changes may have on other programs that interpret the image data based on the header values.

A header value is edited by double-clicking in the field and editing the value using the keyboard. The keyword values are locked by default, but can be edited after deselecting the Lock Keyword Values checkbox. The Value field may contain a string, integer, real number, or boolean (T or F). AIJ checks the formatting of the Value field to ensure that the new entry meets the FITS specification for one of the data types allowed. The Type field is automatically set based on contents of the Value field and cannot be directly edited. Rows with keyword values SIMPLE, BITPIX, NAXIS, NAXIS1, and NAXIS2 can not be edited since these values are automatically set by AIJ according to the image's characteristics. The END keyword must always be present in the last row and

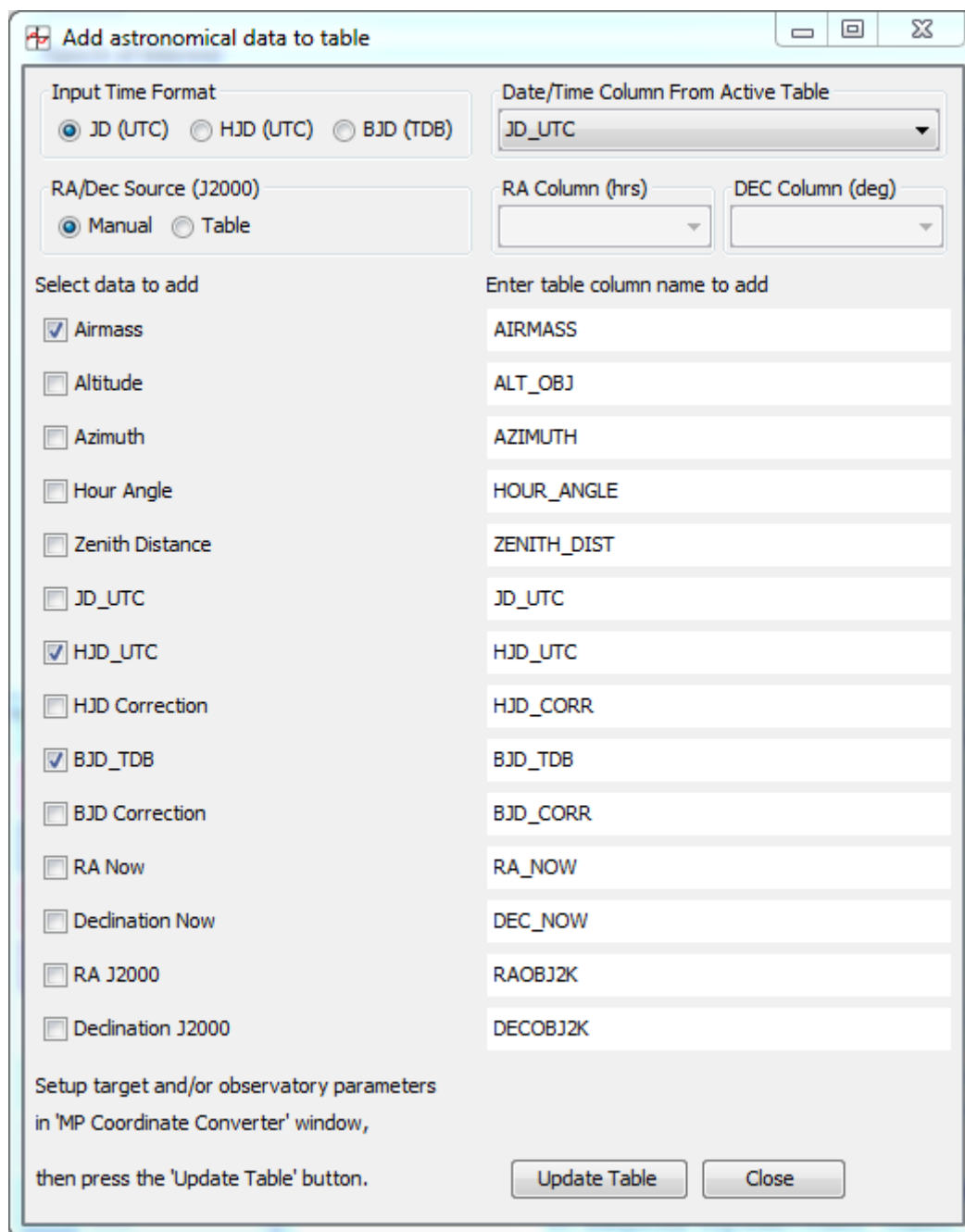



Figure 28. The AIJ Add astronomical data to table panel. The user sets the time format and data column name to be used for extraction of time from each row in the measurements table. An instance of CC referred to as MPCC is also opened along with the Add Data panel. In the RA/Dec Source "Manual" mode shown here, the target coordinates and observatory location should be manually entered into the MPCC panel. Then, when the Update Table button is clicked, the settings shown here will cause new data columns AIRMASS, HJD_UTC, and BJD_TDB to be calculated and added to the measurements table.

cannot be edited.

The buttons along the bottom of the editor, from left to right, allow the user to delete the selected row (which shows highlighted in blue) of data from the header, insert a new row below the currently selected row, save the contents of the FITS header to a text file, save the new header to the image in memory, save the image and new header to disk (and memory) using the same filename, save the image and new header to disk using a new filename, or cancel the changes and exit the editor.

4.1.10 Astrometry/Plate Solving

The AIJ astrometry feature "plate solves" images using an internet connection to the astrometry.net web portal at nova.astrometry.net (Lang et al., 2010). After a successful astrometric solution, WCS headers will be added to the FITS image header and the file can optionally be automatically resaved with the new headers. AIJ searches the image and extracts the source locations. Only the x,y coordinates for a subset of the brightest extracted sources are sent to astrometry.net. The actual image is not transferred across the network, which limits network traffic and improves the solve time.

A left-click on the Astrometry icon () above an image opens the Astrometry Settings panel shown in Figure 30. A right-click on the Astrometry icon starts the plate solve process using the previous settings panel values. DP also provides the option in the FITS Header Updates sub-panel (see Figure 20) to plate solve each image as part of the calibration process. A free user key must be obtained from nova.astrometry.net and entered into the User Key field on the Astrometry Settings panel to enable the astrometry feature.

Images can be blindly solved with no knowledge of the sky coordinates or plate scale of the image. The default settings shown in Figure 30 should work for most images. Solve time may be faster if the Plate Scale is known and entered into the field on the setup panel. If the approximate sky coordinates of the center of the image are known, entering the Center RA and Center Dec values may also improve solve time. However, the search

FITS Header Editor (WASP-12b_00020_bsdff.fits)

#	Keyword	Value	Comment	Type
1	SIMPLE	T	Created by ImageJ FITS_Writer	B
2	BITPIX	-32	number of bits per data pixel	I
3	NAXIS	2	number of data axes	I
4	NAXIS1	4096	length of data axis 1	I
5	NAXIS2	4096	length of data axis 2	I
6	EXTEND	T	FITS dataset may contain extensions	B
7	COMMENT	FITS (Flexible Image Transport System) format is defined in 'Astronomy		C
8	COMMENT	and Astrophysics', volume 376, page 359; bibcode: 2001A&A...376..359H		C
9	EXPTIME	100.	exposure time (seconds)	R
10	DATE-OBS	'2014-12-21T02:37:49.041'	date of observation (UT)	S
11	IMAGETYP	'Light Frame'	image type	S
12	TARGET	'WASP-12b'	target	S
13	INSTRUME	'U16M2 '	instrument	S
14	CCD-TEMP	-20.06	temperature (C)	R
15	FILTER	'(2) r (530-700) '	filter	S
16	TELESCOP	'MORC24 '	telescope	S
17	DATE	'2014-12-21T02:39:47'	file creation date (YYYY-MM-DDThh:mm:ss UT)	S
18	JD_OBS	2457012.6095953705	Julian Date at start of exposure	R
19	JD_UTC	2457012.6101740743	Julian Date (UTC) at mid-exposure	R
20	HJD_UTC	2457012.6157694855	Heliocentric JD (UTC) at mid-exposure	R
21	BJD_TDB	2457012.6165399384	Barycentric JD (TDB) at mid-exposure	R
22	ALT_OBJ	44.93657539900799	Target altitude at mid-exposure	R
23	AZ_OBJ	84.13511583960808	Target azimuth at mid-exposure	R
24	HA_OBJ	-3.6101187339756553	Target hour angle at mid-exposure	R
25	ZD_OBJ	45.06342460099201	Target zenith distance at mid-exposure	R
26	AIRMASS	1.413964370353721	Target airmass at mid-exposure	R
27	RAOBJ2K	6.509109444444444	J2000 right ascension of target (hours)	R
28	DECOBJ2K	29.67230277777778	J2000 declination of target (degrees)	R
29	RA_OBJ	6.525558287856426	EOD right ascension of target (hours)	R
30	DEC_OBJ	29.65791927922945	EOD declination of target (degrees)	R
31	SITELAT	38.344791666666666	geographic latitude of observatory	R
32	SITELONG	-85.528475	geographic longitude of observatory	R
33	HISTORY	Previous Filename = WASP-12b_00020.fits		H
34	HISTORY	Bias corrected with mbias_-20_20140926.fits		H
35	HISTORY	Non-linear corrected with coefficients:		H
36	HISTORY	a0 = 0.0		H
37	HISTORY	a1 = 1.0		H
38	HISTORY	a2 = 8.0E-7		H
39	HISTORY	a3 = 0.0		H
40	HISTORY	Dark corrected with mdark_-20_100_20140926.fits		H
41	HISTORY	and exposure time scaling factor = 1.0		H
42	HISTORY	Flat corrected with mflat_r_-20_20121117.fits		H
43	END			E

Lock keyword values DELETE INSERT SAVE AS TEXT... SAVE SAVE FILE SAVE FILE AS... CANCEL

Figure 29. The AIJ FITS Header Editor user interface. Most fields can be directly edited by double clicking in the fields and editing the contents using the keyboard. The DELETE button at the bottom of the display will delete the selected row. The INSERT button adds a new row under the currently selected row. The header can be saved to a text file, back to the image header in memory, or directly to disk. See the text for more details and a list of fields that cannot be directly edited.

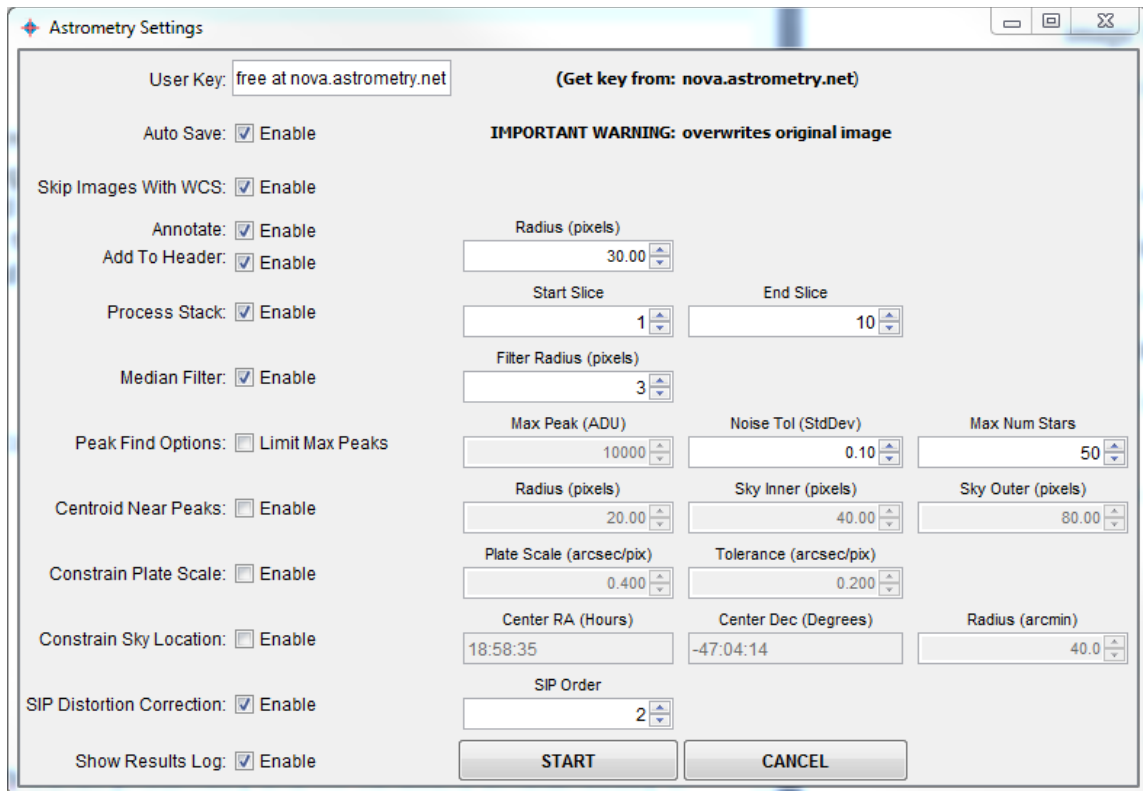



Figure 30. The AIJ Astrometry/Plate Solve Settings panel.

Radius must be at least as large as the field of view in the image. If an image has been defocused to improve photometric precision, the "Centroid Near Peaks" option may improve the determination of the location of the center of each source.

When the START button is pressed, the setup panel closes and the plate solve process starts. Progress is shown in the lower half of the AIJ Toolbar. By default, a log file is created to record the results of each plate solve. If a time-series of images have been opened into an AIJ image stack, the full set of images can be solved by selecting Process Stack. The entire plate solve process takes $\sim 10-20$ seconds per image.

When a field is successfully solved, Astrometry.net returns a list of sources that are in the image. The source names can be displayed in the image by enabling Annotate and/or saved to the FITS header by enabling Add to Header.

4.1.11 Image Alignment

The images within a stack can be aligned using the Stack Aligner icon () above an image stack. The Stack Aligner panel shown in Figure 31 opens and provides two methods to align images. At the time of writing, Stack Aligner only supports image translation for alignment. Image rotation and scaling are not currently implemented.

If all images in the stack have been plate solved, the images can be aligned using information from the WCS headers. To use that mode, enable the "Use only WCS headers..." option and click the OK button to start the alignment process. All images in the stack will then be aligned to the first image.

If images have not been plate solved, apertures are used to identify alignment stars. Aperture placement is performed in the same way as described for Multi-Aperture in §4.1.4. Images are aligned based on the average of alignment star centroid offsets between consecutive images. Aperture alignment works best when at least a few ($\sim 3-5$) isolated stars are available in the images. Aperture alignment will fail if the shift from one image to the next is larger than the aperture radius. However, the aperture radius can be made arbitrarily large as long as centroid doesn't capture a neighboring star instead of the alignment star. For cases with large image shifts, the "Use single step mode" option allows the user to click on the first alignment star in each image of the sequence, avoiding apertures centroiding on the wrong star. However, this mode requires the user to click in each image of the sequence, which may become impractical for very long image sequences.

4.1.12 AstroImageJ Updater

AIJ can be easily upgraded to the latest version using the update facility at `Toolbar->Help->Update_AstroImageJ`. The AstroImageJ Updater panel shown in Figure 32 opens. The latest release notes are displayed by clicking the Release Notes button. The default value displayed in the Upgrade To: field is the latest version. The update is installed by clicking the OK button. When the installation is finished, AIJ automatically

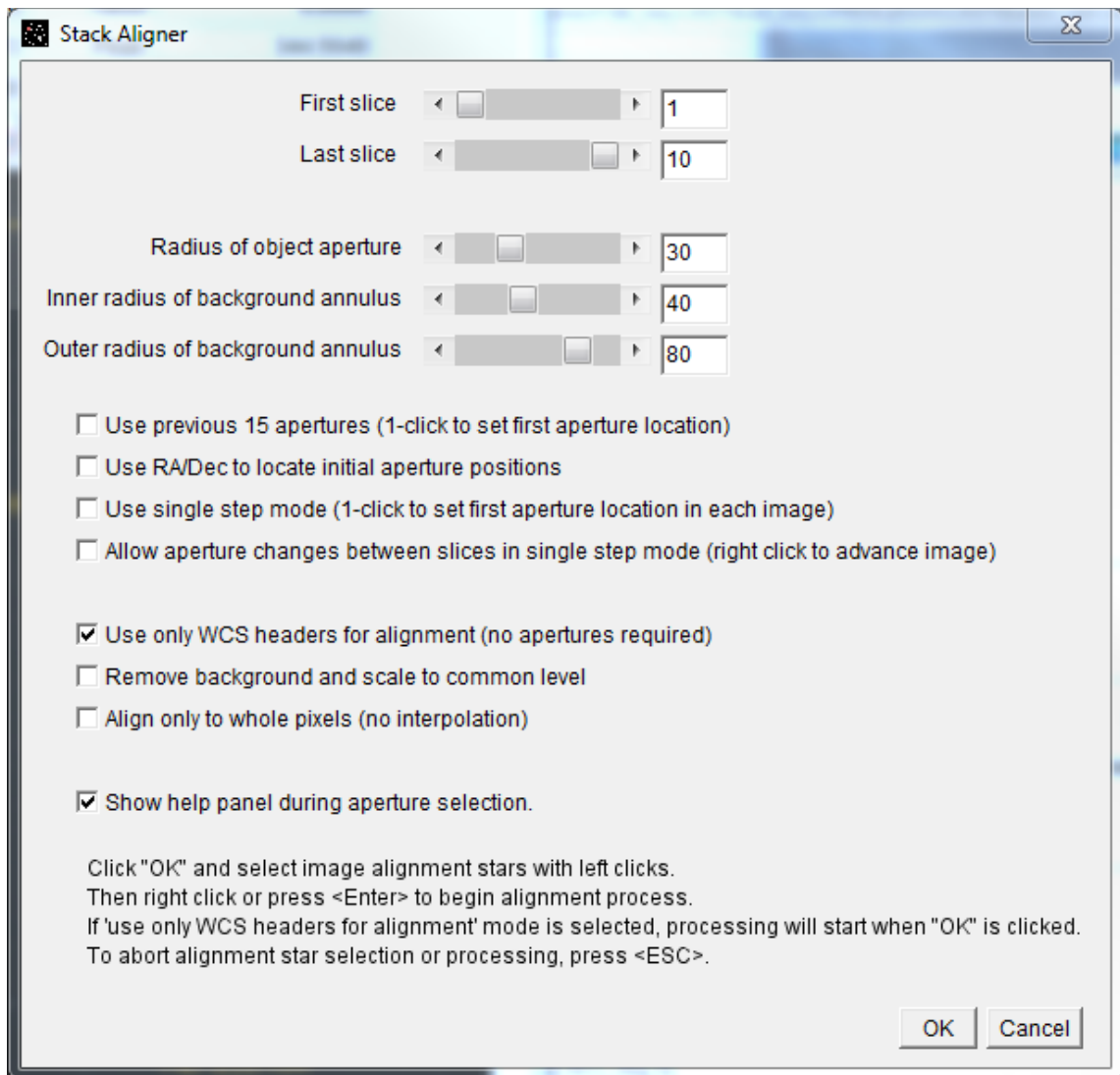


Figure 31. The AIJ Stack Aligner panel. Images can be aligned using information in the WCS headers, if images have been plate solved. Otherwise, apertures are placed around selected alignment stars, and images are aligned based on the centroid offsets between consecutive images. See text for more details.

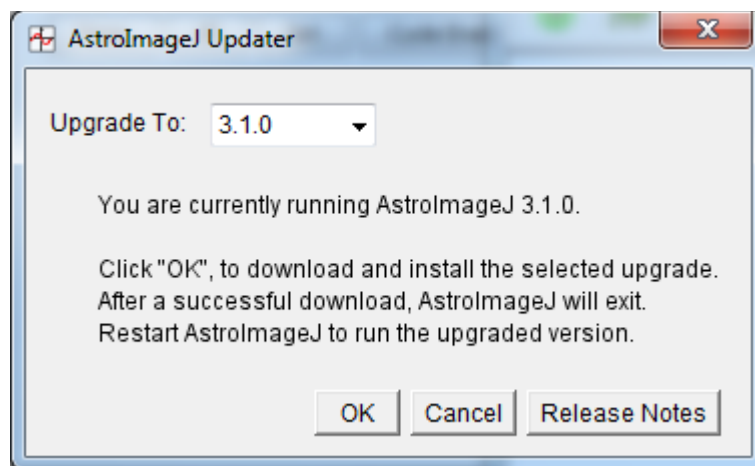


Figure 32. The AstroImageJ Updater panel. AIJ updates are easily installed by selecting the desired release number in the Upgrade To: field. The latest release notes are displayed by clicking the Release Notes button. The selected update is installed by clicking the OK button. When the installation is finished, AIJ automatically closes. The new version is activated when AIJ is restarted.

closes. The new version is activated when AIJ is restarted.

4.2 EXOFAST

EXOFAST (Eastman et al., 2013) is computer code that fits exoplanetary transit photometry and RV variations simultaneously or separately along with host star spectroscopic parameters. EXOFAST determines the model parameter uncertainties and covariances using Markov Chain Monte Carlo. The transit model is described in §1.5.1. EXOFAST can fit only one transit light curve and/or one RV data set. The program is written in the proprietary IDL language and requires the purchase of an IDL license, although there is a web-based interface⁷ that runs under an IDL demo license.

EXOFAST first finds the best fit to the RV and light curve data separately using the AMOEBA (Nelder & Mead, 1965) downhill simplex method to find the local χ^2 minimum of the model fits. To ensure that the correct local minima are found, the user

⁷<http://astrutils.astronomy.ohio-state.edu/exofast/exofast.shtml>

should provide reasonable priors on the starting points for the model parameters. For analysis of most planets discovered by ground-based wide-field surveys, typical hot Jupiter-like priors work well.

Once the best fits to the RV and light curve data are found, the data uncertainties are scaled such that the $\chi_{red}^2 = 1.0$ for each of the best fit models. Scaling the errors in this way attempts to correct for underestimated or overestimated data uncertainties before continuing with the analysis.

With the uncertainties scaled, the RV and light curve best fit parameter values are used as a starting priors for a joint fit of the RV and transit data. M_* and R_* are constrained by the spectroscopy parameters T_{eff} , $[\text{Fe}/\text{H}]$, and $\log g_*$ through the Torres relations (Torres et al., 2010). The joint best fit model is then used to start a Markov Chain Monte Carlo (MCMC) run (see Eastman et al. 2013 for an MCMC overview). The MCMC run perturbs the model parameters in a serial fashion, accepting new model parameters based on certain criteria involving the new χ^2 value at each step. At the end of the MCMC run, the resulting parameter distributions (i.e., the histogram of steps for each parameter) are proportional to the posterior probability of each parameter. EXOFAST quotes the median of the distribution of each parameter as the parameter's final value and the 34% confidence interval on either side of the median as the uncertainty.

Although EXOFAST is not used directly in my research, it is the core code from which multi-EXOFAST is derived. Multi-EXOFAST is the analysis tool used to perform all global system fits presented herein.

4.3 Multi-EXOFAST

Multi-EXOFAST is based on and operates in the same way as EXOFAST. However, it is designed to handle multiple transit light curves, in multiple filter bands, and RV datasets from multiple telescopes (including Rossiter-McLaughlin RV data). The power of multi-EXOFAST is that it enforces a common (or global) set of physical system model parameters for all of the data sets. For example, the orbital inclination must be the

same for all data sets describing a transiting system. The global system parameters enable the use of multiple light curves and RV data to better constrain the system parameters and reduce parameter uncertainties. Another important benefit is that a common set of system parameters reduces the total number of fitted model parameters compared to fitting all of the data sets individually. The reduction in model parameters then allows more detrending parameters to be included in the light curve model without creating unmanageable degeneracies in the fit. I take advantage of this and include many detrending parameters for the global fits presented herein.

Jason Eastman provided the core of the multi-EXOFAST code (private communication), but I have implemented several minor changes and bug fixes that have been folded into the version used for my research and the global fits for all KELT planet discovery papers since KELT-6b (see Chapter 8). Changes I have made include the ability to use a different number of detrending parameters for each light curve, a more user friendly front-end program to control plotting and other options from the front-end program rather than having to make code changes in the individual IDL procedures that make up multi-EXOFAST. Also, with Eastmann's support, I have fixed several bugs that were discovered during the KELT-6b global modeling effort presented in Chapter 8.

CHAPTER 5

WASP-12b CHARACTERIZATION AND TTV ANALYSIS

5.1 Introduction

WASP-12b is a hot Jupiter exoplanet discovered by the WASP survey (see §1.6.1) and announced by Hebb et al. 2009 (H09). It orbits a $V \sim 11.7$ evolved late-F star and has an orbital period of $P = 1.09$ d, a semi-major axis of only 3.1 stellar radii, and a highly inflated radius $R_P = 1.8 R_J$. Bergfors et al. (2013) reported a faint ($\Delta i' = 4.03$) elongated object $\sim 1''$ from WASP-12. Crossfield et al. (2012) confirmed the detection. Using the Keck telescope, Bechter et al. (2014) resolved the neighboring object and confirmed it to be a binary composed of two M3V stars that are orbiting WASP-12 as part of a hierarchical triple star system. The projected separation of the binary from WASP-12 is ~ 300 AU, corresponding to a period of several thousand years, so any influence on the orbital dynamics of WASP-12b should be negligible.

The short orbital period of WASP-12b results in relatively frequent opportunities to observe complete transit events from the ground, which has prompted other groups to conduct detailed studies of the system. Maciejewski et al. 2013 (M13) acquired 61 partial or complete transit light curves from 2009 to 2012 from 14 telescopes distributed around the world. They classified 19 of the transits as high quality based on RMS and transit coverage of at least 75%. Out of the 19 high quality transits, 11 have both ingress and egress coverage and baseline data before and after the transit. Data reduction and differential photometry were performed using differing methods, depending on the originating observatory. Detrending was implemented by fitting a second order polynomial and a fixed WASP-12b transit model from Maciejewski et al. (2011), which

was based on one transit. M13 find tentative evidence for a transit timing variation (TTV) signal which has a period of 545 ± 22 d and a semi-amplitude of 59 ± 11 s, and they suggest that the possible perturbing body has a mass of $0.1 M_J$ and a 3.6 day eccentric orbit.

In this chapter I present 23 new high-precision transits of WASP-12b. I discuss the observations in §5.2, data reduction in §5.3, global fitting in §5.4, system parameter results in §5.5, and TTV results in §5.6.

5.2 Observations

I observed 22 complete and one nearly complete high-precision transits of WASP-12b with the MORC telescope over the time span of November 2009 to February 2015. The date, exposure time, number of exposures, filter, photometric precision, and the error scaling factor (as determined by multi-EXOFAST; see §5.4) of each time-series of observations are listed in Table 1. All observations were guided from the science images and were defocused to improve photometric precision as discussed in sections 2 and 3. We carefully synchronized our timing source and converted to BJD_{TDB} as discussed in §3.5.5. All exposures times were 100 s, resulting in a ~ 2 minute cadence. All observations were in the Sloan r' filter, except for the g' observation on UT 2010-01-14, the CBB observation on UT 2011-12-08, and the V observation on UT 2013-11-11. All transit observations include coverage of pre-ingress baseline, ingress, flat bottom, egress, and post-egress baseline, except for the light curve on UT 2015-01-01, which has no pre-ingress baseline or time of first contact coverage. A few of the transits have short gaps due to passing clouds or equipment problems.

5.3 Data Reduction

All images were calibrated as discussed in §2 using the AIJ Data Processor module. Calibration included bias subtraction, CCD linearity correction, dark subtraction,

TABLE 1
Summary of WASP-12b Photometric Observations

Telescope	UT Date	Filter	# Data	ExpT ²	RMS ³	Scale ⁴
MORC ¹	2009-11-05	<i>r'</i>	160	100	1.3	1.32
MORC	2009-11-28	<i>r'</i>	134	100	1.0	1.33
MORC	2010-01-13	<i>r'</i>	123	100	1.1	1.24
MORC	2010-01-14	<i>g'</i>	151	100	1.2	1.46
MORC	2010-11-09	<i>r'</i>	129	100	1.2	1.70
MORC	2010-11-10	<i>r'</i>	119	100	0.9	1.29
MORC	2011-02-11	<i>r'</i>	138	100	0.9	1.22
MORC	2011-12-08	CBB	148	100	0.9	1.30
MORC	2012-02-27	<i>r'</i>	167	100	1.0	1.31
MORC	2012-02-28	<i>r'</i>	135	100	1.2	1.43
MORC	2012-03-10	<i>r'</i>	148	100	1.2	1.40
MORC	2012-11-18	<i>r'</i>	135	100	1.0	1.26
MORC	2012-12-12	<i>r'</i>	139	100	1.0	1.09
MORC	2012-12-23	<i>r'</i>	180	100	1.1	1.27
MORC	2013-01-05	<i>r'</i>	160	100	1.1	1.20
MORC	2013-01-27	<i>r'</i>	194	100	1.3	1.07
MORC	2013-11-11	<i>V</i>	93	100	1.3	1.15
MORC	2013-12-28	<i>r'</i>	167	100	1.1	1.40
MORC	2014-01-20	<i>r'</i>	181	100	1.1	1.25
MORC	2014-12-21	<i>r'</i>	201	100	1.4	1.34
MORC	2015-01-01	<i>r'</i>	150	100	1.9	1.20
MORC	2015-02-06	<i>r'</i>	217	100	1.3	1.10
MORC	2015-02-07	<i>r'</i>	138	100	1.1	1.20

¹ MORC=U. of Louisville Moore Obs. 0.6 m RCOS telescope

² Exposure time in seconds

³ RMS in units of 10^{-3}

⁴ Error scaling factor as determined by multi-EXOFAST

and flat-field division. Differential photometry was performed using the AIJ Multi-Aperture module. A superset of 16 comparison stars were selected, ensuring that each one had brightness similar to WASP-12 and no nearby stars that might blend into the aperture. The AIJ Multi-Plot and light curve fitting modules were used to search the superset of comparison stars for a subset that minimized the best fit transit model residuals for each time-series. The final comparison ensembles were different for each time-series due to differing filters and sky transparencies, but each ensemble typically had 10–14 comparison stars. A range of fixed and variable aperture sizes were investigated to find the optimal configuration that minimized transit model residuals for each dataset. The result was a variable aperture radius with a scaling factor in the range of $0.9–1.0 \times \text{FWHM}$, depending on the dataset.

The 23 individual detrended and fitted light curves are shown as black dots in Figure 33. The red lines show the global fit model from section 5.4. The black dots in Figure 34 show the results after phasing (using the global fit T_0 and P from Table 2), combining, and binning all of the WASP-12b light curves in 5 minute intervals. The light curve model is also binned at 5 minute intervals and shown as a red line. This light curve is not used for analysis, but rather to show the best combined behavior of the transit. The model residuals shown in the bottom panel have an RMS of 183 ppm.

5.4 Global Fit

Multi-EXOFAST (see §4.3) was used to perform a global fit to all 23 MORC light curves. As discussed in section §2.9, seven detrend datasets are included with each light curve to simultaneously detrend the light curves as part of the global fit. The detrend datasets are airmass, time, sky background, FWHM of the average PSF in each image, total comparison star counts, and target x-centroid and y-centroid positions on the detector. The global fit also included SOPHIE RV data from H09 and Husnoo et al. (2011) and spectroscopic priors of $T_{\text{eff}} = 6300 \pm 200$ K and $[\text{Fe}/\text{H}] = 0.3 \pm 0.15$ from H09. A spectroscopic prior was not imposed on $\log g_*$, since the value derived exclusively from

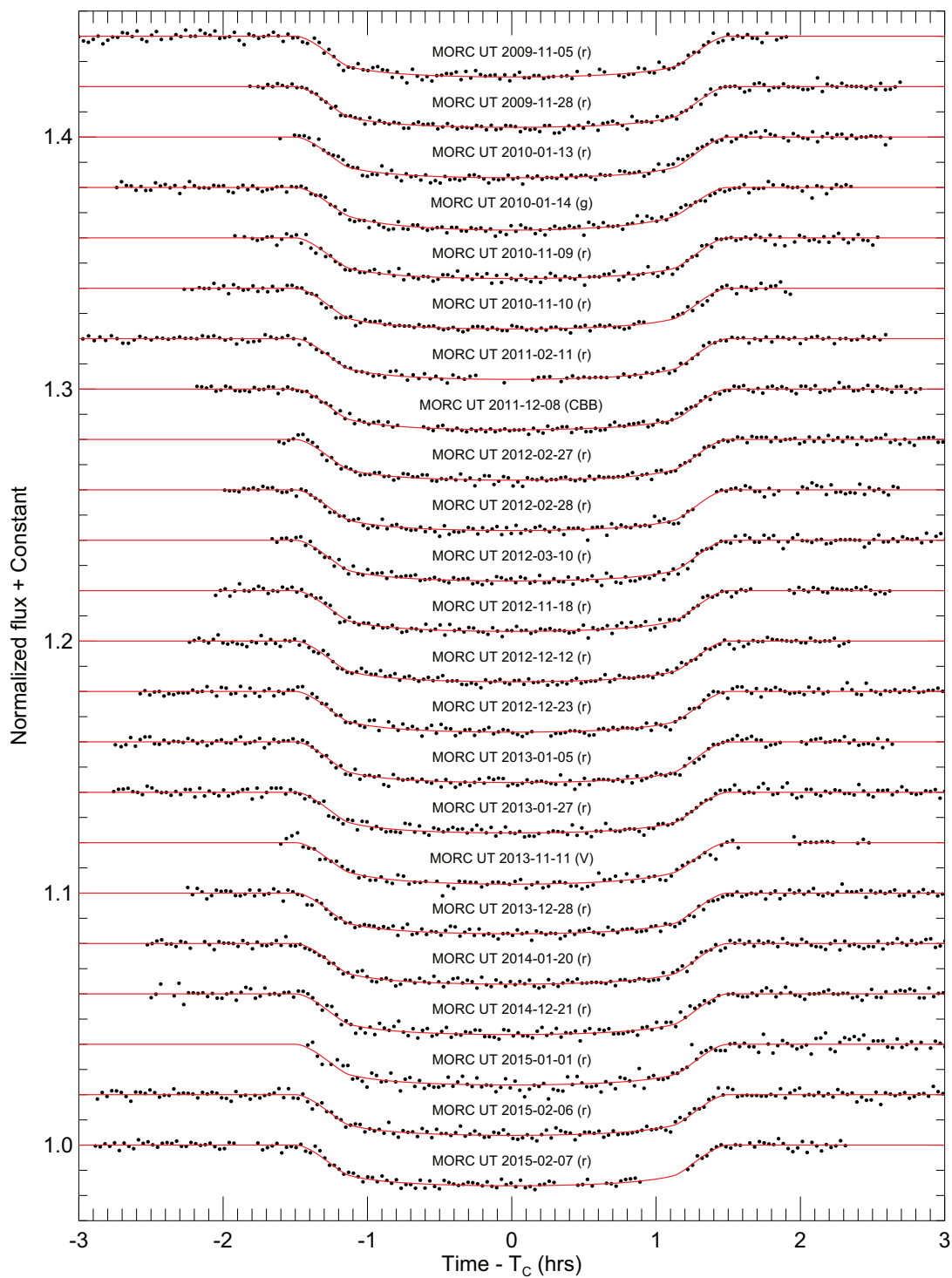


Figure 33. All 23 WASP-12b light curves. Each light curve is detrended and fitted as discussed in §5.4. The exposure time for each data point is 100 s. The black points are the normalized and detrended differential photometric measurements, while the red lines show the global transit model. Each light curve is shifted on the y-axis for clarity.

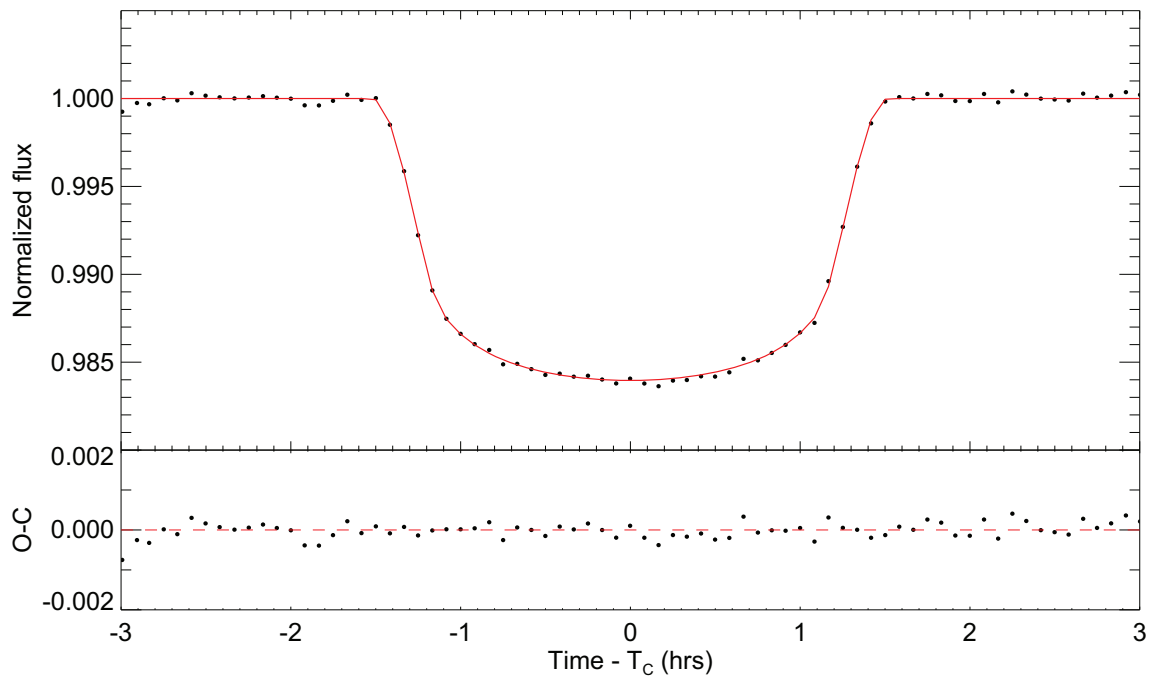


Figure 34. All 23 WASP-12b detrended light curves combined and binned in 5 min intervals (black dots). The light curves are combined by phasing the data using the global T_0 and P from Table 2. The light curve model is also binned at 5 minute intervals and shown as a red line. This light curve is not used for analysis, but rather to show the best combined behavior of the transit. The model residuals shown in the bottom panel have an RMS of 183 ppm.

the light curves should be more accurate than the spectroscopic value (e.g. Mortier et al. 2013, 2014). Based on an initial best fit, multi-EXOFAST scales the RV and photometric errors to target a reduced chi-squared of $\chi_{red}^2 = 1.0$ for the global fit. As a result, the H09 RV errors were scaled by 1.45 and the Husnoo et al. (2011) RV errors were scaled by 2.59. The photometric scaling factors are listed in Table 1 and range from 1.07 to 1.70. The orbital eccentricity was fixed to zero since secondary eclipse observations by Campo et al. (2011) and Croll et al. (2011) and RV observations and analysis by Husnoo et al. (2011) place tight constraints on the circularity of the planet’s orbit. The parameter $v \sin i_*$ was constrained to be within 1 m s^{-1} of 2200 m s^{-1} (the nominal value from spectroscopy in H09), since the RM data do not provide a good constraint on the value. Without a tight $v \sin i_*$ prior, the model fits would not converge. The phased RVs are shown in Figure 35 and a close-up of the in-transit RM data is shown in Figure 36. The SOPHIE RVs from H09 are shown as black dots, and the SOPHIE RVs from Husnoo et al. (2011) are shown as green squares. The RM and RV models from the global fit are shown as red lines.

The Demarque et al. (2004) stellar models were used to estimate M_* and R_* from T_{eff} , $\log g_*$, and $[\text{Fe}/\text{H}]$ at each MCMC step. Separate TTV parameters were fit for each light curve, but common R_p/R_* , a/R_* , and i parameters were fit globally to all light curves. Common sets of quadratic limb darkening parameters, $u1_\lambda$ and $u2_\lambda$, were determined for each filter band from the models of Claret & Bloemen (2011) using T_{eff} , $\log g_*$, and $[\text{Fe}/\text{H}]$ at each MCMC step. The publicly available Claret & Bloemen (2011) limb darkening tables that are included in multi-EXOFAST do not contain coefficients for the CBB filter band. At my request, A. Claret computed them from the Claret & Bloemen (2011) models. The nominal CBB band coefficient values for a star with spectroscopic parameters like WASP-12 turn out to be within 0.02 of the coefficients for the *Kepler* band that are already included in multi-EXOFAST. The difference in the coefficients is negligible for our ground-based data, so I used the *Kepler* band coefficients for the global fit.

The $\sim 1''$ stellar binary discovered by Bergfors et al. (2013) is blended with

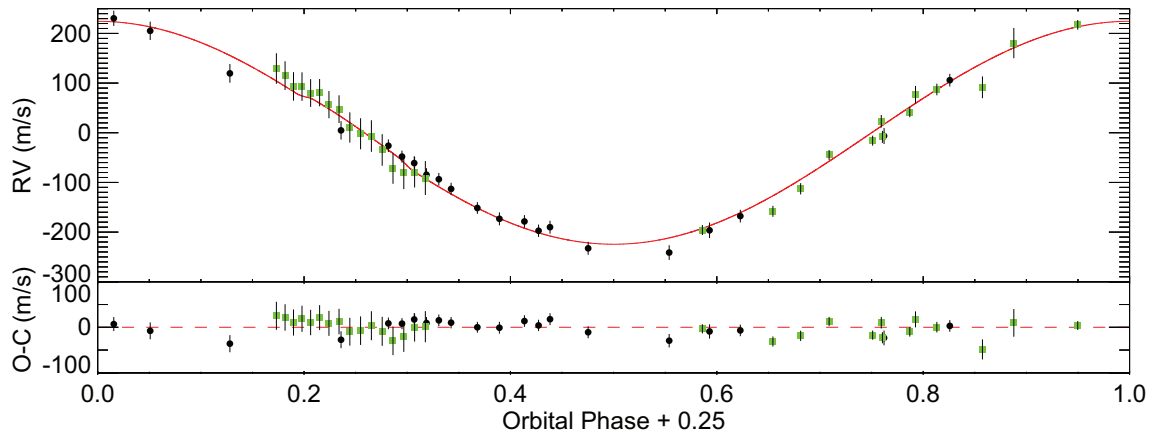


Figure 35. WASP-12b phased RVs and the combined RV plus RM model. The SOPHIE RVs from H09 are shown as black dots. The SOPHIE RVs from Husnoo et al. (2011) are shown as green squares. The red line shows the best fit RV plus RM model from the global fit. The bottom panel shows the model residuals.

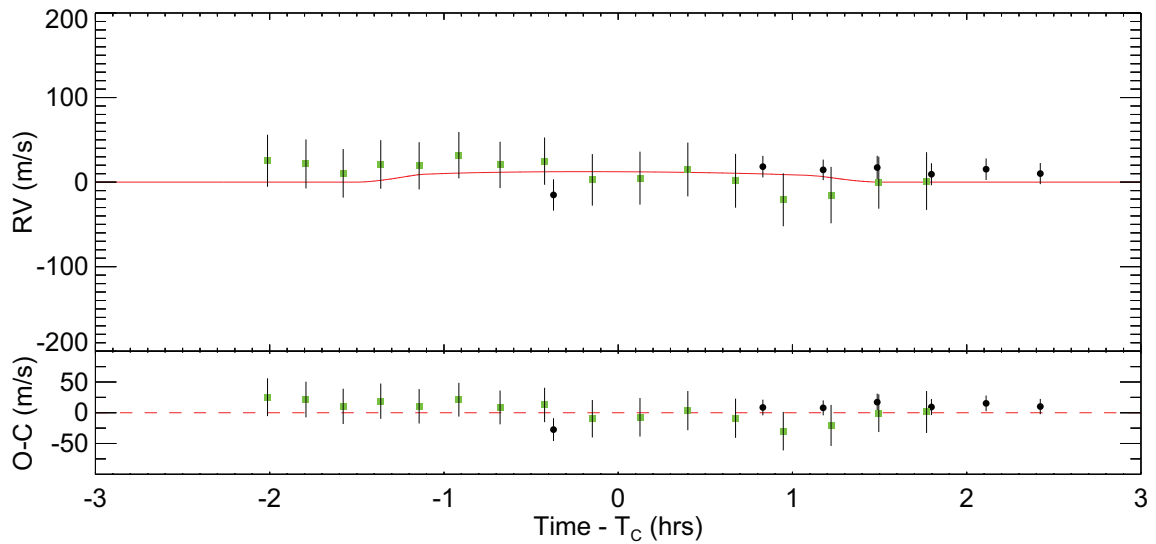


Figure 36. WASP-12b phased in-transit RVs and RM model. The SOPHIE RVs from H09 are shown as black dots. The SOPHIE RVs from Husnoo et al. (2011) are shown as green squares. The red line shows the best fit RM model from the global fit. The RV data have had the best fit RV model subtracted to remove the orbital velocity component. The bottom panel shows the model residuals.

WASP-12 in all of the MORC photometry. The binary is four magnitudes fainter than WASP-12 in the i' band, so the ratio of the blended flux to the WASP-12 flux is 1.026 in the i' band, and would be slightly less in the r' band used for most of the MORC observations. Using the blended flux will therefore underestimate the true transit depth and R_p/R_* by $\sim 2.6\%$ and $\sim 1.2\%$, respectively. Based on the nominal blended transit depth of ~ 14 mmag from the literature, the nonblended depth would increase by ~ 0.35 mmag. Any other parameters dependent on the transit depth will also be affected. Since typical M_* and R_* uncertainties from stellar models are $\sim 10\%$ (e.g. Basu, Verner, Chaplin, & Elsworth 2012) and those uncertainties are not accounted for in this or other typical works, I do not attempt to account for the flux from the blended binary in the global system fit.

5.5 System Parameter Results

In addition to the original WASP-12b system parameter analysis by H09, Chan et al. 2011, 2012 (C12), Southworth et al. (2012), and M13 have performed follow-up analyses of the WASP-12b system. The follow-up analyses use various tools to fit the transit data and determine parameter errors, and they use differing methods to constrain M_* and R_* , but none self-consistently perform a global system analysis based on the RV data, spectroscopy, light curves, and stellar models. All of the analyses except M13 included 2 to 4 light curves. M13 simultaneously fit 19 light curves to model the system parameters, but only light curves were included in the fit.

The system parameter values and uncertainties from a self-consistent global fit to two RV datasets, 23 MORC light curves, spectroscopic T_{eff} and $[\text{Fe}/\text{H}]$, the Demarque et al. (2004) stellar models, and the Claret & Bloemen (2011) stellar limb darkening models are shown in Table 2, and a comparison to values from the literature is shown in Table 3. Since M13 used a modeling tool that fits only light curves, many physical parameter values were not reported and are thus not listed in column M13 of the table. Our transit derived parameter values agree with the M13 values to well within 1σ , except the highly

precise orbital periods differ by 3σ . This difference is discussed more in §5.6.

The orbital semi-major axis, a , from this work agrees with the other studies within $\sim 1\sigma$. All of the transit derived parameters agree within 1σ as well, except the C12 R_p/R_* value is $2-3\sigma$ lower than the values listed from the other studies, which causes significant differences in some of the derived physical parameters. The C12 inclination value is higher by 1σ compared to the other studies. It is possible that one or both of the transits included in their analysis had a systematic that was not compensated for, or there could have been an astrophysical anomaly, so the C12 results are excluded from the remainder of the comparison discussion.

The transit derived values R_p/R_* , a/R_* , and i agree with the other three studies within 1σ . The stellar values M_* , R_* , $\log g_*$, and ρ_* all agree within 1σ , although M_* and R_* from this work are at the upper end of the 1σ range of the other studies. The planetary parameter values M_p , R_p , and T_{EQ} from this work are also higher by $\sim 1\sigma$, and $\log g_p$ and ρ_p are smaller by $\sim 1\sigma$.

The presence of a correlated non-periodic component in the SOPHIE RVs is especially obvious during the in-transit sequence (Figure 36), which was also noticed and discussed in Husnoo et al. (2011). SOPHIE is a spectrograph that is optimized for precise radial velocity measurements in the "High Resolution" mode. However, WASP-12b is on the faint end of the range of the 1.93 m telescope and was measured in the "High Efficiency" mode, which is less optimized for RV measurements. Husnoo et al. (2011) discuss that the RV anomaly could be due to instrumental noise, stellar variability, or a planetary companion that is unaccounted for in the system. Given their experience with SOPHIE in "High Efficiency" mode, they conclude that instrumental noise is the likely cause. The impact on this study is that the value of spin-orbit angle, $\lambda = -90_{-26}^{+23}$, derived from the global fit, may not be reliable.

TABLE 2

Median Values and 68% Confidence Intervals for the Physical and Orbital Parameters of the WASP-12b System from the Global Fit Described in §5.4.

Parameter	Units	Value
Stellar Parameters:		
M_*	Mass (M_\odot)	$1.434^{+0.11}_{-0.090}$
R_*	Radius (R_\odot)	$1.657^{+0.046}_{-0.044}$
L_*	Luminosity (L_\odot)	$4.05^{+0.54}_{-0.53}$
ρ_*	Density (cgs)	$0.446^{+0.015}_{-0.014}$
$\log g_*$	Surface gravity (cgs)	$4.157^{+0.013}_{-0.012}$
T_{eff}	Effective temperature (K)	6360^{+130}_{-140}
[Fe/H]	Metallicity	$0.33^{+0.14}_{-0.17}$
λ	Spin-orbit alignment (degrees)	-90^{+23}_{-26}
Planetary Parameters:		
a	Semi-major axis (AU)	$0.02340^{+0.00056}_{-0.00050}$
M_P	Mass (M_J)	$1.470^{+0.076}_{-0.069}$
R_P	Radius (R_J)	$1.900^{+0.057}_{-0.055}$
ρ_P	Density (cgs)	$0.266^{+0.015}_{-0.014}$
$\log g_P$	Surface gravity	3.004 ± 0.015
T_{eq}	Equilibrium temperature (K)	2580^{+58}_{-62}
Θ	Safronov number	$0.02520^{+0.00087}_{-0.00084}$
$\langle F \rangle$	Incident flux ($10^9 \text{ erg s}^{-1} \text{ cm}^{-2}$)	10.06 ± 0.94
Primary Transit Parameters:		
T_0	Linear ephemeris from transits (BJD_{TDB})	$2456176.668258 \pm 7.7650773 \times 10^{-5}$
P	Linear eph. period from transits (days) ..	$1.0914203 \pm 1.4432653 \times 10^{-7}$
R_P/R_*	Radius of the planet in stellar radii	$0.11785^{+0.00053}_{-0.00054}$
a/R_*	Semi-major axis in stellar radii	$3.039^{+0.034}_{-0.033}$
i	Inclination (degrees)	$83.37^{+0.72}_{-0.64}$
b	Impact parameter	$0.351^{+0.030}_{-0.034}$
δ	Transit depth	0.01389 ± 0.00013
T_{FWHM}	FWHM duration (days)	0.10958 ± 0.00023
τ	Ingress/egress duration (days)	0.01526 ± 0.00044
T_{14}	Total duration (days)	$0.12483^{+0.00044}_{-0.00043}$
P_T	A priori non-grazing transit probability ..	$0.2903^{+0.0030}_{-0.0031}$
$P_{T,G}$	A priori transit probability	$0.3679^{+0.0041}_{-0.0042}$
Secondary Eclipse Parameter:		
T_S	Time of eclipse (BJD_{TDB})	$2456176.12256 \pm 0.00020$
RV Parameters:		
K	RV semi-amplitude (m/s)	226.4 ± 4.1
e	RV eccentricity	0.0 (FIXED)
K_{RM}	RM amplitude (m/s)	$30.99^{+0.28}_{-0.29}$
$M_P \sin i$	Minimum mass (M_J)	$1.460^{+0.075}_{-0.068}$
M_P/M_*	Mass ratio	0.000977 ± 0.000028
γ_{SOPHIE09}	m/s	72.4 ± 3.6
γ_{SOPHIE10}	m/s	19083.0 ± 3.1

TABLE 3
Comparison of WASP-12b Selected Physical System Parameters to Values from the Literature

Parameter	This Work	M13	S12	C12	H09
Stellar Parameters:					
M_*	1.434 ± 0.11	—	1.38 ± 0.18	1.36 ± 0.14	1.35 ± 0.14
R_*	1.657 ± 0.046	—	1.619 ± 0.076	1.595 ± 0.071	1.57 ± 0.07
$\log g_*$	4.157 ± 0.013	—	4.159 ± 0.023	4.164 ± 0.029	4.17 ± 0.03
ρ_*	0.446 ± 0.015	0.444 ± 0.01	0.458 ± 0.023	0.475 ± 0.038	0.493 ± 0.04
Planetary Parameters:					
M_P	1.470 ± 0.076	—	1.43 ± 0.13	1.403 ± 0.099	1.41 ± 0.10
R_P	1.900 ± 0.057	1.86 ± 0.09	1.825 ± 0.091	1.732 ± 0.092	1.79 ± 0.09
$\log g_P$	3.004 ± 0.015	—	3.027 ± 0.023	3.069 ± 0.031	2.99 ± 0.03
ρ_P	0.266 ± 0.015	—	0.292 ± 0.025	0.340 ± 0.039	0.318 ± 0.04
T_{eq}	2580 ± 62	—	2523 ± 45	—	2516 ± 36
Orbital Parameters:					
P	$1.0914203(1)$	$1.0914209(2)$	—	$1.0914222(11)$	$1.0914230(30)$
a	0.02340 ± 0.00056	—	0.02309 ± 0.00096	0.02293 ± 0.00078	0.0229 ± 0.0008
Transit Parameters:					
R_P/R_*	0.11785 ± 0.00054	0.1173 ± 0.0005	0.1158 ± 0.005	0.1119 ± 0.002	0.1175 ± 0.0008
a/R_*	3.039 ± 0.034	3.033 ± 0.022	3.067 ± 0.05	3.105 ± 0.082	—
i	83.37 ± 0.72	82.96 ± 0.50	83.3 ± 1.1	86.2 ± 3.0	83.1 ± 1.4

Notes: Parameter variable names and units are the same as in Table 2, a value enclosed in parentheses is the uncertainty in the same number of last digits, M13=Maciejewski et al. (2013), S12=Southworth et al. (2012), C12=Chan et al. (2011, 2012), H09=Hebb et al. (2009)

5.6 TTV Results

The global system model includes a TTV parameter for each of the 23 light curves, allowing the transit center time at each epoch to differ from the linear ephemeris. The resulting TTV values are listed in Table 4 and a linear plot of TTV vs. epoch is shown in Figure 37. The epoch 776 TTV displayed in yellow with the large uncertainty is from the transit on UT 2015-01-01 which does not have coverage of pre-ingress baseline or time of first contact and has been excluded from the analysis. This data point illustrates the importance of including only complete transits with good baseline in high precision TTV studies. Ignoring epoch 776, the TTVs have a maximum value of 79 s, a standard deviation of 32.88 s, and reduced chi-squared of $\chi_{red}^2 = 1.1$, with respect to the linear ephemeris. The mean of the timing uncertainty is 31 s.

Figure 38 shows a Lomb-Scargle periodogram of the WASP-12b TTVs. All peaks are well below the analytical 10% false alarm probably (FAP) indicated by the short-dashed line. Nevertheless, I investigated the highest power peak at 3.6615 epochs (3.996 days), which is marked in Figure 38 with a down-pointing arrow labeled 3.6615. The phased plot and model are shown in Figure 39. The sinusoidal fit has $\chi_{red}^2 = 0.66$ and a semi-amplitude of 34 s (nearly the same as the standard deviation of the TTVs and the mean timing uncertainty). The 500 epoch signal that was detected and investigated by M13 is marked in Figure 38 with the down-pointing arrow labeled 500 and shows very little power in the periodogram. Time domain searches around 500 epochs confirm the periodogram results.

M13 included TTVs from an early follow-up light curve from the H09 discovery paper, and two more early light curves from C12. Figure 40 shows the TTVs analyzed by M13 with timing errors < 40 s (red dots), after rephasing them to the linear ephemeris derived in this work (solid gray line). The TTVs from this work are indicated by blue dots. The transits at epochs -1522 and -1224 arrive significantly early relative to the ephemeris from this work, but not quite so early relative to the M13 linear ephemeris (dashed gray line).

TABLE 4
WASP-12b Transit Times

T_C (BJD _{TDB})	Epoch	TTV (s)	σ_{TTV} (s)	TTV/ σ_{TTV}
2455140.909815	-949	-48.89	36	-1.33
2455163.830613	-928	35.05	28	1.21
2455209.668946	-886	-79.01	40	-1.93
2455210.761506	-885	19.46	35	0.55
2455509.809713	-611	-63.37	32	-1.95
2455510.902181	-610	27.15	27	0.97
2455603.672606	-525	1.09	25	0.04
2455903.813566	-250	33.41	28	1.19
2455984.577971	-176	-26.91	28	-0.93
2455985.669747	-175	3.82	36	0.10
2455996.583783	-165	-10.62	32	-0.32
2456249.794041	67	53.79	34	1.58
2456273.805140	89	41.01	26	1.57
2456284.718565	99	-26.22	26	-1.00
2456297.816050	111	11.90	26	0.45
2456319.644239	131	-6.87	33	-0.21
2456607.779376	395	8.21	61	0.13
2456654.710469	438	9.90	29	0.33
2456677.630387	459	17.80	28	0.62
2457012.696166	766	-4.41	42	-0.10
2457023.609018*	776	-121.14	71	-1.69
2457059.627132	809	-13.69	30	-0.45
2457060.718388	810	-27.89	31	-0.89
Standard Deviation		32.88	—	1.00
Mean		—	31	—

* This measurement is from the transit on UT 2015-01-01 that does not have coverage of pre-ingress baseline or time of first contact and has been excluded from the analysis.

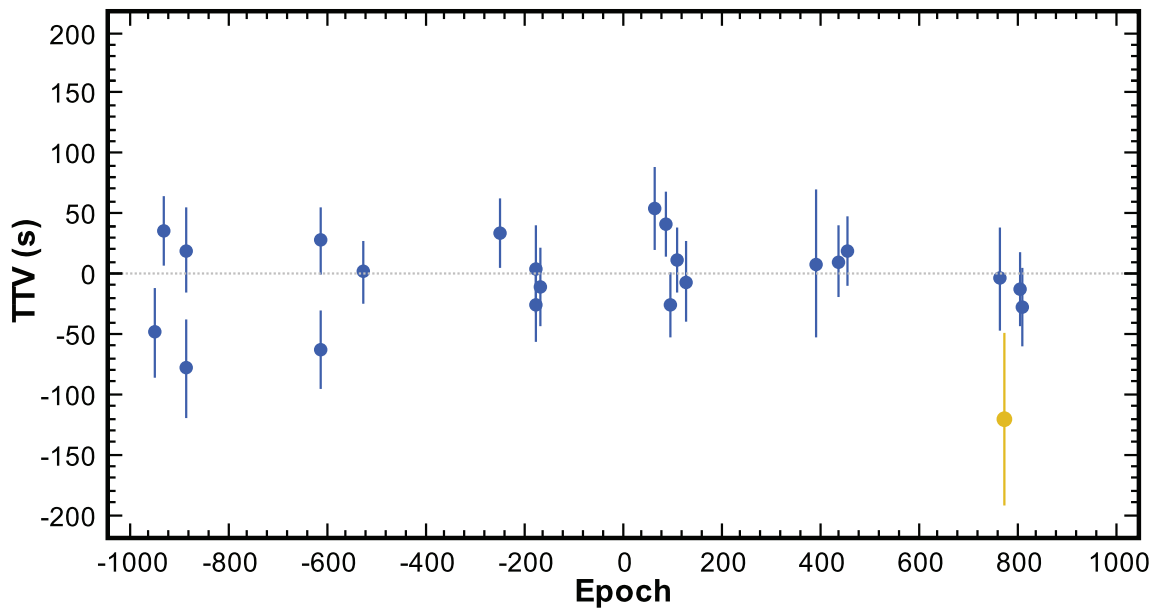


Figure 37. WASP-12b TTVs vs. transit epoch. The epoch is calculated from the global fit ephemeris in Table 2. TTV is defined as the observed T_C minus T_C calculated from the linear ephemeris (i.e. $O-C$). The epoch 776 TTV displayed in yellow with the large uncertainty is from the transit on UT 2015-01-01 that does not have coverage of pre-ingress baseline or time of first contact and has been excluded from the analysis.

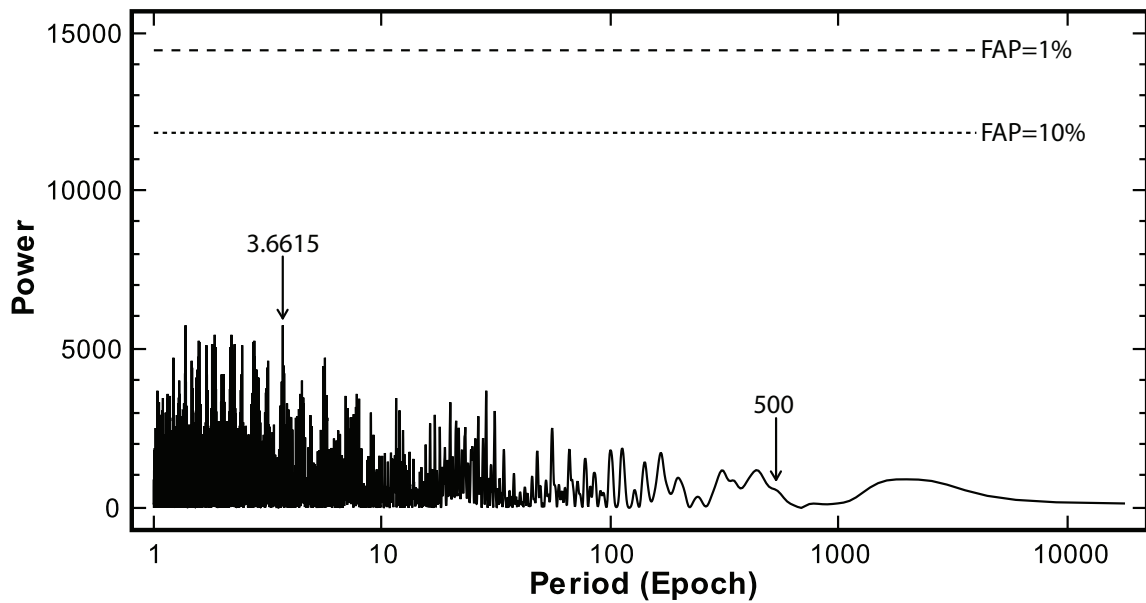


Figure 38. Lomb-Scargle periodogram for the WASP-12b TTVs. Analytical FAP levels of 10% and 1% are indicated by the short-dashed and long-dashed lines, respectively. The down-pointing arrow labeled 3.6615 marks the peak power component. The down-pointing arrow labeled 500 marks the location of the strongest peak in the M13 periodogram.

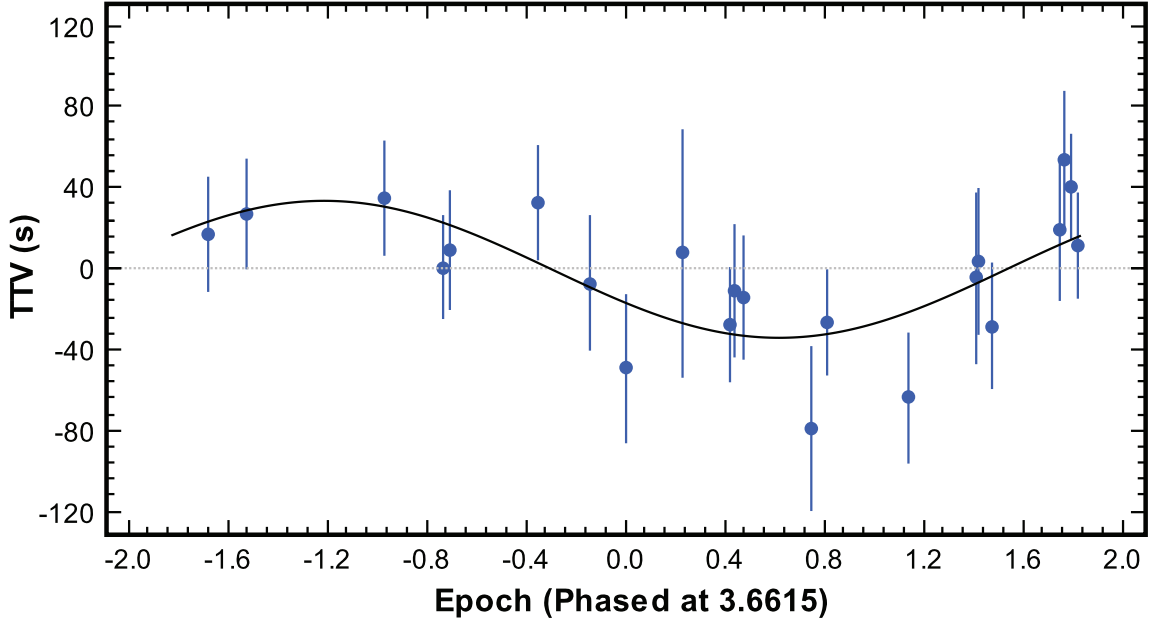


Figure 39. WASP-12b TTVs phased at 3.6615 epochs (3.996 days). The sinusoidal fit has $\chi_{red}^2 = 0.66$ and a semi-amplitude of 34 s. The interpretation is a chance fit to noise.

Combining all of the TTV data, a fit to the linear ephemerides gives $\chi_{red}^2 = 1.83$ (ephemeris from this work) and $\chi_{red}^2 = 1.71$ (ephemeris from M13). Excluding the early epochs -1522 and -1224 gives $\chi_{red}^2 = 1.48$ (this work) and $\chi_{red}^2 = 1.69$ (M13). An even longer time baseline of observations may be required to determine which ephemeris best describes the WASP-12b orbital period.

The periodogram of the combined TTVs was also investigated. Again, there were no peaks with a reasonably low FAP, and in particular, little support was found for the 500 epoch signal in either the frequency or time domain.

5.7 Conclusions

I present the results of a self-consistent global fit to 23 MORC light curves (that have been homogeneously reduced starting from the individual images), two RV datasets, spectroscopic T_{eff} and $[\text{Fe}/\text{H}]$, the Demarque et al. (2004) stellar models, and the Claret &

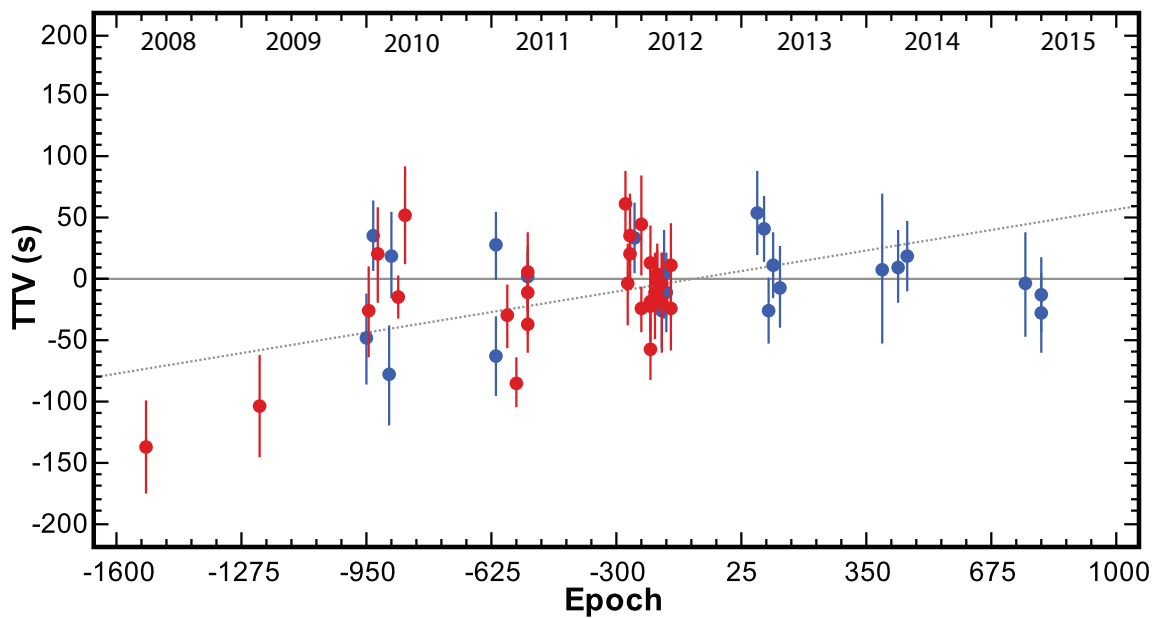


Figure 40. WASP-12b TTVs from this work and the literature. TTVs from this work are shown as blue dots. TTVs collected by M13 with timing errors < 40 s have been rephased to the ephemeris from this work and are shown as red dots. The solid gray line shows the linear ephemeris from this work. The dashed gray line shows the linear ephemeris from M13. The numbers across the top indicate the approximate calendar year.

Bloemen (2011) stellar limb darkening models. I reach the space-like photometric precision of 183 ppm per 5 minute bin in the combined light curve model residuals. Multi-EXOFAST implements input data uncertainty scaling and MCMC to robustly determine system parameter uncertainties. Even with the careful treatment, most of the uncertainties reported herein are improved by $\sim 40-50\%$ compared to previous studies. The derived system parameters in this work are consistent with values from the literature at a level of 1σ , except for the period of the linear ephemeris compared to M13. M_* , R_* , M_P , R_P , and T_{EQ} from this work are at the upper end of the 1σ range of the other studies, while $\log g_P$ and ρ_P are at the lower end of the 1σ range.

The linear ephemeris from this work differs from the M13 ephemeris by 3σ , so a longer baseline of observations may be required to determine the precise ephemeris. Or, if the two earliest TTV measurements shown in Figure 40 are accurate, a long term TTV signal (of about ~ 20 years) may be causing the apparent changes in the shifting linear ephemeris. If the two measurements are found to be inaccurate and are removed from the analysis, the linear ephemeris from this work is a good fit to the combined high-precision timing data from M13 and this work. The uncertainties in the stellar models have not been accounted for, so no attempt was made to correct for the flux from the blended binary in the global system fit. The primary effect is that R_P/R_* is underestimated by about 1.2% in this work and the analyses in the literature.

Unless multi-EXOFAST is overestimating the parameter errors, the transit center times from this work are well modeled by a linear ephemeris with $T_0 = 2456176.668258 \pm 7.7650773 \times 10^{-5}$ and $P = 1.0914203 \pm 1.4432653 \times 10^{-7}$, which has $\chi_{red}^2 = 1.09$. A sinusoidal fit to the data using the period corresponding to the highest power peak in the periodogram (3.996 days), yields an improved fit with $\chi_{red}^2 = 0.66$. However, that peak has an analytical false alarm probability of more than 100%, so my interpretation is that the improvement is due to a chance fit to noise in the data. Based on the reduced chi-squared value for the linear ephemeris model and the lack of signals in the periodogram, I find no convincing evidence for sinusoidal TTVs with a semi-amplitude of more than ~ 35 s in

the MORC data or the combined data. This interpretation is consistent with the Steffen et al. (2012) study that found no evidence of TTVs in the orbits of Kepler hot Jupiter planets with $1 \leq P \leq 5$ days. On the other hand, the data are sparsely sampled and it may be possible that short period, low level, or non-sinusoidal TTV signals are lurking in the data. In particular, the timing data between epochs 0 and 200 (the 2012-2013 observing season) seem to show a correlated downward trend. However, the data are too sparse to consider fitting non-sinusoidal TTV signals.

CHAPTER 6

QATAR-1b CHARACTERIZATION AND TTV ANALYSIS

6.1 Introduction

Qatar-1b is a hot Jupiter exoplanet and is the first planet discovered by the Qatar Exoplanet Survey (see §1.6.1). The planet was announced by Alsubai et al. 2011 (A11). The host star is a $V \sim 12.8$ metal-rich K-dwarf star, and the planet has a circular orbital with period $P = 1.42$ d, a semi-major axis of ~ 6 stellar radii, a mass $M_p = 1.09 M_J$ and a radius $R_p = 1.2 R_J$.

The short orbital period of Qatar-1b results in relatively frequent opportunities to observe complete transit events from the ground, which has prompted a number of other groups to conduct detailed studies of the system. Covino et al. 2013 (C13) obtained HARPS-N in-transit high-precision radial velocities to measure the RM effect in the Qatar-1b system, and out-of-transit measurements to redetermine the spectroscopic orbit. They found that the orbit is consistent with circular and has a well-aligned spin-orbit angle of $\lambda = -8.4 \pm 7.1^\circ$. von Essen, Schröter, Agol, & Schmitt 2013 (E13) presented a detailed TTV analysis of 26 Qatar-1b transits covering a baseline of 18 months and found evidence for a 190 or 380 day TTV signal with semi-amplitude ~ 1 min that could be reproduced by either a weak perturber in resonance with Qatar-1b, or by a massive body in the brown dwarf regime. Mislis et al. 2015 (DM15) analyzed 12 complete Qatar-1b transits and provided updated system parameters. After reviewing all TTV data available, DM15 suggest further and more precise data to determine if TTVs exist in the system. Croll et al. (2015) presented near-infrared secondary eclipse observations of Qatar-1b thermal emission showing a mid-eclipse time consistent with a circular orbit. Maciejewski et al.

2015 (GM15) analyzed 18 Qatar-1b transits to redetermine system parameters and found no evidence of periodic TTV's $\gtrsim 1$ min.

In this chapter I present 18 new high-precision transits of Qatar-1b. I discuss the observations in §6.2, data reduction in §6.3, global fitting in §6.4, system parameter results in §6.5, and TTV results in §6.6.

6.2 Observations

I observed 18 complete high-precision transits of Qatar-1b with the MORC telescope over the time span of June 2011 to September 2014. The date, exposure time, number of exposures, filter, photometric precision, and the error scaling factor (as determined by multi-EXOFAST; see §6.4) of each time-series of observations are listed in Table 5. All observations were guided from the science images and were defocused to improve photometric precision as discussed in sections 2 and 3. We carefully synchronized our timing source and converted to BJD_{TDB} as discussed in §3.5.5. All exposures times were 100 s, resulting in a ~ 2 minute cadence. The first seven transits were observed with no filter (i.e. open) and the remaining 11 transits were observed in the Astrodon CBB filter (see §3.3). All transit observations include coverage of pre-ingress baseline, ingress, flat bottom, egress, and post-egress baseline. A few of the transits have short gaps due to passing clouds or equipment problems, including the UT 2014-07-23 transit which has no coverage of the time of fourth contact, but has good post transit baseline.

6.3 Data Reduction

All images were calibrated as discussed in §2 using the AIJ Data Processor module. Calibration included bias subtraction, CCD linearity correction, dark subtraction, and flat-field division. Differential photometry was performed using the AIJ Multi-Aperture module. A superset of 15 comparison stars were selected, ensuring that

TABLE 5
Summary of Qatar-1b Photometric Observations

Telescope	UT Date	Filter	# Data	ExpT ²	RMS ³	Scale ⁴
MORC ¹	2011-06-30	Open	109	100	1.2	1.49
MORC	2011-07-10	Open	120	100	1.3	1.47
MORC	2011-08-16	Open	101	100	1.4	1.49
MORC	2011-08-23	Open	116	100	1.1	1.30
MORC	2011-09-22	Open	86	100	1.1	1.42
MORC	2011-10-09	Open	83	100	1.1	1.22
MORC	2011-12-02	Open	92	100	1.3	1.25
MORC	2012-06-19	CBB	115	100	1.3	1.38
MORC	2012-06-29	CBB	163	100	1.3	1.31
MORC	2012-08-02	CBB	138	100	1.6	1.37
MORC	2012-08-12	CBB	110	100	1.5	1.53
MORC	2012-08-22	CBB	145	100	1.4	1.40
MORC	2012-10-25	CBB	97	100	1.4	1.43
MORC	2013-07-16	CBB	168	100	1.2	1.18
MORC	2014-07-16	CBB	175	100	1.5	1.34
MORC	2014-07-23	CBB	164	100	1.6	1.32
MORC	2014-08-19	CBB	139	100	1.7	1.25
MORC	2014-09-25	CBB	162	100	1.6	1.44

¹ MORC=U. of Louisville Moore Obs. 0.6 m RCOS telescope

² Exposure time in seconds

³ RMS in units of 10^{-3}

⁴ Error scaling factor as determined by multi-EXOFAST

each one had brightness similar to Qatar-1 and no nearby stars that might blend into the aperture. The AIJ Multi-Plot and light curve fitting modules were used to search the superset of comparison stars for a subset that minimized the best fit transit model residuals for each time-series. The final comparison ensembles were different for each time-series due to differing filters and sky transparencies, but each ensemble typically had 6–10 comparison stars. A range of fixed and variable aperture sizes were investigated to find the optimal configuration that minimized transit model residuals for each dataset. The result was a variable aperture radius with a scaling factor of $1.1 \times \text{FWHM}$.

The 18 individual detrended and fitted light curves are shown as black dots in Figure 41. The red lines show the global fit model from section 6.4. The black dots in Figure 42 show the results after phasing (using the global fit T_0 and P from Table 6), combining, and binning all of the Qatar-1b light curves in 5 minute intervals. The light curve model is also binned at 5 minute intervals and shown as a red line. This light curve is not used for analysis, but rather to show the best combined behavior of the transit. The model residuals are shown in the bottom panel and have an RMS of 255 ppm over the region where many light curves have been combined (i.e. from -1.5 to 2.5 hrs). Each light curve is shifted on the y-axis for clarity.

6.4 Global Fit

Multi-EXOFAST (see §4.3) was used to perform a global fit to all 18 Qatar-1b light curves. As discussed in section §2.9, seven detrend datasets are included with each light curve to simultaneously detrend the light curves as part of the global fit. The detrend datasets are airmass, time, sky background, FWHM of the average PSF in each image, total comparison star counts, and target x-centroid and y-centroid positions on the detector. The global fit also included TRES RV data from A11 and HARPS-N RV and RM data and spectroscopic priors of $T_{\text{eff}} = 4910 \pm 100$ K, $[\text{Fe}/\text{H}] = 0.2 \pm 0.1$, and $v \sin i_{\star} = 1700 \pm 300$ m s⁻¹ from C13. A spectroscopic prior was not imposed on $\log g_{\star}$, since the value derived exclusively from the light curves should be more accurate than the

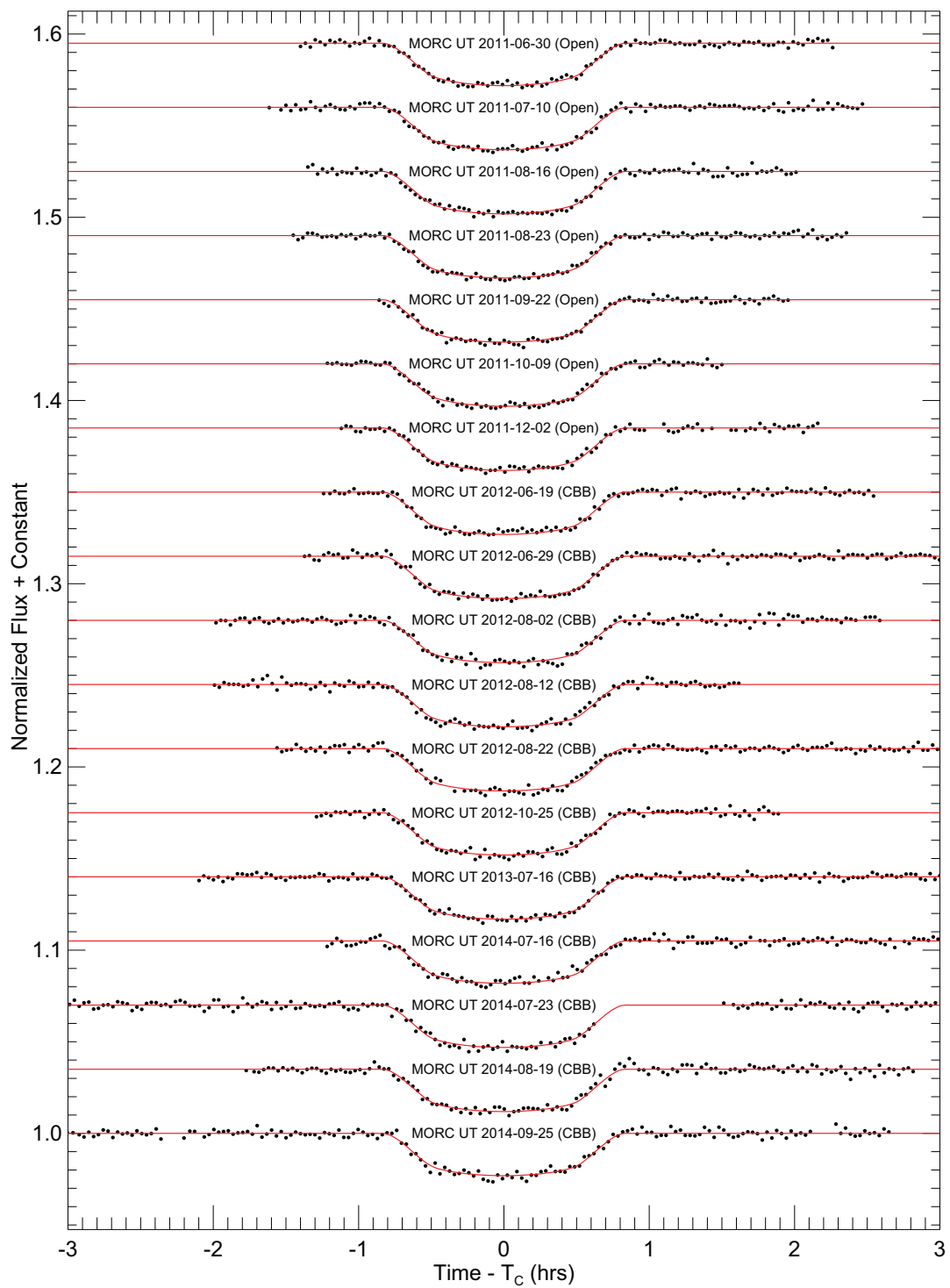


Figure 41. All 18 Qatar-1b light curves. Each light curve is detrended and fitted as discussed in §6.4. The exposure time for each data point is 100 s. The black points are the normalized and detrended differential photometric measurements, while the red lines show the global transit model. Each light curve is shifted on the y-axis for clarity.

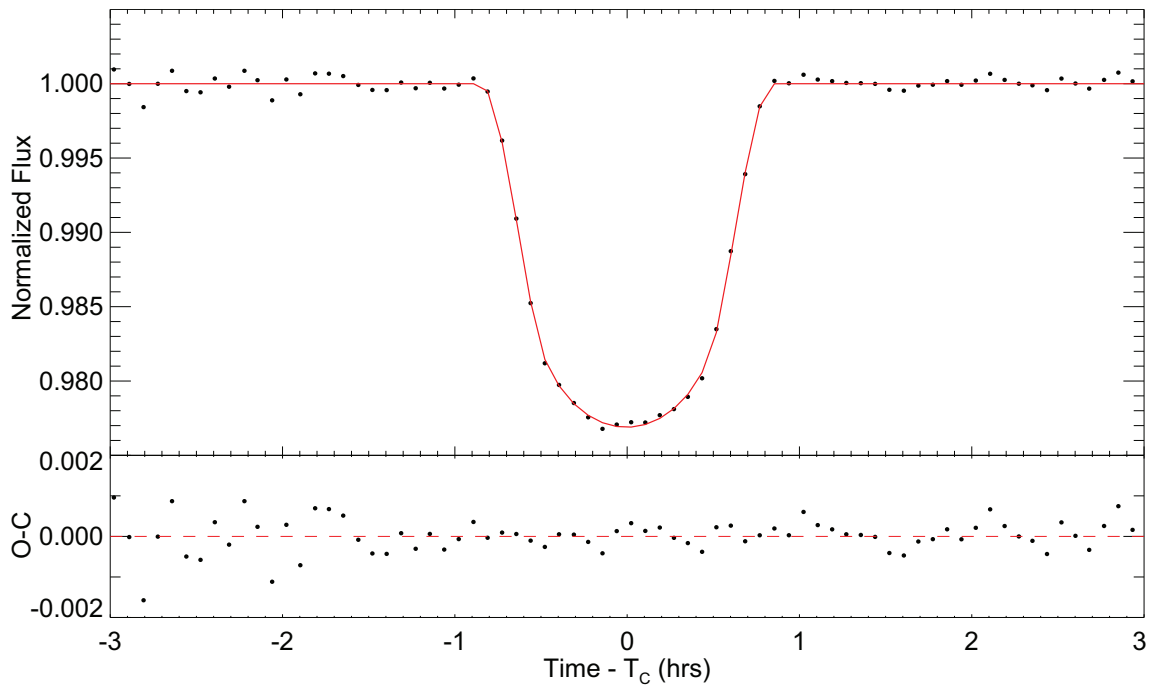


Figure 42. All 18 Qatar-1b detrended light curves combined and binned in 5 min intervals (black dots). The light curves are combined by phasing the data using the global T_0 and P from Table 6. The light curve model is also binned at 5 minute intervals and shown as a red line. This light curve is not used for analysis, but rather to show the best combined behavior of the transit. The model residuals are shown in the bottom panel. In the region where many transits are combined (i.e. from -1.5 to 2.5 hrs), the RMS of the 5 minute binned model residuals is 255 ppm.

spectroscopic value (e.g. Mortier et al. 2013, 2014). Based on an initial best fit, multi-EXOFAST scales the RV and photometric errors to target a reduced chi-squared of $\chi_{red}^2 = 1.0$ for the global fit. As a result, the C13 RV errors were scaled by 1.93 and the A11 RV errors were scaled by 1.59. The photometric scaling factors are listed in Table 5 and range from 1.18 to 1.53. The orbital eccentricity was fixed to zero since secondary eclipse and RV observations are consistent with a circular orbit as discussed in §6.1. The phased RVs are shown in Figure 43 and a close-up of the in-transit RM data is shown in Figure 44. The HARPS-N RVs and RMs from C13 are shown as black dots and green squares, respectively. The TRES RVs from A11 are shown as blue triangles. The RM and RV models from the global fit are shown as red lines.

The Demarque et al. (2004) stellar models were used to estimate M_* and R_* from T_{eff} , $\log g_*$, and $[\text{Fe}/\text{H}]$ at each MCMC step. Separate TTV parameters were fit for each light curve, but common R_p/R_* , a/R_* , and i parameters were fit globally to all light curves. Common sets of quadratic limb darkening parameters, $u1_\lambda$ and $u2_\lambda$, were determined for each filter band from the models of Claret & Bloemen (2011) using T_{eff} , $\log g_*$, and $[\text{Fe}/\text{H}]$ at each MCMC step. The publicly available Claret & Bloemen (2011) limb darkening tables that are included in multi-EXOFAST do not contain coefficients for the CBB or Open (i.e. the U16M CCD QE curve) bands. At my request, A. Claret computed them from the Claret & Bloemen (2011) models. The nominal CBB and Open band coefficient values for a star with spectroscopic parameters like Qatar-1 turn out to be within 0.02 of the coefficients for the *R* and *Kepler* bands, respectively, which are already included in multi-EXOFAST. The difference in the coefficients is negligible for our ground-based data, so I used the *R* and *Kepler* band coefficients for the global fit.

6.5 System Parameter Results

In addition to the original Qatar-1b system analysis by A11, multi-light curve analyses have been performed by C13, E13, DM15, and GM15. The follow-up analyses use various tools to fit the transit data and determine parameter errors, and they use

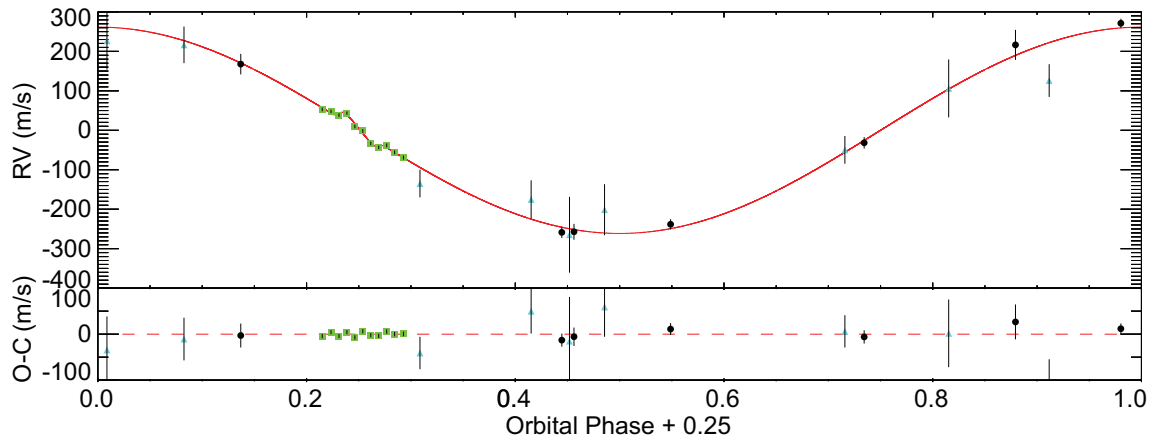


Figure 43. Qatar-1b phased RVs and the combined RV plus RM model. The HARPS-N RVs and RMs from C13 are shown as black dots and green squares, respectively. The TRES RVs from A11 are shown as blue triangles. The red line shows the best fit RV plus RM model from the global fit. The bottom panel shows the model residuals.

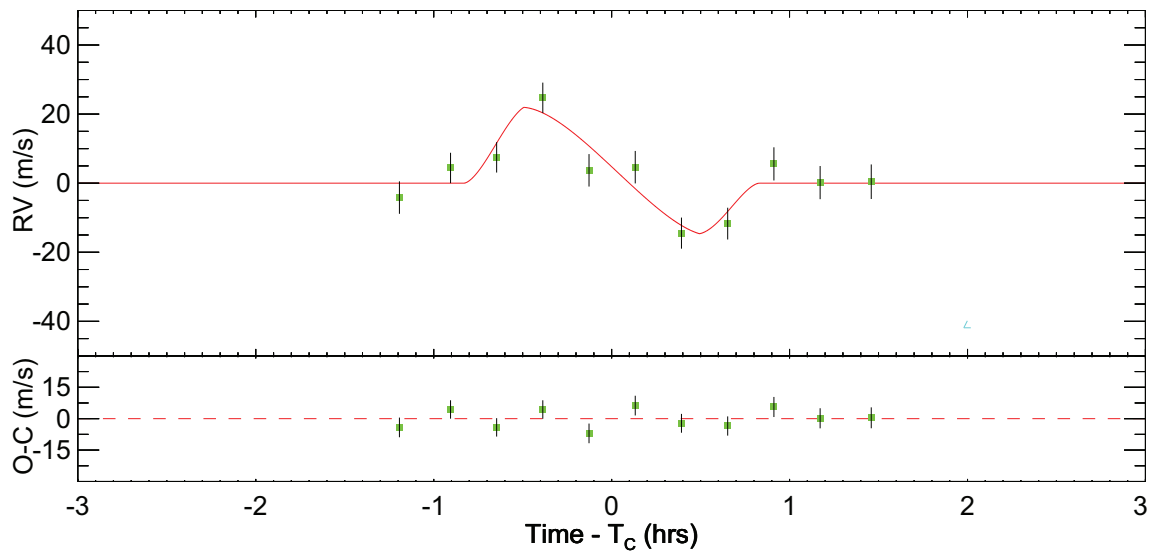


Figure 44. Qatar-1b RM data and model. The HARPS-N RMs from C13 are shown as green squares. The red line shows the best fit RM model from the global fit. The RM data have had the best fit RV model subtracted to remove the orbital velocity component. The bottom panel shows the model residuals.

differing methods to constrain M_* and R_* , but none self-consistently perform a global system analysis based on the RV data, spectroscopy, light curves, and stellar models.

The system parameter values and uncertainties from a self-consistent global fit to two RV datasets, 18 MORC light curves, spectroscopic T_{eff} , [Fe/H], and $v \sin i_*$, the Demarque et al. (2004) stellar models, and the Claret & Bloemen (2011) stellar limb darkening models are shown in Table 6, and a comparison to values from the literature is shown in Table 7. Since E13 only reported values determined exclusively from the transit model fit, physical parameter values are not listed in column E13 of the table.

The stellar parameters, M_* , R_* , $\log g_*$, and ρ_* from this work agree with values from all five literature sources to well within 1σ . C13 revised the RV semi-amplitude upward based on new HARPS-N velocities, which resulted in an increase in planet mass. Since I include the new RVs in this global fit, my planetary parameters are best compared to the literature values starting with C13. They all agree to within 1σ and are almost identical to the DM15 results, except my T_{eq} is higher by about 1σ . The orbital and transit parameters agree within 1σ , except R_p/R_* from C13 and E13 differ from all others by more than 3σ and i from E13 is high by 2σ .

In summary, the parameters from this work agree well with the literature values, except for the few outliers mentioned in the previous paragraph.

TABLE 6

Median Values and 68% Confidence Intervals for the Physical and Orbital Parameters of the Qatar-1b System from the Global Fit Described in §6.4.

Parameter	Units	Value
Stellar Parameters:		
M_*	Mass (M_\odot)	$0.838^{+0.043}_{-0.041}$
R_*	Radius (R_\odot)	0.803 ± 0.016
L_*	Luminosity (L_\odot)	$0.365^{+0.040}_{-0.034}$
ρ_*	Density (cgs)	$2.286^{+0.074}_{-0.070}$
$\log g_*$	Surface gravity (cgs)	$4.552^{+0.012}_{-0.011}$
T_{eff}	Effective temperature (K)	5013^{+93}_{-88}
[Fe/H]	Metallicity	$0.171^{+0.097}_{-0.094}$
$v \sin I_*$	Rotational velocity (m/s)	1760 ± 210
λ	Spin-orbit alignment (degrees)	$-7.5^{+7.5}_{-7.6}$
Planetary Parameters:		
a	Semi-major axis (AU)	$0.02332^{+0.00040}_{-0.00038}$
M_P	Mass (M_J)	$1.294^{+0.052}_{-0.049}$
R_P	Radius (R_J)	$1.143^{+0.026}_{-0.025}$
ρ_P	Density (cgs)	$1.076^{+0.057}_{-0.053}$
$\log g_P$	Surface gravity	3.390 ± 0.015
T_{eq}	Equilibrium temperature (K)	1418^{+28}_{-27}
Θ	Safronov number	0.0629 ± 0.0019
$\langle F \rangle$	Incident flux ($10^9 \text{ erg s}^{-1} \text{ cm}^{-2}$)	$0.918^{+0.075}_{-0.069}$
Primary Transit Parameters:		
T_0	Linear ephemeris from transits (BJD_{TDB})	$2456234.103218 \pm 6.0708415 \times 10^{-5}$
P	Linear eph. period from transits (days) . .	$1.4200242 \pm 2.1728848 \times 10^{-7}$
R_P/R_*	Radius of the planet in stellar radii	$0.14629^{+0.00063}_{-0.00064}$
a/R_*	Semi-major axis in stellar radii	$6.247^{+0.067}_{-0.065}$
i	Inclination (degrees)	$84.08^{+0.16}_{-0.15}$
b	Impact parameter	$0.645^{+0.010}_{-0.011}$
δ	Transit depth	0.02140 ± 0.00019
T_{FWHM}	FWHM duration (days)	0.05498 ± 0.00020
τ	Ingress/egress duration (days)	$0.01423^{+0.00039}_{-0.00038}$
T_{14}	Total duration (days)	0.06921 ± 0.00033
P_T	A priori non-grazing transit probability .	$0.1367^{+0.0013}_{-0.0014}$
$P_{T,G}$	A priori transit probability	0.1835 ± 0.0020
Secondary Eclipse Parameter:		
T_S	Time of eclipse (BJD_{TDB})	2456233.3931 ± 0.0021
RV Parameters:		
K	RV semi-amplitude (m/s)	261.6 ± 5.5
e	RV eccentricity	0.0 (FIXED)
K_{RM}	RM amplitude (m/s)	38.5 ± 4.6
$M_P \sin i$	Minimum mass (M_J)	$1.287^{+0.052}_{-0.048}$
M_P/M_*	Mass ratio	0.001474 ± 0.000039
γ_{HARPS}	m/s	$-50.5^{+6.0}_{-6.1}$
$\gamma_{\text{HARPS}_{\text{rm}}}$	m/s	-59.6 ± 2.0
γ_{TRES}	m/s	118 ± 16

TABLE 7
Comparison of Qatar-1b Selected Physical System Parameters to Values from the Literature

Parameter	This Work	DM15	GM15	C13	E13	A11
Stellar Parameters:						
M_*	0.838 ± 0.043	0.818 ± 0.047	0.803 ± 0.072	0.850 ± 0.030	—	0.850 ± 0.030
R_*	0.803 ± 0.016	0.796 ± 0.016	0.782 ± 0.025	0.800 ± 0.050	—	0.823 ± 0.025
$\log g_*$	4.552 ± 0.012	4.549 ± 0.011	4.556 ± 0.020	4.550 ± 0.100	—	4.536 ± 0.024
ρ_*	2.286 ± 0.074	2.282 ± 0.065	2.365 ± 0.079	2.281 ± 0.113	—	2.140 ± 0.169
Planetary Parameters:						
M_P	1.294 ± 0.052	1.293 ± 0.052	1.275 ± 0.079	1.330 ± 0.050	—	1.090 ± 0.084
R_P	1.143 ± 0.026	1.142 ± 0.026	1.136 ± 0.037	1.180 ± 0.090	—	1.164 ± 0.045
$\log g_P$	3.390 ± 0.015	3.390 ± 0.012	3.409 ± 0.012	3.372 ± 0.024	—	3.265 ± 0.045
ρ_P	1.076 ± 0.057	1.075 ± 0.048	1.154 ± 0.133	1.061 ± 0.265	—	0.915 ± 0.130
T_{eq}	1418 ± 28	1388 ± 29	—	1389 ± 39	—	1399 ± 42
Orbital Parameters:						
P	$1.4200242(2)$	$1.4200259(28)$	$1.4200241(2)$	$1.4200250(7)$	$1.4200246(4)$	$1.4200330(160)$
a	0.02332 ± 0.00040	0.02313 ± 0.00044	0.02298 ± 0.00069	0.02343 ± 0.00120	—	0.02343 ± 0.00026
Transit Parameters:						
R_P/R_*	0.1463 ± 0.0006	0.1475 ± 0.0009	0.1459 ± 0.0008	0.1513 ± 0.0008	0.1435 ± 0.0008	0.1455 ± 0.0016
a/R_*	6.25 ± 0.07	6.25 ± 0.08	6.32 ± 0.07	6.25 ± 0.10	6.42 ± 0.10	—
i	84.08 ± 0.16	84.03 ± 0.16	84.26 ± 0.17	83.82 ± 0.25	84.52 ± 0.24	83.47 ± 0.40

Notes: Parameter variable names and units are the same as in Table 6, a value enclosed in parentheses is the uncertainty in the same number of last digits, DM15=Mislis et al. (2015), GM15=Maciejewski et al. (2015), C13=Covino et al. (2013), E13= von Essen, Schröter, Agol, & Schmitt (2013), A11=Alsubai et al. (2011)

6.6 TTV Results

The global system model includes a TTV parameter for each of the 18 light curves, allowing the transit center time at each epoch to differ from the linear ephemeris. The resulting TTV values are listed in Table 8 and a linear plot of TTV vs. epoch is shown in the top panel of Figure 45. The TTVs have a maximum absolute value of 47 s, RMS= 23.32 s, and $\chi_{red}^2 = 1.08$, with respect to the linear ephemeris. The mean of the timing uncertainty is 22 s. The top panel of Figure 46 shows the Lomb-Scargle periodogram of the MORC TTV data. The down-pointing arrows labeled 133 and 267 (epochs) mark the ~ 190 and ~ 380 d periods investigated by E13. I find no evidence for those or any other convincing periodic signals in the MORC TTV data.

GM15 reanalyzed light curves from E13 and C13 and combined the results with 18 new Qatar-1b transits. I re-phase the GM15 transit center times based on the refined ephemeris from this work (which is nearly identical to the GM15 ephemeris; see Table 7) and plot the resulting TTVs, along with the TTVs from this work, in the bottom panel of Figure 45. Clearly the observation and analysis methods described in Chapters 2, 3, and 4 of this work are producing very competitive TTV results. With respect to the linear ephemeris model, $\chi_{red}^2 = 0.82$ for the combined data. It appears that the TTV uncertainties from GM15 are slightly overestimated, and that the linear model is a good representation of the combined dataset, unless the uncertainties from this work and GM15 are significantly overestimated. The bottom panel of Figure 46 shows the combined data Lomb-Scargle periodogram. The significance of the strongest peak is even less than in the periodogram of our data alone. I find no support for periodic TTVs with semi-amplitude greater than ~ 25 sec in the Qatar-1b system.

6.7 Conclusions

I present the results of a self-consistent global fit to 18 MORC light curves that have been homogeneously reduced starting from the individual images, two RV datasets,

TABLE 8

Qatar-1b Transit Times

T_C (BJD _{TDB})	Epoch	TTV (s)	σ_{TTV} (s)	TTV/ σ_{TTV}
2455742.774748	-346	-7.41	19	-0.38
2455752.714992	-339	-0.98	21	-0.05
2455789.635401	-313	-20.08	22	-0.88
2455796.735833	-308	6.78	18	0.36
2455826.556175	-287	-7.64	19	-0.39
2455843.596639	-275	7.33	19	0.37
2455897.557680	-237	17.71	21	0.83
2456097.780697	-96	-16.82	20	-0.83
2456107.721518	-89	39.46	18	2.09
2456141.801755	-65	9.69	25	0.38
2456151.741312	-58	-43.24	24	-1.74
2456161.681666	-51	-27.31	23	-1.17
2456225.583358	-6	24.67	23	1.07
2456489.707616	180	3.14	17	0.18
2456854.653255	437	-47.71	27	-1.70
2456861.754168	442	20.71	28	0.74
2456888.734234	461	-13.37	26	-0.51
2456925.655231	487	18.34	22	0.81
Standard Deviation		23.32	—	1.00
Mean		—	22	—

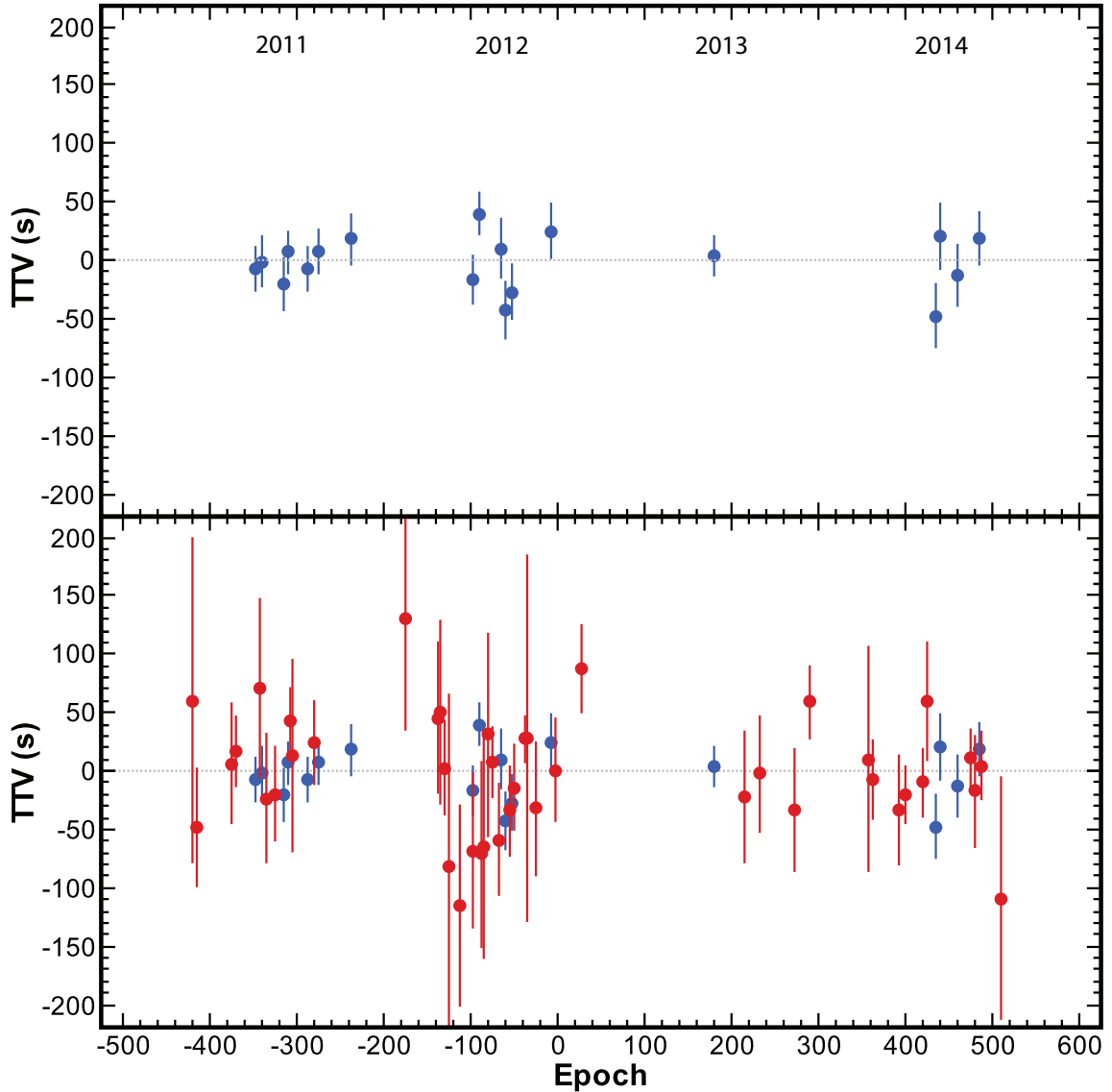


Figure 45. Qatar-1b TTVs vs. transit epoch. The epoch is calculated from the global fit ephemeris in Table 2. TTV is defined as the observed T_C minus T_C calculated from the linear ephemeris (i.e. $O-C$). MORC data are displayed with blue dots. GM15 derived data are displayed with red dots. The numbers across the top of the top panel indicate the approximate calendar year. *Top Panel:* MORC TTVs alone. *Bottom Panel:* MORC plus GM15 derived TTVs.

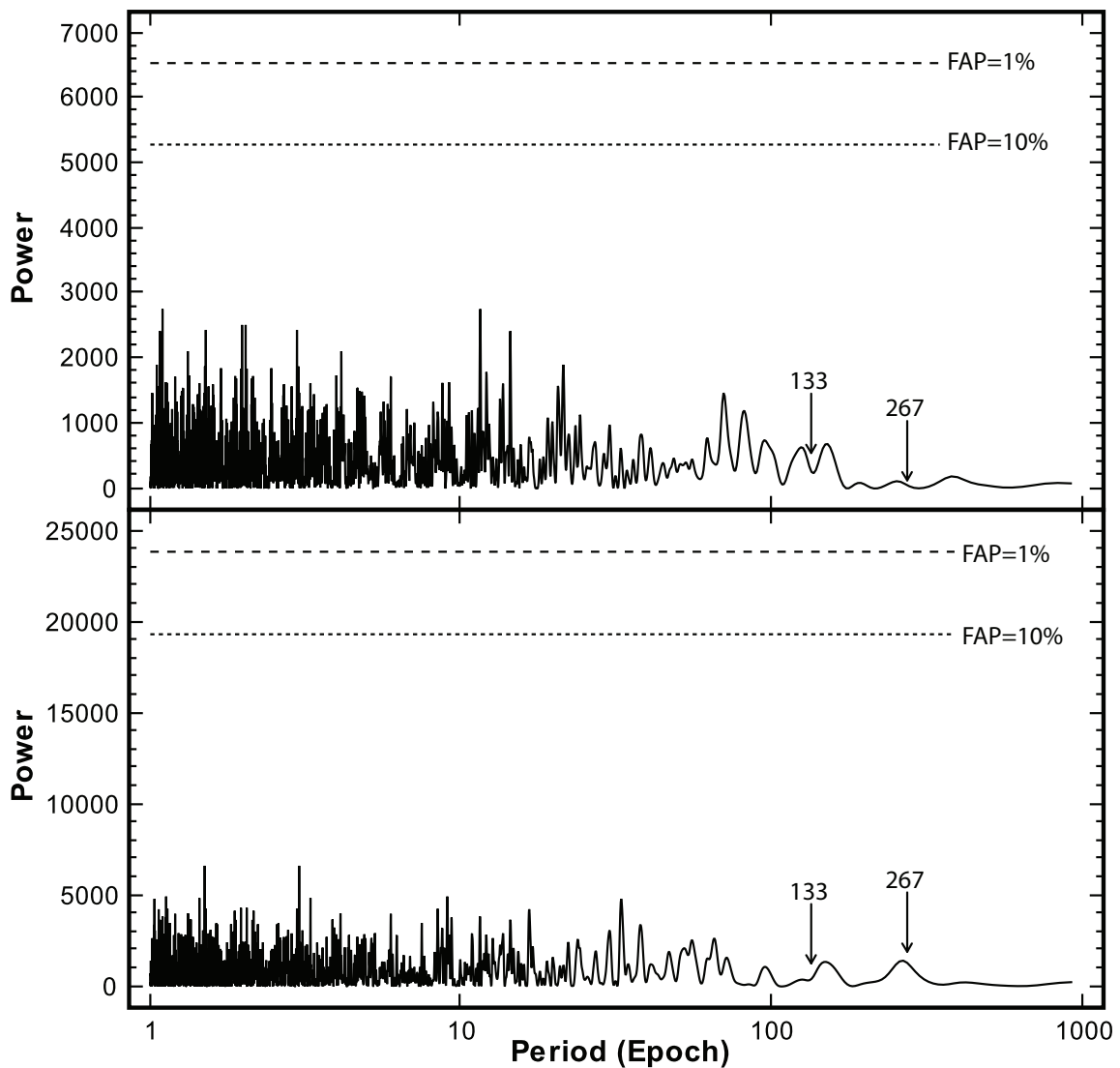


Figure 46. Lomb-Scargle periodograms for the Qatar-1b TTVs. Analytical FAP levels of 10% and 1% are indicated by the short-dashed and long-dashed lines, respectively. The down-pointing arrows labeled 133 and 267 epochs mark the ~ 190 and ~ 380 d periods investigated by E13. *Top Panel:* Periodogram of MORC TTVs alone. *Bottom Panel:* Periodogram of MORC plus GM15 derived TTVs. I find no evidence for convincing periodic signals in either periodogram.

spectroscopic T_{eff} , $[\text{Fe}/\text{H}]$, and $v \sin i_*$, the Demarque et al. (2004) stellar models, and the Claret & Bloemen (2011) stellar limb darkening models. Multi-EXOFAST implements input data uncertainty scaling and MCMC to robustly determine system parameter uncertainties. The system parameters derived in this work are consistent with values from the literature at a level of $\sim 1\sigma$, except for the initial planetary mass underestimate by A11. The values fall near the mean of the literature values, except T_{eq} from this work is at the upper end of 1σ relative to the literature values.

Unless multi-EXOFAST is overestimating the parameter errors (which is unlikely given the error scaling values listed in Table 5), the transit center times are well modeled by a linear ephemeris with $T_0 = 2456234.103218 \pm 6.0708415 \times 10^{-5}$ and $P = 1.4200242 \pm 2.1728848 \times 10^{-7}$, which has $\chi_{\text{red}}^2 = 1.08$. A Lomb-Scargle periodogram shows no periodic signals in the TTV data that have an analytical false alarm probability less than 100%. Based on the reduced chi-squared value for the linear ephemeris model and the lack of significant signals in the periodogram, I find no convincing evidence for periodic TTVs with a semi-amplitude of more than ~ 25 s in the MORC data. This interpretation is consistent with the conclusion by MG15 and with the Steffen et al. (2012) study that found no evidence of TTVs in the orbits of Kepler hot Jupiter planets with $1 \leq P \leq 5$ days. On the other hand, the data are sparsely sampled and it may be possible that short period, low level, or non-sinusoidal TTV signals are lurking in the data.

CHAPTER 7

HD 189733Ab ATMOSPHERIC CHARACTERIZATION

7.1 Introduction

There are a limited but growing number of detections of exoplanet atmospheres reported in the literature. Transmission spectroscopy (see §1.5.3) of transiting exoplanets is a key method used to measure atomic and molecular species in atmospheres of exoplanets, given the technology available today. The best targets for transmission spectroscopy are exoplanets with bright host stars ($V \lesssim 10$) and with atmospheres that have a large scale height (i.e. the altitude for which the atmospheric pressure decreases by a factor of e). Jensen et al. (2011) provide an excellent history of atmospheric detections, so I will include only a short summary here.

Charbonneau et al. (2002) were the first to detect the atmosphere of an exoplanet. They detected Na D in the atmosphere of HD 209458b using optical spectroscopy from the Space Telescope Imaging Spectrograph (STIS) instrument on-board the Hubble Space Telescope (HST). Shortly thereafter, Vidal-Madjar et al. (2003, 2004) discovered hydrogen, carbon, and oxygen in the extended upper atmosphere of HD 209458b using STIS, and Lecavelier Des Etangs et al. (2010) detected hydrogen in the atmosphere of HD 189733Ab using spectroscopy from the Advanced Camera for Surveys (ACS) on-board the HST. Redfield et al. (2008) made the first ground-based detection of an exoplanetary atmosphere using the High-Resolution Spectrograph (HRS) on the Hobby-Eberly Telescope (HET), detecting Na D in the atmosphere of HD 189733Ab. Snellen et al. (2008) also confirmed the Charbonneau et al. (2002) detection of Na D in HD 209458b from the ground using the High Dispersion Spectrograph (HDS) on the

Subaru telescope. In the near-IR, many molecular species have been detected in the atmospheres of HD 209458b and HD 189733Ab, but many of these are in dispute (see Jensen et al. 2011 and references therein for more details).

Clearly, the study of exoplanet atmospheres has been focused on HD 209458b and HD 189733Ab. Both of these systems are nearby and therefore the apparent brightness of their host stars provides the highest signal-to-noise levels for transmission spectroscopy. More recently, detections in systems with less favorable conditions for transmission spectroscopy have appeared in the literature. Wood et al. (2011) reported sodium in the atmosphere of WASP-17b using the GIRAFFE spectrograph on the VLT, Colón et al. (2010) reported the detection of potassium in HD 80606b using photometry in a tunable narrow-band filter and Sing et al. (2011) reported potassium in XO-2b using the same tunable filter. Fossati et al. (2010) reported the detection of metals in the extended atmosphere of WASP-12b using the Cosmic Origins Spectrograph on the HST. Additional observations of the above systems are ongoing and will hopefully settle the disputed detections. However, next generation observatories may be required to make significant improvements in the confidence of currently claimed detections. The KELT survey (Pepper et al., 2003, 2007) is producing discoveries of new hot Saturn and Jupiter mass planets with host stars bright enough to expand the number of targets available for transmission spectroscopy.

7.2 HD 189733Ab Overview

HD 189733Ab is a gas giant planet orbiting a K dwarf star in 2.2 days. The planet was discovered using the radial velocity method and confirmed to transit its host star, HD 189733A, by Bouchy et al. (2005). Because of its bright host star and relatively high value of R_p/R_* , HD 189733Ab is one of the two best-studied hot Jupiter exoplanets. Bakos et al. (2006) show that HD 189733A is the primary of a double star system. The secondary, HD 189733B, is a mid-M dwarf with a projected separation of 216 AU or $\sim 11''$. Hereafter, the notation HD 189733 refers to the primary star of the system and

HD 189733b refers to the exoplanet orbiting the primary star.

Extensive theoretical work has been presented on the atmosphere of HD 189733b by Seager & Sasselov (2000), Brown (2001), Fortney et al. (2006), Barman (2008), Burrows et al. (2008), Showman et al. (2008) and others. The models predict strong atomic absorption lines at 589 nm from sodium (Na D) and 769 nm from potassium (K I), and several molecular bands due to water, but they can be hidden by broad absorption from clouds or hazes higher up in the atmosphere. In the near-IR, the models predict molecular signatures of water, methane, ammonia and carbon monoxide.

Detailed spectroscopic studies of the system have detected several atomic and molecular components in the atmosphere of HD 189733b. Redfield et al. (2008) first measured sodium in the exoplanet's atmosphere using the High Resolution Spectrograph on the 9.2 m Hobby-Eberly Telescope. They obtained 11 in-transit and 25 out-of-transit spectroscopic observations over the course of about a year. They found that the in-transit spectra showed a Na D absorption feature that was stronger by $0.0672 \pm 0.0207\%$ when compared to the out-of-transit spectra. The additional Na D absorption when the planet and its atmosphere are passing in front of the host star is attributed to sodium in the atmosphere of the planet. Additional components detected in the planet's atmosphere include water (Tinetti et al., 2007), methane (Swain et al., 2008), and hydrogen (Jensen et al., 2012).

In the remaining sections of this chapter, data are presented that I collected using the 0.6m MORC telescope in an attempt to detect the atmosphere of HD 189733b using our small aperture telescope.

7.3 Observing Strategy

7.3.1 Target and Atmospheric Species Selection

HD 189733b has one of the most favorable combinations of host star brightness, planet-to-star radius ratio, and atmospheric scale height (as predicted by theoretical

models) of all known transiting exoplanets, resulting in one of the highest signal-to-noise opportunities for atmospheric detection. Since Na D lines are predicted to be strong in the optical band by many theoretical atmospheric models, and since Redfield et al. (2008) had reported, just prior to the beginning of my observing program, a $\sim 3\sigma$ detection of Na D in the atmosphere of HD 189733b, I set as a primary goal to attempt confirmation of the that measurement.

Redfield et al. (2008) and most other efforts to measure an exoplanet’s atmospheric components make use of space-based or 10 m class ground-based telescopes. Even using the most sophisticated instrumentation available today, the detection of components in an exoplanet’s atmosphere is challenging. Although a few recent measurements from these high-precision instruments report detections with significance $> 3\sigma$, many measurements of exoplanet atmospheres reported in the literature struggle to reach 3σ significance. Since 10 m class telescope apertures collect $200\text{--}300\times$ more flux than our 0.6 m telescope aperture, and since scintillation noise for a 0.6 m telescope is much greater than for a 10 m class telescope (see §2.11), an alternative method of measuring a planet’s effective radius at different wavelengths is required to enable atmospheric work from the MORC telescope.

7.3.2 Na D Measurement Methods and Trade-offs

The high-end echelle spectrographs typically used to detect species in the atmospheres of exoplanets generally have low ($\sim 5\text{--}10\%$) overall throughput efficiency (e.g. HRS at HET, Tull 1998; HDS on Subaru, Noguchi et al. 2002; HIRES at Keck, Vogt et al. 1994). Seeing dependent slit losses combine to make the overall throughput even less. To determine the effective planet-to-star radius ratio for a particular absorption line or continuum region from spectroscopy, the spectrum is integrated over the desired wavelength band (typical ~ 1 nm), effectively filtering out all of the other wavelengths in the spectrum. High-quality narrow-band optical interference filters can perform the same task and can be constructed to provide a throughput of $\gtrsim 70\%$ with relatively sharp

cutoffs. The downsides are that the desired integration bands must be known before the observations take place, and data can be collected in only one band at a time unless additional components are introduced into the optical path. The price of an echelle spectrograph can range from \$100,000 on the low end to millions of dollars on the high end, while a quality custom-built ~ 1 nm FWHM filter can be purchased for \sim \$3000. Given our limited budget and the potential ~ 10 – $20\times$ gain in throughput, it was decided that the narrow-band optical filter approach was the best path for an attempt at an atmospheric detection with a small telescope. To attempt to recover the remaining factor of ~ 10 deficiency in flux, multiple transit observations of HD 189733b were required to reduce the uncertainty in differential transit depth. To overcome the limitation of observing in only one filter at a time with the MORC hardware, two filters were alternated from exposure to exposure between one that covers the Na D doublet and another that covers a region of stellar continuum. Observing a full transit in one filter, and the next available full transit in the other filter, etc., would invalidate any atmospheric detection since transit depths can vary slightly from one epoch to another due to the effects of star spots on the transit depth.

For ground-based observations, time variable spectral features in the Earth's atmosphere contaminate the transmission spectrum being measured. Standard stars must be observed to determine the effect of the telluric contamination, or for very high resolution spectroscopy that is capable of detecting RV variations in the data, cross-correlation with atmospheric models can be used to reduce the telluric (and stellar) contamination. Echelle spectroscopy is generally capable of observing only one star at a time, so if a standard star is observed, the telescope must slew between the target star and a nearby reference star in alternating exposures to obtain the best telluric correction. However, with narrow-band photometry, there are generally multiple reference stars available on the detector in each exposure to facilitate the high-precision removal of atmospheric effects on the photometry. This photometric advantage should partially compensate for the reduced exposure cadence resulting from the requirement to alternate

between narrow-band filters with my approach.

7.3.3 Filter Choices and Design

The Na D lines occur at 5889.9510 \AA and 5895.9242 \AA . The Charbonneau et al. (2002) and Redfield et al. (2008) measurements were reported as integrations over a 12 \AA bandpass. A filter design was selected for this work to provide a FWHM of 10 \AA to approximate the Redfield et al. (2008) bandpass. Figure 47 shows the Na D filter transmittance curve, measured with a 2-pixel resolution of 0.08 \AA , as a red solid line. The peak transmission and bandwidth are near the design specifications of 70% and 10 \AA . The residual transmission of about 5% off-band is likely scattered light in the laboratory instrumentation. The measurement was made through a few mm central region of the $50 \times 50 \text{ mm}$ filter. The Na D and other absorption lines shown on the plot by the narrow blue lines are from the theoretical models of Coelho et al. (2005). HD 189733 has spectroscopic values of $T_{eff} = 5040 \pm 50 \text{ K}$, $\log g = 4.587 \pm 0.015$, and $[\text{Fe}/\text{H}] = -0.03 \pm 0.08$ (Torres et al., 2008). The closest available model parameter values of $T_{eff} = 5000 \text{ K}$, $\log g = 4.5$, and $[\text{Fe}/\text{H}] = 0.0$ were selected. The line identifications are from the Rowland atlas (Moore, Minnaert, & Houtgast, 1966).

For the adjacent continuum measurement, a cost effective (< \$400) off-the-shelf Astrodon Red Continuum (RC) bandpass filter was selected which has a center wavelength near 6450 \AA and a FWHM of 50 \AA . This filter is centered far enough away from the Na D lines to avoid cross-contamination with the doublet, but close enough to give a good continuum reference measurement. Since the RC filter has a width $5\times$ that of the Na D filter, more time can be allocated to the Na D exposures compared to a scenario with both filter widths set to 10 \AA . Figure 48 shows the RC filter transmittance curve as a thick red line. Spectra from the theoretical models of Coelho et al. (2005), using the same parameters as in Figure 47, are shown as thin blue absorption lines. The line identifications are from the Rowland atlas.

Na D Filter Transmittance and HD 189733b Synthetic Spectrum
 Coelho, et al. (2005) for $T_{\text{eff}}=5000$ $\log g=4.5$ $[\text{Fe}/\text{H}]=0.0$

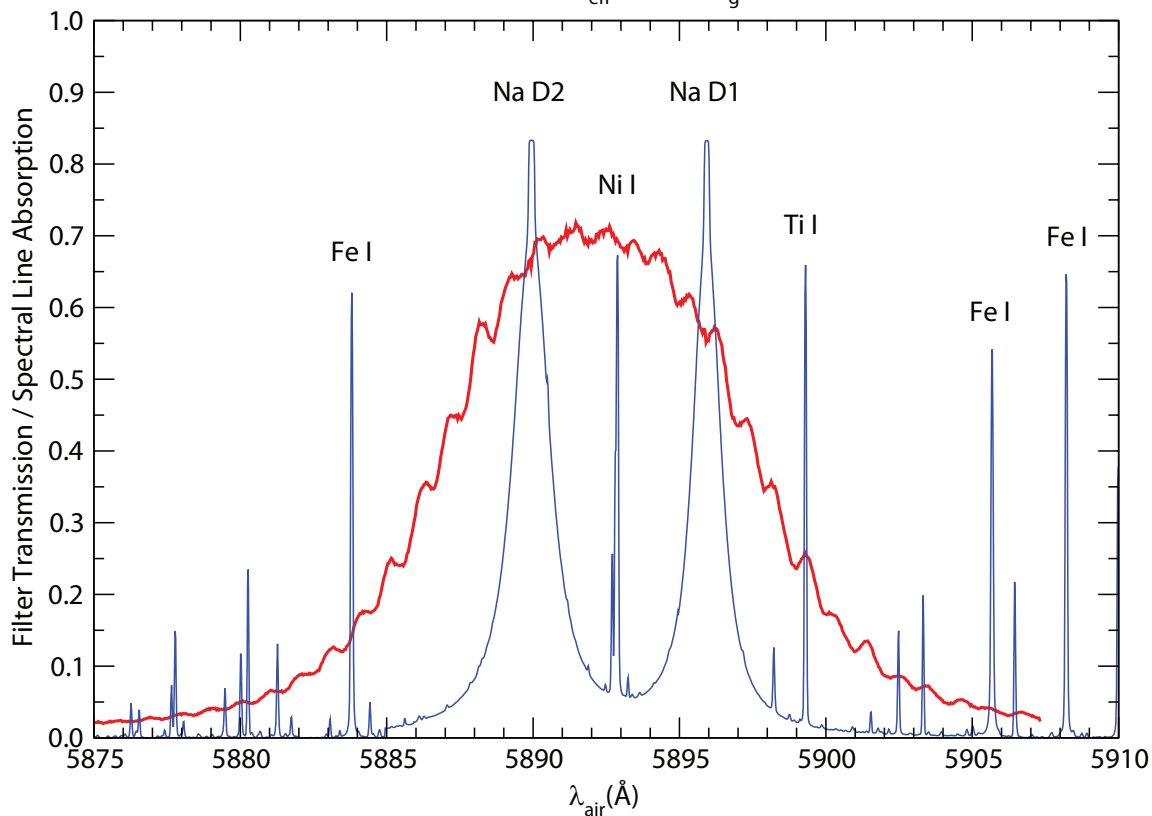


Figure 47. The transmittance curve (thick red line) as measured in the lab for the custom designed Na D filter from Custom Scientific. Transmittance was measured with a 2-pixel resolution of 0.08 Angstrom. The peak transmittance and bandwidth are near the design specifications of 70% and 10 Å. The Na D and other absorption lines shown on the plot by the narrow blue lines are from the theoretical models of Coelho et al. (2005). The selected model parameter values of $T_{\text{eff}} = 5000$ K, $\log g = 4.5$, and $[\text{Fe}/\text{H}] = 0.0$ are representative of HD 189733 (see text). The line identifications are from the Rowland atlas (Moore, Minnaert, & Houtgast, 1966).

RC Filter Transmittance and HD 189733 Synthetic Spectrum
Coelho, et al. (2005) for $T_{\text{eff}}=5000$ $\log_g=4.5$ $[\text{Fe}/\text{H}]=0.0$

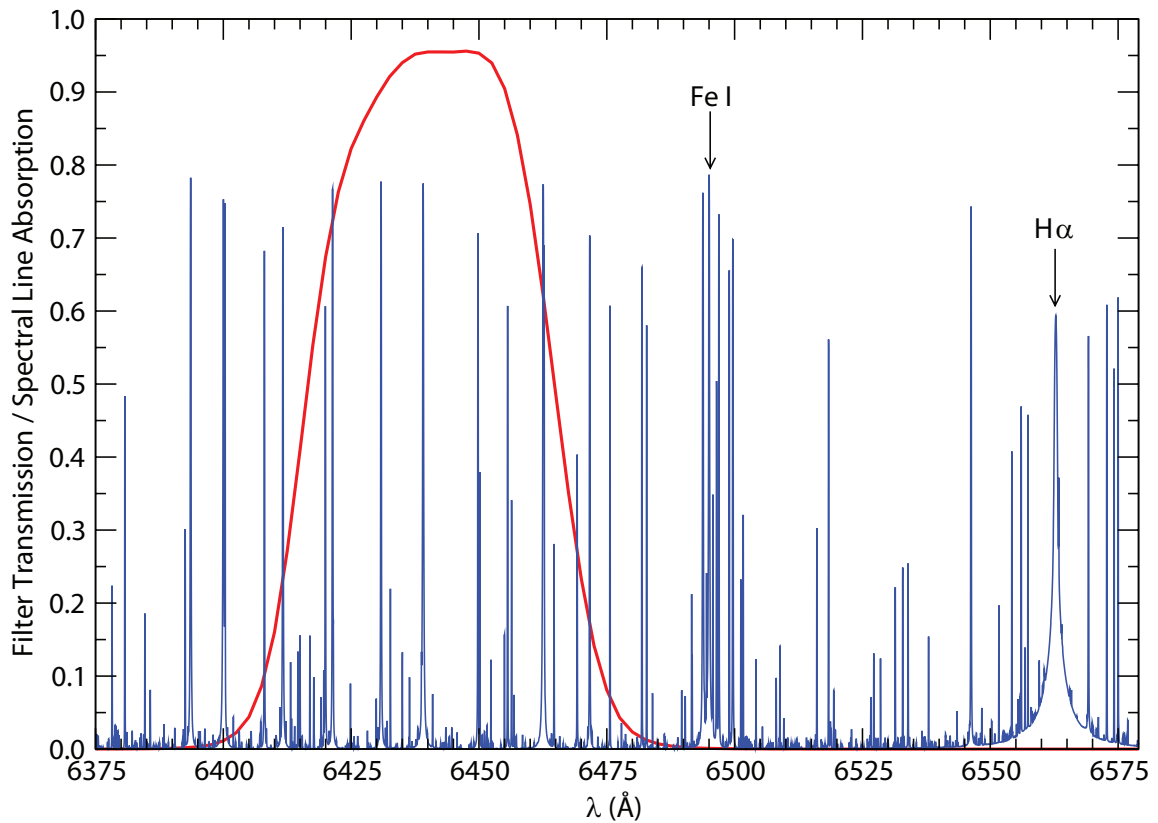


Figure 48. The Red Continuum filter transmittance curve. The RC bandpass filter transmittance curve is shown as a thick red line. The $\text{H}\alpha$ and other absorption lines shown on the plot by the narrow blue lines are from the theoretical models of Coelho et al. (2005) using the same parameters as in Figure 47. The line identifications are from the Rowland atlas (Moore, Minnaert, & Houtgast, 1966).

7.4 Observations

We observed 13 full transits of HD 189733b in alternating Na D and RC filters from UT2011-07-12 to UT2014-09-30. A summary of all HD 189733b observations is shown in Table 9.

As previously discussed for MORC broadband filter observations, the general goal is to extend exposure times as long as possible to maximize the amount of photons collected by limiting time spent reading data from the detector. But, exposure times must be limited to avoid saturating the detector, to avoid poor telescope guiding/tracking (since we guide using the science images), and to ensure good temporal sampling of the light curve for physical modeling of the system. A secondary goal is to approach ~ 1.0 mmag differential photometric precision per exposure which requires $\gtrsim 1 \times 10^6$ net integrated counts in the target star and comparison ensemble apertures with our detector gain setting of 1.5 electrons/ADU (see §2).

On-sky MORC test observations of HD 189733b in the Na D and RC filters were conducted to determine reasonable exposure times. Telescope guiding and temporal sampling is good for my preferred 100 s exposure time, which results in a ~ 2 min cadence including the ~ 20 s detector read-out time. However, the flux in the Na D filter reaching the detector, even from the very bright host star, is relatively low compared to our usual broadband filter observations. HD 189733 produces only $\sim 2.5 \times 10^5$ integrated counts in the Na D filter in a 100 s exposure. Although it was known that telescope guiding was good at a 2 min exposure cadence, it was unknown how long exposure times could be extended while continuing to maintain good guiding from the science images (since tracking errors can only be corrected once per science exposure), so I decided to double the known good exposure time to 200 s initially.

After the first three transit observations in 2011, it was clear that guiding still worked well with 200 s exposures and that temporal sampling was acceptable. However, light curve scatter was not as low as expected, which resulted in worse precision in the light curve depth measurements than expected. Since the precision in the depth difference

TABLE 9
Summary of HD 189733b Photometric Observations

Telescope	UT Date	# Na Data	# RC Data	ExpTime Na (s)	ExpTime RC (s)
MORC	2011-07-12	28	28	200	40
MORC	2011-08-10	40	40	200	40
MORC	2011-08-30	63	64	200	40
MORC	2012-07-01	33	33	240	100
MORC	2012-07-21	22	23	240	100
MORC	2012-08-30	49	49	240	100
MORC	2012-09-19	34	36	240	100
MORC	2012-10-09	36	37	240	100
MORC	2013-06-21	48	48	240	100
MORC	2014-07-12	49	48	240	100
MORC	2014-07-21	48	49	240	100
MORC	2014-08-01	57	56	240	100
MORC	2014-09-30	52	52	240	100

Notes: MORC=University of Louisville Moore Observatory 0.6 m RCOS Telescope

is dependent on both the Na D and RC light curve depth precisions, and since we have $> 5\times$ the flux in the RC filter than the Na D filter, I decided to extend the RC exposure time to 100 s in the second year to minimize the uncertainty in the depth of the RC light curve, while only adding one more minute to the exposure cycle time. At the same time, I decided to push the Na D exposure time to 240 s to get a small gain in depth precision with little loss in temporal sampling. These exposure times improved the depth precision, so I kept the same settings through the end of my observations in 2014.

7.5 Data Reduction

All images were calibrated as discussed in §2 using the AIJ Data Processor module. Calibration included bias subtraction, CCD linearity correction, dark subtraction, and flat-field division. The Multi-Aperture (MA) module of AIJ was used to process the calibrated images to produce differential photometry (see §2.5) and associated photometric error (see §2.11) for the target star relative to the only two reasonably bright comparison stars in the $26' \times 26'$ field of view. The comparison stars, HD 345459 and

HD 345464, are marked C2 and C3, respectively, in Figures 49 and 50. The total of the integrated counts from the two comparison stars is within $\sim 15\%$ of the target star integrated counts in both the Na D and RC filters.

A fixed aperture radius of 19 pixels was selected to ensure that most of the flux from HD 189733A is included in the measurement, and to ensure that virtually all of the flux from the faint $11''$ companion is excluded, except in images with very poor seeing. Figures 51 and 52 show high-contrast images of the field near the target star in the Na D and RC filters, respectively. The aperture size and placement relative to HD 189733A is shown by the green circle in both figures. The center of each aperture is placed at the corresponding star's centroid location by the AIJ photometer. Since HD 189733B is readily visible $11''$ to the WSW of the primary in the RC image (marked B in Figure 52), it is clear that its flux is virtually excluded from the 19 pixel photometric aperture used for the image sequences in both filters.

The local sky background is subtracted from each pixel within an aperture before calculating the net integrated counts for the target and comparison stars. The local background value is determined from the pixel values in an annulus between a radius of 40 and 100 pixels from the centroid of each star. An iterative process excludes pixels with values more than 2σ from the mean in each iteration, and the mean of the remaining pixels is used as the local sky background value for all pixels in the photometric aperture.

7.6 Global Fit

To determine the transit depths in the Na D and RC filters, I fit global models to each of the two sets of 13 light curves using multi-EXOFAST. As discussed in section §2.9, seven detrend datasets are included with each light curve to simultaneously detrend the light curves as part of the global fit. The detrend datasets are airmass, time, sky background, FWHM of the average PSF in each image, total comparison star counts, and target x-centroid and y-centroid positions on the detector. Multi-EXOFAST requires RV data and spectroscopic priors as input, in addition to the transit light curve data. For both

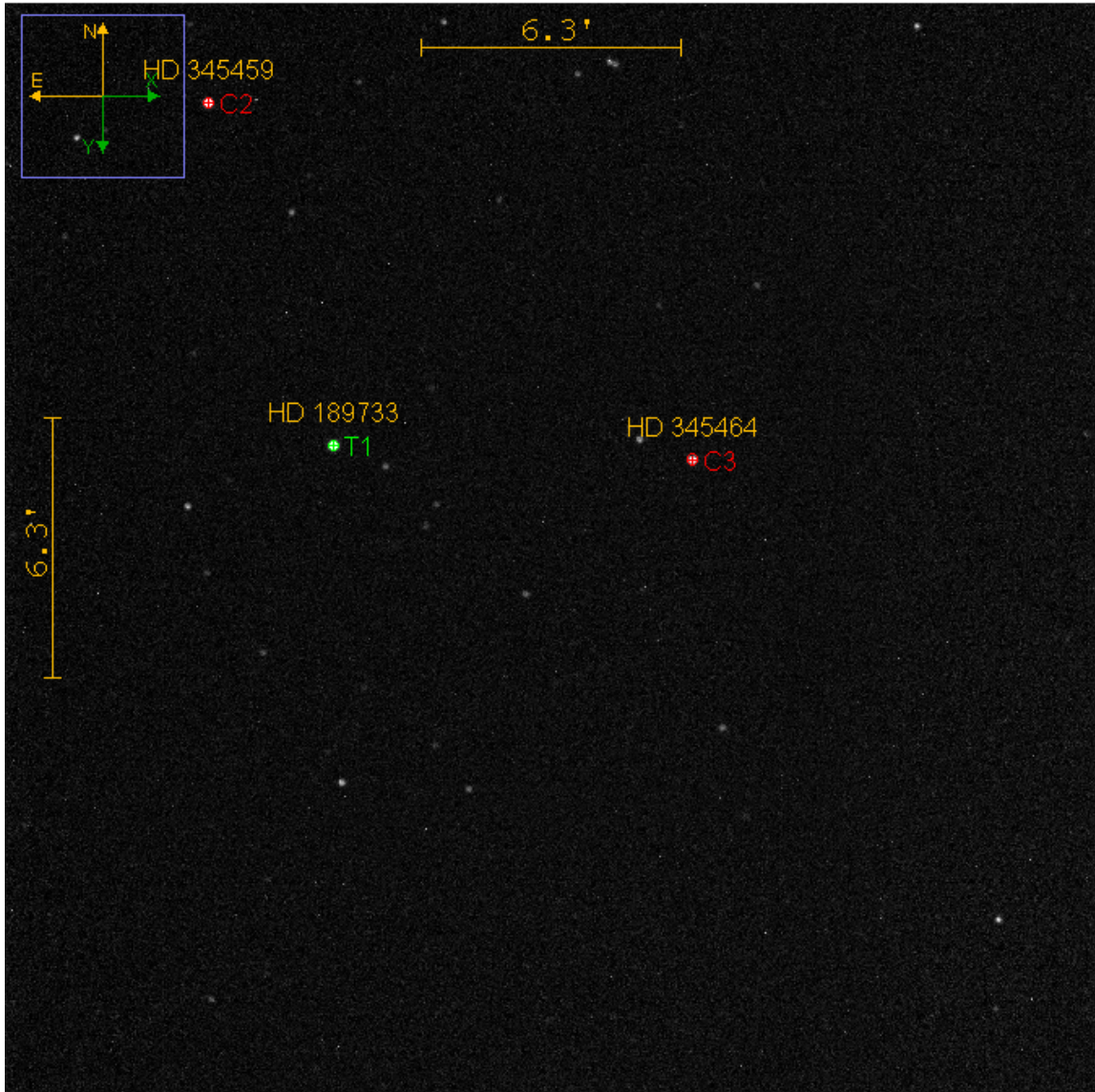


Figure 49. Typical image of the HD 189733 field in the Na D filter. The target star is marked T1 and the two comparison stars are marked C2 and C3.

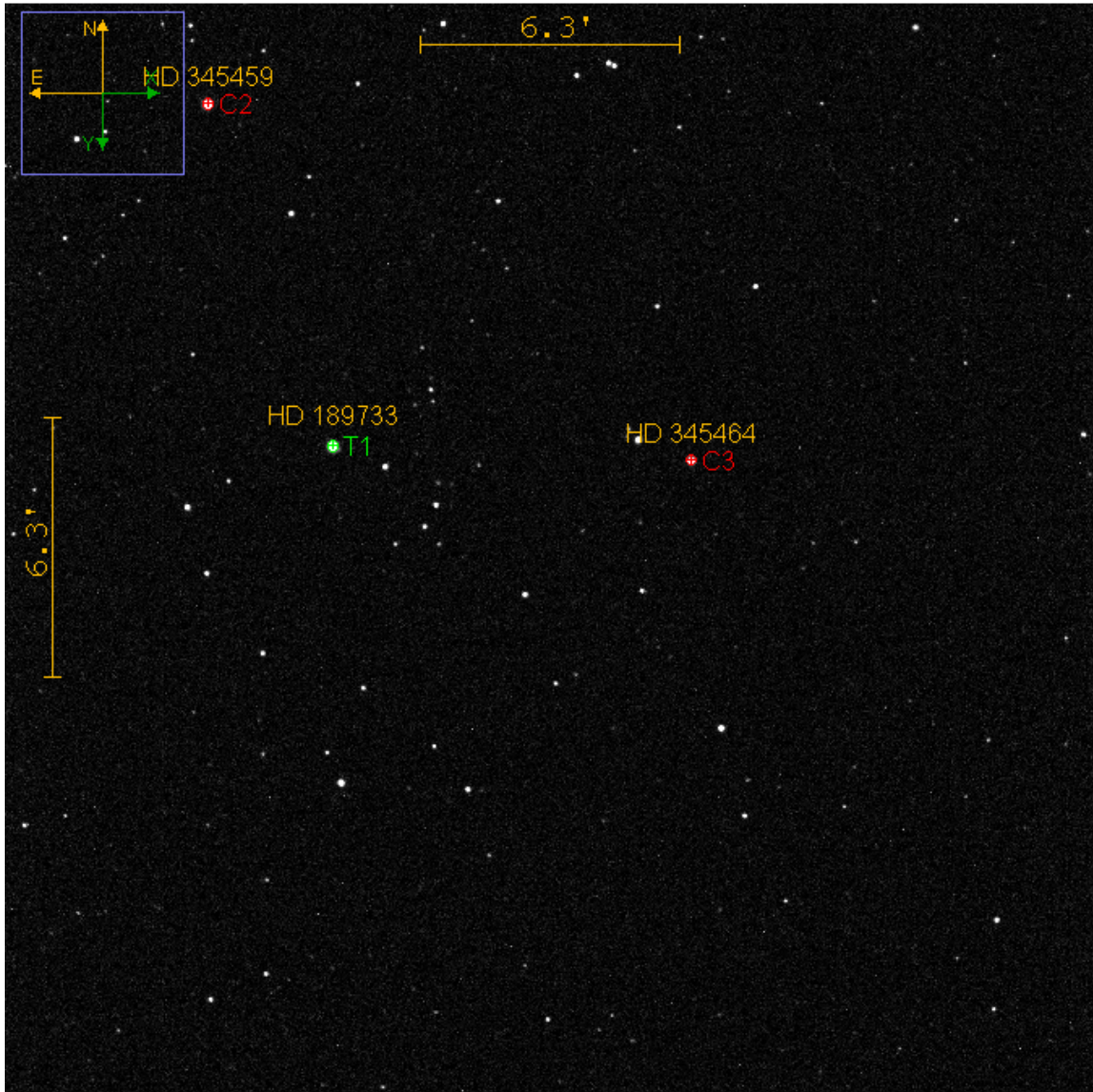


Figure 50. Typical image of the HD 189733 field in the RC filter. The target star is marked T1 and the two comparison stars are marked C2 and C3.



Figure 51. Typical image of the field within $\sim 3'$ of HD 189733 in the Na D filter. The target star is marked T1. The companion star, HD 189733B, is not readily visible in the Na D filter data.

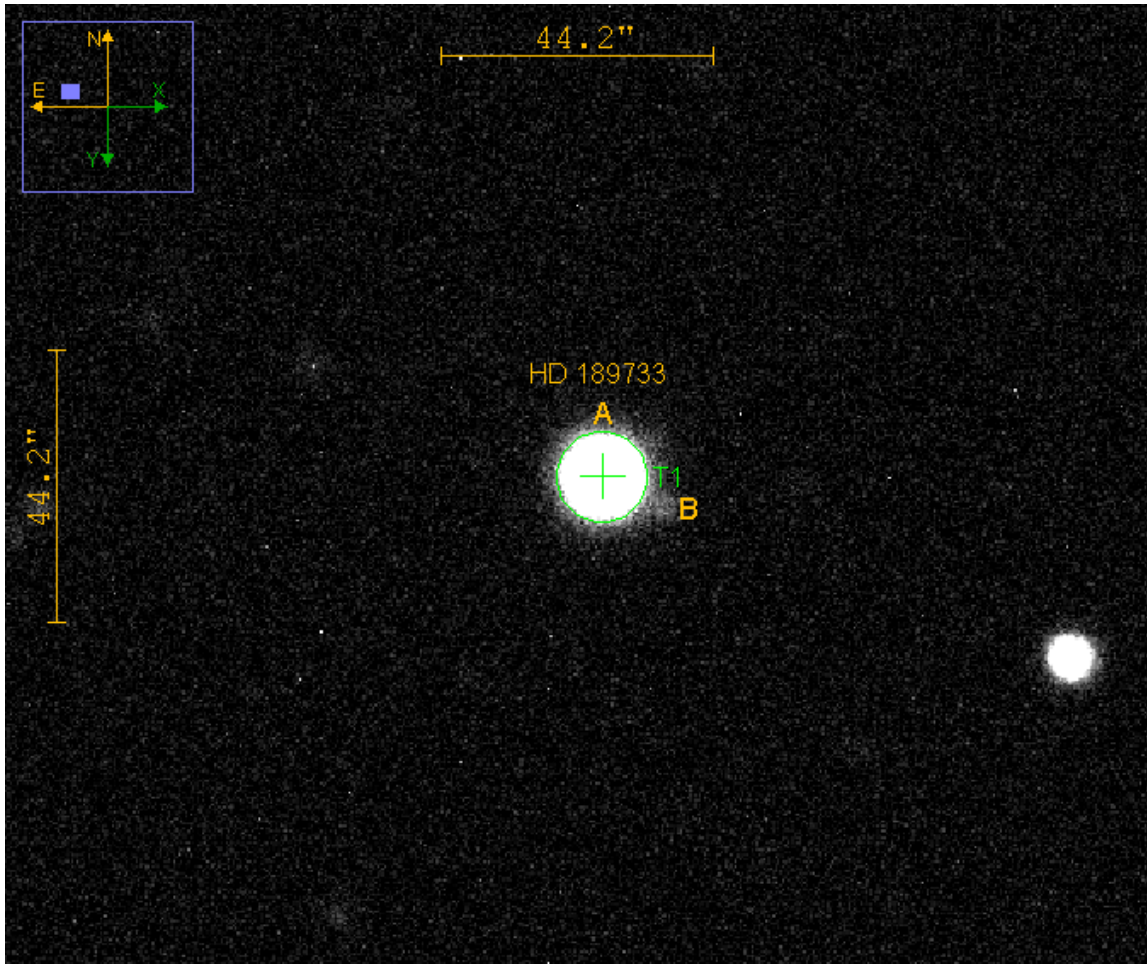


Figure 52. Typical image of the field within $\sim 3'$ of HD 189733 in the RC filter. The target star is marked T1. The primary star, HD 189733A, is marked A and the faint companion star, HD 189733B, is marked B and is clearly visible and resolved in the RC data.

global fits, I used $T_{eff} = 5040 \pm 50$ K and $[Fe/H] = -0.03 \pm 0.08$ from Torres et al. (2008) as spectroscopic priors, $P = 2.21857567 \pm 1.5 \times 10^{-7}$ from Agol et al. (2010) as an orbital period prior, and ELODIE RVs from Bouchy et al. (2005).

The global fits include constraints on the stellar parameters M_* and R_* from the empirical relations of Torres et al. (2010) in order to break the well-known degeneracy between M_* and R_* for single-lined spectroscopic eclipsing systems. To ensure the resulting parameter uncertainties are roughly accurate, multi-EXOFAST scales the RV and photometric errors to target a reduced chi-squared $\chi_{red}^2 = 1.0$ for the global fit.

Kipping (2010) showed that finite integration times may induce morphological distortions to the transit light curve. These distortions, if uncorrected for, may lead to erroneous system parameters. The distortions are significant for *Kepler* long cadence data (30 minute exposures) and are not expected to be critical for my 240 s Na D exposures. Nevertheless, since I am attempting to measure a small difference in transit depth, I used the capability of multi-EXOFAST to interpolate the model fit of the Na D data by a factor of 3 to ensure a result that could be directly compared to the model derived from the shorter RC filter exposures.

Since the same physical system produces all of the light curve data, multi-EXOFAST finds the best fit of each light curve model parameter to all light curves. For each of the Na D and RC filter global fits, a single parameter for each of the light curve parameters R_p/R_* , a/R_* , and i , was fit to all 13 light curves. Furthermore, no transit timing variations were allowed as part of the global fit since observations from the Spitzer Space Telescope by Agol et al. (2010) provide extremely tight constraints on the transit timing of HD 189733b. The timing precision is ~ 3 s and excludes the presence of second planets above 20% of the mass of Mars in low-order mean-motion resonance at 95% confidence. A separate baseline flux parameter is individually fit for each light curve.

The only remaining parameters of the seven parameter light curve model are the quadratic limb darkening coefficients u_1 and u_2 . Multi-EXOFAST groups all light curves observed in the same filter together and applies a common set of quadratic limb darkening

coefficients derived from the models of Claret & Bloemen (2011). Multi-EXOFAST uses tables published as part of Claret & Bloemen (2011) for standard broadband filters. Since our Na D filter is a custom design and the RC filter is not commonly used for exoplanet transit observations, there were no coefficients for those filters supported in multi-EXOFAST . At my request, A. Claret computed the coefficients from the Claret & Bloemen (2011) models for both filters (private communication, A. Claret, 12/2014), and I added support for them in multi-EXOFAST .

The 13 detrended and fitted Na D light curves are shown in Figure 53 with the global Na D light curve model over-plotted on each light curve in red. The 13 detrended and fitted RC light curves are shown in Figure 54 with the global RC light curve model over-plotted on each light curve in red.

7.7 Results

The system parameter values from the Na D and RC global fits are listed in Table 10. Of key interest for the detection of Na D in the atmosphere of HD 189733b are the values of transit depth, δ , from the two global fits. A larger value from the Na D fit implies a larger planet radius in the Na D filter than in the RC filter. I find

$\delta_{RC} = 0.02531 \pm 0.00027$ and $\delta_{Na D} = 0.02581 \pm 0.00039$, resulting in a difference of $\delta_{RC} - \delta_{Na D} = -0.00050 \pm 0.00047$. Na D is detected in the atmosphere of HD 189733b, but with a significance of only $\sim 1\sigma$. My original calculation showing that I should be able to reach a 3σ detection for HD 189733b was flawed due to not properly accounting for the relatively short period of time the disk of the planet is completely inside the disk of the star, and because the amount of flux in the Na D filter was overestimated.

Figures 55 and 56 show the combined and binned (in 5 min intervals) Na D and RC light curves, respectively. The light curves were combined by phasing each set of data using the global T_c and P from Table 10. The light curve model for each filter is also binned at 5 minute intervals and shown as a red line. These light curves are not used for analysis, but rather to show the best combined behavior of the transit in each filter. The

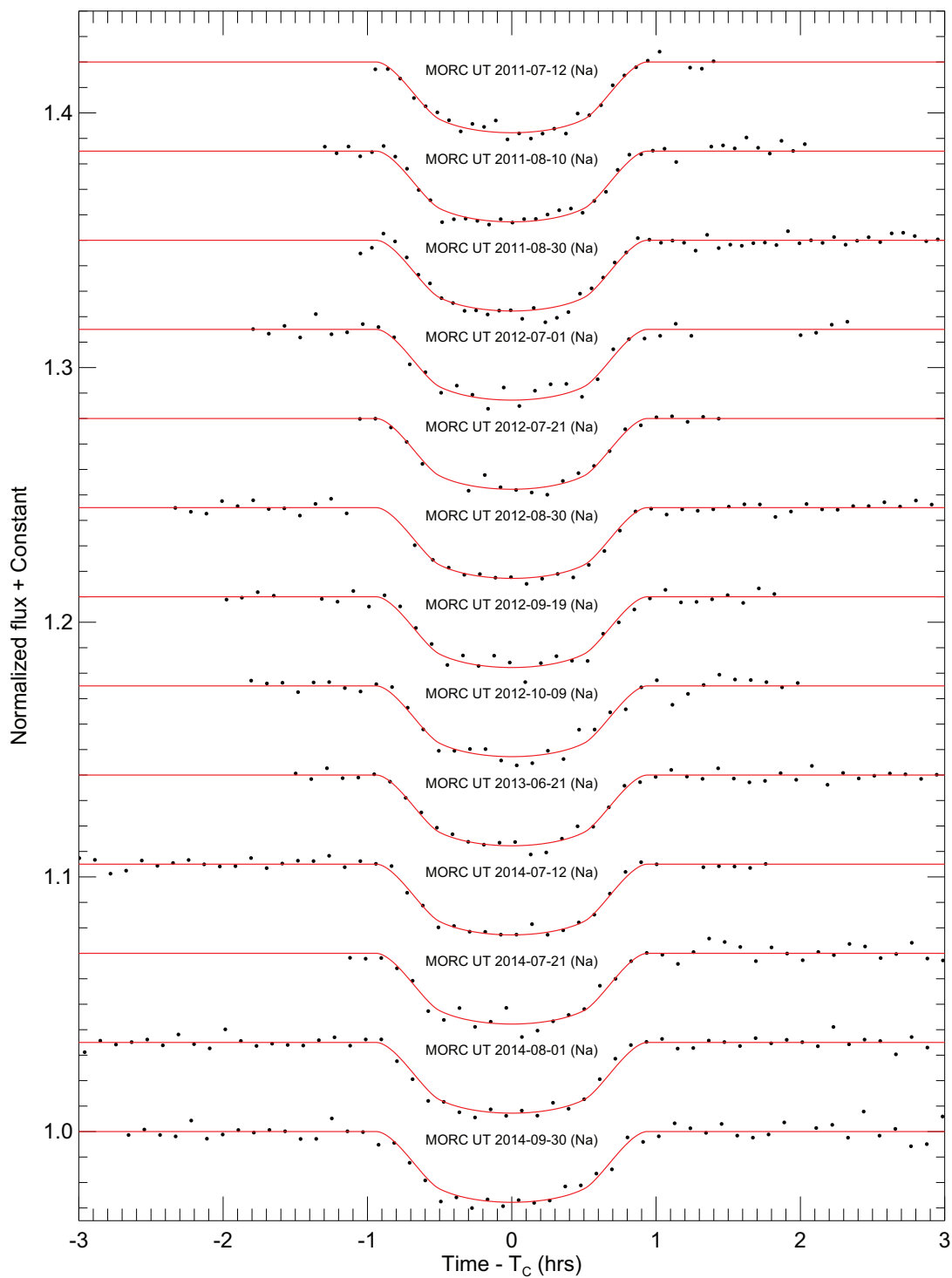


Figure 53. All thirteen HD 189733b Na D filter light curves. Each light curve has been detrended as discussed in §7.6. The exposure times for each light curve are listed in Table 9. The black points are the normalized and detrended differential photometric measurements, while the red lines show the global Na D transit model.

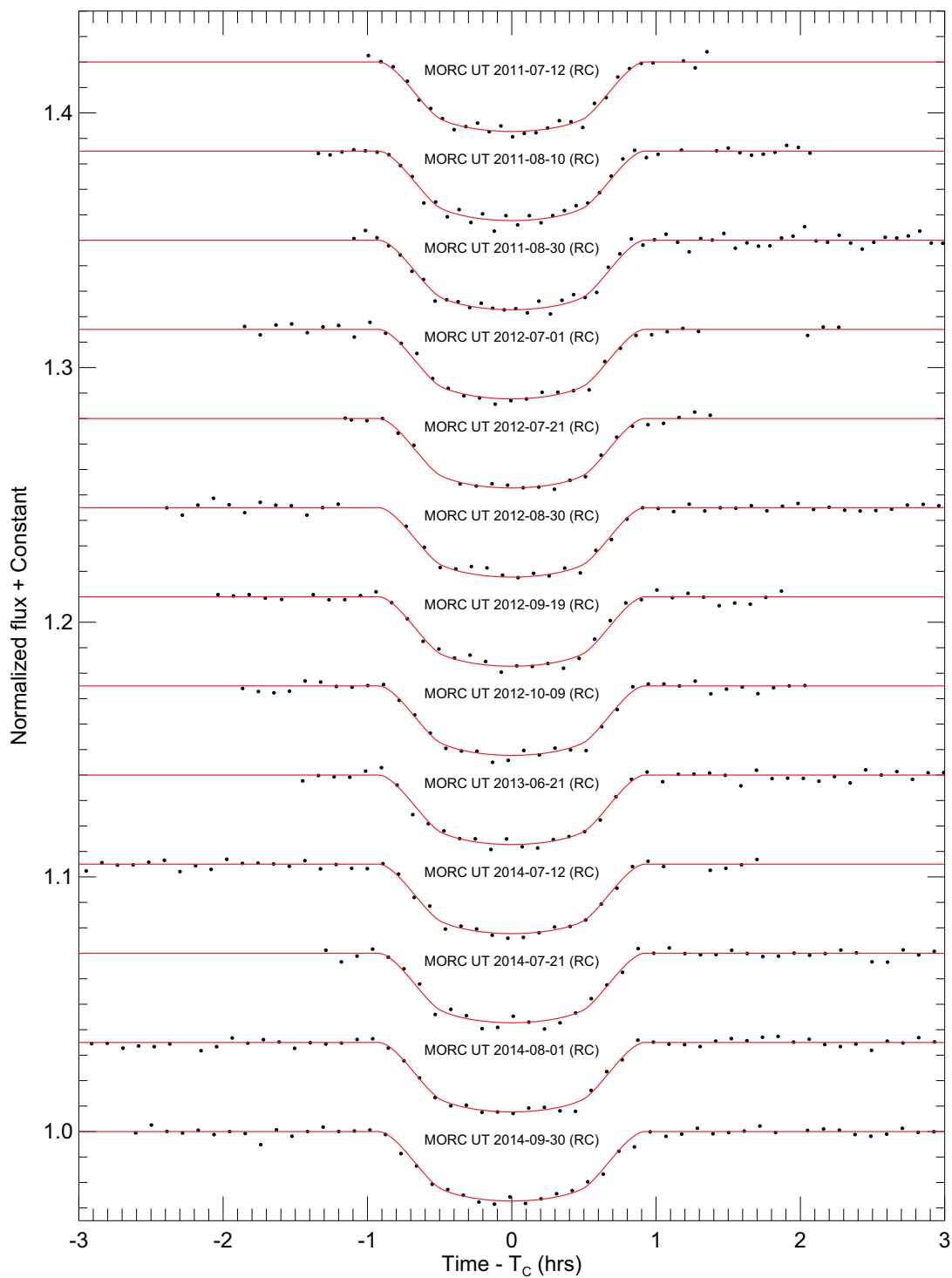


Figure 54. All thirteen HD 189733b Red Continuum (RC) filter light curves. Each light curve has been detrended as discussed in §7.6. The exposure times for each light curve are listed in Table 9. The black points are the normalized and detrended differential photometric measurements, while the red lines show the global RC transit model.

model residuals are shown in the bottom panel of each figure.

7.8 Discussion

7.8.1 Results of this Work Compared to the Literature

During the five years of my data collection, additional measurements of Na D in the atmosphere of HD 189733b have been reported in the literature. Jensen et al. (2011) reevaluated the Redfield et al. (2008) observations and found Na D absorption in the atmosphere of HD 189773b at a level of 0.000526 ± 0.000169 ($\sim 3\sigma$ significance) for a 12 Å bandpass. Huitson et al. (2012) used STIS aboard HST and measured absorption from the Na D doublet in the atmosphere of HD 189733b at a level of 0.000511 ± 0.000059 ($\sim 9\sigma$ significance) for a 12 Å bandpass. Given the low 1σ confidence in my measurement, it is likely a coincidence that the median value of my measured depth difference is very nearly equal to the two measured values from the literature.

7.8.2 Detection of Na D in Transit Duration

Transit timing and duration can be determined to high precision for deep transits such as HD 189733b, because there are many data samples on the steep slopes of the ingress and egress segments of the light curve. Considering that the HD 189733b light curve has about the same number of data samples during ingress and egress as in the "bottom" of the transit, I investigated the possibility of a detectable transit duration difference due to Na D in the atmosphere of the planet.

Based on the depth difference in the Na D and RC filters, the detected height of the Na D atmosphere is:

$$h_{atm} = (R_p)_{Na} - (R_p)_{RC} \quad (24)$$

$$h_{atm} = (\sqrt{0.02581} - \sqrt{0.02531})R_* \times 696342 \text{ km}/R_\odot \times 0.756R_\odot/R_* \approx 825 \text{ km}. \quad (25)$$

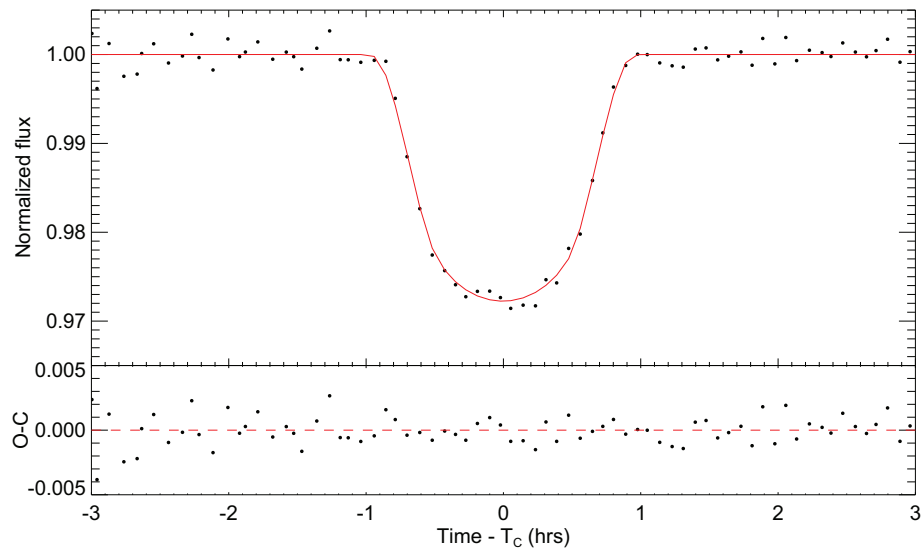


Figure 55. All thirteen HD 189733b detrended Na D light curves combined and binned in 5 min intervals (black dots). The light curves were combined by phasing the data using the global T_c and P from Table 10. The Na D light curve model is also binned at 5 minute intervals and shown as a red line. This light curve is not used for analysis, but rather to show the best combined behavior of the transit. The model residuals are shown in the bottom panel.

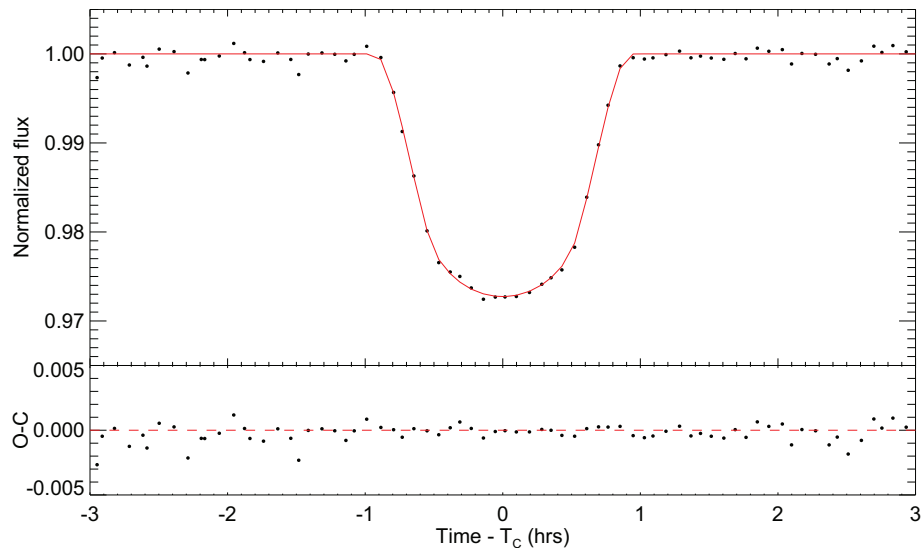


Figure 56. All thirteen HD 189733b detrended RC light curves combined and binned in 5 min intervals (black dots). The light curves were combined by phasing the data using the global T_c and P from Table 10. The RC light curve model is also binned at 5 minute intervals and shown as a red line. This light curve is not used for analysis, but rather to show the best combined behavior of the transit. The binned model residuals are shown in the bottom panel.

TABLE 10

Adopted Median Values and 68% Confidence Intervals for the Physical and Orbital Parameters of the HD 189733 System from the Global Fits Described in §7.6.

Parameter	Units	Value (Na D)	Value (RC)
Stellar Parameters:			
M_*	Mass (M_\odot).....	$0.818^{+0.037}_{-0.036}$	$0.808^{+0.037}_{-0.036}$
R_*	Radius (R_\odot).....	0.764 ± 0.012	0.753 ± 0.012
L_*	Luminosity (L_\odot).....	$0.338^{+0.020}_{-0.019}$	$0.327^{+0.019}_{-0.018}$
ρ_*	Density (cgs).....	$2.592^{+0.034}_{-0.033}$	2.672 ± 0.025
$\log g_*$	Surface gravity (cgs) .	$4.5850^{+0.0071}_{-0.0072}$	$4.5920^{+0.0068}_{-0.0069}$
T_{eff}	Effective temp. (K)...	5040 ± 49	5036 ± 49
[Fe/H].....	Metallicity.....	-0.028 ± 0.079	$-0.034^{+0.078}_{-0.079}$
Planetary Parameters:			
P	Period (days).....	$2.21857560 \pm 0.00000015$	$2.21857569 \pm 0.00000015$
a	Semi-major axis (AU)	0.03114 ± 0.00047	$0.03101^{+0.00047}_{-0.00046}$
M_P	Mass (M_J).....	$1.117^{+0.060}_{-0.058}$	$1.107^{+0.060}_{-0.058}$
R_P	Radius (R_J).....	1.193 ± 0.021	1.165 ± 0.019
ρ_P	Density (cgs).....	$0.815^{+0.044}_{-0.042}$	$0.869^{+0.044}_{-0.043}$
$\log g_P$	Surface gravity.....	$3.288^{+0.020}_{-0.021}$	$3.306^{+0.019}_{-0.020}$
T_{eq}	Equilibrium temp. (K)	1203 ± 12	1196 ± 12
$\langle F \rangle$	($10^9 \text{ erg s}^{-1} \text{ cm}^{-2}$)....	$0.476^{+0.020}_{-0.019}$	$0.465^{+0.019}_{-0.018}$
RV Parameters:			
T_C	Inf. conj. (BJD _{TDB}) ..	$2455754.78952 \pm 0.00022$	$2455754.78989 \pm 0.00016$
K	RV semi-amp. (m/s) ..	$198.4^{+8.6}_{-8.7}$	198.3 ± 8.7
$M_P \sin i$	Minimum mass (M_J) .	$1.113^{+0.060}_{-0.058}$	$1.104^{+0.060}_{-0.058}$
M_P/M_*	Mass ratio.....	0.001304 ± 0.000060	$0.001309^{+0.000061}_{-0.000060}$
γ_{ELODIE}	m/s.....	3.5 ± 5.3	3.4 ± 5.3
Primary Transit Parameters:			
R_P/R_*	Planet radius (R_*)....	0.1607 ± 0.0012	0.15910 ± 0.00086
a/R_*	Semi-major axis (R_*) .	8.771 ± 0.038	8.860 ± 0.028
i	Inclination (degrees)..	85.7101 ± 0.0023	85.7100 ± 0.0023
b	Impact parameter....	$0.6561^{+0.0029}_{-0.0028}$	0.6628 ± 0.0021
δ	Transit depth.....	$0.02581^{+0.00038}_{-0.00039}$	0.02531 ± 0.00027
T_{FWHM}	FWHM dur. (days)...	$0.05988^{+0.00048}_{-0.00049}$	$0.05877^{+0.00036}_{-0.00035}$
τ	Ing./egr. dur. (days) ..	0.01759 ± 0.00014	0.017382 ± 0.000099
T_{14}	Total duration (days) .	0.07746 ± 0.00050	$0.07615^{+0.00037}_{-0.00036}$
u_{1Na}	Lin. Limb-darkening .	$0.605^{+0.016}_{-0.017}$	$0.540^{+0.016}_{-0.017}$
u_{2Na}	Quad. Limb-darkening	0.156 ± 0.013	0.173 ± 0.013

The orbital time of the planet is

$$P_{orbit} = 2.21857567 \text{ d} \times 86400 \text{ s/d} = 191,685 \text{ s.} \quad (26)$$

The distance traveled by the planet in one orbit is

$$d_{orbit} = 0.031 \text{ AU} \times 1.496 \times 10^8 \text{ km/AU} \times 2\pi = 29,138,900 \text{ km.} \quad (27)$$

The orbital velocity is then

$$v_{orbit} = d_{orbit}/P_{orbit} \approx 150 \text{ km/s.} \quad (28)$$

Assuming a circular atmospheric disk and a transit impact parameter of zero, the atmosphere's ingress/egress time is

$$\tau_{atm} = \frac{h_{atm}}{v_{orbit}} = \frac{825 \text{ km}}{150 \text{ km/s}} = 5.5 \text{ s.} \quad (29)$$

Then the total extra transit duration due to the atmosphere is 11 s. However, when the impact parameter is greater than zero, the atmosphere crosses the disk of the host star at an angle which increases the atmospheric ingress/egress time. Using the implementation of the Mandel & Agol (2002) model in AIJ and an impact parameter of $b = 0.663$, along with the other parameter values in Table 10, the total extra transit duration due to a circular atmospheric disk is 14 s.

The global fits show a difference in transit duration of

$$(T_{FWHM})_{Na} - (T_{FWHM})_{RC} = 0.05988 \pm 0.00049 \text{ d} - 0.05877 \pm 0.00036 \text{ d} = 96 \pm 53 \text{ s} \quad (30)$$

which is nearly a 2σ detection, but is a much larger duration difference than the 14 s difference calculated for the circular atmospheric disk case. However, Lecavelier Des Etangs et al. (2010) detected an evaporating atmosphere around HD 189733b. Using the HST/ACS, they found the transit depth in H I Lyman- α to be on average \sim double the depth of the 2.4% optical broadband filter depth. If the shape of HD 189733b's atmosphere is being affected by the intense stellar radiation incident on the planet's

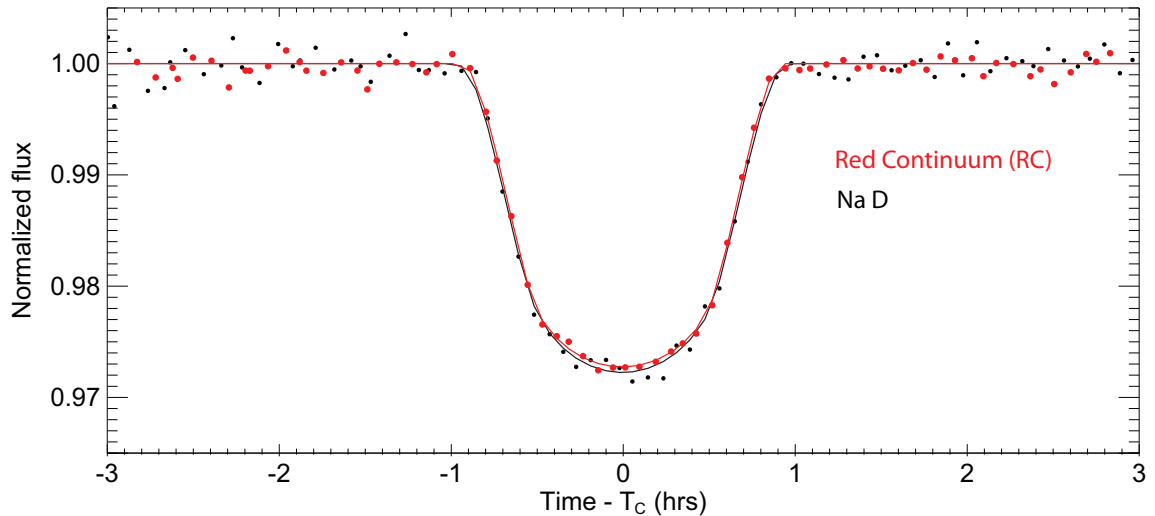


Figure 57. The HD 189733b combined and binned RC filter light curve compared to the combined and binned Na D filter light curve. The RC and Na D data are shown as red and black dots, respectively. The RC and Na D models are shown as red and black lines, respectively. The Na D model is deeper and wider than the RC model.

atmosphere, the transit duration difference measured in this work could be real and suggestive of a Na atmosphere that is extended along the path the planet takes as it crosses the face of the star. Figure 57 shows the combined and binned RC filter light curve compared to the combined and binned Na D filter light curve. The Na D transit model is deeper and wider than the RC transit model.

The highest precision HD 189733b Na D measurement available is the Huitson et al. (2012) 9σ detection of Na D from HST/STIS. However, those data are limited to high precision transit depth measurements, since the 90 minute orbit of HST prevents the complete observation of full transits. In particular, the HST/STIS observations provided a pre-ingress baseline sequence, an in-transit sequence, and a post-egress sequence, but no observations during ingress and egress are available. Thus, no transit duration measurements are possible from the Huitson et al. (2012) data. Additional HST observations with good coverage of ingress and egress would be useful to qualify our $\sim 2\sigma$ detection of a transit duration difference due to Na in the atmosphere of HD 189733b.

7.9 Summary and Conclusions

To my knowledge, I have presented the first tentative detection of the atmosphere of an exoplanet from a small aperture (<1 m) ground-based telescope. Observations of 13 HD 189733b transits using alternating Na D and RC narrow-band filters have produced a 1σ detection of a transit depth that is deeper in the Na D filter than in the continuum RC filter by 0.05%. Our nominal excess depth is nearly identical to the value obtained from a 9σ detection using HST/STIS spectroscopy, but that is likely by chance, given the low significance of my measurement. A few days before this work was finalized, Wyttenbach et al. (2015) released a preprint reporting that they spectrally resolved the Na D doublet in the atmosphere of HD 189733b using archival transit data from the HARPS spectrograph. They measure the excess absorption of each of the Na D lines separately using various integration bandwidths, and they measure an excess absorption of $0.062 \pm 0.008\%$ (7.8σ) when both lines are included in a 12 Å bandpass, which is comparable to and consistent with our measurement and others reported herein.

We investigate a new method of detecting a non-circular atmospheric disk by measuring the transit duration difference in the two narrow-band filters. We find a duration difference of 96 ± 53 s, which if real suggests a Na atmosphere that is significantly extended along the orbital path. I am not aware of high-precision HST data that is currently available to confirm our $\sim 2\sigma$ detection of duration difference. HST data that include observations of ingress and egress should be collected to qualify the detection of the transit duration difference which suggests an extended, non-symmetric Na atmosphere around HD 189733b.

The narrow-band filter technique could be extended to larger aperture telescopes to enable atmospheric component detection from observations of a single transit. Colón et al. (2010) and Sing et al. (2011) have already used the the Optical System for Imaging and low Resolution Integrated Spectroscopy (OSIRIS) narrow-band tunable filter on the 10.4-m Gran Telescopio Canarias to detect potassium in HD 80606b and XO-2b, respectively. However, the tunable filter is only 25-50% as efficient as our Na D filter and

OSIRIS requires special attention to placement of target and comparison star(s) on the detector because its bandpass is not uniform across the field of view, with the effective center wavelength decreasing by 10 nm from the center to the edge of the detector.

With a novel approach, precise observations, and careful data reduction and modeling, small aperture telescopes can compete with larger ground-based and space-based telescopes to produce cutting edge scientific results. The same approach could be extended to larger telescopes to advance our knowledge of exoplanetary atmospheres.

CHAPTER 8

KELT-6b DISCOVERY AND CHARACTERIZATION

The contents of this chapter appeared in the February 2014 issue of the *Astronomical Journal* (Collins et al., 2014). The authors and affiliations are listed in Appendix B.

8.1 KELT-6b Abstract

We report the discovery of KELT-6b, a mildly-inflated Saturn-mass planet transiting a metal-poor host. The initial transit signal was identified in KELT-North survey data, and the planetary nature of the occulter was established using a combination of follow-up photometry, high-resolution imaging, high-resolution spectroscopy, and precise radial velocity measurements. The fiducial model from a global analysis including constraints from isochrones indicates that the $V = 10.38$ host star (BD+31 2447) is a mildly evolved, late-F star with $T_{\text{eff}} = 6102 \pm 43$ K, $\log g_{\star} = 4.07^{+0.04}_{-0.07}$ and $[\text{Fe}/\text{H}] = -0.28 \pm 0.04$, with an inferred mass $M_{\star} = 1.09 \pm 0.04 M_{\odot}$ and radius $R_{\star} = 1.58^{+0.16}_{-0.09} R_{\odot}$. The planetary companion has mass $M_{\text{P}} = 0.43 \pm 0.05 M_{\text{J}}$, radius $R_{\text{P}} = 1.19^{+0.13}_{-0.08} R_{\text{J}}$, surface gravity $\log g_{\text{P}} = 2.86^{+0.06}_{-0.08}$, and density $\rho_{\text{P}} = 0.31^{+0.07}_{-0.08} \text{ g cm}^{-3}$. The planet is on an orbit with semimajor axis $a = 0.079 \pm 0.001 \text{ AU}$ and eccentricity $e = 0.22^{+0.12}_{-0.10}$, which is roughly consistent with circular, and has ephemeris of $T_{\text{c}}(\text{BJD}_{\text{TDB}}) = 2456347.79679 \pm 0.00036$ and $P = 7.845631 \pm 0.000046$ d. Equally plausible fits that employ empirical constraints on the host star parameters rather than isochrones yield a larger planet mass and radius by $\sim 4-7\%$. KELT-6b has surface gravity and incident flux similar to HD 209458b, but orbits a host that is more metal poor than HD 209458 by ~ 0.3 dex. Thus, the KELT-6 system offers an opportunity to perform a comparative measurement of two similar planets in similar environments around stars of very different metallicities. The precise radial velocity data also reveal an acceleration

indicative of a longer-period third body in the system, although the companion is not detected in Keck adaptive optics images.

8.2 Identification of Contributions

The discovery and characterization of KELT-6b required a multi-institutional collaboration and contributions from several scientists with highly specialized capabilities and/or access to instrumentation with highly specialized capabilities. In this section, my contributions to the overall process are identified and delineated from the contributions of other collaborators. In some cases, many team members contributed to a task for which I was not directly involved, so I will identify work that I did not perform as being from collaborators in general to avoid improperly or inadequately acknowledging contributions within each sub-team.

As lead author, I was responsible for writing all text in this chapter. However, collaborators provided substantial input, especially in sections related to the observations, data reductions, and analyses identified below as being performed by collaborators. I organized all of the photometric follow-up observations and collected the results from the follow-up team. I observed and reduced all of the datasets identified as being from the MORC telescope. I analyzed all photometric follow-up data to determine the best detrending parameters to include in the global fit. I gathered and formatted all of the datasets required for the global fits. I set up and executed the 12 global fits and analyzed and formatted the resulting outputs presented in this chapter, including the TTV data. I performed the secondary transit analysis and participated in deriving the results for most of the false positive analysis section, and performed the gyrochronological age analysis. I also created the exoplanetary system parameter comparison figures presented in the Discussion section, except the Transit Depth vs. Apparent V magnitude figure.

Collaborators provided the KELT-N discovery data, HIRES and TRES radial velocity and spectroscopic data, follow-up photometry other than from the MORC telescope, Keck adaptive optics data and associated analyses, UVW space motion analysis, SED analysis, and insolation evolution analysis. For each of the datasets and/or

analyses contributed, the responsible sub-team usually provided text suggestions and in some cases figures that are included in this chapter.

All team members provided valuable contributions during the review and publication phases.

8.3 Introduction

Ground-based surveys have discovered dozens of transiting exoplanets around bright ($V < 11$) stars. Those discoveries are of considerable importance because they enable cost-effective detailed measurements of physical properties of extrasolar planets and their host stars (see reviews by Winn 2009, 2010). Discoveries of transiting exoplanets that have characteristics similar to an already well-measured exoplanet, but that differ significantly in one aspect, are of particularly high importance because they enable comparative studies.

The high scientific value of transiting planet systems motivated the first dedicated wide-field transit surveys, which have now produced a large number of discoveries (TrES, Alonso et al. 2004; XO, McCullough et al. 2006; HATNet, Bakos et al. 2007; SuperWASP, Collier Cameron et al. 2007a, QES, Alsubai et al. 2011). SuperWASP and HATNet have been especially productive, with each survey discovering dozens of new transiting planets. The space-based missions CoRoT (Baglin, 2003) and Kepler (Borucki et al., 2010) have dramatically expanded the parameter space of transit surveys, enabling the detection of transiting planets with sizes down to that of the Earth and below, planets with periods of several years, and planets orbiting host stars with a wider range of physical characteristics.

The Kilodegree Extremely Little Telescope-North (KELT-North) transit survey (Pepper et al., 2007) is designed to detect transiting planets around bright stars. Pepper et al. (2003) designed the aperture, optical system, and exposure time for KELT-North to provide better than 1% RMS photometry for stars with $8 < V < 10$. That magnitude range represents the brightness gap between comprehensive RV surveys and most other transit surveys. The KELT-North telescope system was constructed using commercial

off-the-shelf equipment and has been collecting data since September 2006.

The KELT-North survey has already announced three low-mass transiting companions. KELT-1b (Siverd et al., 2012) is a highly inflated $27 M_J$ brown dwarf transiting a $V = 10.7$ mid-F star. KELT-2Ab (Beatty et al., 2012) is a hot Jupiter transiting the bright ($V = 8.77$) primary star of a binary system. KELT-3b (Pepper et al., 2013) is a hot Jupiter planet transiting a $V = 9.8$ late-F star. The designations KELT-4 and KELT-5 are currently reserved for two candidates in the confirmation phase.

Because KELT-North has focused on the same fields for an extended length of time (> 6 years), longer period ($P \geq 5$ d) planets are now detectable in the data. The large number of observations of each field also enables the detection of smaller planet-to-star radius ratios. In this paper we describe the discovery and characterization of KELT-6b, a transiting mildly-inflated Saturn-mass planet orbiting a $V = 10.38$ metal-poor host BD+31 2447 (hereafter KELT-6). KELT-6b is currently the sixth longest period exoplanet discovered by a ground-based transit survey, after HAT-P-15b, HAT-P-17b, WASP-8b, WASP-59b, and WASP-84b¹. In several important aspects, KELT-6b resembles a metal-poor analog of one of the most well-studied transiting planets, HD 209458b (Charbonneau et al., 2000; Henry et al., 2000). Both hosts have similar effective temperatures of ~ 6100 K, although KELT-6 is significantly more evolved and therefore has a larger radius. On the other hand, KELT-6b has a substantially larger orbit than HD 209458b. As a result, the incident fluxes at both planets are very similar. In addition, the surface gravity of KELT-6b differs from that of HD 209458b by only $\sim 20\%$.

The discovery of KELT-6b offers an opportunity to perform a comparative measurement of two similar planets in similar environments around stars of very different metallicities. The comparison may, for example, elucidate the effect of bulk composition of the planet atmosphere on the cause of atmospheric temperature inversions (e.g., Madhusudhan & Seager 2010). In addition, host-star metallicity has been shown to affect

¹The Exoplanet Orbit Database (Wright et al. 2011; Han et al. 2014; <http://exoplanets.org/>) lists four planets with longer periods as of November 5th, 2013. WASP-84b (Anderson et al., 2013) is not in the database at the time of writing, but we include it here for completeness.

the physical and orbital properties of planets. In particular, there is a rough correlation between metallicity and estimated core mass (Burrows et al. 2007; Torres et al. 2008; Sato et al. 2005), and there are indications of trends in the properties of planets with metallicity, which may signal the existence of multiple mechanisms for the formation and/or delivery of close-in giant planets (e.g., Ribas & Miralda-Escudé 2007; Dawson & Murray-Clay 2013).

8.4 Discovery and Follow-up Observations

We provide a brief summary of the KELT survey data reduction process in §8.4.1; for more details, see §2 of Siverd et al. (2012).

8.4.1 KELT-North Observations and Photometry

KELT-6 is in KELT-North survey field 08, which is centered on ($\alpha = 13^h 38^m 28^s .25$, $\delta = +31^\circ 41' 12'' .67$; J2000). We monitored field 08 from December 2006, to June 2011, collecting a total of 7359 observations. We reduced the raw survey data using a custom implementation of the ISIS image subtraction package (Alard & Lupton, 1998; Alard, 2000), combined with point-spread fitting photometry using DAOPHOT (Stetson, 1987). Using proper motions from the Tycho-2 catalog (Høg et al., 2000) and J and H magnitudes from 2MASS (Skrutskie et al. 2006; Cutri et al. 2003), we implemented a reduced proper motion cut (Gould & Morgan, 2003) based on the specific implementation of Collier Cameron et al. (2007b), in order to select likely dwarf and subgiant stars within the field for further post-processing and analysis. We applied the trend filtering algorithm (TFA; Kovács et al., 2005) to each remaining light curve to remove systematic noise, followed by a search for transit signals using the box-fitting least squares algorithm (BLS; Kovács et al., 2002). For both TFA and BLS we used the versions found in the VARTOOLS package (Hartman et al., 2008).

One of the candidates from field 08 was star BD+31 2447 / TYC 2532-556-1, located at ($\alpha = 13^h 03^m 55^s .65$, $\delta = +30^\circ 38' 24'' .3$; J2000). The star has Tycho magnitudes

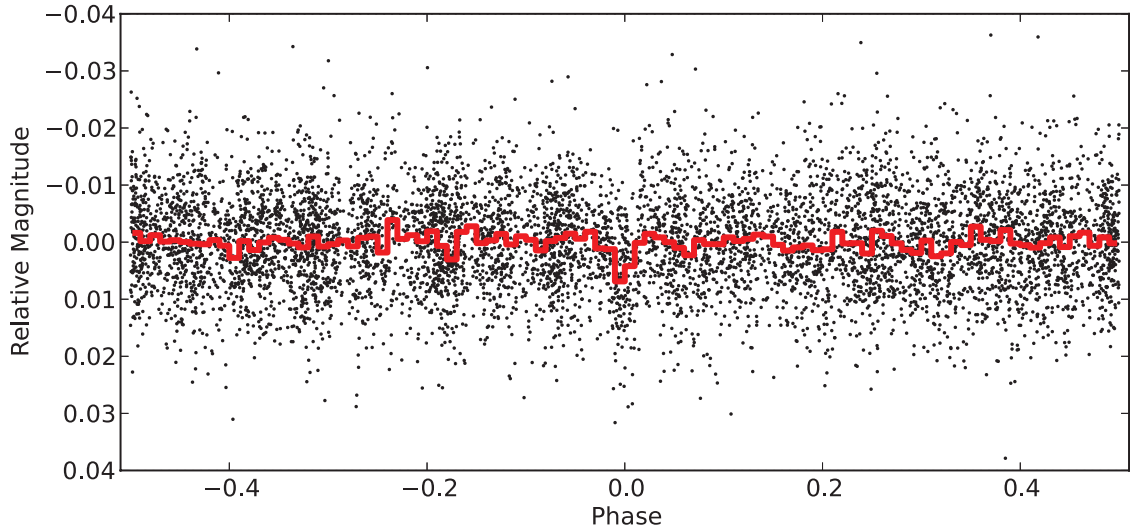


Figure 58. Discovery light curve of KELT-6 from the KELT-North telescope. The light curve contains 7359 observations spanning 4.5 years, phase-folded to the orbital period of 7.8457 days. The solid red line represents the same data binned at ~ 2 -hour intervals after phase-folding.

$B_T = 10.736 \pm 0.048$ and $V_T = 10.294 \pm 0.050$ (Høg et al., 2000), and passed our initial selection cuts. The discovery light curve of KELT-6 is shown in Figure 58. We observed a transit-like feature at a period of 7.8457 days, with a depth of about 5 mmag.

8.4.2 Radial-Velocity Observations

After KELT-6 was selected as a candidate, we conducted radial-velocity (RV) observations to identify possible false-positive signatures and to determine the RV orbit. We obtained data using the Tillinghast Reflector Echelle Spectrograph² (TRES; Fűrész, 2008), on the 1.5m Tillinghast Reflector at the Fred L. Whipple Observatory (FLWO) at Mt. Hopkins, AZ. We observed KELT-6 three times with TRES over three months, from UT 2012-04-12 to UT 2012-07-09. The spectra have a resolving power of $R=44,000$, and were extracted following the procedures described by Buchhave et al. (2010). These three initial TRES single-order absolute RVs are listed in Table 11 and are consistent with no RV variations to within the errors, ruling out some classes of astrophysical false positives.

²<http://tdc-www.harvard.edu/instruments/tres/>

However, the TRES RV uncertainties are large enough to still allow for a low-mass companion at the ~ 7.8 d period of the KELT-North candidate signal, and on that basis we chose to continue with photometric follow-up. Note that due to the relatively large uncertainties, we chose not to include these TRES velocities in the final global analysis described in §8.6.

On UT 2012-06-26, we obtained high precision KELT-6 follow-up photometry of the final third of a predicted transit and detected an apparent shallow egress (see §8.4.3). Based on that detection and the lack of RV variations in the TRES data, we decided to pursue higher-precision RV data.

Using the High Resolution Echelle Spectrometer (HIRES) instrument (Vogt et al., 1994) on the Keck I telescope located on Mauna Kea, Hawaii, we obtained 16 exposures between UT 2012-08-24 and UT 2013-02-21 with an iodine cell, plus a single iodine-free template spectrum. The absolute and precise relative RV measurements are listed in Table 11, and Figure 59 shows the HIRES relative RV data phased to the orbit fit with a linear trend of $\dot{\gamma} = -0.239 \text{ m s}^{-1} \text{ day}^{-1}$ (see §8.6) removed, along with the residuals to the model fit.

The HIRES radial velocity observations were made using the standard setup of the California Planet Search (CPS) program (Johnson et al., 2010; Howard et al., 2011). A pyrex cell containing gaseous iodine is placed in front of the spectrometer entrance slit, which imprints a dense set of molecular iodine lines on each stellar spectrum. The iodine lines provide a calibration of the instrumental profile as well as a precise measure of the wavelength scale at the time of observation (Marcy & Butler, 1992). We measured the relative stellar radial velocities using the forward-modeling scheme of Butler et al. (1996) with improvements made over the years. We measured the absolute RVs using the methods of Chubak et al. (2012).

The PSF varies quite dramatically in the slit-fed HIRES instrument simply from guiding and spectrometer focus variations. Since line asymmetries due to instrumental and stellar sources cannot be easily distinguished, we do not attempt to measure bisector

spans for the HIRES observations.

We also obtained five RV measurements between UT 2013-02-01 and UT 2013-02-15 using the Hobby-Eberly Telescope (HET). However, these data were taken without an iodine cell for wavelength reference, and as a result the uncertainties are $>6 \text{ km s}^{-1}$, so we do not list them in the RV table or use them in the global fit analysis in §8.6.

Finally, 21 additional TRES RVs were obtained and reduced using multi-order analysis after most of the global analysis had been completed. The full TRES RV dataset is listed in Table 11 and contains measurements from 24 different nights between UT 2012-04-12 and UT 2013-07-31, with typical relative uncertainties of 20 m s^{-1} . Although we do not use the TRES RV data in our global fit analysis (see §8.6.2), we note that these data independently confirm both the amplitude of the KELT-6b RV variations (see Figure 59) and the linear trend of the fiducial global fit (see §8.7), albeit with larger uncertainties due to the somewhat worse precision than the Keck data. Bisector spans were calculated from the TRES spectra following Torres et al. (2007) and are used in §8.8 as part of the false positive analysis. The bisector spans are listed in Table 11, and shown in the bottom panel of Figure 59 phased to the orbital fit.

8.4.3 Follow-up Time-Series Photometry

We acquired follow-up time-series photometry of KELT-6 to check for other types of false positives and to better determine the transit shape. To schedule follow-up photometry, we used the `Tapir` software package (Jensen, 2013). We obtained 16 partial or full primary transits in multiple bands between June 2012 and June 2013. The transit duration (> 5.5 hours) and orbital period (> 7.8 days) are long, so opportunities to observe full transits are rare. Figure 60 shows all the primary transit follow-up light

TABLE 11
Radial Velocity and Bisector Span Variation Measurements of KELT-6

BJD _{TDB}	Abs RV ^a	Rel RV ^b	Rel σ_{RV} ^c	BS ^d	σ_{BS} ^e	Source
2456029.869867	1085	27.02	20.27	-3.9	21.6	TRES
2456114.681684	1188	-5.96	28.33	-18.0	19.0	TRES
2456117.673406	1166	63.43	19.73	17.3	14.4	TRES
2456163.733467	1300	19.38	3.90	-	-	HIRES
2456164.729771	1216	61.75	3.76	-	-	HIRES
2456165.727060	1202	46.70	3.76	-	-	HIRES
2456172.720200	1209	64.03	3.36	-	-	HIRES
2456173.720971	1163	69.62	3.31	-	-	HIRES
2456175.727980	1081	-5.05	5.06	-	-	HIRES
2456177.719323	1161	-14.71	3.56	-	-	HIRES
2456178.716548	1000	2.82	3.57	-	-	HIRES
2456179.715151	1214	43.05	3.67	-	-	HIRES
2456290.173359	1311	29.64	3.81	-	-	HIRES
2456318.978815	1132	-46.73	3.50	-	-	HIRES
2456320.088103	1319	-35.17	3.48	-	-	HIRES
2456326.175000	1185	-62.66	3.50	-	-	HIRES
2456327.103147	1340	-49.24	3.52	-	-	HIRES
2456328.106726	1333	-11.70	3.32	-	-	HIRES
2456345.026477	1291	8.71	3.58	-	-	HIRES
2456443.707006	1109	-33.79	22.37	7.4	13.4	TRES
2456450.707562	1125	-18.64	19.40	-8.2	15.4	TRES
2456451.710411	1021	-54.28	19.92	-0.2	15.3	TRES
2456452.667049	1022	-79.97	17.75	0.5	10.2	TRES
2456453.661056	1044	16.31	21.20	-50.3	18.9	TRES
2456458.688259	1015	-71.18	18.35	8.5	10.8	TRES
2456459.685632	1147	-54.01	17.19	16.6	11.0	TRES
2456460.684562	1022	-57.04	20.36	6.1	10.1	TRES
2456461.669084	1127	-30.88	18.32	11.8	11.6	TRES
2456462.673881	1181	0.00	14.42	5.2	9.0	TRES
2456463.673604	1150	19.16	15.25	12.8	11.2	TRES
2456464.684882	1141	10.16	14.42	1.9	13.9	TRES
2456466.733703	1045	-69.70	17.79	-18.7	13.2	TRES
2456467.707369	1089	-66.40	24.43	-5.8	11.4	TRES
2456468.720609	1071	-78.93	24.46	-13.3	11.2	TRES
2456469.719214	1080	-36.11	22.32	6.0	10.1	TRES
2456470.658849	1168	34.53	19.41	-4.3	9.8	TRES
2456472.704518	1211	-11.86	25.12	30.9	22.1	TRES
2456501.663546	1628	-20.17	33.33	0.5	12.2	TRES
2456503.653861	1697	58.79	33.22	5.4	11.6	TRES
2456504.645862	1577	-2.35	19.21	-8.3	10.8	TRES

Notes: Absolute RVs are on the IAU scale. The native absolute velocity scale of TRES has been transformed to the IAU absolute velocity scale by subtracting 610 m s⁻¹. The absolute RV error is 100 m s⁻¹ and is dominated by the long-term RMS for velocity standard stars. The bisector spans (BS) from the TRES spectra are computed as described in the text. ^a absolute RVs (m s⁻¹)

^b relative RVs (m s⁻¹) ^c unrescaled relative RV errors (m s⁻¹) ^d spectral line bisector spans (m s⁻¹)

^e spectral line bisector span errors (m s⁻¹)

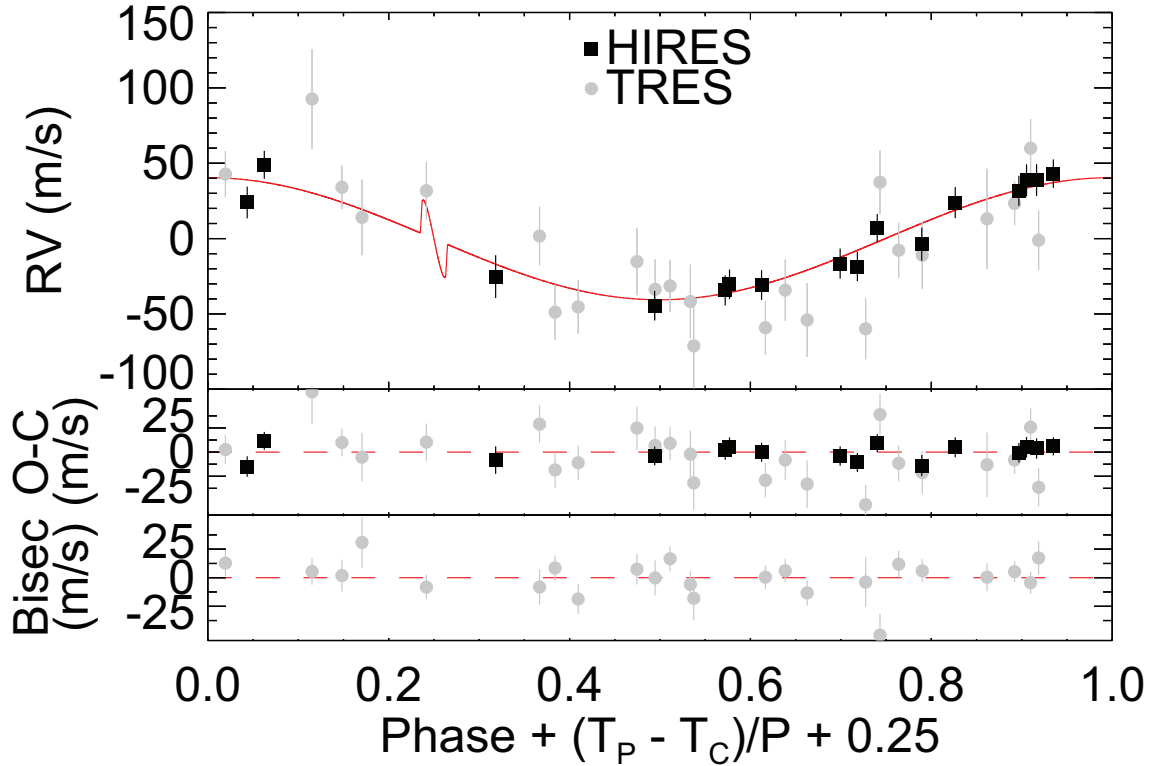


Figure 59. HIRES and TRES relative radial velocity measurements of KELT-6. *Top panel:* Relative RV observations phased to our fiducial orbital model (see §8.6.2) which is fit to the HIRES data only with eccentricity and the RV linear trend as free parameters. The fiducial model is shown as a solid red line. The predicted Rossiter-McLaughlin effect incorporates an assumption that $\lambda = 0$ (i.e. that the projected spin-orbit alignment of the system is 0 degrees). HIRES observations are shown as black squares and the error bars are scaled according to the method described in §8.6. TRES observations are shown as gray circles with unrescaled errors. These data were not used in the fit, but are simply phased to the period of the fiducial model, and shifted by a constant offset that minimizes the χ^2 of the data from the fiducial model. *Middle panel:* Residuals of the RV observations to the fiducial fit. The RMS of the HIRES RV residuals is 8.0 m s^{-1} . *Bottom panel:* Bisector spans of the TRES spectra.

curves assembled. A summary of the follow-up photometric observations is shown in Table 12. We find consistent R_p/R_* ratios in all light curves, which include observations in the g , r , i , z , V , I , and CBB filters³, helping to rule out false positives due to blended eclipsing binaries. Figure 61 shows all primary transit follow-up light curves from Figure 60 (except the WCO light curve which contains significant residual systematics after detrending), combined and binned in 5 minute intervals. This combined and binned light curve is not used for analysis, but rather to show the best combined behavior of the transit. We also observed KELT-6 near the uncertain time of secondary transit on five different epochs (see §8.8).

Unless otherwise noted, all photometric follow-up observations were reduced with the AstroImageJ (AIJ) package⁴ (K. A. Collins & J. F. Kielkopf 2015, in preparation). AIJ is a general purpose image processing package, but is optimized for processing time-series astronomical image sequences. It is open source software written in Java and is compatible with all computing platforms commonly used to process astronomical data. AIJ is a graphical user interface driven package that provides an interactive multi-image display interface, CCD image calibration (bias, dark, flat-field, and non-linearity correction), astronomical time and coordinate calculations, multi-aperture differential photometry, multi-dataset plotting, and interactive light curve detrending. It can be operated in combination with any camera control software to reduce data and plot differential light curves in real time, or can be used in standard mode to post process data.

Also unless otherwise noted, calibration of all photometric follow-up observations included bias and dark subtraction followed by flat-field correction. Calibration of the MORC data also included a correction for CCD non-linearity. Differential photometry was performed on the calibrated images using a circular aperture.

We observed three complete and three partial transits of KELT-6 using two telescopes at Moore Observatory, operated by the University of Louisville. The 0.6 m

³In all references to SDSS filters in this paper, we use the unprimed notation to denote generic SDSS-like filters, which in practice are often labeled with the primed notation. CBB denotes the Astrodon clear with blue block filter which starts transmitting near 500 nm and continues to transmit into the near-infrared.

⁴<http://www.astro.louisville.edu/software/astroimagej/>

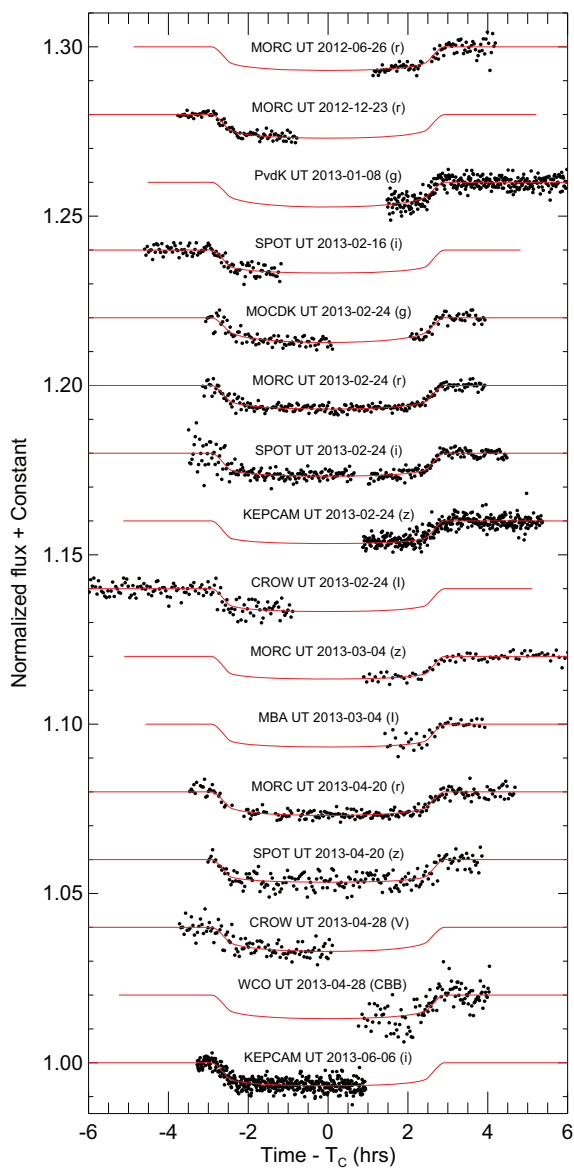


Figure 60. Follow-up transit photometry of KELT-6. The red overplotted lines are the best fit transit model from global fit 6 described in §8.6.2 and summarized in Table 14. The transit times are shown in Table 16. The labels are as follows: MORC=University of Louisville Moore Observatory 0.6 m RCOS Telescope; PvdKO=Peter van de Kamp Observatory 0.6 m RCOS Telescope; SPOT=Spot Observatory 0.6 m RCOS Telescope; MOC DK=University of Louisville Moore Observatory PlaneWave 0.5 m CDK Telescope; KEPCAM=Keplecam at the Fred Lawrence Whipple Observatory 1.2 m Telescope; CROW=Canela’s Robotic Observatory 0.3 m LX200 Telescope; MBA=Montgomery Bell Academy 0.6 m PlaneWave CDK Telescope; WCO=Westminster College Observatory 0.35 m C14 Telescope.

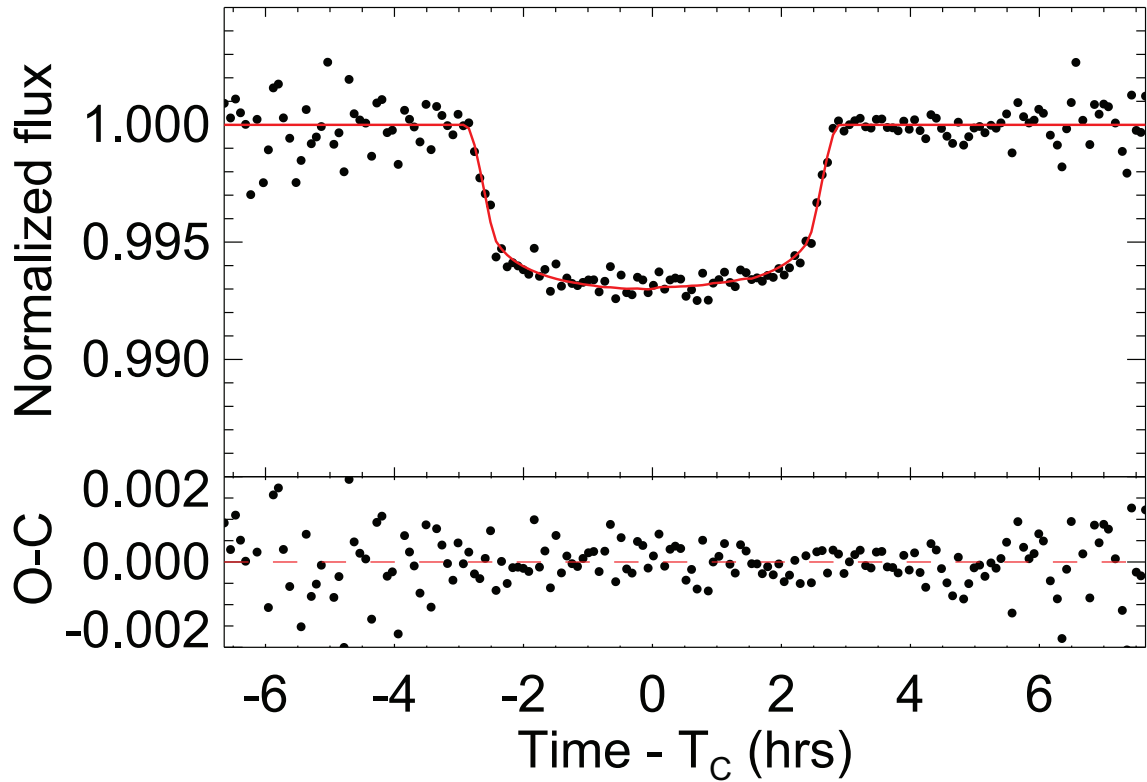


Figure 61. *Top panel:* All follow-up light curves from Figure 60 (except the WCO light curve - see text), combined and binned in 5 minute intervals. This light curve is not used for analysis, but rather to show the best combined behavior of the transit. The red curve shows the 15 transit models from global fit 6 described in Table 14 for each of the individual fits combined and binned in 5 minute intervals the same way as the data, with the model points connected. *Bottom panel:* The residuals of the binned light curve from the binned model in the top panel.

RCOS telescope with an Apogee U16M 4K \times 4K CCD, giving a 26' \times 26' field of view and 0.39 arcseconds pixel⁻¹, was used to observe the *r* egress on UT 2012-06-26, the *r* ingress on UT 2012-12-23, the full *r* transit on UT 2013-02-24, the *z* egress on UT 2013-03-04, and the full *r* transit on UT 2013-04-20. The 0.6 m was also used to observe near the time of secondary transit on UT 2013-04-16 in *z*. The Planewave Instruments 0.5 m CDK telescope with an Apogee U16M 4K \times 4K CCD, giving a 37' \times 37' field of view and 0.54 arcseconds pixel⁻¹, was used to observe most of a transit in *g* on UT 2013-02-24. The gap in the data is due to a meridian flip.

We observed an egress in *g* at Swarthmore College's Peter van de Kamp Observatory on UT 2013-01-08. The observatory uses a 0.6 m RCOS telescope with an Apogee U16M 4K \times 4K CCD, giving a 26' \times 26' field of view. Using 2 \times 2 binning, it has 0.76 arcseconds pixel⁻¹.

We observed one partial and two full transits at Spot Observatory. The observatory uses a 0.6 m RCOS telescope with an SBIG STX 16803 4K \times 4K CCD, giving a 26' \times 26' field of view and 0.39 arcseconds pixel⁻¹. An ingress in *i* was observed on UT 2013-02-16, and full transits were observed on UT 2013-02-24 in *i* and UT 2013-04-20 in *z*. We also observed near the time of secondary transit on UT 2013-02-20 in *z*.

We observed an egress in *z* on UT 2013-02-24 and an ingress in *i* on UT 2013-06-06 with KeplerCam on the 1.2 m telescope at FLWO. KeplerCam has a single 4K \times 4K Fairchild CCD with 0.366 arcseconds pixel⁻¹, and a field of view of 23.1' \times 23.1'. We also observed near the time of secondary transit on UT 2013-02-28, UT 2013-04-08, and UT 2013-04-24 in *z*.

We observed one full and one partial transit at Montgomery Bell Academy (MBA) Long Mountain Observatory. The observatory uses a PlaneWave Instruments 0.6 m CDK telescope with an SBIG STL 11002 4008 \times 2672 CCD, giving a 30' \times 20' field of view and 0.45 arcseconds pixel⁻¹. A full transit was observed in *V* on UT 2013-02-24. However, the resulting light curve had large systematics that we were unable to adequately remove. Since the same transit epoch was observed by both Moore Observatory

telescopes in overlapping filter bands, these data added no new information to the analysis and was not included in the global fit described in §8.6. An egress in I was observed on UT 2013-03-04, and observations near the time of secondary transit were collected in z on UT 2013-02-20.

We observed two partial transits at Canela’s Robotic Observatory (CROW) in Portugal. The observations were obtained using a 0.3 m LX200 telescope with an SBIG ST-8XME 1530×1020 CCD, giving a $28' \times 19'$ field of view and 1.11 arcseconds pixel^{-1} . An ingress was observed in I_c on UT 2013-02-24, and an ingress was observed in V on UT 2013-04-28.

We observed a partial transit at Westminster College Observatory (WCO) in Pennsylvania. The observations were obtained using a Celestron 0.35 m C14 telescope with an SBIG STL-6303E 3072×2048 CCD, giving a $24' \times 16'$ field of view and 1.4 arcseconds pixel^{-1} at 3×3 pixel binning. An egress was observed using an Astrodon Clear with Blue Blocking (CBB) filter on UT 2013-04-28.

We observed near the time of secondary transit on UT 2013-04-08 and UT 2013-04-24 using the 1.0 m telescope at the ELP node of the Las Cumbres Observatory Global Telescope (LCOGT) network at McDonald observatory in Texas (Brown et al., 2013). The observations were obtained in the Pan-STARRS-Z band with an SBIG STX-16803 4096×4096 CCD, giving a $15.8' \times 15.8'$ field of view and 0.464 arcseconds pixel^{-1} (2×2 binning). The ELP data were processed using the pipeline discussed in Brown et al. (2013).

8.4.4 Adaptive Optics Observations

We obtained adaptive optics (AO) imaging using NIRC2 (instrument PI: Keith Matthews) at Keck on UT 2012-12-07. The AO imaging places limits on the existence of nearby eclipsing binaries that could be blended with the primary star KELT-6 at the resolution of the KELT and follow-up data, thereby causing a false positive planet detection. In addition, it places limits on any nearby blended source that could contribute

TABLE 12
Summary of KELT-6 Photometric Observations

Telescope	UT Date	# Obs	Band	Cycle ^a (sec)	RMS ^b (10 ⁻³)	PNR ^c ($\frac{10^{-3}}{\text{minute}}$)	Detrend Variables
<i>Primary:</i>							
MORC	2012-06-26	87	<i>r</i>	119	1.6	2.3	AM
MORC	2012-12-23	91	<i>r</i>	119	0.8	1.1	AM
PvdKO	2013-01-08	315	<i>g</i>	52	1.7	1.6	AM,PK
SPOT	2013-02-16	104	<i>i</i>	119	1.4	2.0	AM,TM
MOC DK	2013-02-24	131	<i>g</i>	141	1.3	2.0	AM,MF,SK
MORC	2013-02-24	212	<i>r</i>	119	1.0	1.4	AM,FW
SPOT	2013-02-24	278	<i>i</i>	99	1.8	2.3	AM,MF
KEPCAM	2013-02-24	361	<i>z</i>	45	1.6	1.4	AM,SK
CROW	2013-02-24	148	<i>I</i>	142	1.9	2.9	AM,PK,TM
MORC	2013-03-04	95	<i>z</i>	259	1.0	2.1	AM,TM
MBA	2013-03-04	39	<i>I</i>	236	1.5	3.0	AM
MORC	2013-04-20	212	<i>r</i>	119	1.2	1.7	AM
SPOT	2013-04-20	179	<i>z</i>	139	2.0	3.0	AM,TM
CROW	2013-04-28	102	<i>V</i>	135	2.1	3.2	AM,MF
WCO	2013-04-28	114	<i>CBB</i>	105	3.0	4.0	AM,TM
KEPCAM	2013-06-06	441	<i>i</i>	35	1.6	1.2	AM
<i>Secondary:</i>							
MBA	2013-02-20	58	<i>z</i>	236	1.5	3.0	AM
SPOT	2013-02-20	47	<i>z</i>	259	1.3	2.7	AM
KEPCAM	2013-02-28	757	<i>z</i>	35	2.0	1.5	AM
KEPCAM	2013-04-08	324	<i>z</i>	45	1.7	1.5	AM,XY
ELP	2013-04-08	162	<i>PS-Z</i>	90	1.9	2.3	AM,XY
MORC	2013-04-16	72	<i>z</i>	259	1.4	2.9	AM
ELP	2013-04-24	204	<i>PS-Z</i>	90	2.5	3.1	AM,XY
KEPCAM	2013-04-24	701	<i>z</i>	35	2.4	1.8	AM

Notes: MORC=University of Louisville Moore Observatory 0.6 m RCOS Telescope; PvdKO=Peter van de Kamp Observatory 0.6 m RCOS Telescope; SPOT=Spot Observatory 0.6 m RCOS Telescope; MOC DK=University of Louisville Moore Observatory PlaneWave 0.5 m CDK Telescope; KEPCAM=Keplercam at the Fred Lawrence Whipple Observatory 1.2 m Telescope; CROW=Canela's Robotic Observatory 0.3 m LX200 Telescope; MBA=Montgomery Bell Academy 0.6 m PlaneWave CDK Telescope; WCO=Westminster College Observatory 0.35 m C14 Telescope; ELP=McDonald 1.0 m Telescope (Las Cumbres Observatory Global Telescope Network); AM=airmass; PK=peak count in aperture; TM=time; MF=meridian flip; SK=sky background; FW=average FWHM in image; XY=detector x,y coordinates of target star centroid; *PS-Z*=Pan-STARRS-Z. ^a Cycle time in seconds, calculated as the mean of exposure time plus dead time during periods of back-to-back exposures. ^b RMS of residuals from the best fit model in units of 10⁻³. ^c Photometric noise rate in units of 10⁻³ minute⁻¹, calculated as $\text{RMS}/\sqrt{\Gamma}$, where RMS is the scatter in the light curve residuals and Γ is the mean number of cycles (exposure time and dead time) per minute during periods of back-to-back exposures (adapted from Fulton et al. 2011).

to the total flux, and thereby result in an underestimate of the transit depth and thus planet radius in the global fit presented in §8.6. Our observations consist of dithered frames taken with the K' filter. We used the narrow camera setting to provide fine spatial sampling of the stellar point-spread function, and used KELT-6 as its own on-axis natural guide star. The total on-source integration time was 225 seconds. The resulting image is shown in Figure 62.

We find no significant detection of off-axis sources in the immediate vicinity of KELT-6. We note that there are some conspicuous sources at the threshold of detection. However, without an image in a different filter, we are unable to determine if the position of these sources are wavelength dependent, which would indicate that they are speckles rather than real sources. Nevertheless, we can still place a conservative upper limit on any real sources based on the contrast sensitivity. Figure 63 shows the 10σ contrast sensitivity (in Δ magnitude) versus angular separation computed from Figure 62 using a three-point dither pattern to build signal and subtract sky-background (see Crepp et al. 2012). The top scale in Figure 63 shows projected separation in AU for a distance of 222 pc (see Table 13). The scale on the right side of the plot estimates the mass in units of M_{\odot} at a given contrast, estimated using the Baraffe et al. (1998) models. We can exclude companions beyond a distance of 0.5 arcseconds (111 AU) from KELT-6 down to a magnitude difference of 6.0 magnitudes at 10σ .

8.5 Host Star Properties

8.5.1 Properties from the Literature

Table 13 lists various properties and measurements of KELT-6 collected from the literature and derived in this work. The data from the literature include FUV and NUV fluxes from GALEX (Martin et al., 2005), $B-V$ color from Harris & Upgren (1964), optical fluxes in the B_T and V_T passbands from the Tycho-2 catalog (Høg et al., 2000), V and I_C from The Amateur Sky Survey (TASS; Richmond et al. 2000), near-infrared (IR)

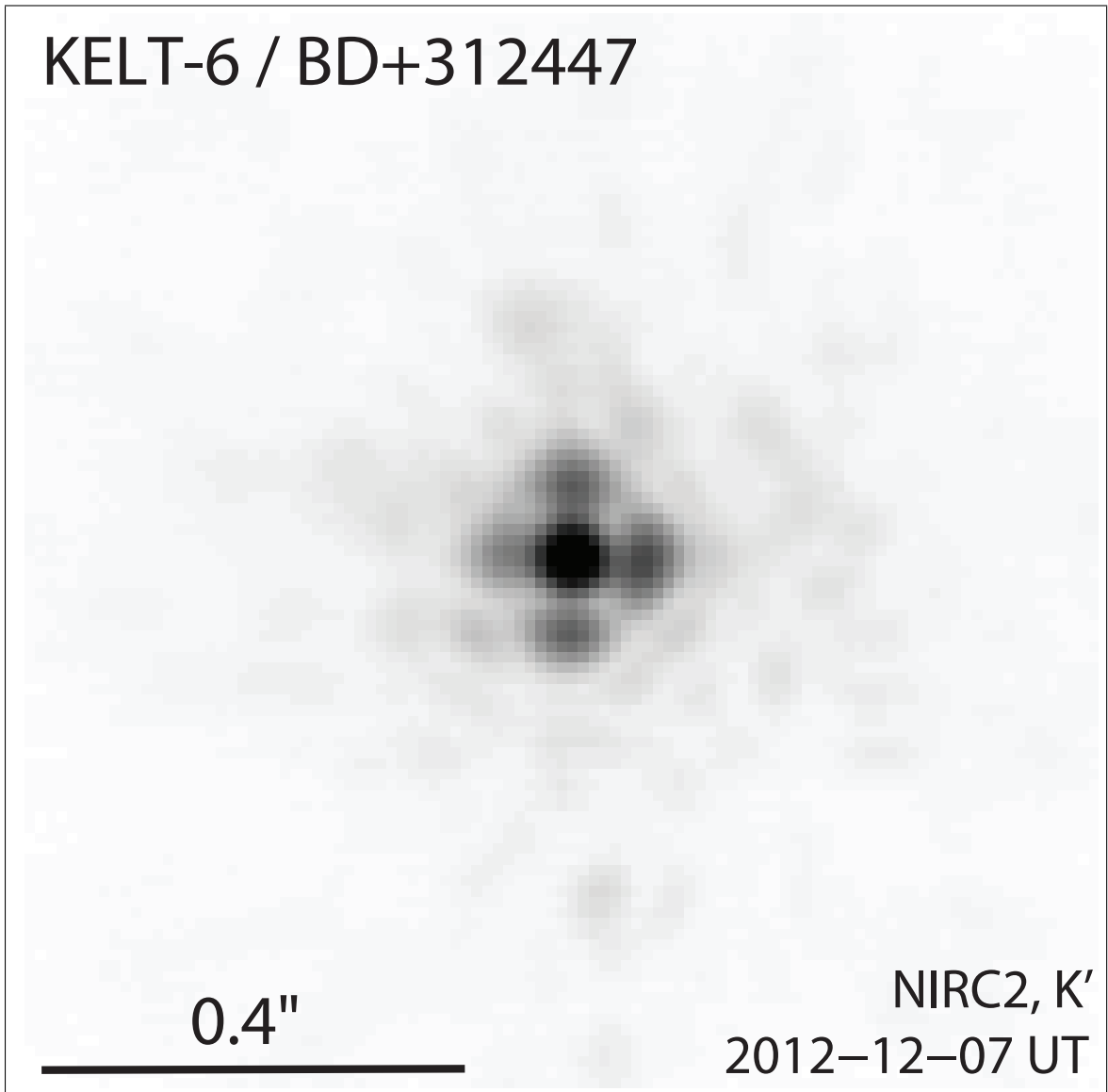


Figure 62. Keck adaptive optics image of KELT-6 taken with NIRC2 in the K' filter. The image is displayed on a negative square-root intensity scale to emphasize the surrounding regions. North is up, and east is left.

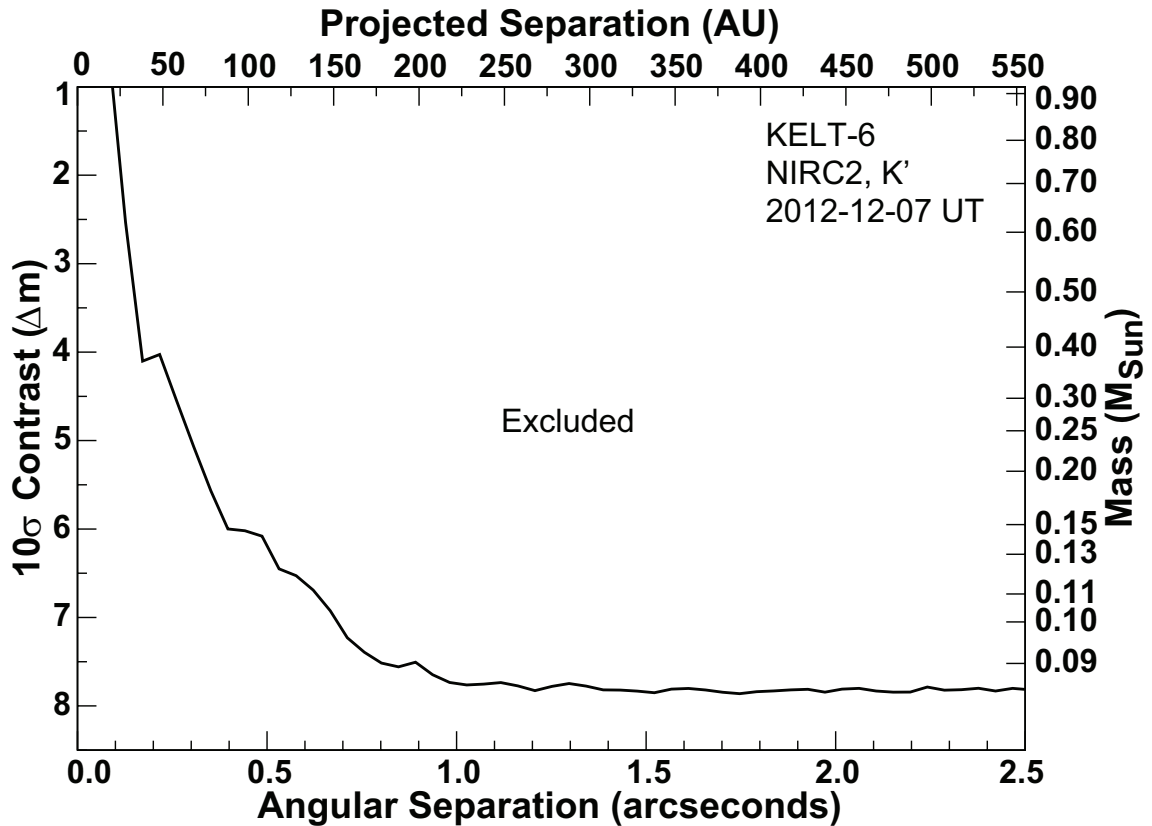


Figure 63. Contrast sensitivity derived from the Keck adaptive optics image of KELT-6 shown in Figure 62. The 10σ contrast in Δ magnitude is plotted against angular separation in arcseconds. The scale on top shows projected separation in AU for a distance of 222 pc (see Table 13). The scale on the right side of the plot estimates the mass in units of M_{\odot} at a given contrast, estimated using the Baraffe et al. (1998) models. We can exclude companions beyond a distance of 0.5 arcseconds (111 AU) from KELT-6 down to a magnitude difference of 6.0 magnitudes at 10σ .

fluxes in the J , H and K_S passbands from the 2MASS Point Source Catalog (Skrutskie et al. 2006; Cutri et al. 2003), near- and mid-IR fluxes in three WISE passbands (Wright et al. 2010; Cutri et al. 2012), and proper motions from the NOMAD catalog (Zacharias et al., 2004).

8.5.2 Spectroscopic Analysis

We use both the TRES and HIRES spectra to derive the stellar properties of KELT-6. To analyze the TRES spectra, we use the Spectral Parameter Classification (SPC) procedure version 2.2 (Buchhave et al., 2012) with T_{eff} , $\log g_*$, $[\text{m}/\text{H}]$, and $v \sin i_*$ as free parameters. Since each of the 24 TRES spectra yielded similar results, we took the mean value for each stellar parameter. The uncertainties are dominated by systematic rather than statistical errors, so we adopt the mean error for each parameter. The results are: $T_{\text{eff}} = 6098 \pm 50$ K, $\log g_* = 3.83 \pm 0.10$, $[\text{m}/\text{H}] = -0.34 \pm 0.08$, and $v \sin i_* = 6.7 \pm 0.5$ km s⁻¹, giving the star an inferred spectral type of F8.

To analyze the HIRES spectra, we use spectral synthesis modeling with Spectroscopy Made Easy (SME, Valenti & Piskunov 1996, Valenti & Fischer 2005). The free parameters for the model included T_{eff} , $v \sin i_*$, $\log g_*$, and $[\text{Fe}/\text{H}]$. The microturbulent velocity was fixed to 0.85 km s⁻¹ in this model and the macroturbulent velocity was specified as a function of effective temperature (Valenti & Fischer, 2005). After the first model was generated, two other iterations were run with temperature offsets of ± 100 K from the model temperature to evaluate degeneracy between the model parameters. If the RMS for these new fit parameters relative to the original model values exceeds the uncertainties on the original model values estimated using the error analysis of Valenti & Fischer (2005), then these larger uncertainties are adopted. However, in this case, the fits starting with the temperature offsets settled on values very close to those found using the original model, differing by much less than the estimated uncertainties on the original model values. Therefore, we adopted these original uncertainties, which include systematic error sources as described in Valenti & Fischer (2005). Based on this

TABLE 13
KELT-6 Stellar Properties

Parameter	Description (Units)	Value	Source	Ref.
Names		TYC 2532-556-1 BD+31 2447 Weis 32018		
α_{J2000}		13:03:55.647	Tycho-2	1
δ_{J2000}		+30:38:24.26	Tycho-2	1
FUV_{GALEX}		20.328 ± 0.242	GALEX	2
NUV_{GALEX}		14.263 ± 0.190	GALEX	2
B_T		10.837 ± 0.049	Tycho-2	1
V_T		10.418 ± 0.047	Tycho-2	1
$B_J - V_J$		0.49 ± 0.008	Harris	3
V		10.337 ± 0.054	TASS	4
I_C		9.745 ± 0.061	TASS	4
J		9.302 ± 0.05	2MASS	5
H		9.137 ± 0.05	2MASS	5
K_S		9.083 ± 0.05	2MASS	5
WISE1		11.706 ± 0.1	WISE	6
WISE2		12.38 ± 0.1	WISE	6
WISE3		14.311 ± 0.1	WISE	6
μ_α	Proper Motion in RA (mas yr ⁻¹)	-6.4 ± 0.7	NOMAD	7
μ_δ	Proper Motion in Dec. (mas yr ⁻¹)	15.6 ± 0.7	NOMAD	7
γ_{abs}	Absolute Systemic RV (km s ⁻¹)	1.1 ± 0.2	This Paper ^a	
.....	Spectral Type	F8 \pm 1	This Paper	
d	Distance (pc)	222 ± 8	This Paper	
.....	Age (Gyr)	6.1 ± 0.2	This Paper ^b	
A_V	Visual Extinction	0.01 ± 0.02	This Paper	
(U°, V, W)	Galactic Space Velocities (km s ⁻¹)	$(-6.3 \pm 0.9, 23.2 \pm 0.8, 6.9 \pm 0.2)$	This Paper ^d	

Notes: Magnitudes are on the AB system. Uncertainties for the 2MASS and WISE bands were increased to 0.05 mag and 0.10 mag, respectively, to account for systematic uncertainties. 1=Høg et al. (2000), 2=Martin et al. (2005), 3=Harris & Uggren (1964), 4=Richmond et al. (2000), 5=Skrutskie et al. (2006); Cutri et al. (2003), 6=Wright et al. (2010); Cutri et al. (2012), 7=Zacharias et al. (2004).

^a The absolute RV uncertainty is due to the systematic uncertainties in the absolute velocities of the RV standard stars. ^b The uncertainty does not include possible systematic errors in the adopted evolutionary tracks. ^c We adopt a right-handed coordinate system such that positive U is toward the Galactic Center. ^d See §8.5.3

analysis, KELT-6 appears to be a main sequence or very slightly evolved subgiant with $T_{\text{eff}} = 6100 \pm 44\text{K}$, $\log g_{\star} = 3.961 \pm 0.060$ and sub-solar metallicity, $[\text{Fe}/\text{H}] = -0.277$. The star has a projected rotational velocity $v \sin i_{\star} = 5.0 \pm 0.5 \text{ km s}^{-1}$.

Comparing the parameter values determined from the TRES spectra using SPC v2.2 to those determined from the HIRES spectra using SME, we generally find agreement to $\sim 1\sigma$ or better, except for $v \sin i_{\star}$, which differs by $\sim 3\sigma$. We do not have a good explanation for the $v \sin i_{\star}$ discrepancy. However, we do not use $v \sin i_{\star}$ in our global fits, so this discrepancy is unimportant for the present analysis. The individual TRES spectra have a signal-to-noise ratio (SNR) of ~ 40 while the HIRES spectrum used to derive the stellar parameters has a SNR of ~ 180 . We therefore adopt the higher SNR HIRES stellar parameters for the analyses in this paper, although we note that the uncertainties in both determinations are likely to be dominated by systematic errors.

8.5.3 UVW Space Motion

We evaluate the motion of KELT-6 through the Galaxy to place it among standard stellar populations. We adopt an absolute radial velocity of $+1.1 \pm 0.2 \text{ km s}^{-1}$, based on the mean of the TRES and HIRES absolute RVs listed in Table 11, where the uncertainty is due to the systematic uncertainties in the absolute velocities of the RV standard stars. Combining the adopted absolute RV with distance estimated from fitting the spectral energy distribution (§8.5.4) and proper motion information from the NOMAD catalog (Zacharias et al., 2004), we find that KELT-6 has U, V, W space motion (where positive U is in the direction of the Galactic Center) of $-6.3 \pm 0.9, 23.2 \pm 0.8, 6.9 \pm 0.2$, all in units of km s^{-1} , making it unambiguously a thin disk star.

8.5.4 SED Analysis

We construct an empirical, broad-band spectral energy distribution (SED) of KELT-6, shown in Figure 64. We use the FUV and NUV fluxes from GALEX (Martin et al., 2005), the B_T and V_T colors from the Tycho-2 catalog (Høg et al., 2000), V and I_C from

TASS (Richmond et al., 2000), near-infrared (NIR) fluxes in the J , H , and K_S passbands from the 2MASS Point Source Catalog (Cutri et al., 2003; Skrutskie et al., 2006), and the near- and mid-IR fluxes in three WISE passbands (Wright et al., 2010). We fit this SED to NextGen models from Hauschildt et al. (1999) by fixing the values of T_{eff} , $\log g_*$ and $[\text{Fe}/\text{H}]$ inferred from the fiducial model fit to the light curve, RV, and spectroscopic data as described in §8.6 and listed in Table 15, and then finding the values of the visual extinction A_V and distance d that minimize χ^2 . The best fit model has a reduced χ^2 of 1.61 for 10 degrees of freedom. We find $A_V = 0.01 \pm 0.02$ and $d = 222 \pm 8$ pc. We note that the quoted statistical uncertainties on A_V and d are likely to be underestimated because we have not accounted for the uncertainties in values of T_{eff} , $\log g_*$ and $[\text{Fe}/\text{H}]$ used to derive the model SED. Furthermore, it is likely that alternate model atmospheres would predict somewhat different SEDs and thus values of the extinction and distance.

8.6 Characterization of the System

To determine the final orbital and physical parameters of the KELT-6 system, we combine the results from the spectroscopic analysis, the light curves, and the HIRES RVs of KELT-6 as inputs to a global fit using a custom version of EXOFAST (Eastman et al., 2013). The TRES RVs are not used in the global fit analysis. The EXOFAST analysis package does a simultaneous Markov Chain Monte Carlo (MCMC) fit to the photometric and spectroscopic data to derive system parameters. It includes constraints on the stellar parameters M_* and R_* from either the empirical relations in Torres et al. (2010) or from Yonsei-Yale stellar models (Demarque et al., 2004), in order to break the well-known degeneracy between M_* and R_* for single-lined spectroscopic eclipsing systems. EXOFAST scales the RV and light curve data uncertainties such that the probability that the χ^2 is larger than the value we achieved, $P(> \chi^2)$, is 0.5, to ensure the resulting parameter uncertainties are roughly accurate. The global fit method is similar to that

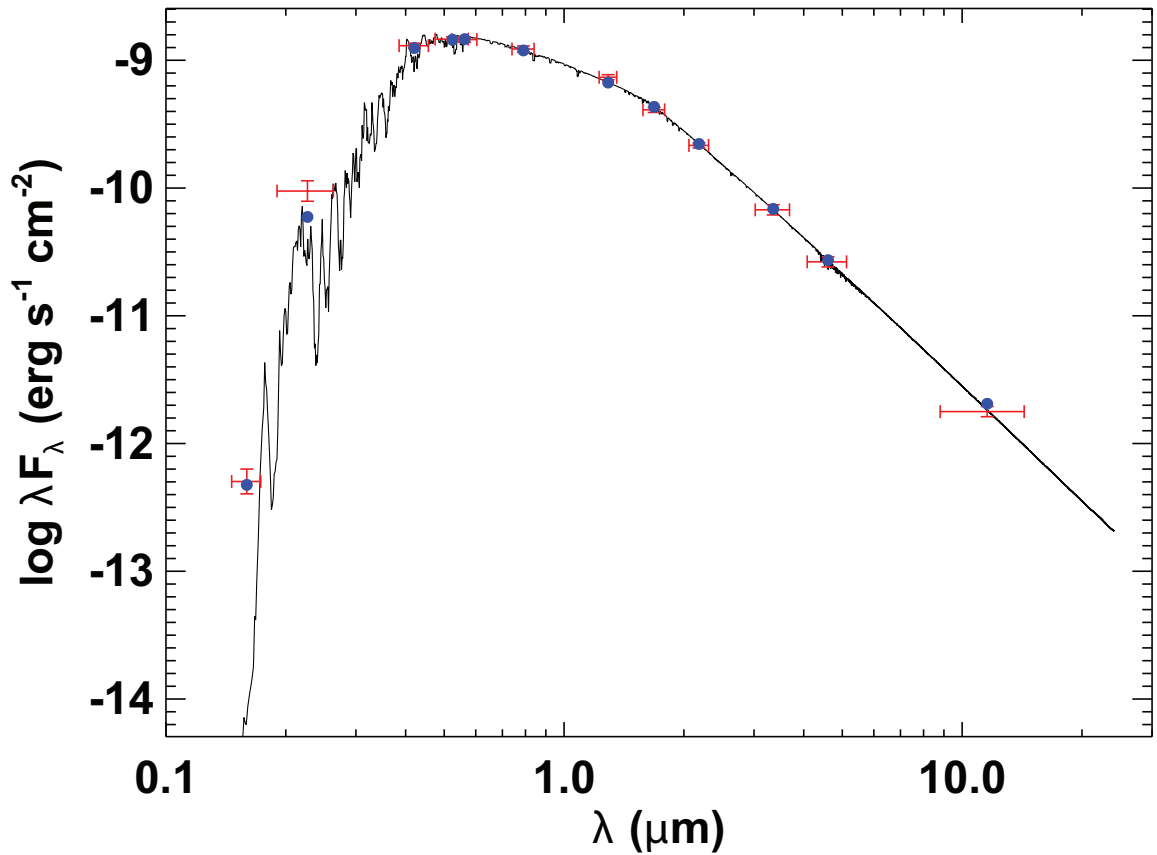


Figure 64. Measured and best-fit SED for KELT-6 from UV through mid-IR. The intersection points of the red error bars indicate measurements of the flux of KELT-6 in the UV, optical, NIR, and mid-IR passbands listed in Table 13. The vertical error bars are the 1σ photometric uncertainties, whereas the horizontal error bars are the effective widths of the passbands. The solid curve is the best-fit theoretical SED from the NextGen models of Hauschildt et al. (1999), assuming stellar parameters T_{eff} , $\log g_\star$ and $[\text{Fe}/\text{H}]$ fixed at the values in Table 15 from the fiducial fit, with A_V and d allowed to vary. The blue dots are the predicted passband-integrated fluxes of the best-fit theoretical SED corresponding to our observed photometric bands.

described in detail in Siverd et al. (2012), but we note a few differences below.⁵

8.6.1 Light Curve Detrending

Because KELT-6b’s transits have an unusually long duration and relatively shallow depth (by ground-based observing standards), treatment of light curve systematics plays an important role in the accuracy of parameters determined by the EXOFAST global fit. The inclusion of detrending parameters into the global fit can often mitigate the effect of light curve systematics, but sometimes at the expense of introducing extra local minima in χ^2 space, which may cause other complications in the analysis. Therefore, it is important to maximize the detrending improvements to the fit of each light curve while minimizing the number of detrending parameters.

Systematically fitting each light curve using all combinations of ~ 15 possible detrending parameters and comparing all of the resulting χ^2 values using the $\Delta\chi^2$ statistic would be prohibitive. Instead, we opted to use the interactive detrending capabilities of the AIJ package (see §8.4.3) to search for up to three parameters that appeared to reduce the systematics in each light curve. We then individually fit each of the full transit light curves using EXOFAST, and repeated the fit using various combinations of the detrending parameters selected for that light curve. Finally, we compared χ^2 from before and after the inclusion of an additional detrending parameter to determine if the probability of a chance improvement was more than a few percent. If so, we did not include the additional detrending parameter in the global fit.

It is important to emphasize that the light curves fitted in EXOFAST were the raw light curves (i.e. not the detrended light curves from AIJ). The only way in which the results of the AIJ analysis entered into the final analysis was in the choice of detrending parameters and the initial conditions adopted. Specifically, the detrend parameter

⁵In the EXOFAST analysis, which includes the modeling of the filter-specific limb darkening parameters of the transit, we employ the transmission curves defined for the primed SDSS filters rather than the unprimed versions. We also use the Kepler transmission curve to approximate the CBB filter. We expect any differences due to those discrepancies to be well below the precision of all our observations in this paper and of the limb darkening tables from Claret & Bloemen (2011).

coefficients determined in AIJ were used as starting points for the EXOFAST fits. However these parameter coefficients were otherwise allowed to vary freely in order to minimize χ^2 .

One detrending parameter we included that warrants additional discussion is an offset in the zero point of the photometry arising from a change in placement of the target and/or comparison star(s) on the CCD pixel array during time series observations. These positional changes typically result in a zero point shift in the photometry at that epoch in the light curve due to interpixel response differences and imperfect flat-field corrections. We found such positional changes due to a meridian flip in the MOC DK light curve on UT 2013-02-24, as well as an equipment failure in the SPOT UT 2013-02-24 light curve (see Table 12 and Figure 60). We therefore included a detrending parameter that accounts for a change in the zero point of the relative photometry before and after the specified time.

In addition, fits to individual partial light curves often resulted in obviously incorrect models. We therefore chose detrending parameters for such ingress- or egress-only data by hand using AIJ without a rigorous $\Delta\chi^2$ analysis.

Light curves from near the time of predicted secondary eclipse were treated somewhat differently. In particular, these were airmass detrended directly in AIJ, and when abrupt changes in the light curve were correlated with a change in position of the target star on the detector, x and y pixel positions of the target star centroid were also used as detrending parameters.

The final detrending parameters adopted for all of the light curves are shown in Table 12.

8.6.2 Global Fits

Using the KELT-6b primary transit light curves, the detrending parameters and priors determined in the previous section, and the results from the HIRES RV and spectroscopic analyses, we computed a series of 12 global fits using our custom version of EXOFAST. The results of six illustrative global fits are shown in Table 14. The table lists

four global fit parameter choices (as detailed in the remainder of this subsection) for each of the six fits, along with the values of several key system parameters computed as part of each fit.

All global fits included a prior on orbital period $P = 7.8457 \pm 0.0002$ days from the KELT-North data and priors on host star effective temperature $T_{\text{eff}} = 6100 \pm 44$ K and metallicity $[\text{Fe}/\text{H}] = -0.277 \pm 0.04$ from the HIRES spectroscopy. The priors were implemented as a χ^2 penalty in EXOFAST (see Eastman et al. 2013 for details). For some of the global fits we also included a prior on stellar surface gravity $\log g_{\star} = 3.961 \pm 0.060$ from the HIRES spectroscopy. For the others, $\log g_{\star}$ was constrained only by the transit data through the well-known direct constraint on ρ_{\star} from the light curve and RV data, combined with a constraint on the stellar mass-radius relation through either the Torres relations or the Yonsei-Yale evolutionary models. Fitting the HIRES RV data independently to a Keplerian model, we found an acceleration (“RV slope”) of $-0.239 \text{ m s}^{-1} \text{ day}^{-1}$, which is highly significant at the $\sim 7\sigma$ level. Therefore, we proceeded with RV slope as a free parameter for all global fits.

In addition to the slope, there were four additional choices that had to be considered when performing the global fit. First, we needed to decide which transits to include in the global fit. We defined two alternative sets of light curve data to consider: (1) the 5 “full” transits with both an ingress and egress and (2) all 16 full and partial transits. Second, as mentioned previously, we had the option to either include a prior on stellar surface gravity $\log g_{\star} = 3.961 \pm 0.060$ based on the HIRES spectroscopy, or to fit for stellar surface gravity without a prior. Third, we had the option to fit the orbital eccentricity and argument of periastron as free parameters or fix them to zero to force a circular orbit. Fourth, we had the option to break the degeneracy between M_{\star} and R_{\star} by imposing external constraints either from the relations of Torres et al. (2010) (Torres constraints) or by imposing constraints from the Yonsei-Yale stellar models (Demarque et al., 2004) (Yonsei-Yale constraints).

We first computed the four combinations of global fits using the 5 full transits with

the Torres constraints. The four global fits are defined by the different combinations of eccentric vs. circular orbits, and $\log g_*$ with a spectroscopic prior vs. $\log g_*$ free. The column labeled “Fit 5” in Table 14 shows the results for the Torres constrained, eccentric global fit, with no $\log g_*$ prior. As discussed in §8.9.1, we plotted Yonsei-Yale stellar evolution tracks corresponding to the stellar mass and metallicity results from these global fits and found that the intersection of $\log g_*$ and T_{eff} values from EXOFAST did not fall within 1σ of the evolutionary tracks. We then computed the four combinations of global fits using the 5 full transits with the Yonsei-Yale constraints and found that for these fits the resulting $\log g_*$ and T_{eff} values were consistent with the corresponding Yonsei-Yale stellar evolution tracks within 1σ error. Parameter values from these four fits are listed in the columns of Table 14 labeled “Fit 1”, “Fit 2”, “Fit 3”, and “Fit 4”. The Torres constrained planet mass and radius are larger than the Yonsei-Yale constrained mass and radius by $\sim 4-7\%$, and although we cannot determine if the Torres relations or the Yonsei-Yale models best represent low metallicity systems, we prefer the Yonsei-Yale constrained global fits for self-consistency with the stellar evolution tracks in §8.9.1.

We next considered the 16 full and partial transit global fits. We computed only the four combinations corresponding to the adopted Yonsei-Yale constrained global fits. Although we computed very long Markov chains with 10^6 links, three of the four global fits resulted in some parameters (mostly detrending parameters corresponding to partial light curves) that did not fully converge. Converged parameters have greater than 1000 independent draws and a Gelman-Rubin statistic less than 1.01 (see Eastman et al. 2013 and Ford 2006). The column labeled “Fit 6” in Table 14 lists the results for the Yonsei-Yale constrained, eccentric global fit, with no $\log g_*$ prior. The system parameters resulting from the 16 transit global fits are nearly identical to the parameters from the 5 transit global fits. This is to be expected since detrended partial light curves will not add significant constraints to transit depth and shape when jointly fit with full transits. Given the partial transit minor convergence issues, concerns about the ability to properly remove systematics from these light curves, and the lack of significant additional constraints on

transit depth and shape from the partial transits, we adopted the global fits based on the 5 full transits. We did however use the 16 transit global fits for the transit timing analysis in §8.6.3.

Next we examined the adopted Yonsei-Yale constrained global fits that use only the 5 full transits. These four global fits are defined by the different combinations of eccentric vs. circular orbits, and $\log g_*$ prior vs. $\log g_*$ free. Since it is typically difficult to measure $\log g_*$ to the same precision spectroscopically that can be measured from a transit, we choose not to impose a prior on $\log g_*$ from the HIRES spectroscopy. However, we are wary of measurements of $\log g_*$ from the transits in this case, since the duration is very long for a ground-based transit observation. Comparing parameter values in column “Fit 4” of Table 14 with column “Fit 1”, and comparing column “Fit 2” with column “Fit 3”, we found that imposing a spectroscopic prior on $\log g_*$ increased the stellar and planetary radii by $\sim 3\%$ in the circular case and by $\sim 7\%$ in the eccentric case. However, all of the system parameters are within $\sim 1\sigma$ of the results from the global fits without a prior on $\log g_*$.

Since we had no strong prior expectation of tidal circularization of KELT-6b’s relatively long ~ 8 day orbit, we adopted the more conservative eccentric orbit global fits which have higher parameter errors. The eccentricity resulting from a fit without a spectroscopic prior on $\log g_*$ is $e = 0.22_{-0.10}^{+0.12}$. The eccentricity resulting from a fit with the HIRES spectroscopic prior on $\log g_*$ is $e = 0.27_{-0.12}^{+0.11}$. As pointed out by Lucy & Sweeney (1971), there is a bias for inferred values of eccentricity with low significance, due to the fact that e is a positive definite quantity. Although we adopt an eccentric orbit global fit, we cannot exclude the hypothesis that the orbit of KELT-6b is, in fact, circular.

Our final adopted fiducial stellar and planetary parameters were derived from the 5 full transit, Yonsei-Yale constrained, eccentric orbit global fit with no prior on $\log g_*$. Table 15 lists the full set of system parameters for the fiducial fit.

TABLE 14

Median Values and 68% Confidence Intervals for Selected System Parameters from Six Global Fits (see §8.6.2)

Parameter	Units	Fit 1 (adopted)	Fit 2	Fit 3	Fit 4	Fit 5	Fit 6
Global Fit Parameters:							
Number of Transits	5 or 16	5	5	5	5	5	16
M_* and R_* Constraint	Torres or Yonsei-Yale	Yonsei-Yale	Yonsei-Yale	Yonsei-Yale	Yonsei-Yale	Torres	Yonsei-Yale
Orbital Constraint	Circular or Eccentric .	Eccentric	Circular	Circular	Eccentric	Eccentric	Eccentric
$\log g_*$ Prior	Prior or No Prior	No Prior	Prior	No Prior	Prior	No Prior	No Prior
Stellar Parameters:							
T_{eff}	Effective temp (K)	6102 ± 43	6101 ± 43	6103 ± 43	6102 ± 44	6105 ± 44	6109 ± 44
[Fe/H]	Metallicity	-0.281 ^{+0.039} _{-0.038}	-0.285 ^{+0.040} _{-0.038}	-0.282 ^{+0.039} _{-0.037}	-0.284 ^{+0.040} _{-0.039}	-0.280 ^{+0.039} _{-0.039}	-0.284 ^{+0.039} _{-0.038}
$\log g_*$	Surface gravity (cgs)	4.074 ^{+0.045} _{-0.070}	4.057 ^{+0.036} _{-0.037}	4.083 ^{+0.022} _{-0.042}	4.012 ^{+0.049} _{-0.054}	4.085 ^{+0.046} _{-0.073}	4.064 ^{+0.049} _{-0.068}
M_*	Mass (M_{\odot})	1.085 ^{+0.043} _{-0.040}	1.086 ^{+0.033} _{-0.036}	1.081 ^{+0.032} _{-0.034}	1.110 ^{+0.041} _{-0.041}	1.199 ^{+0.066} _{-0.060}	1.090 ^{+0.042} _{-0.040}
R_*	Radius (R_{\odot})	1.580 ^{+0.160} _{-0.094}	1.615 ^{+0.086} _{-0.078}	1.562 ^{+0.091} _{-0.046}	1.720 ^{+0.140} _{-0.110}	1.640 ^{+0.170} _{-0.100}	1.600 ^{+0.160} _{-0.100}
Planetary Parameters:							
M_p	Mass (M_J)	0.430 ^{+0.045} _{-0.046}	0.438 ^{+0.038} _{-0.037}	0.436 ^{+0.037} _{-0.037}	0.446 ^{+0.044} _{-0.043}	0.461 ^{+0.049} _{-0.048}	0.431 ^{+0.046} _{-0.046}
R_p	Radius (R_J)	1.193 ^{+0.130} _{-0.077}	1.228 ^{+0.080} _{-0.070}	1.178 ^{+0.083} _{-0.043}	1.304 ^{+0.110} _{-0.093}	1.240 ^{+0.140} _{-0.085}	1.206 ^{+0.120} _{-0.085}
$\log p$	Surface gravity	2.866 ^{+0.063} _{-0.081}	2.855 ^{+0.057} _{-0.061}	2.885 ^{+0.049} _{-0.061}	2.810 ^{+0.065} _{-0.068}	2.865 ^{+0.064} _{-0.083}	2.862 ^{+0.064} _{-0.080}
e	Eccentricity	0.22 ^{+0.12} _{-0.10}	—	—	0.27 ^{+0.11} _{-0.12}	0.22 ^{+0.12} _{-0.10}	0.22 ^{+0.12} _{-0.10}
a	Semi-major axis (AU)	0.079 ^{+0.00100} _{-0.00099}	0.079 ^{+0.00080} _{-0.00087}	0.079 ^{+0.00078} _{-0.00085}	0.080 ^{+0.00098} _{-0.00099}	0.082 ^{+0.00150} _{-0.00140}	0.080 ^{+0.001} _{-0.001}
T_{eq}	Equilibrium temp (K)	1313 ⁺⁵⁹ ₋₃₈	1327 ⁺³³ ₋₃₀	1307 ⁺³⁴ ₋₂₀	1364 ⁺⁴⁸ ₋₄₃	1317 ⁺⁶¹ ₋₃₈	1323 ⁺⁵⁸ ₋₄₁

Comparing the fiducial system parameters with those from the other 11 global fits, we note differences in planetary mass $\Delta M_p \sim 10\%$ ($\sim 1\sigma$), planetary radius $\Delta R_p \sim 10\%$ ($\sim 1\sigma$), orbital radius $\Delta a \sim 5\%$ ($\sim 4\sigma$), planetary equivalent temperature $\Delta T_{\text{eq}} \sim 5\%$ ($\sim 1\sigma$), stellar mass $\Delta M_\star \sim 15\%$ ($\sim 3\sigma$), and stellar radius $\Delta R_\star \sim 15\%$ ($\sim 1.5\sigma$). Clearly, the choice of global fit input parameters, priors, and external constraints, significantly affects some of the inferred system parameters. Thus, it is important to note that other plausible global fits yield significantly different values for some system parameters.

The HIRES RV uncertainty scaling for the fiducial global fit is 2.808, which is fairly high and is suggestive of substantial stellar jitter in the RV data. The RMS of the RV residuals of the fit to these scaled data is 8.0 m s^{-1} , which is somewhat high ($\sim 2\sigma$) compared to what we would expect based on Wright (2005). We do not have a compelling explanation for the high RV residuals. As noted in §8.4.2, we did not attempt to measure line bisectors for the HIRES data.

8.6.3 Transit Timing Variations

We investigated the transit center times of the 16 full and partial transits adopted from the 16 transit, Yonsei-Yale constrained, eccentric orbit global fit with no prior on $\log g_\star$ for any signs of transit time variations (TTVs). We were careful to ensure that all quoted times had been properly reported in BJD_{TDB} (e.g., Eastman et al. 2010). When we performed the global fit, we allowed for transit time $T_{\text{C},i}$ for each of the transits shown in Table 16 to be a free parameter. Therefore, the individual follow-up transit light curves do not constrain the KELT-6b ephemeris (global epoch T_{C} and period P). Rather, the constraints on these parameters in the global fit come only from the RV data, and the prior imposed from the KELT discovery data. Using the follow-up transit light curves to constrain the ephemeris in the global fit would artificially reduce any observed TTV signal.

Subsequent to the global fit, we then derived a separate ephemeris from only the transit timing data by fitting a straight line to all inferred transit center times from the

TABLE 15

Adopted Median Values and 68% Confidence Intervals for the Physical and Orbital Parameters of the KELT-6 System from the Fiducial Global Fit Described in §8.6.2.

Parameter	Units	Value (adopted)
Stellar Parameters:		
M_*	Mass (M_\odot)	$1.085^{+0.043}_{-0.040}$
R_*	Radius (R_\odot)	$1.580^{+0.16}_{-0.094}$
L_*	Luminosity (L_\odot)	$3.11^{+0.68}_{-0.39}$
ρ_*	Density (cgs)	$0.387^{+0.068}_{-0.039}$
$\log g_*$	Surface gravity (cgs)	$4.074^{+0.033}_{-0.070}$
T_{eff}	Effective temperature (K)	6102 ± 43
[Fe/H]	Metallicity	$-0.281^{+0.039}_{-0.038}$
Planetary Parameters:		
e	Eccentricity	$0.22^{+0.12}_{-0.10}$
ω_*	Argument of periastron (degrees)	80^{+110}_{-120}
P	Period (days)	7.8457 ± 0.0002
a	Semi-major axis (AU)	$0.07939^{+0.0010}_{-0.00099}$
M_P	Mass (M_J)	$0.430^{+0.045}_{-0.046}$
R_P	Radius (R_J)	$1.193^{+0.13}_{-0.077}$
ρ_P	Density (cgs)	$0.311^{+0.069}_{-0.076}$
$\log g_P$	Surface gravity	$2.868^{+0.063}_{-0.081}$
T_{eq}	Equilibrium temperature (K)	1313^{+39}_{-38}
Θ	Safronov number	$0.0521^{+0.0059}_{-0.0061}$
$\langle F \rangle$	Incident flux ($10^9 \text{ erg s}^{-1} \text{ cm}^{-2}$)	$0.653^{+0.092}_{-0.076}$
RV Parameters:		
T_C	Time of inferior conjunction (BJD _{TDB})	$2456269.3399^{+0.0071}_{-0.0072}$
T_P	Time of periastron (BJD _{TDB})	$2456269.2^{+1.7}_{-2.5}$
K	RV semi-amplitude (m s^{-1})	$42.8^{+4.5}_{-4.2}$
$M_P \sin i$	Minimum mass (M_J)	$0.430^{+0.045}_{-0.046}$
M_P/M_*	Mass ratio	$0.000378^{+0.000036}_{-0.000037}$
u	RM linear limb darkening	$0.6035^{+0.0040}_{-0.0039}$
γ_{HIRES}	m s^{-1}	-3.1 ± 3.2
$\hat{\gamma}_{\text{HIRES}}$	RV slope ($\text{m s}^{-1} \text{ day}^{-1}$)	-0.239 ± 0.037
$e \cos \omega_*$		$0.02^{+0.13}_{-0.14}$
$e \sin \omega_*$		$0.05^{+0.23}_{-0.22}$
$f(m_1, m_2)$	Mass function (M_J)	$0.000000061^{+0.000000020}_{-0.000000017}$
Primary Transit Parameters:		
R_P/R_*	Radius of the planet in stellar radii	$0.07761^{+0.0010}_{-0.00092}$
a/R_*	Semi-major axis in stellar radii	$10.79^{+0.60}_{-0.89}$
i	Inclination (degrees)	$88.81^{+0.79}_{-0.91}$
b	Impact parameter	$0.20^{+0.14}_{-0.13}$
δ	Transit depth	$0.00602^{+0.00016}_{-0.00014}$
T_0	Best-fit linear ephemeris from transits (BJD _{TDB})	$2456347.796793 \pm 0.000364$
P_{Transit}	Best-fit linear ephemeris period from transits (days)	7.8456314 ± 0.0000459
T_{FWHM}	FWHM duration (days)	$0.212^{+0.039}_{-0.029}$
τ	Ingress/egress duration (days)	$0.0175^{+0.0039}_{-0.0028}$
T_{14}	Total duration (days)	$0.230^{+0.045}_{-0.032}$
P_T	A priori non-grazing transit probability	$0.091^{+0.038}_{-0.021}$
$P_{T,G}$	A priori transit probability	$0.107^{+0.041}_{-0.024}$
Secondary Eclipse Parameters:		
T_S	Time of eclipse (BJD _{TDB})	$2456265.51^{+0.66}_{-0.70}$
b_S	Impact parameter	$0.22^{+0.18}_{-0.14}$
$T_{S,\text{FWHM}}$	FWHM duration (days)	$0.231^{+0.073}_{-0.051}$
τ_S	Ingress/egress duration (days)	$0.0194^{+0.0083}_{-0.0048}$
$T_{S,14}$	Total duration (days)	$0.251^{+0.081}_{-0.056}$
P_S	A priori non-grazing eclipse probability	$0.084^{+0.018}_{-0.010}$
$P_{S,G}$	A priori eclipse probability	$0.098^{+0.020}_{-0.012}$

TABLE 16
KELT-6b Transit Times

Epoch	T_C BJD _{TDB}	σ_{T_C} Sec	O-C Sec	O-C σ_{T_C}	Observatory/ Telescope
-31	2456104.581654	190	-45.17	-0.24	MORC
-8	2456285.030078	104	-145.43	-1.40	MORC
-6	2456300.723507	115	46.31	0.40	PvdKO
-1	2456339.949428	151	-151.18	-1.00	SPOT
0	2456347.797243	118	39.38	0.33	MOCDK
0	2456347.796609	79	-15.31	-0.19	MORC
0	2456347.797368	104	50.44	0.48	SPOT
0	2456347.795916	120	-77.26	-0.64	KEPCAM
0	2456347.795513	213	-112.42	-0.53	CROW
1	2456355.649675	179	625.66	3.48	MORC
1	2456355.648134	220	493.04	2.24	MBA
7	2456402.718026	82	155.28	1.89	MORC
7	2456402.715318	151	-77.39	-0.51	SPOT
8	2456410.554740	381	-618.29	-1.62	CROW
8	2456410.550639	298	-898.14	-3.01	WCO
13	2456449.788514	95	-128.47	-1.35	KEPCAM

Note: The observatory/telescope abbreviations are the same as in Table 12.

global fit. These times are listed in Table 16 and plotted in Figure 65. We find $T_0 = 2456347.796793 \pm 0.000364$, $P_{\text{Transit}} = 7.8456314 \pm 0.0000459$, with a χ^2 of 38.70 and 14 degrees of freedom. While the χ^2 is larger than one might expect, this is often the case in ground-based TTV studies, likely due to systematics in the transit data. There are $\sim 3\sigma$ deviations from the linear ephemeris on epochs 1 and 8. However, although there are consistent TTV measurements from two independent observatories on both of those epochs, we note that these data are all from ingress or egress only observations. Given the likely difficulty with properly removing systematics in partial transit data, we are unwilling to claim convincing evidence for TTVs. Further study of KELT-6b transit timing is required to rule out TTVs.

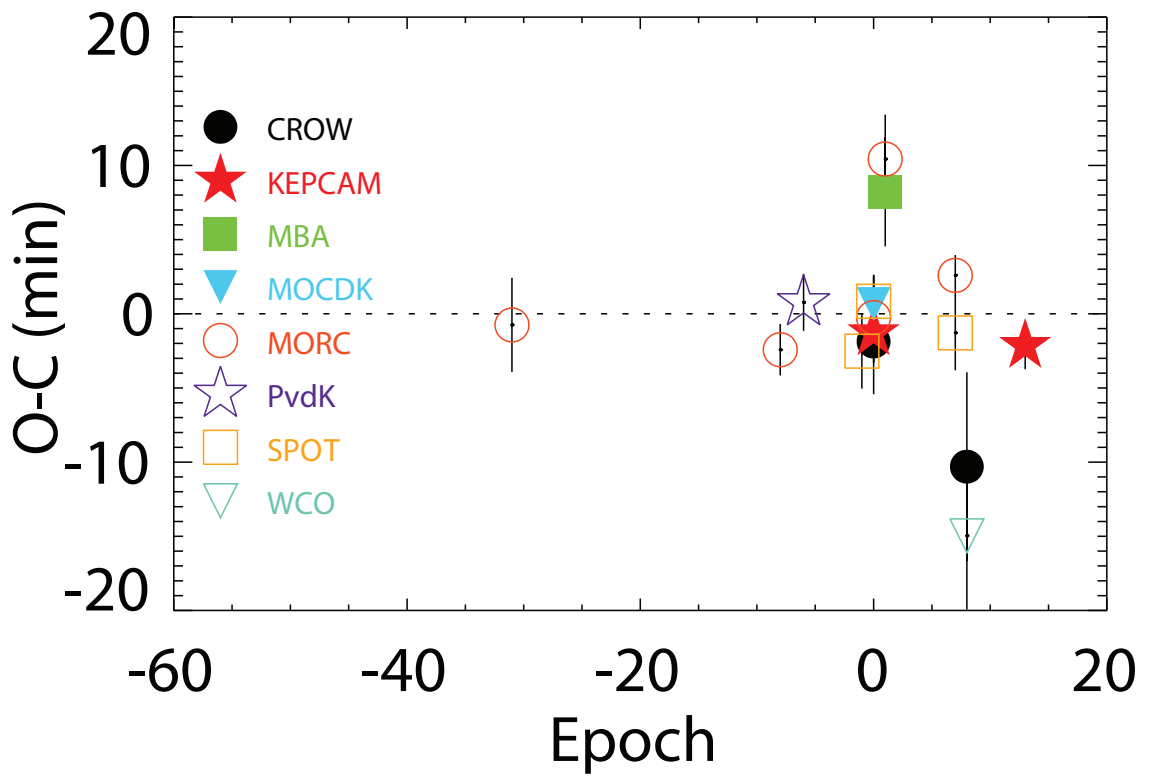


Figure 65. The residuals of the transit times from the best-fit ephemeris. The transit times are given in Table 16. The observatory/telescope abbreviations are the same as in Table 12.

8.7 Evidence for a Tertiary Companion

The Keck HIRES radial velocities show a downward trend that is well modeled by a linear slope over the time span of the HIRES RVs as illustrated in Figure 66. The fiducial model, which is displayed as a solid red line, is fit to the HIRES data only and has a slope of $\dot{\gamma} = -0.239 \pm 0.037 \text{ m s}^{-1} \text{ day}^{-1}$. A two-planet fit with the tertiary in a circular orbit yields a negligible improvement of $\Delta\chi^2 = 2.2$ relative to the fit with constant acceleration, which has a $\sim 30\%$ probability of happening by chance. With the inclusion of the full set of 24 re-reduced TRES RVs (see §8.4.2) into the single-planet plus slope and two-planet fits, $\Delta\chi^2 = 3.8$, which has a $\sim 15\%$ probability of happening by chance. Although the TRES RVs shown in Figure 66 appear to fairly strongly indicate a turn-over in the RV slope, the statistical analysis above finds only marginal evidence for a turn-over. The TRES RVs shown in Figure 66 have been shifted to best fit the HIRES fiducial model. Characterization of the tertiary will require continued RV monitoring of the KELT-6 system.

Our Keck AO K' image shows no significant detection of off-axis sources, although there are a couple of speckles at the threshold of detection (see Figure 62 and §8.4.4). Figure 67 shows the limits on mass from the AO image and from the HIRES RVs. For a given projected separation, masses above the heavy solid black line are excluded by the AO image. The heavy blue dashed line shows the lower limit for mass of the tertiary for circular orbits as a function of semimajor axis implied by the projected acceleration of $\mathcal{A} = 87 \pm 12 \text{ m s}^{-1} \text{ yr}^{-1}$ measured from the HIRES RV data. For a circular orbit with semimajor axis a and a given minimum planet mass $M_p \sin i$, the maximum projected acceleration of the star due to the planet occurs at conjunction (or opposition), and is $\mathcal{A} = GM_p \sin i a^{-2}$ (Torres, 1999). Thus a strict lower limit on the tertiary mass capable of producing the measured acceleration can be defined for a given a , assuming circular orbits⁶. Note that this mass increases as the square of projected separation. The light blue

⁶We note that this constraint assumes that the tertiary imposes a constant acceleration during the time spanned by the RV observations. In particular, it assumes that the systemic radial velocity has varied monotonically between the two groups of HIRES RVs shown in Figure 66. Because there is a substantial gap

dashed lines show the 1σ uncertainty on the minimum $M_P \sin i$ due to the uncertainty in the measured acceleration. Masses for the purported tertiary that fall below the blue dashed lines are excluded, as they do not provide sufficient acceleration at conjunction for a given semimajor axis to explain the observed trend even for an edge-on orbit. However, there could be undetected companions in the region below the blue dashed lines that are not responsible for the observed RV acceleration. The RV and AO mass curves intersect for masses comparable to the primary star, and at the diffraction-limit of a 10 m telescope on the projected separation axis. Therefore, if the speckles at the threshold of detection in Figure 62 are astrophysical, they cannot be responsible for the observed long-term acceleration in the KELT-6 radial velocities.

8.8 False Positive Analysis

One of the many challenges of ground-based photometric surveys for transiting planets is the relatively high rate of astrophysical false positives prior to RV and high precision photometry follow-up observations (e.g. Latham et al. 2009). Blended eclipsing stellar binary or triple systems can mimic some of the observable signatures of transiting low-mass companions to single stars. Brown (2003) estimated the a priori detection rates of such false positives in ground-based transit surveys similar to KELT, finding a rate that was a factor of several times larger than the expected detection rate for transiting giant planets. However, for KELT-6b, we have several lines of evidence that disfavor a false positive scenario.

First, we measured the line bisector spans of the TRES spectra following Torres et al. (2007) to explore the possibility that the RV variations are actually distortions in the spectral line profiles due to a nearby unresolved eclipsing binary or stellar activity. The bisector span variations are listed in Table 11 and plotted in the bottom panel of Figure 59.

between these two groups of points, shorter-period orbits for the tertiary in which the acceleration changes sign twice between the two groups are possible. However, we deem these to be unlikely.

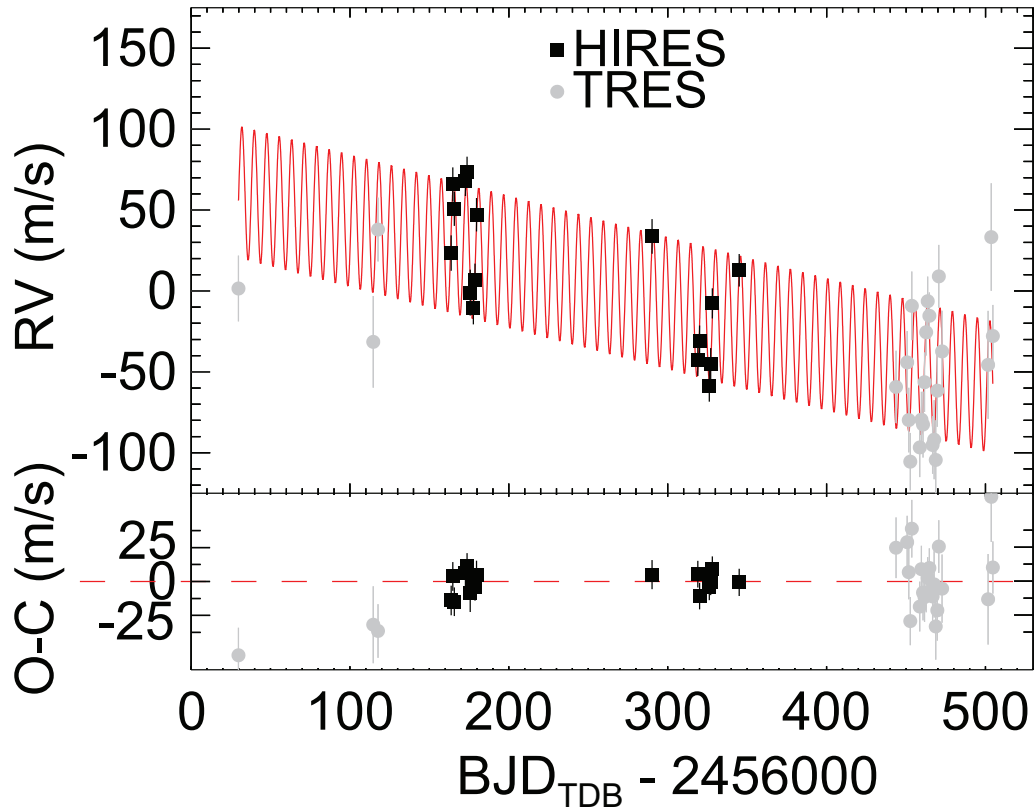


Figure 66. HIRES and TRES unphased KELT-6 radial velocities. HIRES radial velocity measurements are shown as black squares. TRES radial velocities are shown as gray circles. The HIRES error has been scaled by 2.808 as determined by the fiducial EXOFAST global fit (see §8.6). The TRES errors are unrescaled. The single-planet plus linear slope fiducial model of the KELT-6 system fit to the HIRES data only is shown as a solid red line. The TRES RVs have been shifted by a constant offset that best-fits the fiducial model. Although the TRES data appear to indicate a turnover in the RV slope, a joint fit to the HIRES and TRES data indicate only marginal evidence for a turn-over (see §8.7).

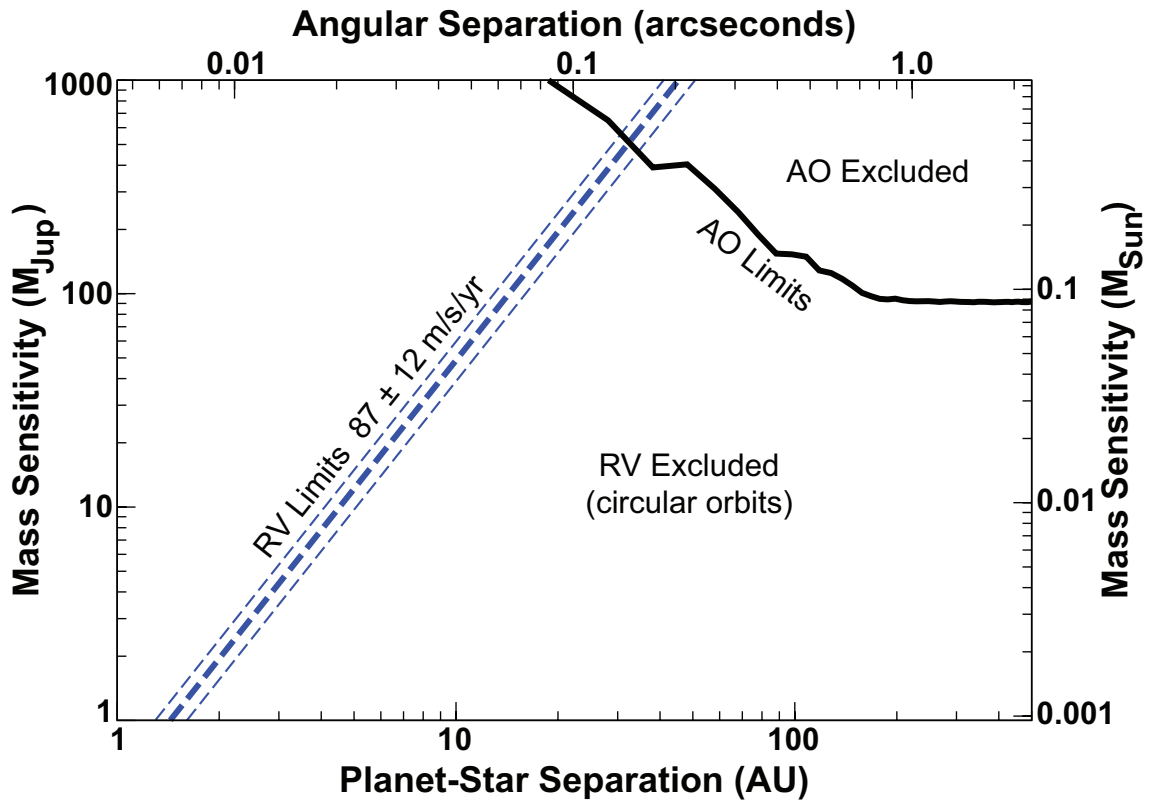


Figure 67. KELT-6 tertiary mass limits derived from the Keck AO image and measured HIRES projected acceleration versus separation in AU. The top scale shows angular separation in arcseconds corresponding to a given projected separation, assuming a distance of 222pc to the system. The AO mass limits as a function of projected separation are shown by the heavy solid black line. For a given projected separation, masses above the heavy solid black line are excluded. The heavy blue dashed line shows the lower limit on mass of the tertiary that could cause the observed projected acceleration, as a function of semimajor axis, and assuming circular orbits. The light blue dashed lines show the 1σ uncertainty in the limit due to the uncertainty in the projected acceleration. Assuming that the systematic radial velocity has varied monotonically between the two groups of HIRES RVs shown in Figure 66, masses for the tertiary causing the acceleration that fall below the dashed blue lines are excluded. However, there could be undetected companions in the region below the blue dashed lines that are not responsible for the observed RV acceleration.

The resulting bisector span variations are consistent with zero and show no correlation with the RV variations. As noted in §8.4.2, we did not attempt to measure line bisectors for the HIRES spectra since the PSF varies quite dramatically in the slit-fed HIRES instrument simply from guiding and spectrometer focus variations, which can cause instrumentally induced line asymmetries that cannot be easily distinguished from stellar sources.

Second, our follow-up photometric observations of full transits in several different filters (*griz*) are all consistent with the primary transit having nearly the same depth, and are well-modeled by transits of a dark companion across a star with the limb darkening consistent with its spectroscopically measured T_{eff} and $\log g_*$ (see Figure 60 and §8.6.2). Since the multi-band depth difference expected for a false positive scenario depends strongly on the color difference of the blended stars, the multi-band transit observations cannot rule out all false positive configurations, but can significantly limit the allowed parameter space.

Third, we collected eight sequences of photometric observations near the time of predicted secondary eclipse (at five different epochs) in *z* and Pan-STARRS-Z bands as detailed in Table 12. The individual phased light curves and the combined binned light curve are shown in Figure 68 and cover 12 hours near the time of predicted secondary eclipse. As shown in Table 15, the fiducial predicted time of secondary eclipse has an uncertainty of ~ 16 hours. We do not find conclusive evidence of a $\gtrsim 1$ mmag secondary eclipse ingress or egress in our data. However, we do not have complete phase coverage of all the secondary eclipse times that are allowed by our global fits, and therefore we cannot place a robust lower limit on the depth of any putative secondary transit arising from a blended eclipsing binary.

Although the multi-band transit and secondary eclipse observations cannot exclude all blend scenarios, they disfavor blend scenarios in which the observed transits are due to diluted eclipses of a much fainter and redder eclipsing binary (e.g., O’Donovan et al. 2006).

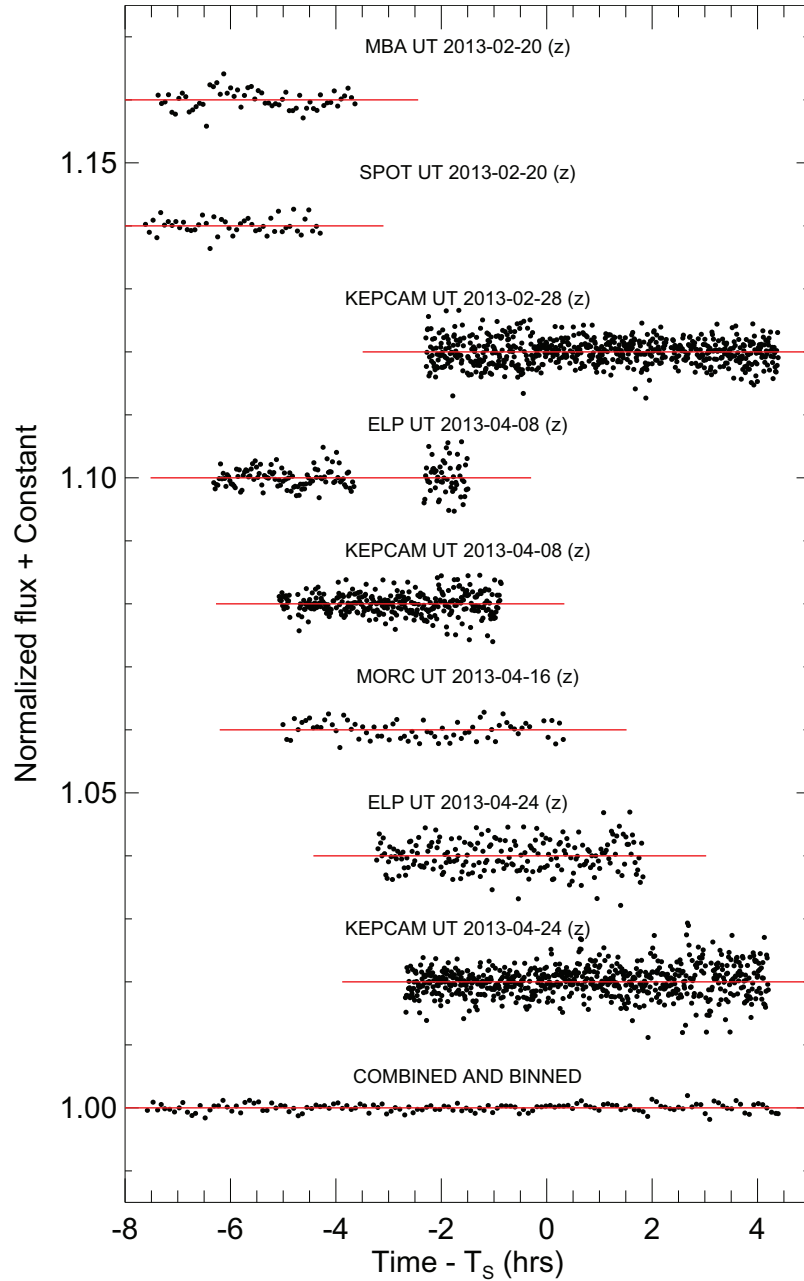


Figure 68. Phased observations of KELT-6 near the time of predicted secondary transit. The ephemeris used to phase the data is $T_0 = 2456265.51$ (BJD_{TDB}) and $P = 7.8457$ (days). The fiducial ephemeris is uncertain by ~ 0.7 days. Our observations cover only $\sim 50\%$ of the region of uncertainty. The red overplotted lines are the constant brightness models. The observatory/telescope abbreviations are the same as in Table 12. The bottom light curve shows all observations combined and binned in 5 minute intervals, and has residuals of 0.06% RMS. We find no evidence for a secondary transit in the data.

Fourth, the fiducial transit derived stellar surface gravity $\log g_{\star\text{transit}} = 4.074_{-0.070}^{+0.045}$ (the fiducial fit does not use a spectroscopic prior on $\log g_{\star}$) and the HIRES spectroscopically derived surface gravity $\log g_{\star\text{HIRES}} = 3.961 \pm 0.060$ are consistent within $\sim 1.5\sigma$.

Finally, our adaptive optics imaging excludes companions beyond a distance of 0.5 arcseconds from KELT-6 down to a magnitude difference of 6.0 magnitudes at 10σ confidence. See Figure 63.

We conclude that all of the available data are best explained by a Jupiter-sized, Saturn-mass companion transiting a slowly-rotating late-F star, with little or no evidence for significant contamination from blended sources.

8.9 Evolutionary Analysis

8.9.1 Stellar Models and Age

We use global fit values for T_{eff} , $\log g_{\star}$, stellar mass, and metallicity (§8.6 and Table 14 columns “Fit 1” and “Fit 5”), in combination with the theoretical evolutionary tracks of the Yonsei-Yale stellar models (Demarque et al., 2004), to estimate the age of the KELT-6 system. We have not directly applied a prior on the age, but rather have assumed uniform priors on $[\text{Fe}/\text{H}]$, $\log g_{\star}$, and T_{eff} , which translates into non-uniform priors on the age. The standard version of EXOFAST uses the Torres et al. (2010) relations to estimate stellar mass and radius at each step of the MCMC chains. The top panel of Figure 69 shows the theoretical HR diagram ($\log g_{\star}$ vs. T_{eff}) corresponding to Table 14 column “Fit 5”. We also show evolutionary tracks for masses corresponding to the $\pm 1\sigma$ extrema in the estimated uncertainty. The Torres constrained global fit values for T_{eff} and $\log g_{\star}$ are inconsistent by more than 1σ with the Yonsei-Yale track corresponding to the stellar mass and metallicity preferred by this global fit. To investigate the inconsistency, we modified EXOFAST to use the Yonsei-Yale models rather than the Torres et al. (2010) relations to estimate stellar mass and radius at each MCMC step. The bottom panel of Figure 69 is the same as the top panel, but for the fiducial Yonsei-Yale constrained global fit corresponding to Table 14

column “Fit 1”. The intersection of global fit values for T_{eff} and $\log g_*$ now fall near the Yonsei-Yale track at 6.1 ± 0.2 Gyr, where the uncertainty does not include possible systematic errors in the adopted evolutionary tracks. The Torres constrained global fit yields an age that is about 25% younger, and planet mass and radius that is larger by $\sim 4-7\%$. Although we cannot explain the inconsistency between the Torres constrained global fit and the Yonsei-Yale track, we expect that it may be due to slight inaccuracies in the Yonsei-Yale models and/or the Torres et al. (2010) relations for metal poor stars. We adopt the Yonsei-Yale constrained global fit for the analyses in this paper.

KELT-6 is evidently a late-F star that is just entering the subgiant stage of evolution. To check that the isochrone age is consistent with other parameters of KELT-6, we use the gyrochronology relations of Barnes (2007) to compute the age based on the rotation period of the star and its $B-V$ color. We checked the KELT light curve for periodic variability associated with spot modulation as an indicator of P_{rot} , but we were unable to detect any significant sinusoidal variability beyond the photometric noise. Lacking a direct measurement, we estimated P_{rot} using the projected rotational velocity from §8.5.2 and the stellar radius from the adopted global fit in §8.6 to be $P_{\text{rot}}/\sin i_{\text{rot}} = 16.2 \pm 3.8$ days. Harris & Upgren (1964) photoelectrically measured magnitudes and colors of KELT-6 and found $B-V = 0.49 \pm 0.008$. Tycho (Høg et al., 2000) measured B_{T} and V_{T} (Table 13), and through the filter transformations described in ESA (1997), the Tycho-based color is $B-V = 0.415 \pm 0.069$. Because the Harris & Upgren (1964) precision is much higher than Tycho’s, and since the Tycho color is consistent with the Harris & Upgren (1964) color at nearly 1σ , we adopt the Harris & Upgren (1964) color for this analysis. In particular, we are worried about inaccuracies in the Tycho-to-Johnson filter-band transformations, especially for metal-poor stars; Høg et al. (2000) state that these filter-band transformations are approximate. Based on the adopted rotation period and $B-V$ color of the star, we calculate the maximum predicted age (subject to the inclination of the rotation axis to our line of sight) to be 5.7 ± 1.3 Gyr, which is fully consistent with the isochrone age. We note that if the Tycho fiducial color is

used with the adopted rotation period, the Barnes (2007) relations yield an unrealistically large age of 46 Gyr, due to the fact that these relations break down for stars with $B - V \lesssim 0.4$, which generally have small or non-existent convective envelopes.

8.9.2 Insolation Evolution

In an investigation of transiting giant exoplanets, Demory & Seager (2011) found that for planets insolated beyond the threshold of $2 \times 10^8 \text{ erg s}^{-1} \text{ cm}^{-2}$ the radii are inflated compared to those planets with lower levels of insolation. KELT-6b currently has incident flux well above that threshold, and is a mildly inflated hot Saturn with a density of $0.248_{-0.050}^{+0.059} \text{ g cm}^{-3}$. It follows the insolation-inflation trend displayed in Figure 1 of Demory & Seager (2011). However, it is worth investigating whether KELT-6b has always been insolated above the Demory & Seager (2011) threshold. If it turns out that KELT-6b only recently began receiving enhanced irradiation, this could provide an empirical probe of the timescale of inflation mechanisms (see Assef et al. 2009 and Spiegel & Madhusudhan 2012).

To answer that question, we simulate the reverse and forward evolution of the star-planet system, using the fiducial global fit parameters listed in Table 15 as the present boundary conditions. This analysis is not intended to examine circularization of the planet's orbit, tidal locking to the star, or any type of planet-planet or planet-disk interaction or migration. Rather, it is a way to infer the insolation of the planet over time due to the changing luminosity of the star and changing star-planet separation.

We include the evolution of the star, which is assumed to follow the YREC stellar model corresponding to $M = 1.1 M_{\odot}$ and $Z = 0.0162$ (Siess et al., 2000). We also assume that the stellar rotation was influenced only by tidal torques due to the planet, with no magnetic wind and treating the star like a solid body. Although the fiducial model from §8.6.2 has an eccentric orbit, we assume a circular orbit throughout the full insolation analysis. The results of our simulations are shown in Figure 70. We tested a range of values for the tidal quality factor of the star Q_* , from $\log Q_* = 5$ to $\log Q_* = 9$. We find

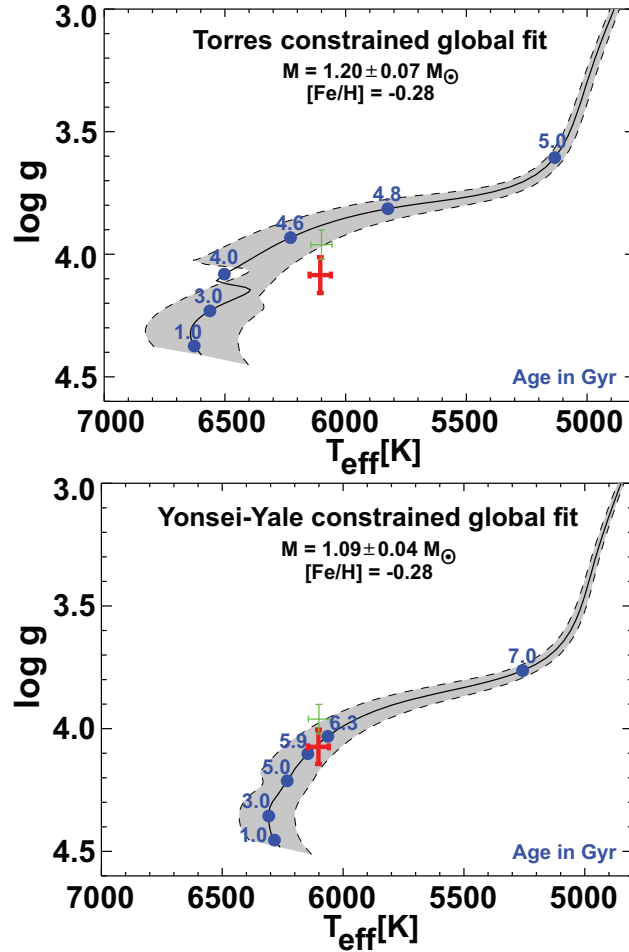


Figure 69. Theoretical HR diagrams based on Yonsei-Yale stellar evolution models (Demarque et al., 2004). The gray swaths represent the evolutionary track for the best-fit values of the mass and metallicity of the host star from the global fits corresponding to Table 14 columns “Fit 1” (bottom panel) and “Fit 5” (top panel) and discussed in §8.6. The tracks for the extreme range of 1σ uncertainties on M_* and $[\text{Fe}/\text{H}]$ are shown as dashed lines bracketing each gray swath. *Top panel:* The Yonsei-Yale track based on the Torres constrained global fit corresponding to Table 14 column “Fit 5” (see §8.9 for explanation). *Bottom panel:* The Yonsei-Yale track based on a Yonsei-Yale constrained fiducial global fit corresponding to Table 14 column “Fit 1”. The thick red crosses show T_{eff} and $\log g_*$ from the EXOFAST global fit analyses. The thin green crosses show the inferred T_{eff} and $\log g_*$ from the HIRES spectroscopic analysis alone. The blue dots represent the location of the star for various ages in Gyr. The Torres constrained global fit is inconsistent with the Yonsei-Yale track at $> 1\sigma$. We adopt the Yonsei-Yale constrained global fit represented in the bottom panel resulting in a slightly evolved star with an estimated age of 6.1 ± 0.2 Gyr, where the uncertainty does not include possible systematic errors in the adopted evolutionary tracks.

that this system is highly insensitive to the value of Q_* , because tides are not important for this system for the parameter ranges we analyzed. In all cases, KELT-6b has always received more than enough flux from its host to keep the planet irradiated beyond the Demory & Seager (2011) insolation threshold required for inflation.

8.10 Discussion

From our global fit to the spectroscopy, light curves, and HIRES RVs, we find that KELT-6b is a metal-poor hot Saturn with a measured mass $M_P = 0.430^{+0.045}_{-0.046} M_J$ and radius $R_P = 1.193^{+0.130}_{-0.077} R_J$. It is on an orbit with eccentricity $e = 0.22^{+0.12}_{-0.10}$ and semimajor axis of $a = 0.07939^{+0.00100}_{-0.00099}$ AU. The host KELT-6 is a slightly evolved late-F star with a mass $M_* = 1.085 \pm 0.043 M_\odot$, radius $R_* = 1.580^{+0.16}_{-0.094} R_\odot$, effective temperature $T_{\text{eff}} = 6102 \pm 43$ K, and a likely age of 6.1 ± 0.2 Gyr. Because of its larger semimajor axis (compared to a typical hot Jupiter), KELT-6b receives a moderate stellar insolation flux of $\langle F \rangle = 6.53^{+0.92}_{-0.76} \times 10^8 \text{ erg s}^{-1} \text{ cm}^{-2}$, implying a moderate equilibrium temperature of $T_{\text{eq}} = 1313^{+59}_{-38}$ K assuming zero albedo and perfect redistribution. The surface gravity and density of KELT-6b are $\log g_P = 2.868^{+0.063}_{-0.081}$ and $\rho_P = 0.311^{+0.069}_{-0.076} \text{ g cm}^{-3}$. We do not have in-transit KELT-6b RV data, so we have no Rossiter-McLaughlin effect constraint on the projected rotation axis of its host star.

Even among the ever growing list of known transiting exoplanets, KELT-6b is unique. We compare planet mass as a function of the orbital period (Figure 71), incident flux as a function of $\log g_P$ (Figure 72), and $[\text{Fe}/\text{H}]$ as a function of $\log g_P$ (Figure 73), for the group of all transiting hot gas giants orbiting bright hosts, which we define as $m > 0.1 M_J$, $P < 20$ days, and host star $V < 11.0$. Within that group, KELT-6 is among the 20 brightest host stars, and KELT-6b has the third longest orbital period (Figure 71), second lowest mass (Figure 71), and is the most metal-poor (Figure 73). In the larger group of all transiting exoplanets discovered by ground-based transit surveys, KELT-6b has the sixth longest period and the second longest transit duration. To our knowledge, the high precision photometric follow-up observations reported in this work include the

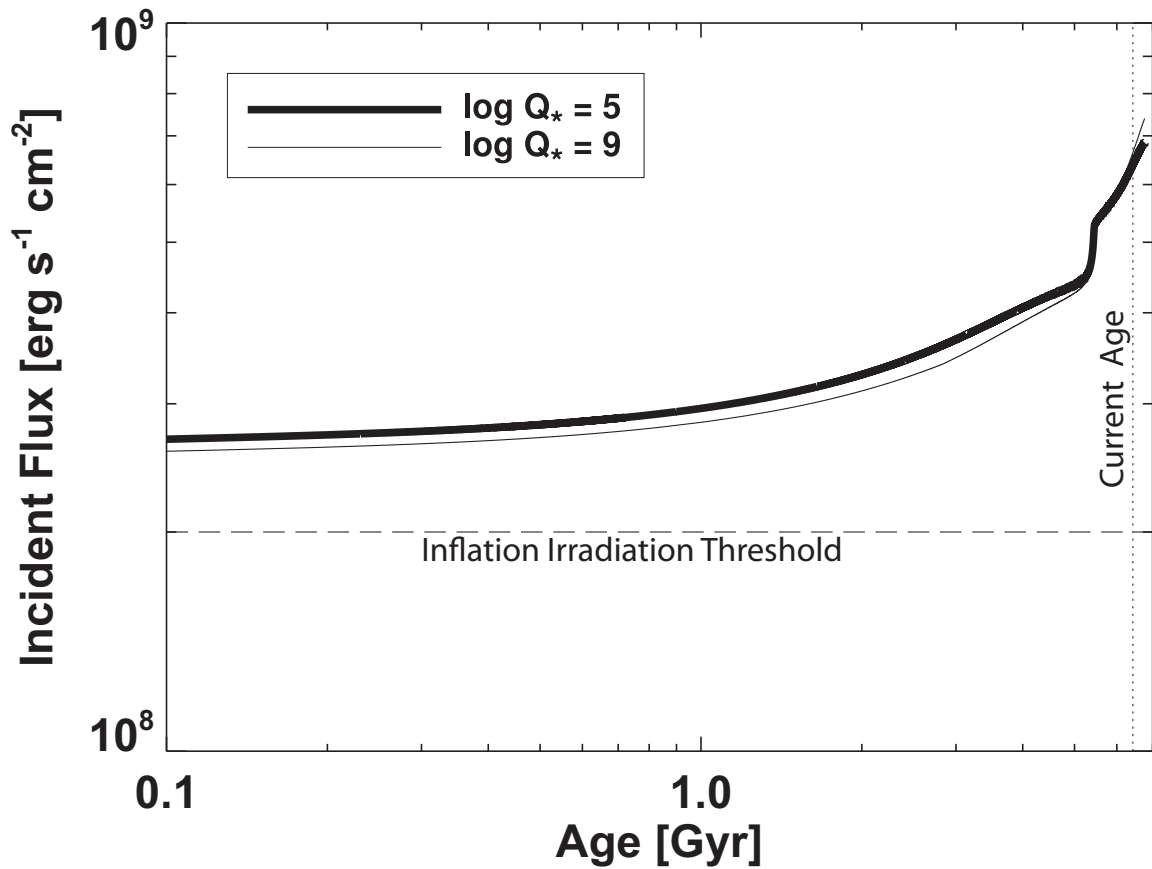


Figure 70. Change in incident flux for KELT-6b, with test values of $\log Q_* = 5$ and $\log Q_* = 9$ for KELT-6. This system is clearly insensitive to the value of Q_* in the range we analyzed. In both cases, the planet has always received more than enough flux from its host to keep the planet irradiated beyond the insolation threshold of $2 \times 10^8 \text{ erg s}^{-1} \text{ cm}^{-2}$ identified by Demory & Seager (2011).

longest duration transit ever fully observed from a single ground-based telescope.

Perhaps the most significant importance of the KELT-6b discovery is that it has similar $\log g_p$ and incident flux as HD 209458b (Figure 72), one of the most studied and best understood exoplanets, but its host has a metallicity that is lower than HD 209458 by $\sim 0.3 \text{ dex}$ ⁷ (Figure 73). This, combined with the fact that KELT-6 is relatively bright at $V \sim 10.4$ (Figure 74), means that this system provides an opportunity to perform comparative measurements of two similar planets in similar environments around stars of very different metallicities. In particular, we advocate attempting to acquire both transmission and secondary eclipse spectroscopy from the ground and space. The resulting spectra can be compared directly with those already in hand for HD 209458b (e.g., Knutson et al. 2008; Désert et al. 2008; Sing et al. 2008; Snellen et al. 2008; Swain et al. 2009). Such direct comparisons may, for example, elucidate the effect of bulk composition of the planet atmosphere on the cause of atmospheric temperature inversions. We note that, in order to properly plan for secondary eclipse observations, additional radial velocity observations will be needed to more precisely constrain the eccentricity of KELT-6b and so predict the time of secondary eclipse. Such observations will also be important for characterizing the orbit of the tertiary object in the KELT-6 system. For these reasons, KELT-6b should prove to be a very interesting object for further study.

8.11 KELT-6b Acknowledgements

K.A.C. was supported by a NASA Kentucky Space Grant Consortium Graduate Fellowship. Early work on KELT-North was supported by NASA Grant NNG04GO70G. J.A.P. and K.G.S. acknowledge support from the Vanderbilt Office of the Provost through the Vanderbilt Initiative in Data-intensive Astrophysics. E.L.N.J. gratefully acknowledges the support of the National Science Foundation's PREST program, which helped to establish the Peter van de Kamp Observatory through grant AST-0721386. K.G.S.

⁷While HAT-P-1b, WASP-13b, WASP-35b, and WASP-62b have $\log g_p$ and incident flux similar to HD 209458b, none of them are metal poor except for WASP-35b, which has a metallicity of $[\text{Fe}/\text{H}] = -0.15$.

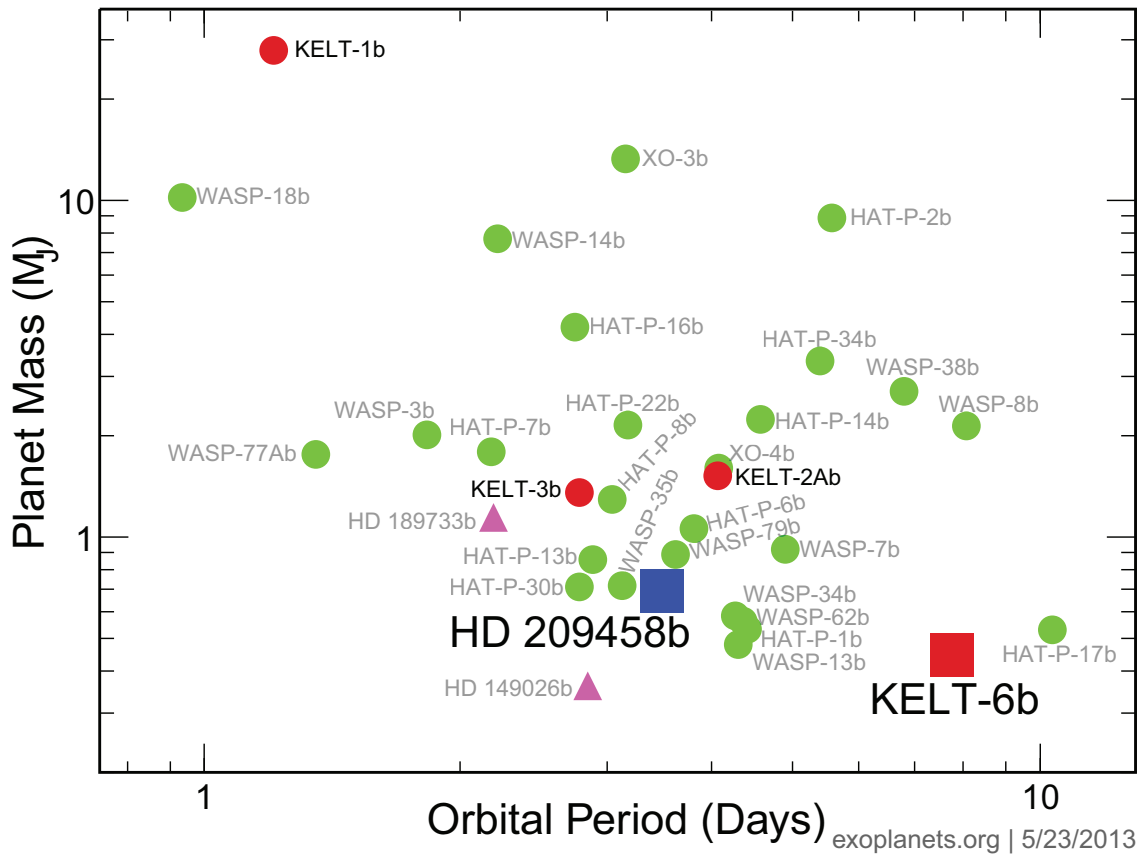


Figure 71. Comparison of KELT-6b planet mass as a function of orbital period with bright, transiting, hot gas giants with $m > 0.1 M_J$, $P < 20$ days, and host star $V < 11.0$. Both KELT-6b and HD 189733b are sub-Jupiter mass planets. The three RV discovered planets are shown as magenta filled triangles (HD 189733b and HD 149026b) and a large blue filled square (HD 209458b). All other transits were discovered by ground-based transit surveys. No Kepler targets currently meet the specified criteria for inclusion in the group. The KELT-North survey planets are shown as red filled circles, except KELT-6b which is shown as a large red filled square. All other planets are shown as green filled circles. KELT-6b and HD 209458b offer an opportunity to perform a comparative measurement of two similar mass planets in similar environments around stars of very different metallicities.

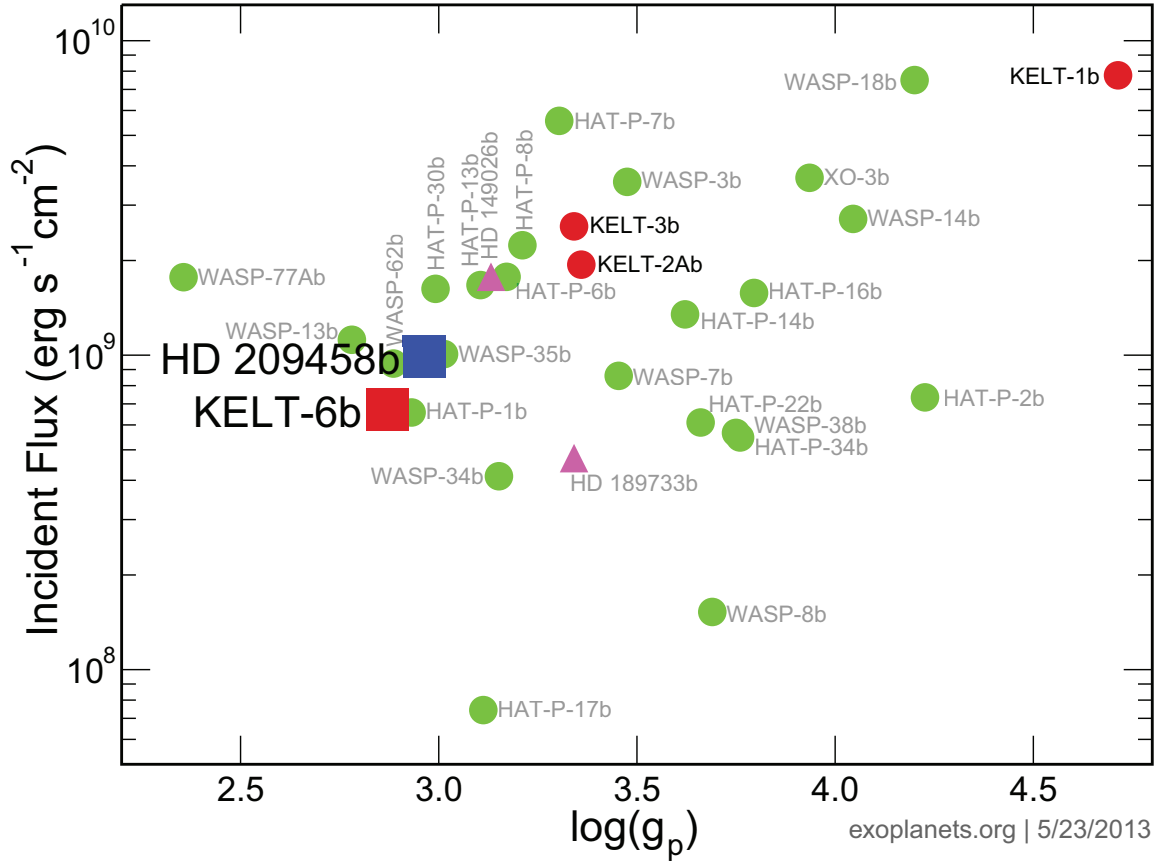


Figure 72. Comparison of KELT-6b incident flux as a function of planet surface gravity with bright, transiting, hot gas giants with $m > 0.1 M_J$, $P < 20$ days, and host star $V < 11.0$. Both KELT-6b and HD 189733b are sub-Jupiter mass planets. The three RV discovered planets are shown as magenta filled triangles (HD 189733b and HD 149026b) and a large blue filled square (HD 209458b). All other transits were discovered by ground-based transit surveys. No Kepler targets currently meet the specified criteria for inclusion in the group. The KELT-North survey planets are shown as red filled circles, except KELT-6b which is shown as a large red filled square. All other planets are shown as green filled circles. KELT-6b has surface gravity and incident flux similar to HD 209458b. All else being equal, objects in the top left have the highest transmission spectroscopy signal. *Bottom panel:* $[Fe/H]$ as a function of planet surface gravity. KELT-6b has metallicity lower than HD 209458b by ~ 0.3 dex. KELT-6b and HD 209458b offer an opportunity to perform a comparative measurement of two similar planets in similar environments around stars of very different metallicities.

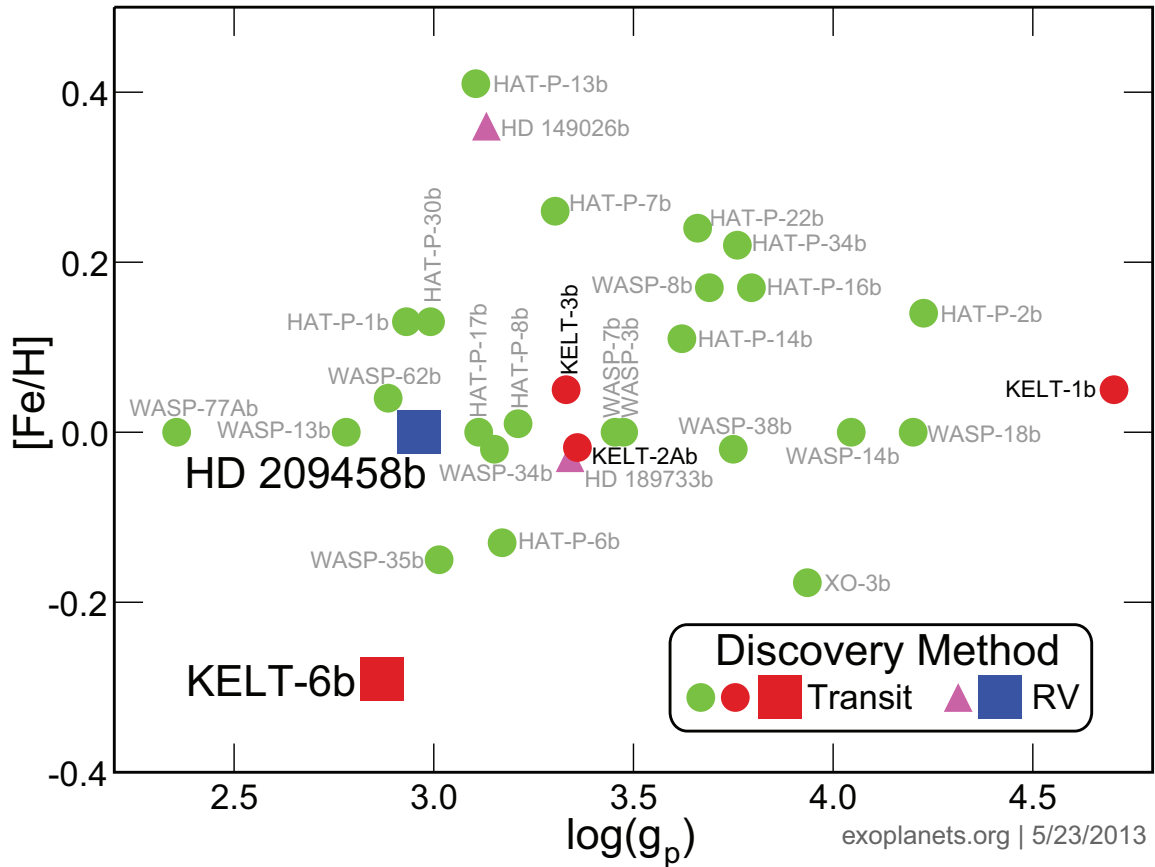


Figure 73. Comparison of KELT-6b metallicity as a function of planet surface gravity with bright, transiting, hot gas giants with $m > 0.1 M_J$, $P < 20$ days, and host star $V < 11.0$. Both KELT-6b and HD 189733b are sub-Jupiter mass planets. The three RV discovered planets are shown as magenta filled triangles (HD 189733b and HD 149026b) and a large blue filled square (HD 209458b). All other transits were discovered by ground-based transit surveys. No Kepler targets currently meet the specified criteria for inclusion in the group. The KELT-North survey planets are shown as red filled circles, except KELT-6b which is shown as a large red filled square. All other planets are shown as green filled circles. KELT-6b has metallicity lower than HD 209458b by ~ 0.3 dex. KELT-6b and HD 209458b offer an opportunity to perform a comparative measurement of two similar planets in similar environments around stars of very different metallicities.

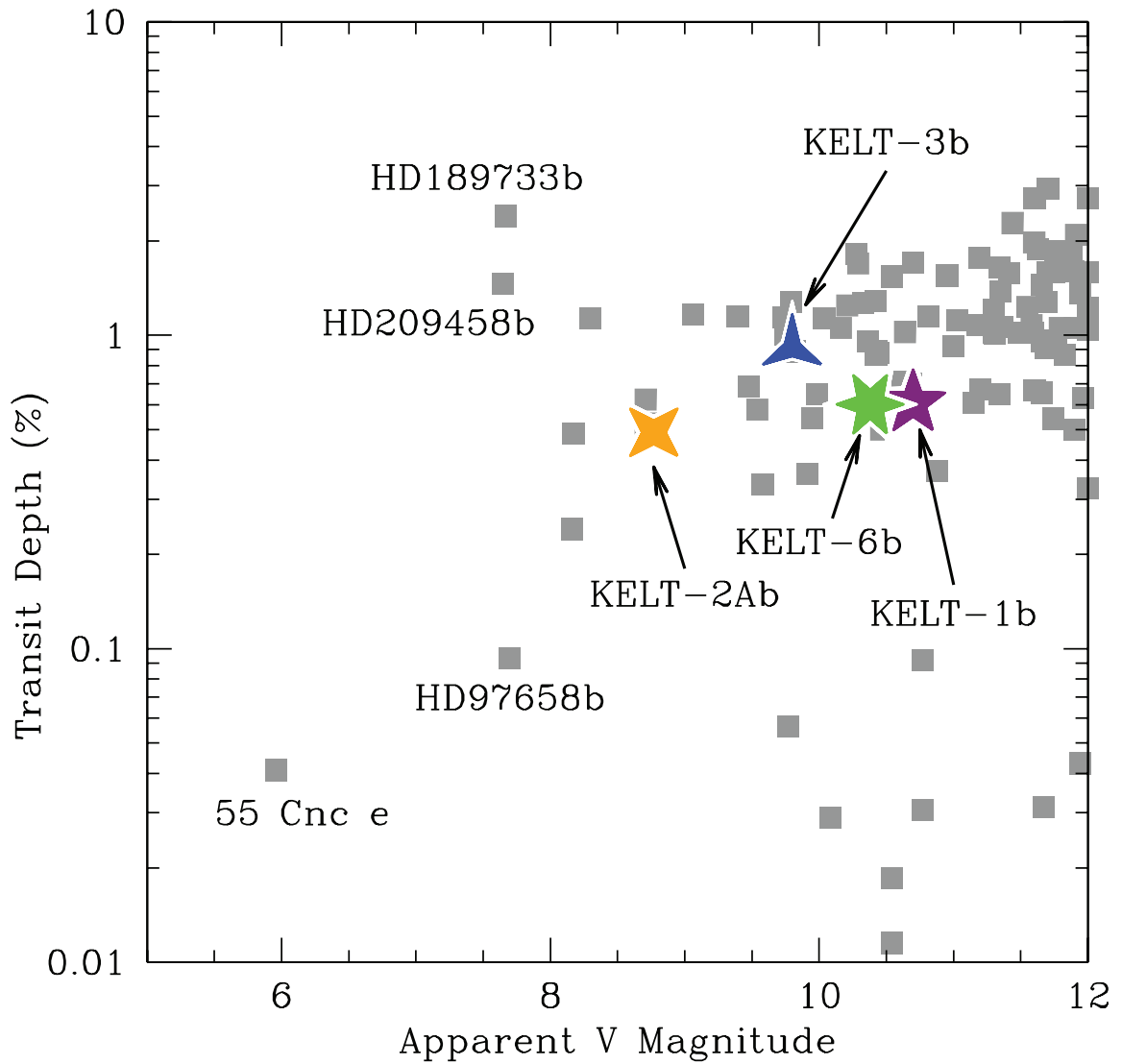


Figure 74. Transit depth assuming no limb darkening as a function of the host star apparent V magnitude for transiting systems with relatively bright ($V \leq 12$) hosts. KELT-6b is shown as the green six-pointed star. The other KELT discoveries are also shown, and the transiting systems with very bright hosts ($V \leq 8$) are labeled. Systems in the top left tend to be the most amenable to detailed spectroscopic and photometric studies.

acknowledges the support of the National Science Foundation through PAARE Grant AST-0849736 and AAG Grant AST-1009810. Work by B.S.G. and T.G.B. was partially supported by NSF CAREER Grant AST-1056524. K.P. acknowledges support from NASA grant NNX09AB29G and NSF award number 1108686. We thank the anonymous referee for a thoughtful reading of the manuscript and for useful suggestions. We thank Geoff Marcy and Howard Isaacson for Keck HIRES observations, calibration, and reduction of spectra to 1-D form. The authors wish to recognize and acknowledge the very significant cultural role and reverence that the summit of Mauna Kea has always had within the indigenous Hawaiian community. We are most fortunate to have the opportunity to conduct observations from this mountain. The TRES and KeplerCam observations were obtained with partial support from the Kepler Mission through NASA Cooperative Agreement NNX11AB99A with the Smithsonian Astrophysical Observatory (PI: D.W.L.). A portion of this work was supported by the National Science Foundation under grant Nos. AST-1203023. We thank Roberto Zambelli of Societa Astronomica Lunae for participation in the KELT followup network. This work has made use of NASA's Astrophysics Data System, the Exoplanet Orbit Database at exoplanets.org, the Extrasolar Planet Encyclopedia at exoplanet.eu (Schneider et al., 2011), the SIMBAD database operated at CDS, Strasbourg, France, and Systemic (Meschiari et al., 2009).

CHAPTER 9

KELT-1b SECONDARY ECLIPSE CHARACTERIZATION

This chapter presents the work I contributed to Beatty et al. (2014) as second author. A summary of the Beatty et al. (2014) introductory material is provided in the next section for context. A description of my contributions and the related results are provided in the remaining sections. To my knowledge, the MORC telescope data contributed to Beatty et al. (2014) provide the first (albeit tentative) optical-band detection of the secondary transit of a low-mass companion by a ground-based telescope.

9.1 Introduction

Among substellar objects, the relationship between giant planets and brown dwarfs is unclear. The generally acknowledged dividing line between these two classes of objects is based on mass. Specifically, objects above the minimum mass needed to burn deuterium are defined as brown dwarfs, whereas objects less massive than this limit are defined as planets. The deuterium burning limit is roughly $\sim 13 M_J$, although in detail this depends on one's definition of "burning deuterium," and on the detailed composition of the object (Spiegel et al., 2011).

On the one hand, distinguishing between objects below and above $13 M_J$ is clearly arbitrary, particularly since after roughly a billion years deuterium burning is over and any evidence of this initial internal energy source is largely gone, i.e., an old $\sim 50 M_J$ object that never fused deuterium would be difficult to distinguish from one that did (Spiegel et al., 2011; Bodenheimer et al., 2013; Mollière & Mordasini, 2012). On the other hand, giant planets and massive brown dwarfs likely have distinct origins, at least for

companions to sunlike stars. This is evidenced by the existence of the brown dwarf desert, the local minimum in the mass function of relatively close-in ($\lesssim 10\text{AU}$) companions to sunlike stars near ~ 30 to $\sim 50M_J$ (e.g., Marcy & Butler, 2000; Grether & Lineweaver, 2006; Sahlmann et al., 2011). Presumably, objects below the brown dwarf desert were formed in a circumstellar disk, whereas objects above were formed in a manner more analogous to stars. However, this hypothesis is relatively untested.

Unfortunately, obtaining empirical constraints on giant planets and brown dwarfs in similar environments has proven difficult. The majority of our empirical constraints on brown dwarfs come from isolated brown dwarfs, brown dwarf binaries, or brown dwarfs as wide companions to stars (Luhman, 2012). These systems are often amenable to detailed study of their atmospheres, including spectra and time series photometry. However, in the vast majority of cases, these objects do not have masses, radii, or age measurements. In contrast to brown dwarfs, the majority of our empirical constraints on giant planets comes from transiting systems. These systems provide masses, radii, and crude ages for most systems, but because of selection biases, nearly all these planets are on short periods and so likely are tidally locked and subject to very strong stellar irradiation, dramatically altering and complicating their atmospheres and atmospheric dynamics. Therefore, the empirical constraints on these systems cannot be directly interpreted in the same context as isolated brown dwarfs, hampering the ability to define the relationship between these two types of objects. The existence of the brown dwarf desert, and the resulting paucity of transiting brown dwarfs, has prevented any direct comparison of observations of brown dwarfs under similarly irradiated environments as close-in giant planets.

KELT-1b (Siverd et al., 2012) is the first low-mass transiting companion announced by the KELT-N transit survey (Pepper et al., 2003, 2007). It is a highly inflated $27M_J$ brown dwarf transiting a $V = 10.7$ mid-F star and provides the best opportunity to directly compare a brown dwarf to giant exoplanets under the same environmental condition of strong external irradiation. Previously discovered transiting brown dwarf companions orbit stars that are too faint to allow for high quality follow-up observations

(see Beatty et al. 2012 for details). KELT-1b allows us to study a brown dwarf where we know the mass and radius, in an irradiation and tidal environment similar to hot Jupiters, and around a star bright enough to allow for precision follow-up observations. To take advantage of the opportunity offered by KELT-1b, we observed several secondary eclipses of the KELT-1 system from the ground and from space during the fall of 2012.

I contributed the Astrodon z' -band ($0.9\mu\text{m}$) ground-based observations and data reduction while other coauthors contributed the $3.6\mu\text{m}$ and $4.5\mu\text{m}$ space-based data from the IRAC instrument on the Spitzer Space Telescope.

9.2 Ground-based Observations

Over the summer and fall of 2012, I observed seven secondary eclipses of KELT-1b in z' at Moore Observatory using the MORC telescope. Since KELT-1 is separated from its nearest detectable neighbor in DSS2 imagery by $\sim 18''$, I was able to defocus the telescope to allow for longer exposures without the risk of blending from the neighbor star. The same observing parameters were used for the ground-based observations across all nights. The exposure time was 240 seconds and the target and comparison stars were placed at the same detector locations, and guiding maintained this placement within a few pixels across all nights. Image calibration consisted of bias subtraction, dark subtraction, flat-field division, and detector non-linearity compensation.

Differential aperture photometry was performed on the calibrated images using AIJ. The comparison stars were selected from sources on the detector which had z' -band brightness similar to KELT-1 and which produced relatively flat light curves (after airmass detrending) when compared to the other stars in the ensemble. The final comparison ensemble included four stars near KELT-1 (TYC 2785-2151-1, TYC 2781-2231-1, LTT 17089, and TYC 2785-1743-1). I chose to allow the photometric aperture radius to vary based on an AIJ estimate of the FWHM of the toroidal PSF. After testing values in the range of 1.0 to 1.4 times the estimated FWHM, it was found that a factor of 1.25 minimized the scatter in the light curves. This factor resulted in an aperture radius that

varied between $\sim 20-30$ pixels across the four nights. The sky background was estimated from an annulus with inner radius 40 pixels and outer radius 80 pixels. Iterative 2σ clipping was first performed to remove outliers and stars from the background annulus. The mean of the remaining pixels was adopted as the sky background value and subtracted from each pixel in the photometric aperture.

Three of the events, on UT 2012 September 7, 2012 October 5 and 2012 October 12, suffered from abnormally poor seeing or interruptions by clouds. Those observations were excluded from consideration. The other four secondary eclipses, on UT 2012 July 30, 2012 August 16, 2012 November 18 and 2012 November 29, were high-quality, complete observations of the eclipses. The typical per point uncertainties on these nights were 0.10% to 0.13%. The top four panels in Figure 75 show the light curves from these four good nights plotted individually, after being detrended against airmass and time as described in Section 9.3.2.

9.3 Light curve Fitting

The light curve fitting of both the Spitzer and MORC data was performed primarily by the lead author T. Beatty, with some support from this author regarding systematic and decorrelation handling of the MORC data. A summary of the MORC data fitting and results is provided here. Refer to Beatty et al. (2014) for the Spitzer data fitting and results.

9.3.1 Secondary Eclipse Model

We modeled the IR data as a combination of a Mandel & Agol (2002) eclipse light curve and a set of decorrelation parameters. To make the eclipse light curves we used the implementation of the Mandel & Agol (2002) light curves built into EXOFAST (Eastman et al., 2013). We modeled the eclipse by assuming KELT-1b was a uniformly bright disk, with no limb-darkening, being occulted by the much larger KELT-1. Compared to a transit light curve, this has the immediate effect that R_p/R_* and the eclipse depth are no longer directly related.

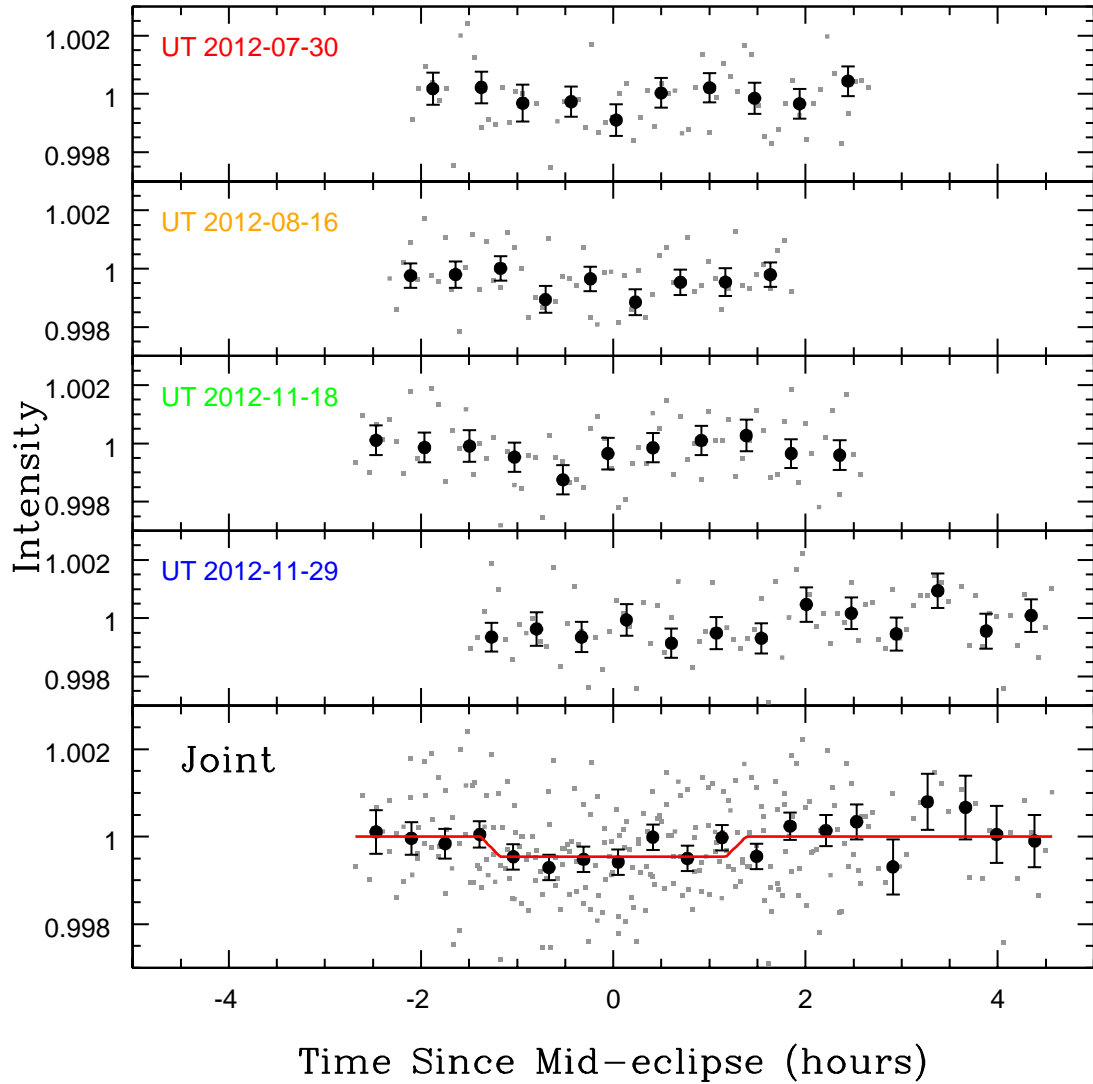


Figure 75. All four of the lightcurves used to calculate the constraint on the eclipse depth in z' . The bottom panel shows all four phased and overplotted. Each lightcurve has also been linearly detrended against airmass and time. The black points are binned versions of the individual and combined lightcurves, while the red line in the bottom panel is the best-fit eclipse model. We marginally detect the eclipse in z' with a depth of $0.049 \pm 0.023\%$.

9.3.2 Model Fit to MORC z' Data

We analyzed each of the four nights individually. We fit only for the depth of a possible eclipse using a trapezoidal eclipse model that had the eclipse time, total duration and ingress/egress duration fixed. We computed the expected eclipse times for each night by extrapolating from our measured $3.6\mu\text{m}$ eclipse time and assuming a fixed period of 1.217514 days. The choice of the $3.6\mu\text{m}$ eclipse time is arbitrary; we repeated our entire analysis of the z' data using the $4.5\mu\text{m}$ eclipse time and found no difference in our results. The total duration and ingress/egress duration we set to the average of our $3.6\mu\text{m}$ and $4.5\mu\text{m}$ results. In addition to the eclipse model, we also included linear decorrelation terms for airmass and time. We scaled the errors on each night so that a baseline zero depth fit had a reduced χ^2 of one. In all cases the scaling factor was within ten percent of unity. We used the baseline fit to calculate the $\Delta\chi^2$ values for the non-zero depth fits.

Combining the data from all four good nights, we find suggestive evidence for an eclipse depth of $0.049 \pm 0.023\%$ in z' . Figure 76 shows the $\Delta\chi^2$ as a function of eclipse depth for these four nights. The black line in Figure 76 is the $\Delta\chi^2$ of all the nights added together, and is valid under the assumption that our uncertainties are uncorrelated night to night. We have adopted this joint constraint as our final determination of the z' eclipse depth of KELT-1b. Figure 75 shows the four complete z' light curves individually, and combined, phased, and over-plotted with our best fit eclipse model.

If the detection in z' is real, then it is the result of thermal emission from KELT-1b, and not reflected light. In the case of an extreme Bond albedo of one, and assuming KELT-1b reflects as a Lambert sphere, then the eclipse depth due to reflected light alone would be $\sim 0.03\%$. A more realistic Bond albedo of 0.1 would reduce this depth by a factor of ten, and place it far below our precision in z' .

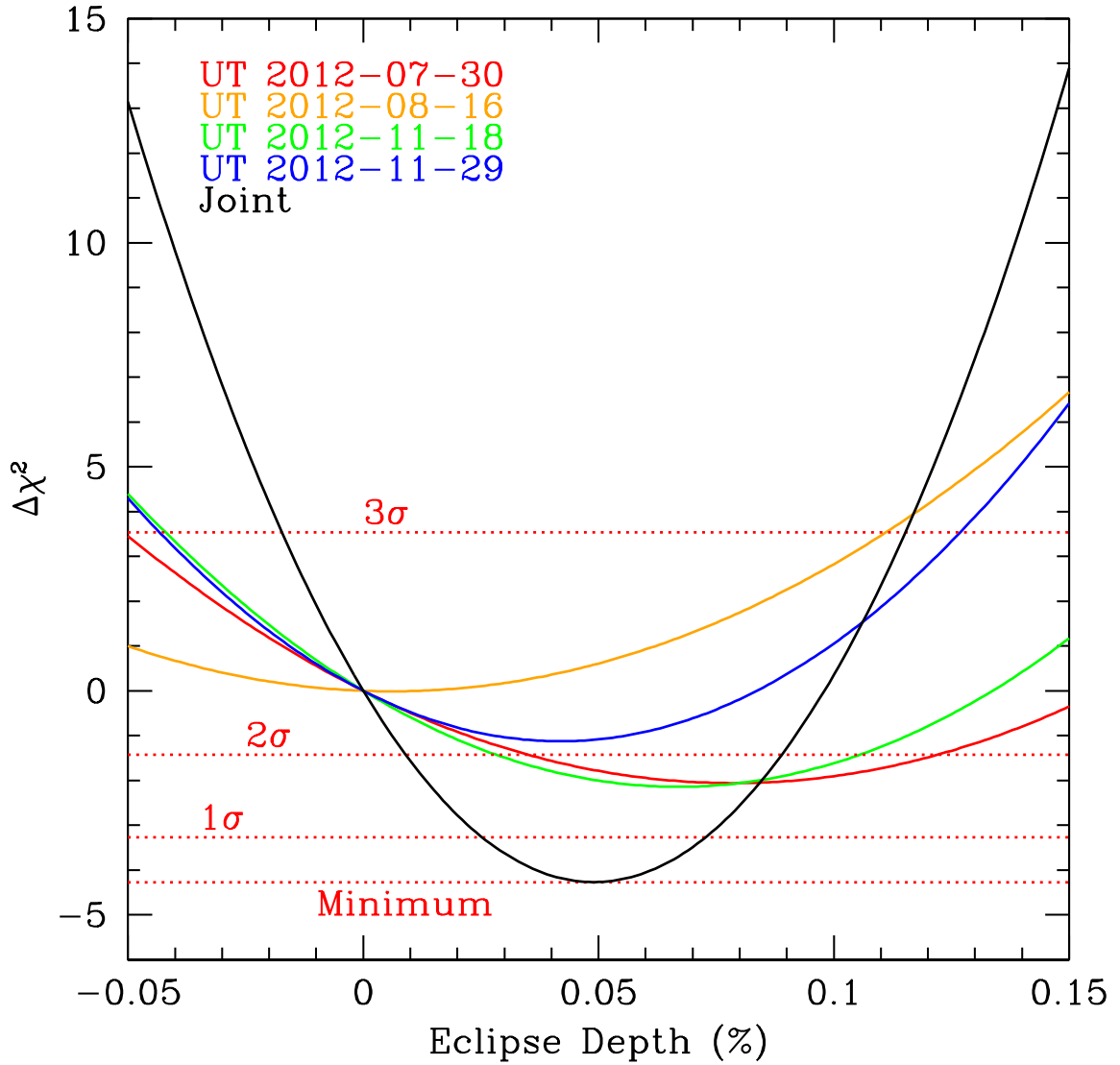


Figure 76. Constraints on the eclipse depth in z' from our ground-based observations. Though we observed seven eclipses, only four of the nights provided high-quality, complete observations. The black line shows the joint constraint on the eclipse depth from all four nights. This assumes that the observational errors are uncorrelated from night to night.

9.4 Secondary Eclipse Detection Results

We strongly detect the secondary eclipses of KELT-1b at both $3.6\mu\text{m}$ and $4.5\mu\text{m}$ (see Beatty et al. 2014), and weakly detect the eclipse in z' (see Figures 75 and 76). We measure eclipse depths of $\delta_z = 0.049 \pm 0.023\%$ in z' , $\delta_{3.6} = 0.195 \pm 0.010\%$ at $3.6\mu\text{m}$ and $\delta_{4.5} = 0.200 \pm 0.012\%$ at $4.5\mu\text{m}$. These depths correspond to brightness temperatures of 3300 K, 3150 K and 3000 K for the $0.9\mu\text{m}$ (z'), $3.6\mu\text{m}$ and $4.5\mu\text{m}$ eclipses, respectively.

9.5 Discussion

Overall, KELT-1b is a unique object: it is a relatively high mass and high surface gravity object that orbits only 3.6 stellar radii away from its host star. Among high mass sub-stellar objects, this places KELT-1b squarely in a radiation environment that until now has been populated solely by hot Jupiters. It has a surface gravity of $\log g_p = 4.74$ (~ 30 times higher than for a typical hot Jupiter), which allows us to test theories of hot Jupiter atmospheres at a very high surface gravity. Of particular interest are the amount of heat redistribution and the presence of a stratospheric temperature inversion within the atmosphere of KELT-1b. Perez-Becker & Showman (2013) have noted that planets hotter than $\sim 2000\text{K}$ are observed to have extremely low amounts of heat redistribution from their daysides to their nightsides, presumably because the shorter radiative timescales in hotter atmospheres cause these planets to reradiate the incident stellar flux, rather than advecting it through winds to the nightside. In KELT-1b, due to its high surface gravity, the theoretical radiative timescale is relatively longer, and the theoretical advection timescale relatively shorter, than in most hot Jupiters.

Similarly, consider the presence of a stratospheric temperature inversion in the atmosphere of KELT-1b. Temperature inversions have been observed in several hot Jupiters, predominantly among those with equilibrium temperatures higher than 2000 K (e.g., Cowan & Agol, 2011). Hubeny et al. (2003) and Fortney et al. (2008) have proposed that gas-phase TiO in an atmosphere causes temperature inversions, since it is a strong

optical absorber and condenses between 1900 K and 2000 K, depending on the pressure. However, the ultimate cause of inversions, and their precise regulatory mechanisms, have not been definitively agreed upon.

Our observations are not sufficient to conclusively determine whether a TiO inversion exists in the atmosphere of KELT-1b, but we can nonetheless provide some useful constraints. Figure 77 shows our measured eclipse depths on top of atmosphere models from Fortney et al. (2008). The models without TiO (dashed lines) are for an atmosphere without an inversion, while the TiO models (solid lines) have an inversion. The best fit to the data is the no-TiO, strong hotspot model, with $\chi^2 = 2.23$ for three degrees of freedom. However, the no-TiO, mild hotspot model has a $\Delta\chi^2$ relative to the best model of only 1.44, while the TiO, day-side redistribution model has a $\Delta\chi^2 = 2.60$, and thus these models are also consistent with the data. On the other hand, the no-TiO, day-side redistribution model is marginally excluded with $\Delta\chi^2 = 11.31$, and while the TiO, complete redistribution model is strongly excluded with $\Delta\chi^2 = 60.07$.

9.6 Summary and Conclusions

We have measured the secondary eclipse of the highly irradiated transiting brown dwarf KELT-1b in three bands. These observations are the first constraints on the atmosphere of a highly irradiated brown dwarf. Specifically, we measure secondary eclipse depths of $0.195 \pm 0.010\%$ at $3.6\mu\text{m}$ and $0.200 \pm 0.012\%$ at $4.5\mu\text{m}$. We also find tentative evidence for the secondary eclipse in the z' band with a depth of $0.049 \pm 0.023\%$. From these measured eclipse depths, we conclude that KELT-1b does not have a high heat redistribution efficiency, and does not show strong evidence for a stratospheric temperature inversion. Our Spitzer measurements reveal that KELT-1b has a $[3.6] - [4.5]$ color of 0.07 ± 0.11 , identical to that of isolated brown dwarfs of similarly high temperature. In contrast, hot Jupiters generally show redder $[3.6] - [4.5]$ colors of ~ 0.4 , with a very large range from ~ 0 to ~ 1 .

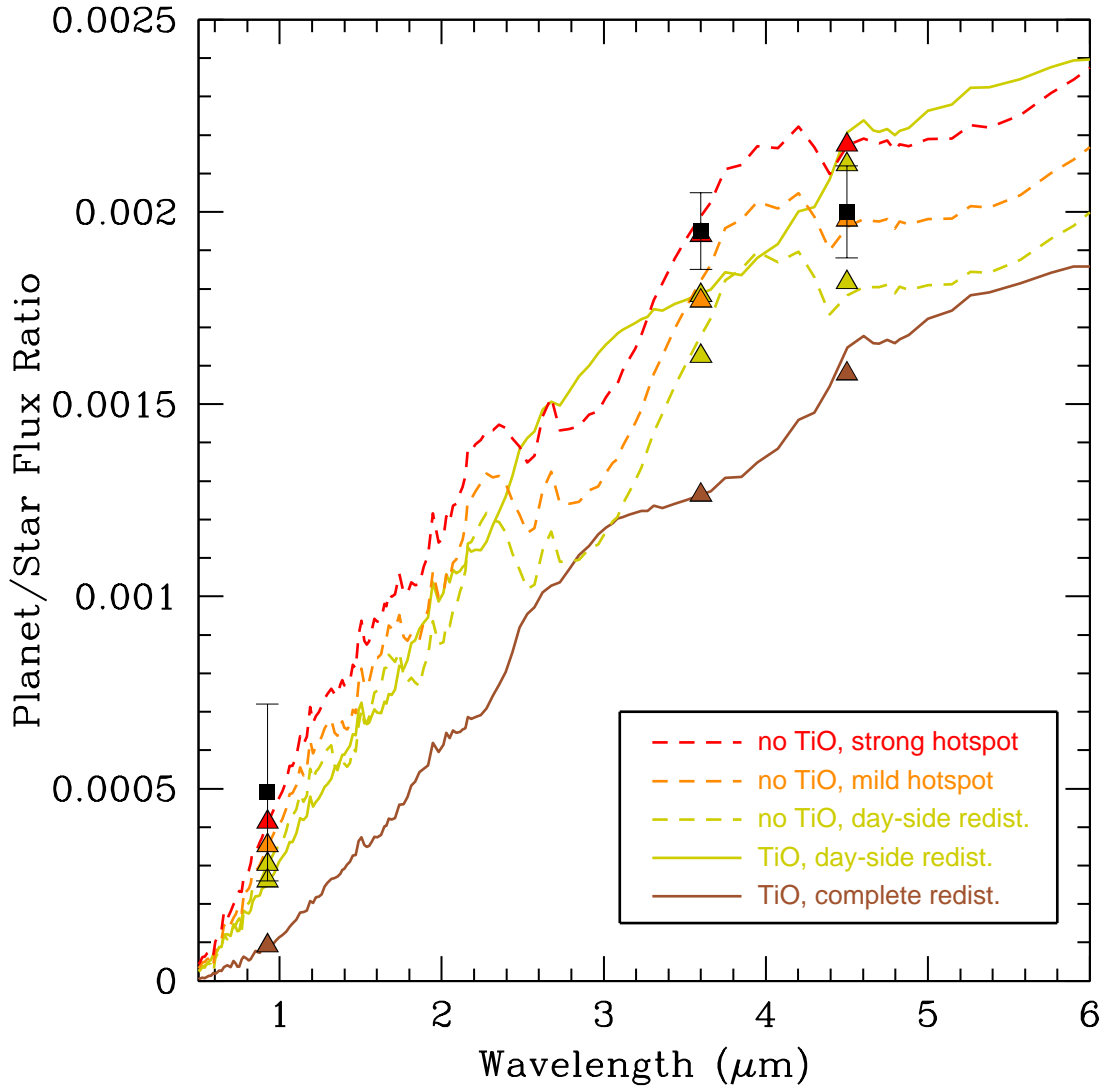


Figure 77. Our measured planet-to-star flux ratios at $0.9\ \mu\text{m}$ (z' -band), $3.6\ \mu\text{m}$, and $4.5\ \mu\text{m}$. The atmosphere models are based on Fortney et al. (2008), and are divided according to the presence of gaseous TiO and the amount of heat redistribution from the day to night side. The ‘TiO’ models have stratospheric temperature inversions, while the ‘no TiO’ models do not. The ‘hotspot’ models are scenarios wherein the heat from the stellar insolation is redistributed over only a portion of the planetary day side. In the ‘strong hotspot’ this redistribution area is smaller than in the ‘mild hotspot’ model. The colored triangles show the predicted flux ratios from each of the models in the three bandpasses.

CHAPTER 10

CONCLUSIONS AND NEXT POSSIBILITIES

10.1 Summary of Results

The data presented in this work show that competitive scientific results can be achieved using telescopes with aperture diameters < 1 m. To achieve these results, best efforts must be made to minimize systematics at the time of observations. Even so, systematic residuals will be ever-present in ground-based data and will need to be addressed in the data reduction process in order to push photometric precision as near as possible to the shot-noise limit. Many light curve fitting tools attempt to minimize systematic trends by making corrections to the data based on a linear or quadratic best fit to time. This approach can help remove airmass and other long term trends, but to remove shorter term or highly irregular systematics, data correlated with those systematics must be recorded and/or calculated and included as part of the detrending and model fitting process. As discussed in Chapter 4, AstroImageJ provides the tools needed to collect, calculate, and assess the effectiveness of various trend datasets as part of the differential photometry and initial light curve fitting process. To maximize the number of trend datasets that can be used when fitting multiple transit light curves, it is imperative to use a tool such as multi-EXOFAST that simultaneously detrends and fits a global model to the data by allocating common parameters to represent physical properties that must be the same for all light curves. Because the use of common parameters reduces the total number of globally fitted parameters, the over-fitting that often occurs when attempting to detrend an individual light curve with more than a few (1–3, depending on the amount of baseline data available) trend datasets is mitigated.

Using the simultaneous global fit and detrend technique, I have demonstrated the capability to reach a 5 minute photometric precision of 183 ppm in the WASP-12b model residuals presented in Chapter 5. Systematic minimization also plays a key role in achieving high-precision timing measurements of transiting planets. Because the ingress and egress slopes of a light curve play a dominant role in defining the modeled transit center time, a slight systematic during those short time periods can induce a significant inaccuracy in the derived TTV. The $\sim 20\text{--}30$ s timing precisions I achieved in the WASP-12b and Qatar-1b TTV studies presented in Chapters 5 and 6 are clear improvements over the precisions achieved by other groups.

In Chapters 7 and 9, the simultaneous global fitting and detrending technique was applied to the study of exoplanet and brown dwarf atmospheres. In Chapter 7, I presented a tentative detection of Sodium in the atmosphere of the hot Jupiter HD 189733b by measuring an increase of 0.05% in the apparent planetary radius in a narrow wavelength band around the Na D doublet using two different techniques. In Chapter 9, I presented the tentative detection of the thermal emission of KELT-1b in the z' band, which helped to show that the brown dwarf's atmosphere does not have a high heat redistribution efficiency, and does not show strong evidence for a stratospheric temperature inversion.

In Chapter 8, I discussed the discovery of a hot Saturn planet around a metal poor star. The high-precision photometry from the MORC and other telescopes was combined with high-precision RVs and high-resolution adaptive optics imagery from the Keck telescope to characterize the system and confirm the planetary nature of the transiting object. Furthermore, the data were used to place limits on the mass and orbital period of a second body orbiting the same host star.

In addition to the light curves presented in this work, I have observed more than 100 light curves of other known transiting exoplanets in a search for additional planets in those systems through high-precision TTV measurements. All of the known transiting system light curves I have collected are summarized in Table 17. Although there are multiple observations of a few systems in addition to the WASP-12b, Qatar-1b, and

HD 189733b systems presented in Chapters 5, 6 and 7, more observations are needed to complete a proper TTV analysis of those systems. Given time and telescope availability, I plan to continue following some of these systems to search for TTVs and to provide detailed characterizations. At an appropriate point in time, any unpublished light curves will be made available to the community through a publicly available database such as the NASA Exoplanet Archive¹ (Akeson et al., 2013). I have also observed ~ 400 follow-up light curves in collaboration with the KELT-N and KELT-S teams in the search for new transiting planets. So far, five transiting planets have been announced and six more are in the publication pipeline. Continued collaboration with the KELT team will hopefully produce many more interesting exoplanet discoveries.

10.2 Near-IR Photometry From Small Telescopes

As discussed in §1.5.3, planetary thermal emission observations provide important measurements to help characterize exoplanets and their atmospheres. Thermal emission is best measured in near-infrared (NIR) and mid-infrared (MIR) bands where the contrast ratio of the emission from the host star and its planetary companion is much lower than in optical bands. Both NIR and MIR observations have generally been limited to large or space-based telescopes. Obtaining time from those facilities is a highly competitive process. Plus, in many cases, transiting planet host stars are too bright to be suitable for NIR photometric observations with large ground-based telescopes. That issue will be even worse for brighter K2 and TESS planet hosts. An additional complication is that the secondary transit ephemeris is not always well constrained due to uncertainties in the eccentricity from RV data (see §8.6.2 regarding KELT-6b), often necessitating an impractical amount of conventional telescope time. Furthermore, some atmospheric models (e.g. Langton & Laughlin 2008, Menou & Rauscher 2009) suggest that temporal variations in thermal emission may exist due to planetary weather. Many secondary transit NIR observations will be required to sort out the potential effects of planetary weather

¹<http://exoplanetarchive.ipac.caltech.edu>

TABLE 17

Summary of MORC time-series photometric observations of known transiting exoplanets.

Planet Name	# Light Curves	Planet Name	# Light Curves
CoRoT-7b	1	HD 189733b	14
GJ 436b	3	HD 209458b	2
HAT-P-2b	1	Kepler-8b	1
HAT-P-3b	1	KELT-1b	6
HAT-P-4b	1	KELT-2Ab	1
HAT-P-6b	2	KELT-3b	1
HAT-P-8b	1	KELT-6b	7
HAT-P-10b	1	KELT-7b	2
HAT-P-11b	4	Qatar-1b	18
HAT-P-12b	2	Qatar-2b	2
HAT-P-13b	2	TrES-2b	3
HAT-P-14b	4	TrES-2b	4
HAT-P-15b	2	TrES-5b	1
HAT-P-16b	8	WASP-1b	5
HAT-P-19b	1	WASP-2b	3
HAT-P-20b	1	WASP-3b	1
HAT-P-21b	1	WASP-12b	23
HAT-P-22b	2	WASP-13b	3
HAT-P-23b	6	WASP-21b	3
HAT-P-24b	1	WASP-24b	1
HAT-P-26b	1	WASP-28b	1
HAT-P-27b	2	WASP-32b	1
HAT-P-29b	7	WASP-33b	6
HAT-P-30b	1	WASP-36b	1
HAT-P-32b	1	WASP-37b	1
HAT-P-34b	1	WASP-38b	2
HAT-P-36b	6	WASP-43b	1
HAT-P-37b	1	WASP-48b	2
HAT-P-39b	1	WASP-52b	1
HD 17156b	1	XO-1b	1
HD 97558b	1	XO-3b	5
HD 149026b	2	XO-4b	2

from measurement inaccuracies in eclipse depth and the associated error.

If smaller telescopes such as MORC could produce observations in the NIR, much progress could be made in the study of exoplanet thermal emission in a relatively short amount of time. Furthermore, ~ 0.6 m telescopes are ideally sized to produce high-precision photometry for stars brighter than $\sim 10-13^{\text{th}}$ magnitude in the band of interest, if dark noise does not dominate for the requisite exposure time, and if systematics are well controlled. Sullivan, Croll, & Simcoe (2014) have shown promising results from on-sky testing with a camera they custom designed around a commercially available InGaAs detector. Even better results should be achievable using commercially available InGaAs cameras that are now available off-the-shelf with deep-cooling (-85 C with thermoelectric cooling or -195 C with liquid nitrogen cooling). These cameras should be capable of producing high-precision time-series photometry in the Y-band, J-band, and part of the H-band. I plan to investigate the capability of these cameras to produce $\sim 1.0-2.0$ mmag minute $^{-1}$ NIR photometry for bright ($J \lesssim 10$) stars. I plan to also investigate the limitations that systematics place on the detection of shallow primary transit and secondary eclipse depths. This could open up to the community the ability to perform small telescope NIR photometry in the same way that high-precision optical photometry has been produced for the last 15 years on small telescopes.

10.3 The Transiting Exoplanet Survey Satellite

The bright systems being discovered by KELT are of high value for detailed atmospheric characterizations. With current technology, only planets with host stars having $V \lesssim 10$ are bright enough for detailed characterizations and atmospheric studies. As of April 2015, only 26 transiting planets have been discovered that have $V = 10$ host stars or brighter². The Transiting Exoplanet Survey Satellite (TESS; Ricker et al. 2014) is an upcoming space-based transit survey that is scheduled for launch in 2017 and will search nearly the entire sky for planets transiting bright ($I_C \approx 4-13$) and nearby stars for a

²The Exoplanets Data Explorer at <http://exoplanets.org>

period of two years. To enable the all-sky search, TESS has four identical cameras. Each one has a lens diameter of 10.5 cm, resulting in a $24^\circ \times 24^\circ$ unvignetted image on a four-CCD mosaic. The combined field of view is $24^\circ \times 96^\circ$. Each CCD has a 2048×2048 pixel array resulting in a pixel scale of $21'' \text{ pixel}^{-1}$, almost identical to the KELT pixel scale.

TESS will observe stars for an interval ranging from one month to one year, depending mainly on the star's ecliptic latitude. Stars from 6° north of the ecliptic plane to the northern ecliptic pole will be monitored for the first year. Stars from 6° south of the ecliptic plane to the southern ecliptic pole will be monitored for the second year. All stars in a field get at least one continuous month of coverage, while stars near the poles get nearly a full year of coverage. TESS is expected to find more than a thousand planets smaller than Neptune, including dozens that are comparable in size to the Earth.

There are significant opportunities to contribute to the TESS mission through follow-up observations. Unlike most Kepler candidates, most TESS candidates will be bright enough for the RV follow-up that is generally required to measure the mass of the transiting object. Photometric follow-up should be useful as well for at least three reasons. First, as with the KELT survey, more than one star will often be blended in the TESS photometric aperture due to the $21''$ pixel scale. Higher resolution ground-based telescopes will be required to confirm which star in the aperture is showing the transit and to measure the unblended transit depth. Second, large parts of the sky are observed by TESS for only about a month and the longest coverage is limited to a year. If only one or two transit events are detected for a TESS transiting planet candidate, high-precision ground-based photometry may be able to confirm that the event is periodic after TESS coverage has ended. Third, TESS observes in a single wide-band filter, so no information can be derived from the TESS data about the achromaticity of the transit depth. I have demonstrated that cost-effective < 1 m aperture ground-based telescopes are capable of delivering much of the data needed to help address all three issues for the TESS mission.

As mentioned in §1.6.2, the *Kepler* mission has now been re-purposed to a new

mission called K2. Data from the first few fields of the K2 mission have already started producing planet discoveries. Since the K2 pixel scale is much finer than for TESS, blending is not as much of a problem. However, since K2 is a monochromatic telescope like TESS, and since each field is observed for at most ~ 75 days, there may be ground-based photometric follow-up opportunities for K2 as well.

10.4 James Webb Space Telescope

Current technology provides the capability to perform transmission and emission spectroscopy of bright ($V \lesssim 10$) stars hosting hot Jupiter planets. However, reaching the signal-to-noise ratio required to characterize the atmospheres of bright transiting terrestrial planets through transmission or emission spectroscopy, which may reveal water or other molecules considered important for life, will require higher precision instrumentation. The James Webb Space Telescope (JWST; Gardner et al. 2006), currently scheduled to launch in 2018, may provide the precision needed to characterize the atmospheres of some terrestrial systems. JWST has a large 6.6 m aperture and is optimized for infrared observations. Instrumentation includes a NIR camera, a NIR spectrograph, a camera with a tunable filter covering the wavelength range $0.6 < \lambda < 5.0 \mu\text{m}$, and a MIR instrument capable of imaging and spectroscopy from $5.0 < \lambda < 29 \mu\text{m}$.

Thirty percent of the sky is viewable by JWST for at least 197 days per year, and all of the sky will have at least 51 days of continuous visibility each year. JWST has continuous visibility of the sky within 5° of the north and south ecliptic poles, which are also the regions with the longest TESS coverage.

10.5 Other Upcoming Space Telescopes

CHEOPS (CHAracterising ExOPlanets Satellite) is a European mission scheduled for launch in 2017 and is dedicated to search for transits around bright stars already known to host RV discovered planets and planets discovered by a new generation of

ground-based transit surveys. CHEOPS is a 32 cm telescope and is targeted to study stars brighter than $V < 12$ and is designed to reach a precision of 150 ppm per minute for a $V = 9$ star. PLATO (Planetary Transits and Oscillations of stars) is another planned European spacecraft and is scheduled for launch in 2024. It will search for transiting planets around bright stars ($4 < V < 11$) using 34 cameras that provide a total field of view of 2250 deg^2 per pointing. PLATO plans to observe up to 1,000,000 stars and detect and characterize hundreds of small planets, and thousands of planets in the Neptune to gas giant regime out to the habitable zone.

10.6 Final Thoughts

Clearly, the future of exoplanet research is aimed at bright stars hosting small transiting planets, with the expectation of discovering many Earth-like planets in the habitable zone. Current and near-future observatories will provide astronomers with the ability to measure to high-precision the characteristics of these planets and their atmospheres. The day when we can conclusively answer the question – "do conditions exist on planets outside the solar system that could support life as we understand it here on Earth?" – is surely drawing near. And, with continued technological innovations, creative ideas, and the funding to support our scientific endeavors, we may soon know if life exists outside the confines of a tiny blue world that orbits one of at least 100 billion stars that orbit a super-massive black hole in the center of one of at least 100 billion galaxies in the observable universe. This is undoubtedly an exciting and fascinating time to be involved in astronomical research.

REFERENCES

- Adorf, H.-M. 1987, *Sterne und Weltraum*, 26, 78
- Agol, E., Steffen, J., Sari, R., & Clarkson, W. 2005, *MNRAS*, 359, 567
- Agol, E., Cowan, N. B., Knutson, H. A., et al. 2010, *ApJ*, 721, 1861
- Aigrain, S., Pont, F., Fressin, F., et al. 2009, *A&A*, 506, 425
- Akeson, R. L., Chen, X., Ciardi, D., et al. 2013, *PASP*, 125, 989
- Alard, C. 2000, *A&AS*, 144, 363
- Alard, C., & Lupton, R. H. 1998, *ApJ*, 503, 325
- Alonso, R., Brown, T. M., Torres, G., et al. 2004, *ApJL*, 613, L153
- Alsubai, K. A., Parley, N. R., Bramich, D. M., et al. 2011, *MNRAS*, 417, 709
- Alsubai, K. A., Parley, N. R., Bramich, D. M., et al. 2013, *Acta Astronomica*, 63, 465
- Anderson, D. R., Collier Cameron, A., Delrez, L., et al. 2013, [arXiv:1310.5654](https://arxiv.org/abs/1310.5654)
- Armstrong, D. J., Veras, D., Barros, S. C. C., et al. 2015, [arXiv:1503.00692](https://arxiv.org/abs/1503.00692)
- Assef, R. J., Gaudi, B. S., & Stanek, K. Z. 2009, *ApJ*, 701, 1616
- Baglin, A. 2003, *Advances in Space Research*, 31, 345
- Bakos, G., Noyes, R. W., Kovács, G., et al. 2004, *PASP*, 116, 266
- Bakos, G. Á., Pál, A., Latham, D. W., et al. 2006, *ApJL*, 641, K57
- Bakos, G. Á., Noyes, R. W., Kovács, G., et al. 2007, *ApJ*, 656, 552

Bakos, G. Á., Csubry, Z., Penev, K., et al. 2013, *PASP*, 125, 154

Ballard, S., Fabrycky, D., Fressin, F., et al. 2011, *ApJ*, 743, 200

Baraffe, I., Chabrier, G., Allard, F., & Hauschildt, P. H. 2008, *A&A*, 337, 403

Barman, T. S. 2008, *ApJL*, 676, L61

Barnes, S. A. 2007, *ApJ*, 669, 1167

Basu, S., Verner, G. A., Chaplin, W. J., & Elsworth, Y. 2012, *ApJ*, 746, 76

Beatty, T. G., Pepper, J., Siverd, R. J., et al. 2012, *ApJL*, 756, L39

Beatty, T. G., Collins K. A., Fortney, J. J., et al. 2014, *ApJ*, 783, 112

Bechter, E. B., Crepp, J. R., Ngo, H., et al. 2014, *ApJ*, 788, 2

Benítez-Llambay, P., Masset, F., Koenigsberger, G., & Szulágyi, J. 2015, *Nature*, 520, 63

Bergfors, C., Brandner, W., Daemgen, S., et al. 2013, *MNRAS*, 428, 182

Bieryla, A., Collins, K., Beatty, T. G., et al. 2015, *arXiv:1501.05565*

Bodenheimer, P., D'Angelo, G., Lissauer, J. J., Fortney, J. J., & Saumon, D. 2013, *ApJ*, 770, 120

Borucki, W. J., Koch, D., Basri, G., et al. 2010, *Science*, 327, 977

Bouchy, F., Udry, S., Mayor, M., Moutou, C., Pont, F., Iribarne, N., Da Silva, R., Ilovaisky, S., Queloz, D., Santos, N. C., Ségransan, D. & Zucker, S. 2005, *A&A*, 444, L15

Boué, G., Oshagh, M., Montalto, M., & Santos, N. C. 2012, *MNRAS*, 422, L57

Brown, T. M. 2001, *ApJ*, 553, 1006

Brown, T. M. 2003, *ApJL*, 593, L125

Brown, T. M., Baliber, N., Bianco, F., et al. 2013, *PASP*, 125, 1031

Buchhave, L. A., Bakos, G. Á., Hartman, J. D., et al. 2010, *ApJ*, 720, 1118

Buchhave, L. A., Latham, D. W., Johansen, A., et al. 2012, *Nature*, 486, 375

Burrows, A., Hubeny, I., Budaj, J., & Hubbard, W. B. 2007, *ApJ*, 661, 502

Burrows, A., Budaj, J., & Hubeny, I. 2008, *ApJ*, 678, 1436

Butler, R. P., Marcy, G. W., Williams, E., McCarthy, C., Dosanjuh, P., Vogt, S. S. 1996, *PASP*, 108, 500

Calabretta, M. R., & Greisen, E. W. 2002, *A&A*, 395, 1077

Caldwell, D. A., van Cleve, J. E., Jenkins, J. M., et al. 2010, *Proc. SPIE*, 7731, 773117

Campo, C. J., Harrington, J., Hardy, R. A., et al. 2011, *ApJ*, 727, 125

Chan, T., Ingemeyr, M., Winn, J. N., et al. 2011, *AJ*, 141, 179

Chan, T., Ingemeyr, M., Winn, J. N., et al. 2012, *AJ*, 144, 90

Charbonneau, D., Brown, T. M., Latham, D. W., & Mayor, M. 2000, *ApJL*, 529, L45

Charbonneau, D., Brown, T. M., Noyes, R. W., & Gilliland, R. L. 2002, *ApJ*, 568, 377

Charbonneau, D., Knutson, H. A., Barman, T., et al. 2008, *ApJ*, 686, 1341

Chubak, C., Marcy, G. W., Fischer, D. A., et al. 2012, *arXiv:1207.6212*

Claret, A., & Bloemen, S. 2011, *A&A*, 529, A75

Coelho, P., Barbuy, B., Meléndez, J., Schiavon, R. P., & Castilho, B. V. 2005, *A&A*, 443, 735

Collier Cameron, A., Pollacco, D., Street, R. A., et al. 2006, *MNRAS*, 373, 799

Collier Cameron, A., Bouchy, F., Hébrard, G., et al. 2007, MNRAS, 375, 951

Collier Cameron, A., Wilson, D. M., West, R. G., et al. 2007, MNRAS, 380, 1230

Collins, K. 2008, M.S. Thesis

Collins, K. A., Eastman, J. D., Beatty, T. G., et al. 2014, AJ, 147, 39

Colón, K. D., Ford, E. B., Lee, B., Mahadevan, S., & Blake, C. H. 2010, MNRAS, 408, 1494

Covino, E., Esposito, M., Barbieri, M., et al. 2013, A&A, 554, AA28

Cowan, N. B., & Agol, E. 2011, ApJ, 729, 54

Cox, Arthur N. et al. 2001, Allen's Astrophysical Quantities (4th ed, 2nd printing; NY, Springer)

Crepp, J. R., Johnson, J. A., Howard, A. W., et al. 2012, ApJ, 761, 39

Croll, B., Lafreniere, D., Albert, L., et al. 2011, AJ, 141, 30

Croll, B., Albert, L., Jayawardhana, R., et al. 2015, ApJ, 802, 28

Crossfield, I. J. M., Barman, T., Hansen, B. M. S., Tanaka, I., & Kodama, T. 2012, ApJ, 760, 140

Crossfield, I. J. M., Petigura, E., Schlieder, J., et al. 2015, arXiv:1501.03798

Cutri, R. M., Skrutskie, M. F., van Dyk, S., et al. 2003, yCat, 2246, 0

Cutri, R. M., Wright, E. L., Bauer, J., et al. 2012, yCat, 2311, 0

Dawson, R. I., & Murray-Clay, R. A. 2013, ApJ, 767, 24

de Kort, J. J. M. A. 1954, Ricerche Astronomiche, 3, 109

Demarque, P., Woo, J.-H., Kim, Y.-C., & Yi, S. K. 2004, ApJS, 155, 667

Demory, B.-O., & Seager, S. 2011, *ApJS*, 197, 12

Des Marais, D. J., Nuth, J. A., III., Allamandola, L. J., et al. 2008, *Astrobiology*, 8, 715

Désert, J.-M., Vidal-Madjar, A., Lecavelier Des Etangs, A., et al. 2008, *A&A*, 492, 585

Downey, E. C. 2011, *Astrophysics Source Code Library*, 1112.013

Eastman, J., Siverd, R., & Gaudi, B. S. 2010, *PASP*, 122, 935

Eastman, J., Gaudi, B. S., & Agol, E. 2013, *PASP*, 125, 83

Eibe, M. T., Cuesta, L., Ullán, A., Pérez-Verde, A., & Navas, J. 2012, *MNRAS*, 423, 1381

Ford, E.B. 2006, *ApJ*, 642, 505

Ford, E. B., & Holman, M. J. 2007, *ApJL*, 664, L51

Ford, E. B. 2014, *Proceedings of the National Academy of Science*, 111, 12616

Fortney, J. J., Saumon, D., Marley, M. S., Lodders, K., & Freedman, R. S. 2006, *ApJ*, 642, 495

Fortney, J. J., Lodders, K., Marley, M. S., & Freedman, R. S. 2008, *ApJ*, 678, 1419

Fossati, L., Haswell, C. A., Froning, C. S., et al. 2010, *ApJL*, 714, L222

Fried, D. L. 1965, *Appl. Opt.*, 4, 79

Fulton, B. J., Shporer, A., Winn, J. N., Holman, M. J., Pál, A., & Gazak, J. Z. 2011, *AJ*, 142, 84

Fűrész, G. 2008, PhD thesis, Univ. Szeged

García-Melendo, E., & López-Morales, M. 2011, *MNRAS*, 417, L16

Gardner, J. P., Mather, J. C., Clampin, M., et al. 2006, *Space Science Reviews*, 123, 485

- Gaudi, B. S., & Winn, J. N. 2007, *ApJ*, 655, 550
- Gilliland, R. L., Brown, T. M., Kjeldsen, H., et al. 1993, *AJ*, 106, 2441
- Gilliland, R. L., Brown, T. M., Guhathakurta, P., et al. 2000, *ApJL*, 545, L47
- Greisen, E. W., & Calabretta, M. R. 2002, *A&A*, 395, 1061
- Greisen, E. W., Calabretta, M. R., Valdes, F. G., & Allen, S. L. 2006, *A&A*, 446, 747
- Grether, D., & Lineweaver, C. H. 2006, *ApJ*, 640, 1051
- Gould, A., & Morgan, C. W. 2003, *ApJ*, 585, 1056
- Guillot, T., Burrows, A., Hubbard, W. B., Lunine, J. I., & Saumon, D. 1996, *ApJL*, 459, L35
- Han, E., Wang, S. X., Wright, J. T., et al. 2014, *PASP*, 126, 827
- Harris, D. L., & Uppgren, A. R. 1964, *ApJ*, 140, 151
- Hartman, J. D., Gaudi, B. S., Holman, M. J., et al. 2008, *ApJ*, 675, 1254
- Hauschildt, P. H., Allard, F., Ferguson, J., Baron, E., & Alexander, D. R. 1999, *ApJ*, 525, 871
- Henry, G. W., Marcy, G. W., Butler, R. P., Baron, E., & Vogt, S. S. 2000, *ApJL*, 529, L41
- ESA. 1997, *The Hipparcos and Tycho Catalogues* (ESA SP-1200; Noordwijk: ESA)
- Hebb, L., Collier-Cameron, A., Loeillet, B., et al. 2009, *ApJ*, 693, 1920
- Høg, E., Fabricius, C., Makarov, V. V., et al. 2000, *A&A*, 355, L27
- Holman, M., Touma, J., & Tremaine, S. 1997, *Nature*, 386, 254
- Holman, M. J., & Murray, N. W. 2005, *Science*, 307, 1288

Holman, M. J., Fabrycky, D. C., Ragozzine, D., et al. 2010, *Science*, 330, 51

Howard, A. W., Johnson, J. A., Marcy, G. W., et al. 2011, *ApJ*, 726, 73

Howell, S. B. 1989, *PASP*, 101, 616

Howell, S. B., Sobeck, C., Haas, M., et al. 2014, *PASP*, 126, 398

Hubeny, I., Burrows, A., & Sudarsky, D. 2003, *ApJ*, 594, 1011

Huitson, C. M., Sing, D. K., Vidal-Madjar, A., et al. 2012, *MNRAS*, 422, 2477

Husnoo, N., Pont, F., Hébrard, G., et al. 2011, *MNRAS*, 413, 2500

Jensen, A. G., Redfield, S., Endl, M., et al. 2011, *ApJ*, 743, 203

Jensen, A. G., Redfield, S., Endl, M., Cochran, W. D., Koesterke, L., & Travis Barman
2012, *ApJ*, 751, 86

Jensen, E. L. N. 2013, Tapir, Astrophysics Source Code Library, record ascl:1306.007

Johnson, J. A., Howard, A. W., Marcy, G. W., et al. 2010, *PASP*, 122, 149

Kalas, P., Graham, J. R., Chiang, E., et al. 2008, *Science*, 322, 1345

Kielkopf, J. F., Hart, R., Carter, B., et al. 2014, American Astronomical Society Meeting
Abstracts #223, 223, #148.08

Kipping, D. M. 2010, *MNRAS*, 408, 1758

Knutson, H. A., Charbonneau, D., Noyes, R. W., Brown, T. M., & Gilliland, R. L. 2007,
ApJ, 655, 564

Knutson, H. A., Charbonneau, D., Allen, L. E., Burrows, A., & Megeath, S. T. 2008, *ApJ*,
673, 526

Lang, D., Hogg, D. W., Mierle, K., Blanton, M., & Roweis, S. 2010, *AJ*, 139, 1782

Lehmann-Filhés, R. 1894, *Astronomische Nachrichten*, 136, 17

Lithwick, Y., Xie, J., & Wu, Y. 2012, *ApJ*, 761, 122

Kovács, G., Zucker, S., & Mazeh, T. 2002, *A&A*, 391, 369

Kovács, G., Bakos, G., & Noyes, R. W. 2005, *MNRAS*, 356, 557

Kuzuhara, M., Tamura, M., Kudo, T., et al. 2013, *ApJ*, 774, 11

Langton, J., & Laughlin, G. 2008, *ApJ*, 674, 1106

Latham, D. W., Bakos, G. A., Torres, G., et al. 2009, *ApJ*, 704, 1107

Laughlin, G., & Adams, F. C. 1998, *ApJL*, 508, L171

Lecavelier Des Etangs, A., Ehrenreich, D., Vidal-Madjar, A., et al. 2010, *A&A*, 514, AA72

Léger, A., Rouan, D., Schneider, J., et al. 2009, *A&A*, 506, 287

Lucy, L. B., & Sweeney, M. A. 1971, *AJ*, 76, 544

Lissauer, J. J. 1993, *ARAA*, 31, 129

Lissauer, J. J., Fabrycky, D. C., Ford, E. B., et al. 2011, *Nature*, 470, 53

Lissauer, J. J., Dawson, R. I., & Tremaine, S. 2014, *Nature*, 513, 336

Luhman, K. L. 2012, *ARAA*, 50, 65

Maciejewski, G., Dimitrov, D., Neuhäuser, R., et al. 2010, *MNRAS*, 407, 2625

Maciejewski, G., Errmann, R., Raetz, S., et al. 2011, *A&A*, 528, AA65

Maciejewski, G., Dimitrov, D., Seeliger, M., et al. 2013, *A&A*, 551, AA108

Maciejewski, G., Fernández, M., Aceituno, F. J., et al. 2015, *arXiv:1503.07191*

Mackay, C. D. 1986, ARAA, 24, 255

Madhusudhan, N., & Seager, S. 2010, ApJ, 725, 261

Madhusudhan, N., Knutson, H., Fortney, J. J., & Barman, T. 2014, Protostars and Planets VI, 739

Mandel, K., & Agol, E. 2002, ApJL, 580, L171

Mandell, A. M., Raymond, S. N., & Sigurdsson, S. 2007, ApJ, 660, 823

Marcy, G. W., & Butler, R. P. 1992, PASP104, 270

Marcy, G. W., & Butler, R. P. 2000, PASP, 112, 137

Marois, C., Macintosh, B., Barman, T., et al. 2008, Science, 322, 1348

Martin, D. C., Fanson, J., Schiminovich, D., et al. 2005, ApJL, 619, L1

Martins, J. H. C., Santos, N. C., Figueira, P., et al. 2015, A&A, 576, A134

Mayor, M., & Queloz, D. 1995, Nature, 378, 355

Mazeh, T., Nachmani, G., Holczer, T., et al. 2013, ApJS, 208, 16

McCullough, P. R., Stys, J. E., Valenti, J. A., et al. 2005, PASP, 117, 783

McCullough, P. R., Stys, J. E., Valenti, J. A., et al. 2006, ApJ, 648, 1228

Menou, K., & Rauscher, E. 2009, ApJ, 700, 887

Merline, W. J., & Howell, S. B. 1995, Experimental Astronomy, 6, 163

Meschiari, S., Wolf, A. S., Rivera, E., et al. 2009, PASP, 121, 1016

Milne, E. A. 1921, MNRAS, 81, 361

Mislis, D., Mancini, L., Tregloan-Reed, J., et al. 2015, MNRAS, 448, 2617

- Misra, A. K., & Meadows, V. S. 2014, *ApJL*, 795, L14
- Mollière, P., & Mordasini, C. 2012, *A&A*, 547, A105
- Montalto, M., Gregorio, J., Boué, G., et al. 2012, *MNRAS*, 427, 2757
- Moore, C. E., Minnaert, M. G. J., & Houtgast, J. 1966, National Bureau of Standards Monograph, Washington: US Government Printing Office (USGPO)
- Mortara, L., & Fowler, A. 1981, *Proc. SPIE*, 290, 28
- Mortier, A., Santos, N. C., Sousa, S. G., et al. 2013, *A&A*, 558, AA106
- Mortier, A., Sousa, S. G., Adibekyan, V. Z., Brandão, I. M., & Santos, N. C. 2014, *A&A*, 572, AA95
- Moutou, C., Deleuil, M., Guillot, T., et al. 2013, *Icarus*, 226, 1625
- National Research Council 2010, *New Worlds, New Horizons in Astronomy and Astrophysics*, The National Academies Press, Washington, DC
- Nelder, J. A., & Mead, R. 1965, *Comput. J.*, 7, 308
- Nesvorný, D., & Morbidelli, A. 2008, *ApJ*, 688, 636
- Noguchi, K., Aoki, W., Kawanomoto, S., et al. 2002, *PASJ*, 54, 855
- O'Donovan, F. T., Charbonneau, D., Torres, G., et al. 2006, *ApJ*, 644, 1237
- Ohta, Y., Taruya, A., & Suto, Y. 2005, *ApJ*, 622, 1118
- Paddock, G. F. 1913, *PASP*, 25, 208
- Payne, M. J., Ford, E. B., & Veras, D. 2010, *ApJL*, 712, L86
- Pence, W. D., Chiappetti, L., Page, C. G., Shaw, R. A., & Stobie, E. 2010, *A&A*, 524, AA42

Pepper, J., Gould, A., & DePoy, D. L. 2003, *Acta Astronomica*, 53, 213

Pepper, J., Pogge, R. W., DePoy, D. L., et al. 2007, *PASP*, 119, 923

Pepper, J., Siverd, R. J., Beatty, T. G., et al. 2013, *ApJ*, 773, 64

Perez-Becker, D., & Showman, A. P. 2013, *ApJ*, 776, 134

Pollacco, D. L., Skillen, I., Collier Cameron, A., et al. 2006, *PASP*, 118, 1407

Pont, F., Gilliland, R. L., Moutou, C., et al. 2007, *A&A*, 476, 1347

Queloz, D., Bouchy, F., Moutou, C., et al. 2009, *A&A*, 506, 303

Rasband, W.S., ImageJ, U. S. National Institutes of Health, Bethesda, Maryland, USA,
<http://imagej.nih.gov/ij/>, 1997-2014.

Rasio, F. A., & Ford, E. B. 1996, *Science*, 274, 954

Redfield, S., Endl, M., Cochran, W. M., & Koesterke, L. 2008, *ApJ*, 674, L87

Reiger, S. H. 1963, *AJ*, 68, 395

Ribas, I., & Miralda-Escudé, J. 2007, *A&A*, 464, 779

Richmond, M. W., Droege, T. F., Gombert, G., et al. 2000, *PASP*, 112, 397

Ricker, G. R., Winn, J. N., Vanderspek, R., et al. 2014, *Proc. SPIE*, 9143, 914320

Robinson, T. D., Meadows, V. S., & Crisp, D. 2010, *ApJL*, 721, L67

Sahlmann, J., Ségransan, D., Queloz, D., et al. 2011, *A&A*, 525, A95

Sato, B., Fischer, D. A., Henry, G. W., Laughlin, G., et al. 2005, *ApJ*, 633, 465

Schneider, J., Dedieu, C., Le Sidaner, P., Savalle, R., & Zolotukhin, I. 2011, *A&A*, 532, AA79

- Seager, S., & Sasselov, D. D. 2000, *ApJ*, 537, 916
- Seager, S., & Mallén-Ornelas, G. 2003, *ApJ*, 585, 1038
- Seager, S., & Deming, D. 2010, *ARAA*, 48, 631
- Showman, A. P., Cooper, C. S., Fortney, J. J., & Marley, M. S. 2008, *ApJ*, 682, 559
- Showman, A. P., Menou, K., & Cho, J. Y.-K. 2008, *Extreme Solar Systems*, 398, 419
- Shu, F. H., Adams, F. C., & Lizano, S. 1987, *ARAA*, 25, 23
- Siess, L., Dufour, E., & Forestini, M. 2000, *A&A*, 358, 593
- Sing, D. K., Vidal-Madjar, A., Désert, J.-M., Lecavelier des Etangs, A., & Ballester, G. 2008, *ApJ*, 686, 658
- Sing, D. K., Désert, J.-M., Fortney, J. J., et al. 2011, *A&A*, 527, AA73
- Sivverid, R. J., Beatty, T. G., Pepper, J., et al. 2012, *ApJ*, 761, 123
- Skrutskie, M. F., Cutri, R. M., Stiening, R., et al. 2006, *AJ*, 131, 1163
- Smithsonian Astrophysical Observatory 2000, *Astrophysics Source Code Library*, 0003.002
- Snellen, I. A. G., Albrecht, S., de Mooij, E. J. W., & Le Poole, R. S. 2008, *A&A*, 487, 357
- Southworth, J., Hinse, T. C., Dominik, M., et al. 2012, *MNRAS*, 426, 1338
- Spiegel, D. S., & Madhusudhan, N. 2012, *ApJ*, 756, 132
- Spiegel, D. S., Burrows, A., & Milsom, J. A. 2011, *ApJ*, 727, 57
- Steffen, J. H., Ragozzine, D., Fabrycky, D. C., et al. 2012, *Proceedings of the National Academy of Science*, 109, 7982
- Steffen, J. H., Fabrycky, D. C., Agol, E., et al. 2013, *MNRAS*, 428, 1077

- Sterne, T. E. 1940, Proceedings of the National Academy of Science, 26, 36
- Stetson, P. B. 1987, PASP, 99, 191
- Sullivan, P. W., Croll, B., & Simcoe, R. A. 2014, Proc. SPIE, 9154, 91541F
- Swain, M. R., Vasisht, G., & Tinetti, G. 2008, Nature, 452, 329
- Swain, M. R., Tinetti, G., Vasisht, G., et al. 2009, ApJ, 704, 1616
- Tinetti, G. et al. 2007, Nature, 448, 169
- Torres, G. 1999, PASP, 111, 169
- Torres, G., Bakos, G. Á., Kovács, G., et al. 2007, ApJL, 666, 121
- Torres, G., Winn, J. N., & Holman, M. J. 2008, ApJ, 677, 1324
- Torres, G., Andersen, J., & Giménez, A. 2010, A&A Rev., 18, 67
- Trauger, J. T., & Brown, D. I. 1992, Space Telescope WFPC2 Instrument Science Report,
3
- Tull, R. G. 1998, Proc. SPIE, 3355, 387
- Udalski, A. 2003, Acta Astronomica, 53, 291
- Udalski, A. 2007, Transiting Extrapolar Planets Workshop, 366, 51
- Valenti, J. A., & Piskunov, N. 1996, A&AS, 118, 595
- Valenti, J. A., & Fischer, D. A. 2005, ApJS, 159, 141
- Vanderburg, A., & Johnson, J. A. 2014, PASP, 126, 948
- Veras, D., Ford, E. B., & Payne, M. J. 2011, ApJ, 727, 74
- Vidal-Madjar, A., Lecavelier des Etangs, A., Désert, J.-M., et al. 2003, Nature, 422, 143

- Vidal-Madjar, A., Désert, J.-M., Lecavelier des Etangs, A., et al. 2004, *ApJL*, 604, L69
- Vogt, S. S., Allen, S. L., Bigelow, B. C., et al. 1994, *Proc. SPIE*, 2198, 362
- von Essen, C., Schröter, S., Agol, E., & Schmitt, J. H. M. M. 2013, *A&A*, 555, AA92
- Weldrake, D. T. F., Sackett, P. D., Bridges, T. J., & Freeman, K. C. 2005, *ApJ*, 620, 1043
- Wells, D. C., Greisen, E. W., & Harten, R. H. 1981, *A&AS*, 44, 363
- Winn, J. N. 2009, in *IAU Symp. 253, Transiting Planets*, ed. F. Pont, D. D. Sasselov, & M. J. Holman (Cambridge: Cambridge Univ. Press), 99
- Winn, J. N. 2010, *Exoplanets*, 55
- Wolszczan, A., & Frail, D. A. 1992, *Nature*, 355, 145
- Wood, P. L., Maxted, P. F. L., Smalley, B., & Iro, N. 2011, *MNRAS*, 412, 2376
- Wright, E. L., Eisenhardt, P. R. M., Mainzer, A. K., et al. 2010, *AJ*, 140, 1868
- Wright, E. L., Fakhouri, O., Marcy, G. W., et al. 2011, *PASP*, 123, 412
- Wright, J. T 2012, *PASP*, 117, 657
- Wytenbach, A., Ehrenreich, D., Lovis, C., Udry, S., & Pepe, F. 2015, *arXiv:1503.05581*
- Yang, M., Liu, H.-G., Zhang, H., Yang, J.-Y., & Zhou, J.-L. 2013, *ApJ*, 778, 110
- Young, A. T. 1967, *AJ*, 72, 747
- Zacharias, N., Monet, D. G., Levine, S. E., et al. 2004, *Bulletin of the American Astronomical Society*, 36, 1418

APPENDIX A

COPYRIGHT AGREEMENTS

Item number 3 in the American Astronomical Society copyright agreements shown in this appendix grants permission to republish the material in Chapters 8 and 9 for educational purposes.

AMERICAN ASTRONOMICAL SOCIETY

This agreement must be signed and returned to the editorial office before the American Astronomical Society (AAS) can publish your paper. In the event the article is not judged acceptable for publication in the journal you will be notified in writing and the copyright and all rights conferred by this agreement shall revert to you.

PUBLICATION AND TRANSFER OF COPYRIGHT AGREEMENT Manuscript number: AJ-11770

Article title: KELT-6b: A P~7.9 d Hot Saturn Transiting a Metal-Poor Star with a Long-Period Companion

Names of authors: Karen Collins Jason Eastman Thomas Beatty Robert Siverd B. Scott Gaudi Joshua Pepper John Kielkopf John Johnson Andrew Howard Debra Fischer Mark Manner Allyson Bieryla David Latham Benjamin Fulton Joao Gregorio Lars Buchhave Eric Jensen Keivan Stassun Kaloyan Penev Justin Crepp Sasha Hinkley Rachel Street Phillip Cargile Claude Mack Thomas Oberst Ryan Avril Samuel Mellon Kim K. McLeod Matthew Penny Robert Stefanik Perry Berlind Michael Calkins Qingqing Mao Alexander Richert Darren DePoy Gilbert Esquerdo Andrew Gould J. Marshall Ryan Oelkers Richard Pogge Mark Trueblood Patricia Trueblood

Author Rights: AAS grants to the author(s) (or their below-named employers, in the case of works made for hire) the following rights. All copies of the Article made under any of these rights shall include notice of the AAS copyright.

- (1) All proprietary and statutory rights other than copyright, such as patent rights.
- (2) The right after publication by the AAS to grant or refuse permission to third parties to republish all or part of the Article or a translation thereof. In the case of whole articles only, third parties must first obtain permission from the AAS before any right of further publication is granted. The AAS may choose to publish an abstract or portions of the Article before the AAS publishes it in a journal.
- (3) The right to use all or part of the Article in future works and derivative works of their own of any type, and to make copies of all or part of the Article for the authors' use for educational or research purposes.
- (4) In the case of a work made for hire, the right of the employer to make copies of the Article for the employer's internal use, but not for resale.

Copyright Assignment: Copyright in the Article is hereby transferred to the AAS for the full term of copyright throughout the world, effective as of date of acceptance of the Article for publication in a journal of the AAS. The copyright consists of all rights protected by copyright laws of the United States and of all foreign countries, in all languages and forms of communication, and includes all material to be published as part of the Article in any format or medium. The AAS shall have the right to register copyright to the Article in its name as claimant, whether separately or as part of the journal issue or other medium in which the Article is included.

Authorized signature Karen Collins Date 9/17/2013

Certification of Government Employment: An article prepared by a government officer or employee as part of his or her official duties may not be eligible for copyright, if the authors are all employed by one of the governments of Australia, Canada, New Zealand, the UK, or the US. If *all* the authors of the article are such government employees, one of the authors should sign here. If *any* of the authors is *not* such a government employee, do not sign in this box.

Author signature _____ Date _____

After signing the form, please scan and upload via the peer review system at <http://aj.msubmit.net> or fax to 608-890-2599.

local_p_id: 18815

time: 1379443699

ip address: 74.129.210.48

AMERICAN ASTRONOMICAL SOCIETY

This agreement must be signed and returned to the editorial office before the American Astronomical Society (AAS) can publish your paper. In the event the article is not judged acceptable for publication in the journal you will be notified in writing and the copyright and all rights conferred by this agreement shall revert to you.

PUBLICATION AND TRANSFER OF COPYRIGHT AGREEMENT Manuscript number: ApJ93390


Article title: Spitzer and z' Secondary Eclipse Observations of the Highly Irradiated Transiting Brown Dwarf KELT-1 b

Names of authors: Thomas Beatty Karen Collins Jonathan Fortney Heather Knutson B. Gaudi Jacob Bruns Adam Showman Jason Eastman Joshua Pepper Robert Siverd Keivan Stassun John Kielkopf

Author Rights: AAS grants to the author(s) (or their below-named employers, in the case of works made for hire) the following rights. All copies of the Article made under any of these rights shall include notice of the AAS copyright.

- (1) All proprietary and statutory rights other than copyright, such as patent rights.
- (2) The right after publication by the AAS to grant or refuse permission to third parties to republish all or part of the Article or a translation thereof. In the case of whole articles only, third parties must first obtain permission from the AAS before any right of further publication is granted. The AAS may choose to publish an abstract or portions of the Article before the AAS publishes it in a journal.
- (3) The right to use all or part of the Article in future works and derivative works of their own of any type, and to make copies of all or part of the Article for the authors' use for educational or research purposes.
- (4) In the case of a work made for hire, the right of the employer to make copies of the Article for the employer's internal use, but not for resale.

Copyright Assignment: Copyright in the Article is hereby transferred to the AAS for the full term of copyright throughout the world, effective as of date of acceptance of the Article for publication in a journal of the AAS. The copyright consists of all rights protected by copyright laws of the United States and of all foreign countries, in all languages and forms of communication, and includes all material to be published as part of the Article in any format or medium. The AAS shall have the right to register copyright to the Article in its name as claimant, whether separately or as part of the journal issue or other medium in which the Article is included.

Authorized signature  Date 10/28/13

Certification of Government Employment: An article prepared by a government officer or employee as part of his or her official duties may not be eligible for copyright, if the authors are all employed by one of the governments of Australia, Canada, New Zealand, the UK, or the US. If all the authors of the article are such government employees, one of the authors should sign here. If any of the authors is not such a government employee, do not sign in this box.

Author signature _____ Date _____

After signing the form, please scan and upload via the peer review system at <http://apj.msubmit.net> or fax to 905-538-7173.

local_p_id: 11817
time: 1382990528
ip address: 140.254.79.14

APPENDIX B

KELT-6b AUTHORS AND AFFILIATIONS

Karen A. Collins¹, Jason D. Eastman^{2,3}, Thomas G. Beatty⁴, Robert J. Siverd⁵, B. Scott Gaudi⁴, Joshua Pepper^{5,6}, John F. Kielkopf¹, John Asher Johnson^{7,8}, Andrew W. Howard⁹, Debra A. Fischer¹⁰, Mark Manner^{11,12}, Allyson Bieryla¹³, David W. Latham¹³, Benjamin J. Fulton⁹, Joao Gregorio¹⁴, Lars A. Buchhave^{15,16}, Eric L. N. Jensen¹⁷, Keivan G. Stassun^{5,18}, Kaloyan Penev¹⁹, Justin R. Crepp²⁰, Sasha Hinkley^{7,21}, Rachel A. Street², Phillip Cargile⁵, Claude E. Mack⁵, Thomas E. Oberst²², Ryan L. Avril²², Samuel N. Mellon²², Kim K. McLeod²³, Matthew T. Penny⁴, Robert P. Stefanik¹³, Perry Berlind¹³, Michael L. Calkins¹³, Qingqing Mao⁵, Alexander J. W. Richert²⁴, Darren L. DePoy²⁵, Gilbert A. Esquerdo¹³, Andrew Gould⁴, Jennifer L. Marshall²⁵, Ryan J. Oelkers²⁵, Richard W. Pogge⁴, Mark Trueblood²⁶, and Patricia Trueblood²⁶

¹Department of Physics & Astronomy, University of Louisville, Louisville, KY 40292, USA

²LCOGT Network, 6740 Cortona Drive, Suite 102, Santa Barbara, CA 93117, USA

³Department of Physics Broida Hall, University of California, Santa Barbara, CA 93106, USA

⁴Department of Astronomy, The Ohio State University, 140 W. 18th Ave., Columbus, OH 43210, USA

⁵Department of Physics and Astronomy, Vanderbilt University, Nashville, TN 37235, USA

⁶Department of Physics, Lehigh University, Bethlehem, PA, 18015, USA

⁷Department of Astrophysics, California Institute of Technology, Pasadena, CA 91125, USA

⁸NASA Exoplanet Sc. Inst., CIT Mail Code 100-22, 770 S. Wilson Avenue, Pasadena, CA 91125, USA

⁹Institute for Astronomy, University of Hawaii, 2680 Woodlawn Drive, Honolulu, HI 96822, USA

¹⁰Department of Astronomy, Yale University, New Haven, Connecticut 06511, USA

¹¹Spot Observatory, Nunnally, TN, USA

¹²Montgomery Bell Academy, Nashville, TN, USA

¹³Harvard-Smithsonian Center for Astrophysics, 60 Garden Street, Cambridge, MA 02138, USA

¹⁴Atalaia Group & Crow-Observatory, Portalegre, Portugal

¹⁵Niels Bohr Institute, University of Copenhagen, Juliane Maries vej 30, 21500 Copenhagen, Denmark

¹⁶Centre for Star & Planet Form., Geological Museum, Øster Voldgade 5, 1350 Copenhagen, Denmark

¹⁷Department of Physics and Astronomy, Swarthmore College, Swarthmore, PA 19081, USA

¹⁸Department of Physics, Fisk University, Nashville, TN 37208, USA

¹⁹Princeton University, Princeton, NJ, USA

²⁰Department of Physics, U. of Notre Dame, 225 Nieuwland Science Hall, Notre Dame, IN 46556, USA

²¹NSF Fellow

²²Westminster College, New Wilmington, PA, USA

²³Wellesley College, Wellesley, MA, USA

²⁴Department of Astronomy and Astrophysics, Pennsylvania State University, University Park, PA, USA

²⁵Department of Physics & Astronomy, Texas A & M University, College Station, TX 77843-4242, USA

²⁶Winer Observatory, Sonoita, AZ 85637, USA

CURRICULUM VITAE

NAME: Karen Alicia Collins

ADDRESS: Department of Physics
University of Louisville
Louisville, KY 40292

DOB: May 22, 1962

EDUCATION: B.S. Electrical Engineering
Georgia Institute of Technology
1984

M.S. Electrical Engineering
Georgia Institute of Technology
1990

M.S. Physics & Astronomy
University of Louisville
2008

HONORS AND AWARDS

Manual Schwartz Award for Outstanding Graduate Performance in Physics, 2015

NASA Kentucky Space Grant Consortium Graduate Fellowship, 2009-2013

The William Marshall Bullitt Award for Best Paper in Astronomy, 2012 and 2013

International Year of Astronomy Ambassador, 2009

International Max Planck Research Sum. Sch. Grant, Heidelberg, Germany, 2009

Kentucky Space Grant Consortium Graduate Fellowship, 2006-2008

Graduate Deans Citation, 2008

Manual Schwartz Award for Outstanding Graduate Performance in Physics, 2008

Outstanding Student in the M.S. in Physics Program, 2007-2008

WORK EXPERIENCE

University of Louisville

Graduate Research Assistant, 2006-2015

Tellabs, Inc.

Engineering Manager, 2001-2002

Future Networks, Inc.

Founder, CMO, & VP Sales and Marketing, 1999-2001

Arris Interactive

Sr. Engineering Manager, 1998-1999

Scientific-Atlanta

Engineering Manager, 1994-1998

Nortel

Engineer and Engineering Manager, 1984-1994

ASTRONOMY RELATED SOFTWARE DEVELOPMENT

AstroImageJ

Role: Primary software developer

General purpose astronomical image analysis, but optimized for time-series photometry

<http://www.astro.louisville.edu/software/astroimagej/>

Collins, K. A. and Kielkopf, J. F. 2013, "AstroImageJ: ImageJ for Astronomy", ASCL.Soft, 1309.001

Multi-EXOFAST

Role: Customization and debugging contributions

Transiting exoplanet global system analysis with full MCMC

Eastman et al. 2013

ORAL PRESENTATIONS

1. Vanderbilt University, Astronomy Colloquium, Aug 2014,
Five Years of High-Precision Transit Photometry: TTVs, Atmospheres, and KELT Planet Discoveries
2. Carnegie Institution for Science, DTM, Astronomy Seminar, Mar 2014,
Five Years of High-Precision Transit Photometry at UofL

3. University of Louisville, Physics and Astronomy Colloquium, Mar 2014,
Hunting Down and Probing the Atmospheres of Exoplanets
4. The Local Group, United Kingdom, Public Outreach Talk via Skype, Apr 2014,
The Transiting Exoplanet Discovery Process
5. AAS Kentucky Area Meeting, Oral Session, May 2014,
KELT-6b: A Transiting Mildly-Inflated Saturn with a Bright Metal-Poor Host
6. National Space Grant Directors 25th Anniversary Meeting, Invited Talk, Oct 2013,
KELT-6b: A Transiting Mildly-Inflated Saturn with a Bright Metal-Poor Host
7. Vanderbilt University, KELT Conference, Invited Talk, Aug 2013
KELT-6b and the Planet Discovery Process
8. Vanderbilt University, KELT Conference, AstroImageJ Workshop, Aug 2013
9. AAS Press Briefing, Discovery of KELT-6b, Jun 2013
10. Collins, K. A., Siverd, R., Beatty, T. G., Eastman, J., Gaudi, B. S., et al. 2013,
"KELT-6b: A Transiting Mildly-Inflated Saturn with a Metal-Poor Host", AAS,
222, #302.03
11. The Ohio State University, Astronomy Seminar, Mar 2013,
KELT-6b Overview and Analysis Status
12. Sagan Exoplanet Summer Workshop, POP Presentation, Jul 2012,
AstroImageJ: A New Image Analysis Tool For Astronomy
13. NASA Goddard Space Flight Center, Astronomy Seminar, Jul 2011,
Exoplanet Atmosphere and TTV Science with Sub-meter Class Telescopes

14. Louisville Astronomical Society, Public Outreach Talk, Mar 2010,
Extra-Solar Planet Discoveries: How Serious Amateur Astronomers Can Contribute
Valuable Data to Research
15. University of Louisville, Astronomy Seminar, Feb 2008,
Proto-Planetary Disk Research at U of L

PEER-REVIEWED PUBLICATIONS

1. Bieryla, A., **Collins, K. A.**, Beatty, T. G., et al. 2014, "KELT-7b: A Hot Jupiter
Transiting a Bright $V=8.57$ F-Star", submitted
2. Beatty, T. G., **Collins, K. A.**, Fortney, J., Knutson, H., Gaudi, B. S., et al. 2014,
"Spitzer and z' Secondary Eclipse Observations of the Highly Irradiated Transiting
Brown Dwarf KELT-1b", ApJ, 783, 112
3. **Collins, K. A.**, Eastman, J. D., Beatty, T. G., Siverd, R. J., Gaudi, B. S., Pepper, J.,
et al. 2014, "KELT-6b: A $P \sim 7.9$ Day Hot Saturn Transiting a Metal-poor Star with
a Long-period Companion", AJ, 147, 39
4. Pepper, J., Siverd, R. J., Beatty, T. G., Gaudi, B. S., Stassun, K. G., Eastman, J.,
Collins, K. A., et al. 2013, "KELT-3b: A Hot Jupiter Transiting a $V = 9.8$ Late-F
Star", ApJ, 773, 64
5. Beatty, T. G., Pepper, J., Siverd, R. J., Eastman, J. D., Bieryla, A., Latham, D. W.,
Buchhave, L. A., Jensen, E. L. N., Manner, M., Stassun, K. G., Gaudi, B. S.,
Berlind, P., Calkins, M. L., **Collins, K. A.**, et al. 2012, "KELT-2Ab: A Hot Jupiter
Transiting the Bright ($V = 8.77$) Primary Star of a Binary System", ApJ, 756, LL39

6. Siverd, R. J., Beatty, T. G., Pepper, J., Eastman, J. D., **Collins, K. A.**, Bieryla, A., Latham, D. W., Buchhave, L. A., et al. 2012, "KELT-1b: A Strongly Irradiated, Highly Inflated, Short Period, 27 Jupiter-mass Companion Transiting a Mid-F Star", *ApJ*, 761, 123
7. Grady, C. A., Hamaguchi, K., Schneider, G., Stecklum, B., Woodgate, B. E., McCleary, J. E., Williger, G. M., ..., and **Collins, K. A.** 2010, "Locating the Accretion Footprint on a Herbig Ae Star: MWC 480", *ApJ*, 719, 1565
8. Grady, C. A., Schneider, G., Sitko, M. L., Williger, G. M., Hamaguchi, K., Brittain, S. D., Ablordeppey, K., Apai, D., Beerman, L., Carpenter, W. J., **Collins, K. A.**, Fukagawa, M., et al. 2009, "Revealing the Structure of a Pre-Transitional Disk: The Case of the Herbig F Star SAO 206462 (HD 135344B)", *ApJ*, 699, 1822
9. **Collins, K. A.**, Grady, C. A., Hamaguchi, K., Wisniewski, J. P., Brittain, S., Sitko, M., Carpenter, W. J., Williams, J. P., Mathews, G. S., Williger, G. M., et al. 2009, "HD 100453: A Link Between Gas-Rich Protoplanetary Disks and Gas-Poor Debris Disks", *ApJ*, 697, 557
10. **Collins, K. A.** 2008, "HD 100453: An evolutionary link between protoplanetary disks and debris disks", M.S. Thesis
11. Grady, C. A., Schneider, G., Hamaguchi, K., Sitko, M. L., Carpenter, W. J., Hines, D., **Collins, K. A.**, Williger, G. M., Woodgate, B. E., et al. 2007, "The Disk and Environment of a Young Vega Analog: HD 169142", *ApJ*, 665, 1391
12. **Collins, K. A.**, Grady, C. A., Woodgate, B. E., and Williger, G. M. 2007, "Detection of Optical Ghost in the HST ACS Solar Blind Channel Filter 122M", HST ACS Report, 5

POSTER PRESENTATIONS

1. Shoup, J., Reed, P. A., Joner, M. D., Jensen, E. L. N., **Collins, K. A.**, and Pepper, J. 2014, "Photometric Analysis of the Recently Discovered W UMa Star NR Camelopardalis: Period Change and Spot Migration", AAS, 224, #219.08
2. Oberst, T. E., Beatty, T. G., Bieryla, A., Bozza, V., **Collins, K. A.**, D'Ago, G., Eastman, J. D., et al. 2014, "The KELT Survey for Transiting Planets", EBI Conf., P3P
3. Sharp, H., Orosz, J. A., Welsh, W. F., Stevick, J., Pepper, J., Bieryla, A., Latham, D. W., **Collins, K. A.**, Kielkopf, J. F., Jensen, E. L., and Reed, P. A. 2014, "Accurate Parameters of Two Bright Eclipsing Binaries with Potential for Asteroseismology", AAS, 223, #155.23
4. Kielkopf, J. F., Hart, R., Carter, B., **Collins, K. A.**, Brown, C., Hay, J., Hons, A., and Marsden, S. 2014, "Shared Skies Partnership: A Dual-Site All-Sky Live Remote Observing Initiative for Research and Education", AAS, 223, #148.08
5. **Collins, K. A.**, Kielkopf, J. F., et al. 2013, "KELT-6b: Discovery of a Transiting Saturn-mass Exoplanet with a Bright Metal-Poor Host", Kentucky EPSCoR Conference
6. Pepper, J., Siverd, R., Beatty, T. G., Berlind, P. L., Bieryla, A., Buchhave, L., Calkins, M. L., Cargile, P., **Collins, K. A.**, Crepp, J. R., Depoy, D. L., Eastman, J., et al. 2013, "KELT-3b: A Hot Jupiter Around a Bright $V=9.8$ Late-F Star", AAS, 221, #315.04
7. **Collins, K. A.** and Kielkopf, J. F. 2012, "AstroImageJ: A New Image Analysis Tool for Astronomy", Sagan Exoplanet Summer Workshop, July 2012

8. **Collins, K. A.**, Kielkopf, J. F., and Roberge, A. 2012, "High Precision Photometry for Astrophysics through Kentucky Skies", Kentucky EPSCoR Conference
9. Beatty, T. G., Bieryla, A., Cohen, D., **Collins, K. A.**, Eastman, J., Fulton, B. J., Gary, B., Gaudi, B. S., et al. 2012, "The KELT-North Transit Survey's First Planetary Detections", AAS, 220, #120.07
10. **Collins, K. A.**, Kielkopf, J. F., and Roberge, A. 2011, "A Search For Earth-Like Planets Outside Our Solar System Using Transit Timing Variations", Kentucky EPSCoR Conference
11. **Collins, K. A.** and Kielkopf, J. F. 2010, "A Search for Alkali Metals in the Atmospheres of Exoplanets", DPS, 42, #27.32
12. **Collins, K. A.** and Kielkopf, J. F. 2010, "A Search for Na in the Atmosphere of HD189733b", Kentucky EPSCoR Conference
13. **Collins, K. A.**, Grady, C. A., Hamaguchi, K., Wisniewski, J. P., Brittain, S., Sitko, M., Carpenter, W. J., Williams, J. P., Mathews, et al. 2009, "HD 100453: An Evolutionary Link Between Protoplanetary Disks and Debris Disks", AIPC (COOL STARS, STELLAR SYSTEMS AND THE SUN), 1094, 409
14. Grady, C. A., Schneider, G., Sitko, M. L., Williger, G. M., Hamaguchi, K., Brittain, S. D., Ablordeppey, K., Apai, D., Beerman, L., Carpenter, W. J., **Collins, K. A.**, Fukagawa, M., et al. 2009, "The Disk and Environment of a Young Altair Analog: SAO 206462", AIPC (COOL STARS, STELLAR SYSTEMS AND THE SUN), 1094, 385
15. **Collins, K. A.**, Grady, C., Wisniewski, J. P., Hamaguchi, K., van Boekel, R.,

- Brittain, S., et al. 2007, "The Disk and Environment of Herbig Ae Star HD 100453", AAS, 39, 199
16. Grady, C., Schneider, G., Woodgate, B. E., Wisniewski, J. P., Brittain, S., Sitko, M. L., and **Collins, K. A.** 2007, "The Evolution of Protoplanetary Disks: A Decade of HST Coronagraphy", LYOT Conf., 34
17. Grady, C. A., Schneider, G., Hamaguchi, K., Sitko, M., Carpenter, W., **Collins, K. A.**, Williger, G., Woodgate, B., et al. 2006, "Young Vega and Altair Analogs: Rotationally-Enhanced Activity in HD 169142 and HD 135344", AAS, 38, 1203